# CRUSTAL MELTING IN THE HIMALAYAN OROGEN: FIELD, GEOCHEMICAL AND GEOCHRONOLOGICAL STUDIES IN THE EVEREST REGION, NEPAL

by

**Karen M. Viskupic**

B.A., Geology
Washington University in St. Louis, 1997

SUBMITTED TO THE DEPARTMENT OF EARTH ATMOSPHERIC AND PLANETARY SCIENCES IN PARTIAL FULFILLMENT OF THE REQUIREMENTS FOR THE DEGREE OF

DOCTOR OF PHILOSOPHY
AT THE
MASSACHUSETTS INSTITUTE OF TECHNOLOGY

FEBRUARY 2003



Signature of Author .....
Department of Earth, Atmospheric and Planetary Sciences
December 19, 2002

Certified by .....
Kip V. Hodges
Professor of Geology
Thesis Supervisor

Accepted by .....
Ronald G. Prinn
TEPCO Professor of Atmospheric Chemistry
Department Head

# CRUSTAL MELTING IN THE HIMALAYAN OROGEN: FIELD, GEOCHEMICAL AND GEOCHRONOLOGICAL STUDIES IN THE EVEREST REGION, NEPAL

by
Karen M. Viskupic

Submitted to the Department of Earth Atmospheric and Planetary Sciences
on December 19, 2002 in Partial Fulfillment of the Requirements for the Degree of
Doctor of Philosophy in Geology

## ABSTRACT

A combination of field studies and geochemical techniques were used to investigate the timing and processes involved in leucogranite generation in the Everest region of the Himalayan orogen. Geochemical investigations focused on samples from three outcrops at different structural levels in the Himalayan metamorphic core where in situ crustal melting and multiple generations of leucogranite intrusions were observed.

Accessory phase thermochronological and U-Pb geochronological studies were combined to determine the timing of anatexis in a migmatite at the structurally lowest outcrop. Quantitative measurement of REE and Y in monazites and xenotimes, that were later dissolved and dated by U-Pb IDTIMS, revealed monazite growth at temperatures appropriate for crustal melting (>650°C) between 25.4 and 24.8 Ma, suggesting that anatexis was ongoing at that time.

Further constraints were placed on the timing of crustal melting, granite crystallization and cooling with a detailed U-Pb IDTIMS and $^{40}Ar/^{39}Ar$ study of leucogranite dikes, sills, and the metamorphic rocks they intrude. Backscattered electron imaging of accessory minerals provided important insights into the petrogenesis of monazite, xenotime and zircon, and guided efforts to isolate accessory phase growth domains. In two granitic sills, extensive accessory phase crystallization between ca. 26 and ca. 23 Ma was interpreted to be the result of episodic to semi-continuous melt generation and crystallization at least between those times. These melt products were later entrained in melts that crystallized as syntectonic sills at 21-22 Ma. Younger crosscutting dikes crystallized between 17.5 and 18.3 Ma. The range in accessory phase dates from these dikes and sills that represent magmatic crystallization ages spans from 26.2 to 17.5 Ma, providing evidence for melt generation in one region over roughly 9 million years.

Neodymium isotopic signatures of the same monazite and xenotime grains dated by U-Pb IDTIMS were used to investigate melting processes and granite source-rock characteristics. The dominant control of monazite on the Nd isotopic composition of its host rock was clearly demonstrated. Some Nd isotopic heterogeneities recorded in monazite and in xenotime support a model for melt generation where accessory phases grow from locally derived sources in an isotopically heterogeneous melt.

Thesis Supervisor: Kip V. Hodges
Title: Professor of Geology

## Acknowledgements

Of the many people I need to thank, the most important are my advisors, Kip Hodges, and Sam Bowring. Kip introduced me to Himalayan geology, got me excited to work on leucogranite genesis, and provided all the resources I needed to do so. Kip's attention to detail (especially when my writing was concerned) as well as his reminders to "think big" were essential ingredients in the completion of my thesis. Sam's "just do it" attitude encouraged me to explore new ideas and techniques, and was the source of much motivation. Although I was not officially one of Sam's students, he always treated me as though I was, giving me full access to his lab, his time, and his advice. Certainly, I could not have completed this thesis had it not been for Sam's generosity and support. Many many thanks to Kip and Sam. I also want to thank the other members of my thesis examination committee, Kelin Whipple, Greg Hirth, and Tracy Rushmer, for their enthusiasm and feedback on my thesis work, and the entire G&G faculty, especially Wiki Royden, Tim Grove and Fred Frey.

Although my interest in geology must have started during visits to many of the nation's National Parks with my parents, that interest would likely have gone nowhere had it not been for the interest and encouragement of two outstanding teachers at Smithtown High School, Mrs. Rosenfeld and Mr. Lacertosa. I left high school knowing that I wanted to be a geologist, and luckily ended up at Washington University in St. Louis, where I was educated and encouraged by Bob Dymek, Larry Haskin, Bob Tucker, Jill Pasteris, Randy Korotev, Brad Jolliff, Brent Owens, and many other faculty, students and staff.

My home-away-from-home for the past 5 years has been the MIT TIMS lab, where I have benefited from interactions with Mark Martin, Kathy Davidek Keefe, Dave Hawkins, Kalsoum Abbassi, Frank Dudás, Jahan Ramezani, Jim Crowley, Dan Condon, Bill Olszewski, and my good friend Greg Hoke. Although not usually in the lab, another essential resident of the 11$^{th}$ floor is Pat Walsh, who in addition to providing a fresh perspective on life always manages to keep things running smoothly. Interactions with Greg Hirth, Jörg Renner and Brian Evans on my second generals project and beyond have been both fun and essential to my evolving thoughts, interest, and understanding of melt migration. Thanks also go to Carol Sprague in the education office, and Kathy Keefe and Joe Hankins in Lindgren Library.

I was very fortunate to start my graduate studies at MIT at the same time as Sinan Akciz, Julie Baldwin, Simon Brocklehurst, Marin Clark, and Lindy Elkins Tanton. Graduate school would have been much less fun, and less interesting without them, and I look forward to seeing where the future takes us. Of the large cast of characters at MIT who have contributed in some way to my MIT experience, the most important have been my fellow graduate students. In rough chronological order these include Jim Van Orman, Kirsten Nicolaysen, Alberto Saal, Anke Freidrich, Eric Kirby, Noah Snyder, Arthur White, José Hurtado, Matt Reuer, Jenny Matzel, Steven Singletary, Lindsay Schoenbohm, Cam Wobus, Blair Schoene, Becky Flowers, Jeremy Boyce and Kate Ruhl. Sharing an office with Julie and Jenny has been one of the most helpful and supportive parts of my time at MIT, and whoever takes my place should consider themselves lucky. Jenny and Eric Matzel have graciously shared their home with me during the past 5 months while I was trying to finish my thesis, and Steven and Heidi Singletary helped to keep me well-fed. Their friendship and generosity deserve a world of thanks. Figuring out how to thank Mark Schmitz in just a sentence or two is causing me much stress, and since I know he'd prefer I just turn this in so we can get on with our lives, I'll just have to thank him later.

Lastly, I'd like to thank my family for their support and encouragement, and for always being able to make me laugh.

Karen Viskupic
January, 2003

## Table of Contents

## Introduction

Granites produced by crustal melting (anatexis) are common in collisional mountain belts, with perhaps the best example being the leucogranites of the Himalaya. The Himalayan orogen preserves a record of the subduction of India beneath Asia over the past fifty million years (Rowley, 1996, 1998). Between 15 and 35 million years after the onset of collision, amphibolite facies metamorphism and anatectic melting began within rocks of the Indian plate (Le Fort et al., 1987), generating leucogranitic melts that are now exposed within the Greater Himalayan Sequence in southernmost Tibet and regions of Nepal, Bhutan, India and Pakistan.

Amphibolite-facies ortho- and paragneisses of the Greater Himalayan Sequence are exposed along strike for over 1500 km, and host a remarkable array of granitic crustal melts. At the deepest structural levels, migmatites with centimeter-scale leucosomes provide evidence for *in situ* crustal melting, while the presence of sills and crosscutting dikes attests to the segregation and mobilization of such melts. At the highest structural levels, the abundance of dikes is often described as an injection complex, and many distinct plutons and batholiths are spectacularly exposed along the crest of the range.

The Himalayan leucogranites are intimately linked to the tectonic and thermal evolution of the orogen, having been generated during both active crustal-scale thrusting along the Main Central Thrust, and tectonic denudation by slip along the South Tibetan Fault system. Movement along these two fault systems was contemporaneous during Early Miocene time, and both fault systems appear to have had episodic slip histories over the past 20 million years (Hodges, 2000). Understanding what processes were responsible for producing anatectic melts, how anatectic melting relates to the thermal and tectonic evolution of the Himalayan orogen, and

how, in turn, crustal melts may have influenced the subsequent thermal and tectonic evolution of the orogen, requires a detailed picture of how melting progressed with time.

The goal of my thesis work has been to gain a better understanding of the process of anatexis and the role it played in the evolution of the Himalaya. This dissertation is a compilation of results from four separate studies related to achieving that goal. In contrast to previous studies of Himalayan crustal melts, most of which focused on large plutons (e.g., Vidal, et al., 1982; Scaillet et al., 1990; Guillot & Le Fort, 1995), I examined small-scale leucogranite dikes, sills, and anatectic migmatites in the Everest region of eastern Nepal. The Everest region was chosen for study because it is well exposed, contains a high proportion of leucogranites, and because crosscutting relationships reveal several generations of leucogranite intrusions. In order to determine the timescales of melt generation, melts of different ages need to be sampled. While different intrusive phases may be difficult to identify within a pluton, they are relatively easy to identify in an outcrop of crosscutting dikes and sills. As the data presented in the following chapters show, determining crystallization ages of crustal melts is rarely straightforward due to the compounded affects of protracted accessory phase growth and the presence of inherited radiogenic Pb in xenocrystic accessory minerals. Knowing relative ages of crustal melts based on crosscutting relationships can serve as a guide for the interpretation of geochronologic data. I chose three key outcrops at different structural levels in the Everest region for detailed field, geochemical, and geochronological study based on the number of intrusive phases present, outcrop freshness, country rock lithology, and, of course, accessibility.

Although the analytical techniques used in my studies (U-Pb geochronology, $^{40}Ar/^{39}Ar$ geochronology, Nd and Sr isotope geochemistry) are well-established, many of the methods I used in applying them are novel. In Chapter 1, I used a combination of accessory phase

thermometry and U-Pb geochronology of monazite and xenotime to examine the melting history of the Namche migmatitic orthogneiss. Every grain that was dated was also characterized by backscattered electron imaging and quantitative electron microprobe chemical analysis. This allowed grains with xenocrystic cores to be identified, and provided temperature estimates that guided the interpretation of U-Pb data. This guidance was much needed because the U-Pb dates for monazite and xenotime spanned 10 million years. Temperatures high enough to be associated with crustal melting (>650°C) were only provided by the oldest monazites, leading to the conclusion that partial melting in the migmatitic orthogneiss occurred at 25.4-24.8 Ma. The timing of this crustal melting is at least one million years older than the oldest dated Himalayan leucogranite pluton (Schärer, 1984). In addition to Himalayan-aged monazite and xenotime, inherited pre-Himalayan grains also were identified.

In Chapter 2, I used U-Pb and $^{40}Ar/^{39}Ar$ geochronology to construct a detailed thermal and intrusive history for the Everest region. The eight samples studied came from three outcrops, and included a dike that cut across the migmatitic layering in the orthogneiss described in Chapter 1 as well as country rock gneisses, concordant granite sills, and post-deformational crosscutting dikes from two outcrops at higher structural levels. Results demonstrate that the upper Greater Himalayan Sequence had a more complicated thermal history than is often implied in thermal models of the orogen (e.g. Harrison et al., 1998). Anatexis between ca. 26 and ca. 23 Ma produced melts that did not mobilize, but were partially transported in ca. 21 Ma sill intrusions. Although these rocks experienced rapid cooling to temperatures below ~370°C by 19 Ma, melts were being generated elsewhere as evidenced by the intrusion of post-deformational dikes between 17.5 and 18.3 Ma, which also experienced rapid cooling. Overall, the history of melting preserved in these outcrops spans from ca. 26-23 Ma, with additional melt crystallization

at 21.3-21.8 Ma, and 17.8 to 18.3 Ma. This history implies that temperatures in the Greater Himalayan Sequence remained high enough to support crustal melting in the same region for nearly 10 million years.

In Chapter 3, I used Nd and Sr isotopic signatures in whole-rock granite and gneiss samples, as well as Nd and Sr isotopic signatures of accessory phases, to investigate leucogranite source characteristics and melting processes. The monazite and xenotime grains measured for Nd isotopic composition were the same grains dated in Chapters 1 and 2 using the U-Pb method. As a consequence, the relationship between Nd isotopic composition and grain age could be examined. Nd isotopic signatures in monazites and their host-rocks are generally not distinguishable, and are consistent with monazite controlling the Nd budget of its host-rock. A few demonstrably magmatic monazites, as well as most of the magmatic xenotimes, do not have the same Nd isotopic signature as their host-rocks; In particular, xenotimes have more radiogenic compositions than their host rock or coexisting monazites. These results suggest that monazite and xenotime grew in an isotopically heterogeneous melt, perhaps from the local dissolution of older, inherited accessory phases.

Chapter 4 is a comprehensive and critical review of U-Th-Pb geochronologic data for the Himalayan leucogranites. This review includes a summary of the relative strengths and weaknesses of the two main dating techniques used: isotope dilution thermal ionization mass spectrometry and ion microprobe secondary ion mass spectrometry. Suggestions for the reinterpretation of early geochronologic studies are made based on current knowledge about Pb closure temperatures in monazite and xenotime, and based on the potential for protracted accessory phase growth. The resulting compilation shows no pattern in the spatial and temporal distribution of the Himalayan granites, and reiterates the conclusion made in Chapter 2 that

conditions appropriate for crustal melting need to be met during a period from ca. 26 Ma to ca. 12 Ma. Importantly, almost the entire history of anatectic melting in the Himalaya was recorded in the single outcrops described in Chapters 1 and 2 demonstrating that observations made at the outcrop scale mimic those made at the pluton scale.

All of the chapters in this dissertation, except for the summary in Chapter 5, were written as independent manuscripts, and as such there is some redundancy in them. Chapter 1 was previously published in *Contributions to Mineralogy and Petrology* in March, 2001 (Viskupic & Hodges, 2001).

## References


Guillot, S., Le Fort, P. (1995) Geochemical constraints on the bimodal origin of the High Himalayan leucogranites. Lithos, v. 35, p. 221-234.

Harrison, T.M., Grove, M., Lovera, O.M., Catlos, E.J. (1998) A model for the origin of Himalayan anatexis and inverted metamorphism. Journal of Geophysical Research, v. 103, p. 27017-27032.

Hodges, K.V. (2000) Tectonics of the Himalaya and southern Tibet from two perspectives. Geological Society of America Bulletin, v. 112, p. 324-350.

Hodges, K.V., Hurtado, J.M., Whipple, K.X. (2001) Southward extrusion of Tibetan crust and its effect on Himalayan tectonics. Tectonics, v. 20, p. 799-809.

Le Fort, P., Cuney, M., Deniel, C., France-Lanord, C., Sheppard, S.M.F., Upreti, B.N., Vidal, Ph. (1987) Crustal generation of the Himalayan leucogranites. Tectonophysics, v. 134, p. 39-57.

Rowley, D.B. (1996) Age of initiation of collision between India and Asia: A review of stratigraphic data. Earth and Planetary Science Letters, v. 145, p. 1-13.

Rowley, D.B. (1998) Minimum age of initiation of collision between India and Asia north of Everest based on the subsidence history of the Zhepure Mountain section. Journal of Geology, v. 106, p. 229-235.

Scaillet, B., France-Lanord, C., Le Fort, P. (1990) Badrinath-Gangotri plutons (Garhwal, India): petrological and geochemical evidence for fractionation processes in a high Himalayan leucogranite. Journal of Volcanology and Geothermal Research, v. 44, p. 163-188.

Schärer, U. (1984) The effect of initial $^{230}$Th disequilibrium on young U-Pb ages: the Makalu case, Himalaya. Contributions to Mineralogy and Petrology, v. 67, p. 191-204.

Vidal, Ph., Cocherie, A., Le Fort, P., (1982) Geochemical investigations of the origin of the Manaslu leucogranite (Himalaya, Nepal). Geochimica et Cosmochimica Acta, v. 46, p. 2279-2292.

Viskupic, K., Hodges, K.V. (2001) Monazite-xenotime thermochronometry: methodology and an example from the Nepalese Himalaya. Contributions to Mineralogy and Petrology, v. 141, p. 233-247.

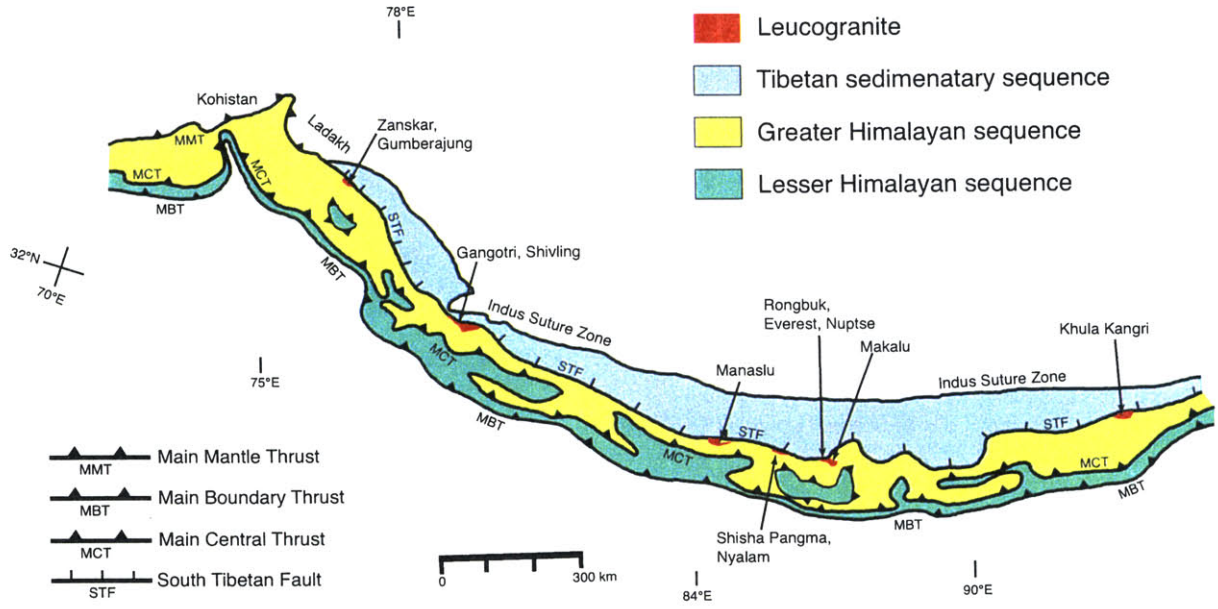


**Figure 1**. Geologic sketch map of the Himalayan orogen.

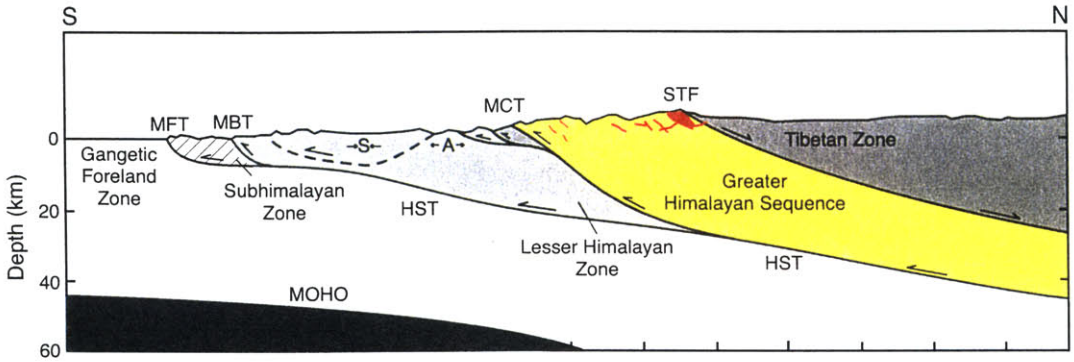


**Figure 2**. Generalized cross section of the Himalayan orogen highlighting the Himalayan metamorphic core, the Greater Himalayan Sequence, which hosts an extensive array of leucogranites. The leucogranites are illustrated schematically in red. Figure modified from Hodges et al. (2001)

Contrib Mineral Petrol (2001) 141: 233–247
DOI 10.1007/s004100100239

Karen Viskupic · Kip V. Hodges

# Monazite–xenotime thermochronometry: methodology and an example from the Nepalese Himalaya

Received: 24 July 2000 / Accepted: 11 December 2000 / Published online: 6 March 2001


**Abstract** Monazite–xenotime thermochronometry involves the integration of petrographic, geochronological, and geochemical techniques to explore the thermal evolution of igneous and metamorphic rocks containing these accessory minerals. The method is illustrated in this paper by application to an orthogneiss sample from the Everest region of the Nepalese Himalaya that contains leucogranitic segregations produced by in-situ anatexis. Observations of phase relationships and the internal structure of accessory minerals made using both transmitted light and electron microscopy revealed the existence of multiple generations of monazite and xenotime and guided microsampling efforts to isolate grain fragments of Himalayan (Tertiary) and pre-Himalayan age. Nearly concordant U–Pb isotopic ratios for 13 single monazite and xenotime grains ranged in age from 28.37 to 17.598 Ma, making determination of the timing of anatexis difficult without additional information. Presuming that monazite and xenotime were in equilibrium over that entire interval, temperatures estimated from the yttrium contents of dated monazites range from 677–535 °C. Only the highest temperatures are consistent with experimental constraints on the conditions necessary to produce anatectic melts of appropriate composition, implying that the ~25.4–24.8 Ma dates for the grains with high apparent equilibration temperatures provide the best estimates for the age of anatexis. Two monazite crystals yielded $^{207}Pb/^{235}U$ dates that are statistically indistinguishable from the $^{207}Pb/^{235}U$ dates of coexisting xenotime crystals, permitting the application of both quantitative Y-partitioning and semi-quantitative Nd-partitioning thermometers as a cross-check for internal consistency. One of these sub-populations of accessory minerals, with a mean $^{207}Pb/^{235}U$ date of 22.364 ± 0.097 Ma, provides inconsistent Y-partitioning (641 ± 39 °C) and Nd-partitioning (515–560 °C) temperatures. We suspect the discrepancy may be caused by the high Th concentration (6.12 wt% $ThO_2$) in this subpopulation's monazite. The Y-partitioning thermometer was derived from experimental data for the (Ce, Y)$PO_4$ binary and may be inappropriate for application to high-Th monazites. For the other subpopulation (mean $^{207}Pb/^{235}U$ date = 22.11 ± 0.22 Ma), the Y- and Nd-partitioning temperatures are indistinguishable: 535 ± 49 and 525–550 °C, respectively. This consistency strongly suggests that the sample experienced a temperature of ~535 °C at 22.11 Ma. This finding is tectonically important because temperatures at higher structural levels were much higher (by ~100 °C) at the same time, lending support to earlier suggestions of a major structural discontinuity within the upper part of the Himalayan metamorphic core at this longitude. An additional finding of uncertain importance is that inherited monazite and xenotime yielded U–Pb discordia with indistinguishable upper intercept ages (465.5 ± 8.7 and 470 ± 11 Ma, respectively) and application of the Y-partitioning thermometer to the inherited monazites produced a restricted range of model temperatures averaging 470 °C. Whether or not these temperatures are geologically meaningful is unclear without independent corroboration of the assumption of equilibrium between the inherited monazites and xenotimes, but it appears that monazite–xenotime thermochronometry may be useful for "seeing through" high-grade metamorphism to extract temperature-time information about inherited mineral suites.

K. Viskupic (✉) · K. V. Hodges
Department of Earth, Atmospheric,
and Planetary Sciences, Massachusetts Institute
of Technology, Cambridge, MA 02139, USA
E-mail: kmviskup@mit.edu
Tel.: +1-617-2585757
Fax: +1-617-2536735

Editorial responsibility: T. L. Grove

## Introduction

The metamorphic cores of many collisional orogens display evidence for crustal melting in the form of

granitic rocks ranging from millimeter-scale anatectic leucosomes to leucogranitic plutons with outcrop areas of hundreds of square kilometers. In many cases, these bodies permit the ages of deformational events to be bracketed if their crystallization ages can be determined both precisely and accurately. The most precise method available for such studies is U–Th–Pb geochronology of accessory minerals such as zircon, monazite, and xenotime, but the accuracy of this method is sometimes clouded by uncertainties in interpreting complex datasets. For example, U–Th–Pb studies of leucogranites from the Himalayan orogen typically result in accessory mineral isotopic ratios that form arrays of nearly concordant points on a concordia diagram with a scatter too large to be explained by analytical uncertainty alone (e.g., Parrish 1990; Zeitler et al. 1993; Noble and Searle 1995; Hodges et al. 1996; Searle et al. 1997; Coleman 1998; Copeland et al. 1988; Hodges et al. 1998; Schneider et al. 1999; Searle et al. 1999; Walker et al. 1999; Simpson et al. 2000). Such scatter results from the combined effects of disequilibrium in the uranium decay series, inheritance, Pb-loss, and protracted mineral growth. Our ability to judge correctly the relative importance of these effects on the isotopic systematics of accessory mineral suites has a profound impact on the quality of an age determination for the host rock.

Advances in determining the effect of temperature on element partitioning between coexisting monazite and xenotime (Gratz and Heinrich 1997; Heinrich et al. 1997; Andrehs and Heinrich 1998; Gratz and Heinrich 1998) suggest a new way to evaluate complex U–Th–Pb data for accessory minerals. We refer to this method – which integrates accessory phase geochemistry and U–Th–Pb geochronology with optical and electron microscopy – as monazite–xenotime thermochronometry. Using data for an anatexite from the Everest region of the Nepalese Himalaya, we show how the method can help guide tectonic interpretations that depend on accurate age or cooling rate determinations for anatectic rocks.

## Geological setting of anatexites and leucogranites in the Everest region

The region around Mount Everest (8,850 m; Fig. 1) is critical for understanding the relationships among Himalayan deformation, metamorphism, and leucogranitic plutonism because it displays field evidence for multiple phases of anatexis interspersed with multiple deformational events. Recent research suggests that rocks form a nested sequence of four packages separated by three N-dipping faults (Carosi et al. 1999; Searle 1999a). The structurally highest package includes Ordovician–Permian carbonate and clastic rocks of the Tibetan Zone (Mu et al. 1973; Yin and Kuo 1978). The base of this succession is marked by a shallowly N-dipping, brittle normal fault mapped as the Qomolungma detachment (Burchfiel et al. 1992). Psammitic and pelitic schists of greenschist to lower amphibolite facies, with subordinate calc-silicate rocks, lie immediately below the Qomolungma detachment. They are referred to as the North Col Formation by Yin and Kuo (1978) and Carosi et al. (1999) and the Everest Series by Searle (1999a). This sequence is separated by a second N-dipping fault (the Lhotse detachment; Searle 1999a) from underlying upper amphibolite facies metapelites and calc-silicate rocks described as the Rongbuk Formation on the north side of the Everest massif by Yin and Kuo (1978) and the Black Gneiss on the south side by Bordet (1961). These rocks are cut by an extensive network of dikes, sills, plutons, and structurally dissected lenses of leucogranite (Carosi et al. 1999; Searle 1999b). Many of the larger leucogranite bodies are shown in Fig. 1. Few of these rocks have been dated, but existing U–Th–Pb data imply protracted leucogranite crystallization over most of the 16–24 Ma interval (Schärer 1984; Copeland et al. 1988; Parrish 1990; Hodges et al. 1992; Harrison et al. 1995; Hodges et al. 1998; Murphy and Harrison 1999; Simpson et al. 2000).

South of the Himalayan range crest, a 3- to 6-km-thick leucogranite complex overlies upper amphibolite-granulite facies orthogneisses and paragneisses, which display abundant textural evidence for in-situ anatectic melting (Bordet 1961; Brunel and Kienast 1986; Lombardo et al. 1993; Pognante and Benna 1993; Carosi et al. 1999). Whereas these units contain variable proportions of leucogranitic leucosome, large bodies of leucogranite similar to those that occur at higher structural levels are absent. Therefore, Searle (1999a) concluded that a regionally extensive, north-dipping reverse fault (the Khumbu thrust) separated the orthogneisses and paragneisses from the overlying Rongbuk Formation–Black Gneiss sequence. This structure is shown in Fig. 1 as mapped by Searle (1999b), although the fault itself has not been observed in the field and was inferred from the distribution of leucogranites and the divergence of foliation above and below the presumed position of the fault (Searle 1999a). If there is no thrust, it is probable that the anatexites exposed at deep structural levels represent the source region of the leucogranite complex and that the large leucogranite bodies are simply the coalesced equivalents of leucosome material in the anatexites. If the thrust exists and postdates leucogranite intrusion, then the source region lies to the north; for example, Searle (1999b) suggested that the leucogranites were derived by melting of protoliths comparable with the Rongbuk Formation–Black Gneiss sequence and were subsequently injected several tens of kilometers along the same structural horizon with little or no vertical transport of magma. In this view, the entire package was then uplifted and thrust southward to its present positional, and the melting history of the anatexites is not related to the melting history of the leucogranite complex source region.

Monazite–xenotime thermochronometry of anatexites allows further examination of these competing

hypotheses by providing constraints on thermal conditions in the orthogneiss–paragneiss sequence over the melting interval: information that can be compared with previously published results for structurally higher rocks that should lie in the hanging wall of the proposed Khumbu Thrust (Simpson et al. 2000). In this paper, we focus on a single representative sample from one of the most common units within the orthogneiss–paragneiss sequence: the Namche Migmatitic Orthogneiss of Lombard (1958).

## Petrography of the Namche Migmatitic Orthogneiss

Regarded by previous workers as an Early Paleozoic granitoid that was remelted during Himalayan orogenesis (Ferrara et al. 1983; Pognante and Benna 1993; Tonarini et al. 1994), the Namche Migmatitic Orthogneiss weathers as a light- to medium-gray, biotite-rich, augen gneiss with minor pods of amphibolite and augen-free, biotite gneiss. The ~1 kg sample we studied (98E5) was collected near the village of Namche Bazaar (Fig. 1). It is conspicuously banded, with ~10% leucogranitic leucosome distributed as millimeter- to centimeter-scale pods and vein-like segregations. Constituent minerals

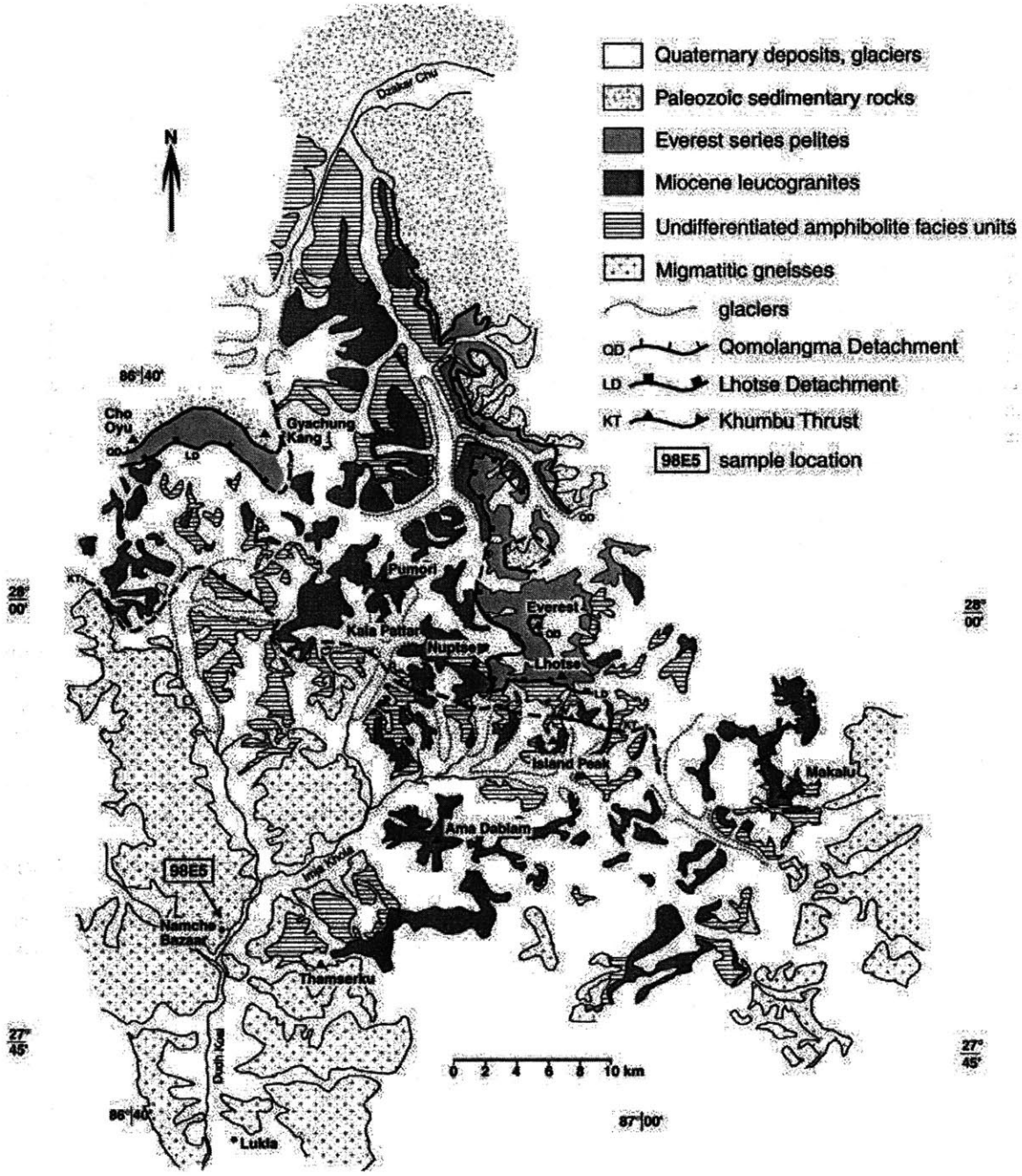


Fig. 1 Geological sketch map of the Everest region of the Nepalese Himalaya (Modified after Carosi et al. 1999; Searle 1999b)

include biotite, sillimanite, cordierite, quartz, plagioclase, and K-feldspar, with accessory apatite, monazite, xenotime and zircon. Limited retrogression is recorded by thin overgrowths of chlorite on some biotite porphyroblasts, patchy pinitization of some cordierites, and minor sericitization of some K-feldspars. A gneissic foliation is defined by biotite, fibrolitic sillimanite, and aligned aggregates of K-feldspar, quartz, plagioclase, and cordierite; we interpret the aggregates as the products of in-situ melting of the host. These leucosomes are slightly coarser grained than the rest of the rock, and are thinly rimmed by biotite and sillimanite. Biotite + sillimanite selvages around the leucosomes may represent hydration of the sample by water released during melt crystallization (Spear et al. 1999). Most crystals in the leucosome are subhedral. A few display straight grain boundaries, and regions of the rock where these grains are abundant display irregular patches of polygonal granoblastic texture. Other crystals, especially large feldspars and cordierites, have conspicuously embayed grain boundaries. A few examples of myrmekitic texture lend additional support to the interpretation of this migmatitic gneiss as an anatexite (Ashworth and McLellan 1985).

Monazite and xenotime in 98E5 occur both as inclusions in major phases and as matrix minerals. Biotite, cordierite, quartz and feldspar host monazite inclusions, and xenotime inclusions are found in biotite and cordierite. Because sillimanite, biotite, and quartz also are found as inclusions in monazite, it is likely that at least these four phases were growing simultaneously at one or more times during the history of the sample. As matrix phases, both monazite and xenotime occur along grain boundaries between all major phases. We observed one mutual contact between monazite and xenotime along a straight grain boundary, suggesting the two minerals were in textural equilibrium during at least some part of the rock's history.

## Internal structure of monazite and xenotime crystals

In order to determine qualitatively whether 98E5 contained multiple accessory mineral suites, we prepared backscattered-electron (BSE) images of a polished thin section, and 26 monazite and 11 xenotime crystals that were hand-picked from a crushed fraction of the sample, mounted in epoxy and polished. All images were obtained with the JEOL Superprobe 733 at the Massachusetts Institute of Technology (MIT) using an accelerating voltage of 15–20 kV and a beam current of 10–15 nA.

BSE images of the mounted grains revealed three types of internal structures in the xenotimes and monazites (Figs. 2 and 3): (1) crystals with no obvious internal zoning; (2) crystals with dark, weakly zoned or unzoned rims mantling anhedral cores that display conspicuous oscillatory zoning and truncated internal crystal faces; and (3) crystals with similar rims mantling

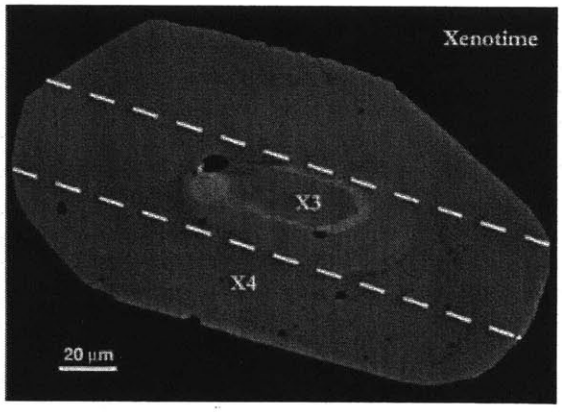


**Fig. 2** Backscattered electron image of xenotime. *Dashed white lines* indicate where the grain was cut to partially isolate the inherited component. Note the truncated oscillatory zoning in the core

anhedral cores with patchy internal zoning. In many cases, a thin bright band marks the interfaces between the rims and cores in monazites. BSE images of the thin section revealed no systematic relationship between the internal structures of grains and their mode of occurrence. For example, zoned and unzoned grains occur both as inclusions and along grain boundaries, and there are no obvious size or shape differences between included and non-included grains.

The gray scale of BSE images of monazite and xenotime is largely a function of U and Th concentration. The 98E5 images suggest the existence of older grains with variable U + Th contents that were partially resorbed prior to the crystallization of rims low in U + Th. The bright (high U + Th) bands between the cores and their overgrowths may represent a reaction boundary, or an intermediate stage of monazite growth. While the BSE images clearly indicate at least two generations of monazite and xenotime occur in 98E5, the cores and rims may represent several generations of growth. This issue, as well as the question of whether the time intervals represented by core-rim "unconformities" were very short or on the order of hundreds of millions of years, were addressed through U–Pb geochronology.

## U–Pb geochronology

Subsequent to BSE imaging, 20 grains and grain fragments of monazite and xenotime were plucked from the mounts for analysis by isotope-dilution, thermal-ionization mass spectrometry (IDTIMS). Prior to analysis, they were washed in acetone and warm water, and dissolved with a mixed $^{205}Pb$–$^{233}U$–$^{235}U$ tracer. Following dissolution, U and Pb were isolated by anion exchange chromatography, and analyzed on a VG Sector 54 mass spectrometer at MIT. Further details of analytical protocols used in the MIT TIMS facility may be found in the caption to Table 1 and in Hawkins and Bowring (1997).

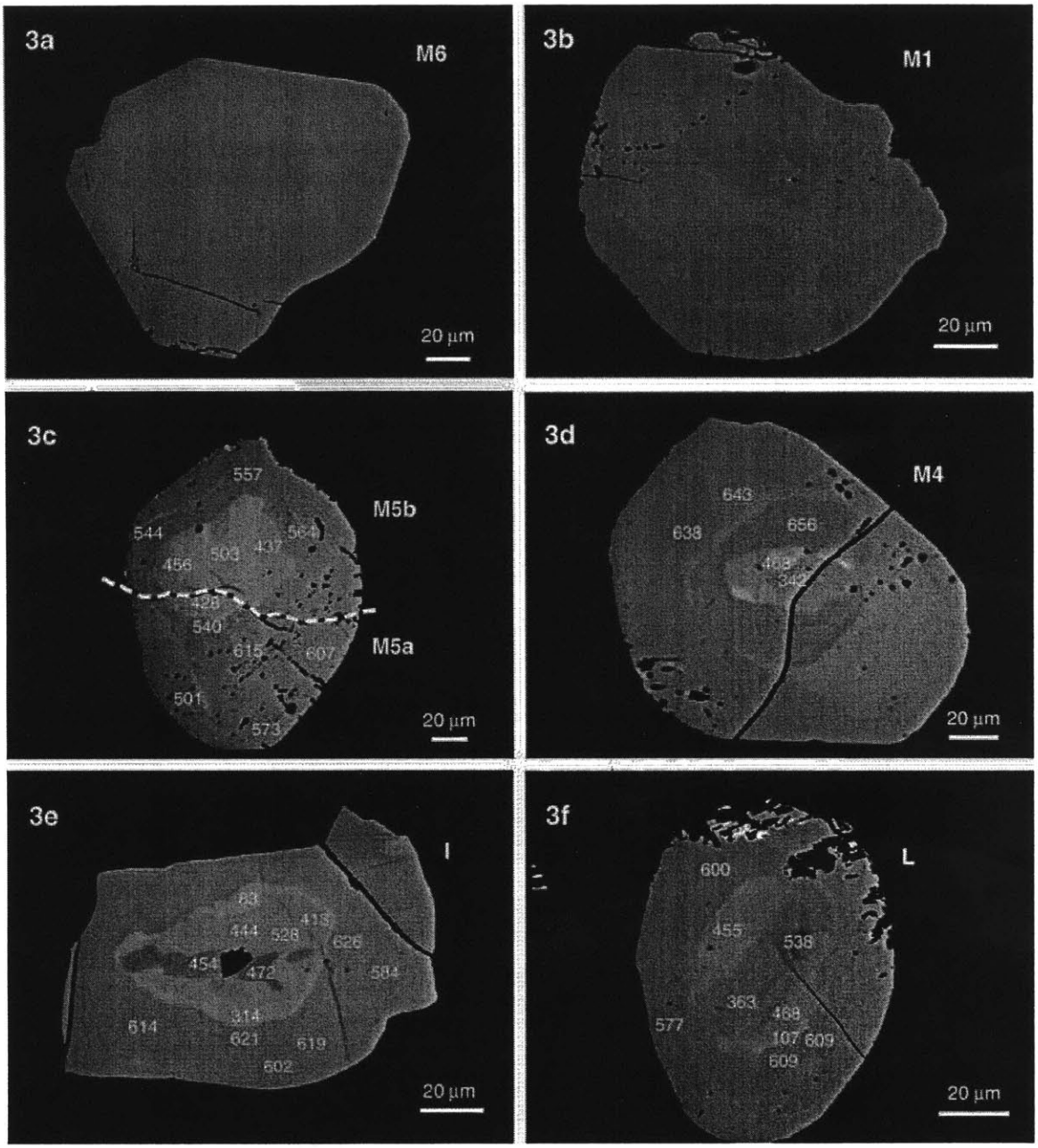


**Fig. 3** Backscattered electron images of monazite showing internal zoning patterns. *White numbers* on images indicate the temperatures calculated at the corresponding location of each electron probe analysis (see Table 3). The grains shown in **e** and **f** were not dated. The *white dashed line* in **c** shows where grain M5 was cut to partially isolate the core and rim components

## Xenotime geochronology

As a first-order test of the age significance of core–rim relationships apparent in BSE images of some xenotimes, an obsidian blade (Hawkins and Bowring 1997) was used to cleave a conspicuously zoned xenotime grain (Fig. 2) into two fragments, one containing the core and a portion of the rim (X3), and another containing mostly rim material (X4). Because of a low radiogenic to common lead ratio (0.7), fragment X4 yielded relatively low-precision isotope ratios of radiogenic lead. X4 plots slightly below concordia with a $^{207}Pb/^{235}U$ date of $20.4 \pm 1.3$ Ma (Table 1, Fig. 4a). Fragment X3 was highly discordant (Fig. 4a) with a $^{207}Pb/^{206}Pb$ date of 441.1 Ma (Table 1). A chord drawn through X3 and X4 has intercepts with concordia that could be interpreted in terms of a ~470-Ma inherited component and a ~20-Ma overgrowth. Isotope ratios for eight additional xenotime grains with no conspicuous cores (X5–X8, X10–X13) plot very near or directly on concordia, with $^{207}Pb/^{235}U$ dates ranging from $28.37 \pm 0.12$ to $17.598 \pm 0.025$ Ma (Table 1, Fig. 4b).

**Table 1** U–Pb results for monazite and xenotime from sample 98E5

| Fraction[a] | Mass[b] (μg) | U[c] (ppm) | Pb[c] (ppm) | Th/U[c] | Common Pb[d] (pg) | $^{206}Pb/^{204}Pb$[e] | $^{208}Pb/^{206}Pb$[f] | $^{206}Pb/^{238}U$[f] | $^{207}Pb/^{235}U$[f] | $^{207}Pb/^{206}Pb$[f] | Correlation coefficient | $^{206}Pb/^{238}U$[g] Date (Ma) | $^{207}Pb/^{235}U$[g] Date (Ma) | $^{207}Pb/^{206}Pb$[g] Date (Ma) |
|---|---|---|---|---|---|---|---|---|---|---|---|---|---|---|
| M7 (1) | 0.4 | 5,892 | 626 | 3.451 | 14.7 | 537.16 | 1.088 | 0.054592(0.23) | 0.42019(0.30) | 0.05582(0.19) | 0.784 | 342.65±0.78 | 356.2±1.1 | 445.4 |
| M5b (f) | 4.4 | 9271 | 1,001 | 4.742 | 8.2 | 1,5701.4 | 1.497 | 0.048876(0.28) | 0.37734(0.08) | 0.05599(0.04) | 0.834 | 307.62±0.20 | 325.08±0.25 | 452.1 |
| X3 (f) | 0.9 | 11,930 | 323 | 0.095 | 13.1 | 1,495.62 | 0.030 | 0.028064(0.11) | 0.21559(0.31) | 0.05572(0.27) | 0.503 | 178.42±0.20 | 198.2±0.6 | 441.1 |
| M5a (f) | 0.6 | 14,810 | 260 | 4.005 | 6.8 | 728.44 | 1.283 | 0.008508(0.34) | 0.05995(0.42) | 0.05110(0.23) | 0.843 | 54.62±0.19 | 59.12±0.25 | 245.4 |
| M4 (1) | 1.3 | 4,694 | 71 | 4.419 | 22.3 | 118.35 | 1.417 | 0.005678(0.66) | 0.03798(1.67) | 0.04851(1.46) | 0.494 | 36.50±0.24 | 37.85±0.63 | 124.2 |
| X13 (1) | 16.4 | 3,942 | 22 | 0.182 | 96.7 | 207.94 | 0.058 | 0.004400(0.12) | 0.02834(0.43) | 0.04671(0.40) | 0.398 | 28.303±0.035 | 28.37±0.12 | 34.3 |
| M10 (1) | 2.9 | 8,360 | 72 | 4.242 | 8.2 | 778.51 | 1.361 | 0.004076(0.28) | 0.02564(0.32) | 0.04563(0.16) | 0.869 | 26.221±0.073 | 25.707±0.083 | -22.1 |
| M1 (1) | 7.4 | 3,247 | 31 | 4.824 | 16.2 | 403.78 | 1.548 | 0.004047(0.27) | 0.02533(0.44) | 0.04539(0.34) | 0.652 | 26.035±0.069 | 25.39±0.11 | -34.8 |
| M9 (1) | 1.8 | 11,654 | 105 | 4.365 | 20.7 | 269.48 | 1.400 | 0.003861(0.32) | 0.02467(0.44) | 0.04634(0.29) | 0.751 | 24.839±0.079 | 24.75±0.11 | 15.6 |
| X12 (1) | 10.2 | 8,426 | 31 | 0.175 | 23.8 | 854.32 | 0.056 | 0.003605(0.10) | 0.02323(0.18) | 0.04673(0.15) | 0.580 | 23.195±0.024 | 23.313±0.043 | 35.5 |
| X6 (1) | 3.6 | 10,424 | 37 | 0.182 | 8.0 | 1,100.21 | 0.058 | 0.003608(0.21) | 0.02321(0.49) | 0.04666(0.41) | 0.529 | 23.216±0.050 | 23.30±0.11 | 31.9 |
| X11 (1) | 3.2 | 9,084 | 50 | 0.160 | 67.0 | 114.33 | 0.051 | 0.003488(0.23) | 0.02234(0.77) | 0.04646(0.71) | 0.426 | 22.443±0.053 | 22.44±0.17 | 21.7 |
| X10 (1) | 2.9 | 15,584 | 111 | 0.150 | 170.0 | 78.83 | 0.048 | 0.003572(0.14) | 0.02229(0.73) | 0.04526(0.69) | 0.399 | 22.98±0.30 | 22.38±0.16 | -41.7 |
| M8 (1) | 0.6 | 17,584 | 177 | 4.841 | 23.8 | 121.80 | 1.553 | 0.003617(0.59) | 0.02221(0.90) | 0.04453(0.65) | 0.695 | 23.27±0.14 | 22.30±0.20 | -81.4 |
| M6 (1) | 5.9 | 5,572 | 36 | 3.180 | 7.7 | 983.33 | 1.020 | 0.003528(0.23) | 0.02208(0.26) | 0.04539(0.12) | 0.881 | 22.70±0.50 | 22.172±0.058 | -34.8 |
| X5 (1) | 1.6 | 24,597 | 158 | 0.156 | 124.1 | 91.34 | 0.050 | 0.003567(0.23) | 0.02208(1.59) | 0.04489(1.50) | 0.474 | 22.952±0.052 | 22.17±0.35 | -61.5 |
| X7 (1) | 0.8 | 6,944 | 22 | 0.162 | 2.5 | 499.35 | 0.052 | 0.003413(0.40) | 0.02191(0.71) | 0.04655(0.56) | 0.608 | 21.965±0.089 | 22.00±0.16 | 26.1 |
| X4 (f) | 0.6 | 11,801 | 78 | 0.131 | 29.5 | 67.43 | 0.042 | 0.003153(0.95) | 0.02024(6.23) | 0.04656(5.85) | 0.466 | 20.29±0.19 | 20.3±1.3 | 26.5 |
| X8 (1) | 8.7 | 12,841 | 33 | 0.105 | 3.8 | 5,222.2 | 0.034 | 0.002726(0.12) | 0.01748(0.14) | 0.04651(0.08) | 0.827 | 17.549±0.020 | 17.598±0.025 | 24.3 |

[a] Fractions are designated by mineral: *M* monazite; *X* xenotime. All fractions were single grains, or fragments of grains, signified by (1) or (f)

[b] Sample weights, estimated using sample dimensions determined from a grided video monitor, are known to within 20% based on comparisons of estimated and measured weights

[c] Compositions expressed as ppm U, ppm total Pb, and Th/U. Th/U ratios were calculated from the $^{208}Pb/^{206}Pb$ ratios

[d] Total common Pb

[e] Measured ratio corrected for fractionation and spike only; Pb fractionation is 0.12±0.04% per a.m.u. for multicollector Faraday analyses and 0.015±0.04% per a.m.u. for single collector Daly analysis based on repeated analyses of NBS-981

[f] Isotopic ratios are corrected for fractionation, spike, blank, and initial common Pb. U blank = 1 pg ± 50%; data were reduced using a Pb blank of 3.5 pg ± 50% except for analyses with <3.5 pg total common Pb, in which case this value was used as blank and the uncertainty reduced to 20%. Blank composition: $^{206}Pb/^{204}Pb = 19.10$, $^{207}Pb/^{204}Pb = 15.71$, $^{208}Pb/^{204}Pb = 38.65 \pm 0.1\%$ ($1\sigma$); initial common Pb composition estimated by that of leached R113 leucogranite feldspars (Hodges et al. 1998): $^{206}Pb/^{204}Pb = 18.73$, $^{207}Pb/^{204}Pb = 15.71$, $^{208}Pb/^{204}Pb = 38.82 \pm 0.01\%$ ($2\sigma$). Numbers in parentheses are the % error reported at the $2\sigma$ confidence interval

[g] Uncertainties in millions of years at the $2\sigma$ confidence interval

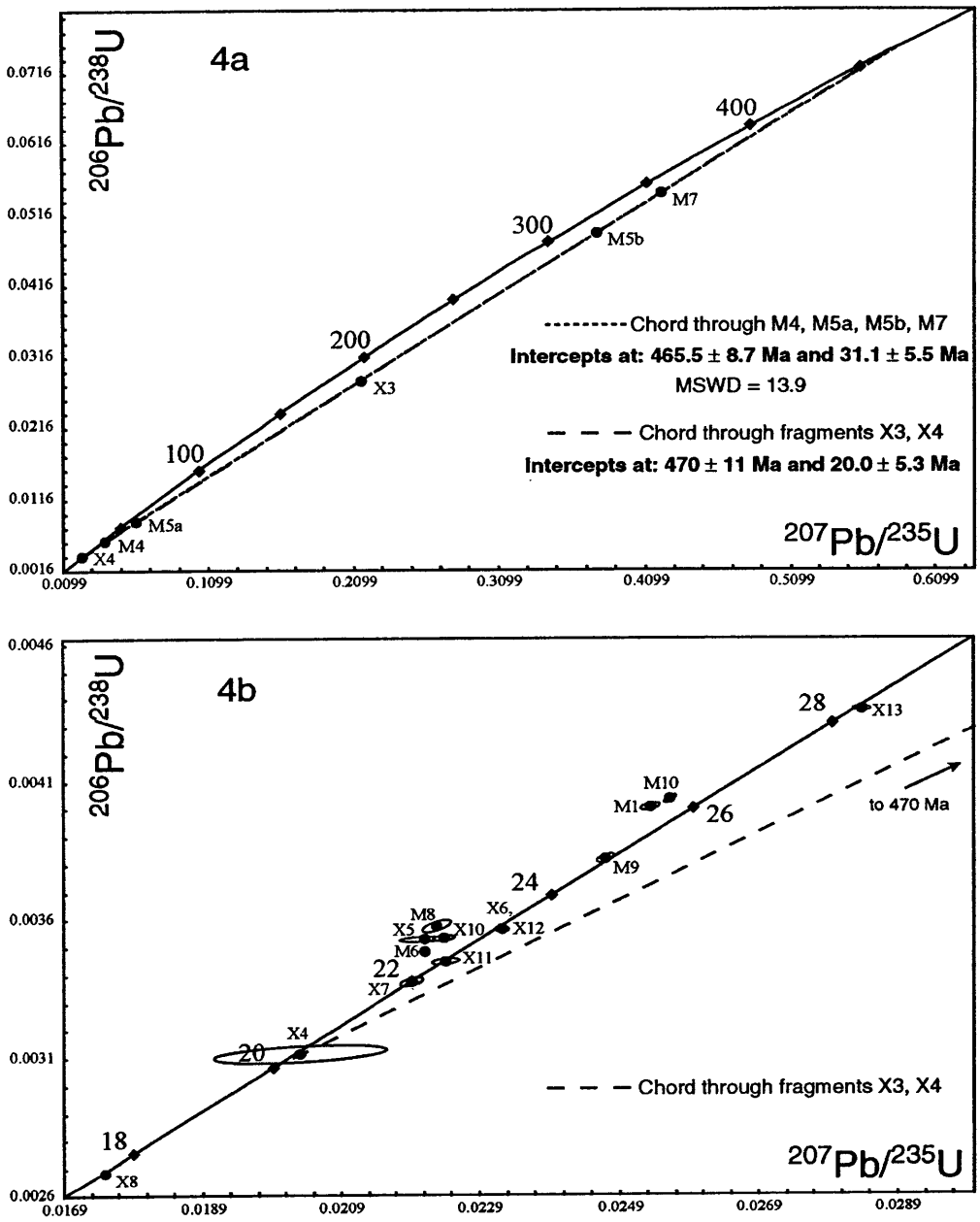


**Fig. 4** Concordia diagrams for **a** monazite grain fragments, composite monazites and xenotime grain fragments, and **b** for single monazite and xenotime grains

## Monazite geochronology

U–Pb isotopic data for a monazite crystal with an older core and a neoblastic overgrowth (Fig. 3c) add further support to the interpretation that the Namche Migmatitic Orthogneiss protolith is an Early Paleozoic granitoid. Taking advantage of a pre-existing fracture in the grain, we cleaved it into rim-rich (M5a) and core-rich (M5b) fragments. Analysis of the former yielded highly discordant U–Pb isotope ratios with a $^{207}Pb/^{206}Pb$ date of 452.1 Ma (Table 1, Fig. 4a), which is about 10 Ma older than the $^{207}Pb/^{206}Pb$ date of the core-rich xenotime fragment X3. Rim-rich fragment M5a also displayed normal discordance, with a $^{207}Pb/^{206}Pb$ date of 245.4 Ma. Two other zoned grains (M4 and M7) yielded discordant isotope ratios with $^{207}Pb/^{206}Pb$ dates of 124.2 (M4) and 445.4 Ma (M7, Table 1). A best-fit chord drawn through M7, M4, M5a, and M5b (Fig. 4a) intersects concordia at $466 \pm 9$ and $31 \pm 6$ Ma with a mean squared weighted deviation (MSWD; Wendt and Carl 1991) of 13.9. Despite the high MSWD, which probably reflects real differences in the ages of overgrowths during Himalayan orogenesis, these data strongly argue for inherited Ordovician monazites of similar or identical age to the inherited xenotime.

Five monazite grains with little or no discernable zoning (M1, M6, M8, M9, M10; Table 3) yielded reversely discordant isotope ratios (Fig. 4b). Reverse discordance is a common feature of U–Pb data sets for young monazites and is thought to indicate $^{230}Th$ disequilibrium (Schärer 1984; Parrish 1990); as a conse-

quence, we regard the $^{207}Pb/^{235}U$ dates – ranging from $25.707 \pm 0.083$ to $22.172 \pm 0.058$ Ma – as the most reliable estimates of the ages of these grains.

## Alternative interpretations of nearly concordant monazite and xenotime data

Unzoned crystals and rim fragments of monazite and xenotime from sample 98E5 yield U–Pb isotopic data scattered along concordia from 28.37 to 17.598 Ma, an age range that is two or three orders of magnitude larger than the typical $2\sigma$ analytical uncertainty for any single analysis. We review below the effects that could be responsible for data dispersion of this kind and show how each, if presumed to be the sole mechanism for dispersion, has a different implication for the age of melting in 98E5.

### Inheritance

Although there is clear evidence for the existence of very old (Ordovician) accessory minerals in 98E5, it is also possible that the sample contains an inherited population that is not much older than the thermal event responsible for anatexis. At higher structural levels in the Everest area, U–Pb monazite data for pelitic gneisses and titanite data for calc-silicate rocks from the Rongbuk Formation–Black Gneiss sequence provide evidence for two metamorphic events at ~32 and ~23–20 Ma (Hodges et al. 1992; Simpson et al. 2000). One extreme interpretation of the data in Fig. 4b is that the youngest date in the array (X8 – $17.598 \pm 0.025$ Ma) is the best estimate of the timing of leucosome crystallization and that all older, nearly concordant crystals and fragments contain inherited material that grew during earlier Early Oligocene–Early Miocene metamorphic events. If this were the case, it would be difficult to ascertain exactly how many monazite–xenotime growth events are represented by the array because even the apparently unzoned grains that were used for our study may have very thin overgrowths of ~17.6 Ma material that went undetected in the BSE images. However, the simplest interpretation of the data, presuming that the apparently unzoned grains actually represent single-event growth, is that there were three main pre-anatexis growth intervals at ~22.0–23.3, ~24.8–25.7, and ~28.4 Ma.

### Lead loss

A completely different view of the 98E5 data emerges if we presume that all scatter in the near-concordant analyses is caused by Pb loss by volume diffusion or some other mechanism. Studies of the diffusion of Pb in monazite (Harrison et al. 1994; Suzuki et al. 1994; Smith and Giletti 1997) and zircon (Lee et al. 1997; Ashwal et al. 1999) suggest that accessory minerals may experience significant diffusive Pb loss if metamorphism and anatexis occurred at relatively high temperatures and the rocks subsequently were maintained at those temperatures during a protracted thermal event or were subjected to later metamorphism. Although there has been no published evidence for significant Pb loss from xenotime, the possibility cannot be dismissed given the lack of Pb diffusion data for this mineral. If Pb loss alone was the cause of the dispersion shown in Fig. 4b, the oldest nearly concordant $^{207}Pb/^{235}U$ date in the array (X13 – $28.37 \pm 0.12$ Ma) could be reasonably regarded as the best estimate of the age of leucosome crystallization in 98E5. Following this interpretation, the youngest date in the array (X8 – $17.598 \pm 0.025$ Ma) provides a maximum estimate for the age of the Pb loss event (or events) because any discordance produced by Pb loss over the past 20 million years will form a trajectory subparallel to the concordia curve.

### Protracted mineral growth

A third interpretation of Fig. 4b is that each isotope ratio represents exactly the crystallization age of that grain, or a physical mixture of intra-grain domains with different ages. In this case, some grains were peak metamorphic/anatectic phases – perhaps crystallizing over a significant time interval – whereas others grew at lower, prograde or retrograde subsolidus temperatures. The array in Fig. 4b, if interpreted as solely caused by peak metamorphic/anatectic and subsequent subsolidus retrograde mineral growth, would represent leucogranite crystallization at 28.37 Ma, followed by (1) several episodes of accessory mineral growth, the youngest at 17.598 Ma; or (2) a single episode of metamorphic mineral growth at ~17.6 Ma, with intermediate ages representing intergrowths of the magmatic and metamorphic components that could not be distinguished in the BSE images.

## Choosing the best interpretation

While the end-member interpretations described above imply that anatexis occurred at either 28.37 or 17.598 Ma in 98E5, many intermediate interpretations are equally viable if a combination of inheritance, Pb loss, and protracted mineral growth played a role in the dispersion shown in Fig. 4b. For example, we could construct an ad hoc interpretation of the 98E5 data that is consistent with just the two metamorphic "events" at 32.2 and 22.7 Ma deduced by Simpson et al. (2000) for the Kala Pattar–Everest Basecamp area (Fig. 1) 25 km to the northeast of the 98E5 sample locality. In this interpretation, crystals X6, X10, X11 and X12 (with a mean $^{207}Pb/^{235}U$ age of 22.85 Ma) represent the age of peak metamorphism and anatexis, the older near-concordant grains are 32.2 Ma metamorphic monazites and xeno-

times that experienced varying degrees of Pb loss during the anatectic event, and the near-concordant grains with dates younger than 22.7 Ma have lost some of their radiogenic Pb during cooling from the metamorphic peak. The question is: what additional evidence can be brought to bear on the problem to help us determine the best interpretation of a complex data set when there are so many viable alternatives? Certainly knowing the crystallization temperatures of the monazites and xenotimes would be an asset, and we next explore the utility of trace-element partitioning thermometry for providing such information.

## The temperature dependence of trace-element partitioning between monazite and xenotime

A limited solid solution exists between the rare-earth phosphates monazite and xenotime. It can be described as (LREE)$PO_4$–(Y, HREE)$PO_4$, where LREE represents the light rare-earth elements lanthanum through gadolinium and HREE refers to the heavy rare-earth elements terbium through lutetium. Experimental and empirical studies show that the equilibrium partitioning of the rare-earth elements and yttrium between coexisting monazite and xenotime is both pressure and temperature dependent (Gratz and Heinrich 1997; Heinrich et al. 1997; Andrehs and Heinrich 1998; Gratz and Heinrich 1998). In particular, the partitioning of yttrium has been calibrated as a geothermometer by Gratz and Heinrich (1997) through experiments on the $CePO_4$–$YPO_4$ binary. Their thermometer can be expressed as:

$$T = \frac{\ln\left[\frac{100X_{Ymz}}{1.459+0.0852P}\right]}{2.2745 \times 10^{-3}} \quad (1)$$

where T is the equilibration temperature in °C, $X_{Ymz}$ is the mole fraction of Y in monazite, and P is the pressure in kbar. Calculation of a temperature using Eq. (1) – hereafter referred to as YMX thermometry – requires an independent estimate of pressure, but the pressure dependence of the reaction is weak; varying the estimated pressure by a kilobar leads to a change in the calculated temperature of only about 10 °C for most samples. A more important concern is whether or not coexisting monazite and xenotime in a sample were, in fact, at chemical equilibrium at the time of their crystallization, particularly given the persistence of both minerals through high-grade metamorphism and melting at crustal pressure and temperature conditions. The combination of U–Pb geochronology with YMX thermometry offers some assistance with this problem. If a sample contains both monazite and xenotime that yield the same U–Pb dates, there is a higher probability that the two were in equilibrium, and that the temperature calculated with Eq. (1) is geologically meaningful. If no xenotime in the sample yields an age equivalent to that of the monazite, then the argument that a YMX temperature for the monazite is meaningful is less persuasive, though still permissible.

Another way to evaluate the assumption of monazite–xenotime equilibrium is to compare the temperature calculated with the YMX thermometer with somewhat less well-understood constraints on the temperature dependence of rare-earth element partitioning between the two minerals. One of the most useful elements in this regard is Nd which – at least for empirical data sets (Andrehs and Heinrich 1998) – shows a much stronger affinity for monazite at lower temperatures. In our study of sample 98E5, we used this characteristic to determine semi-quantitative temperature estimates for comparison with YMX temperatures.

### Trace element analytical methods

Using the same grain mounts that were prepared for BSE imaging, we obtained quantitative concentration data for LREE, Y, Ca, Th, and P in monazites and xenotimes from sample 98E5 with the JEOL Superprobe 733 at MIT. Microprobe operating conditions for these analyses are shown in Table 2. All analyses were made using a beam diameter of 1 μm, and corrections for peak overlaps were made according to empirically determined factors similar to those of Amli and Griffin (1975). Assuming an equilibration pressure of 5.09 kbar based on thermobarometric results for pelitic gneisses collected near the 98E5 sample locality (Hubbard 1989), YMX temperatures were calculated for 74 spots in 25 monazite grains. They are reported in Table 3 along with $2\sigma$ precision estimates derived by propagating analytical uncertainties from the microprobe measurements, and from the pressure estimate. Nd partitioning temperatures (Table 4) were estimated for coeval xenotime and monazite grains (as discussed below) by comparison of calculated Nd distribution coefficients with graphs in Andrehs and Heinrich (1998). No uncertainties are quoted for these estimates because they are only semi-quantitative.

**Table 2** Electron microprobe operating conditions for monazite and xenotime analysis

| Element[a] | X-ray line | Crystal | Count time (s) | Standard |
|---|---|---|---|---|
| P | Kα | TAP | 20 | $CePO_4$ |
| Y | Lα | TAP | 40 | $YPO_4$ |
| Th | Mα | PET | 40 | $ThSiO_4$ |
| Ca | Kα | PET | 40 | Apatite |
| La | Lα | LIF | 40 | $LaPO_4$ |
| Ce | Lα | LIF | 40 | $CePO_4$ |
| Pr | Lα | LIF | 40 | $PrPO_4$ |
| Nd | Lα | LIF | 40 | $NdPO_4$ |
| Sm | Lα | LIF | 40 | $SmPO_4$ |
| Gd | Lα | LIF | 40 | $GdPO_4$ |

[a] Analyses were made at an accelerating voltage of 15 kV, with a beam current of 10 nA and a beam diameter of 1 μm

**Table 3** Compositions and calculated temperatures for monazites in sample 98E5

| Grain[a] | Location[b] | $La_2O_3$[c] | $Ce_2O_3$[c] | $Pr_2O_3$[c] | $Nd_2O_3$[c] | $Sm_2O_3$[c] | $Gd_2O_3$[c] | $Y_2O_3$[c] | CaO[c] | $ThO_2$[c] | $P_2O_5$[c] | Total | $Y_{mz}$[d] | T[e] (°C) | 2σ error in T[f](°C) |
|---|---|---|---|---|---|---|---|---|---|---|---|---|---|---|---|
| M1 | h | 10.09 | 23.81 | 2.74 | 10.55 | 2.33 | 2.03 | 4.04 | 1.85 | 6.74 | 30.55 | 94.73 | 0.0883 | 677 | 37 |
| A | h | 12.14 | 26.65 | 2.84 | 10.84 | 2.05 | 1.34 | 3.93 | 1.39 | 5.31 | 30.30 | 96.80 | 0.0834 | 652 | 38 |
| M8 | h | 11.08 | 25.63 | 2.68 | 10.52 | 2.19 | 1.67 | 3.76 | 1.60 | 6.12 | 30.07 | 95.31 | 0.0813 | 641 | 39 |
| B | h | 12.07 | 25.81 | 2.95 | 10.82 | 2.24 | 1.41 | 3.62 | 1.27 | 4.95 | 30.48 | 95.61 | 0.0786 | 626 | 41 |
| M9 | h | 12.34 | 26.46 | 2.86 | 10.83 | 2.39 | 1.67 | 3.63 | 1.27 | 4.41 | 30.42 | 96.29 | 0.0778 | 622 | 41 |
| C | h | 12.75 | 26.83 | 3.10 | 10.96 | 2.30 | 1.36 | 3.58 | 1.23 | 4.49 | 30.87 | 97.46 | 0.0760 | 612 | 41 |
| D | h | 11.84 | 26.83 | 2.90 | 11.04 | 2.39 | 1.38 | 3.40 | 1.28 | 5.01 | 30.47 | 96.54 | 0.0730 | 593 | 43 |
| E | h | 13.17 | 27.36 | 3.09 | 11.39 | 2.04 | 1.37 | 3.28 | 1.08 | 4.32 | 30.44 | 97.54 | 0.0695 | 572 | 45 |
| F | h | 12.03 | 26.86 | 2.84 | 11.27 | 2.26 | 1.60 | 3.16 | 1.28 | 5.18 | 29.70 | 96.19 | 0.0676 | 560 | 47 |
| M6 | h | 12.56 | 27.57 | 2.81 | 11.55 | 2.24 | 1.39 | 3.04 | 1.37 | 4.90 | 30.95 | 98.38 | 0.0639 | 535 | 49 |
| G | h | 12.65 | 27.61 | 3.00 | 11.41 | 2.24 | 1.48 | 2.88 | 1.22 | 4.26 | 30.68 | 97.43 | 0.0613 | 517 | 51 |
| M7 | c | 11.86 | 26.49 | 2.93 | 11.28 | 2.55 | 1.73 | 2.77 | 1.53 | 4.83 | 31.04 | 97.01 | 0.0594 | 503 | 53 |
| H | h | 12.35 | 26.08 | 2.81 | 11.17 | 2.29 | 1.41 | 2.73 | 1.49 | 4.90 | 31.04 | 96.27 | 0.0592 | 501 | 54 |
| I | c | 12.26 | 26.08 | 2.63 | 11.08 | 2.14 | 1.35 | 2.91 | 1.54 | 5.47 | 30.70 | 96.16 | 0.0629 | 528 | 51 |
| | c | 15.37 | 30.49 | 3.17 | 13.03 | 2.66 | 1.19 | 2.69 | 0.36 | 0.35 | 30.95 | 100.25 | 0.0554 | 472 | 55 |
| | c | 15.77 | 31.64 | 3.09 | 11.70 | 2.05 | 1.54 | 2.60 | 0.32 | 0.07 | 30.32 | 99.10 | 0.0531 | 454 | 56 |
| | c | 12.37 | 27.65 | 2.93 | 11.50 | 2.13 | 1.61 | 2.68 | 1.37 | 4.19 | 30.50 | 96.93 | 0.0520 | 444 | 55 |
| | c | 12.66 | 25.97 | 2.98 | 11.62 | 2.31 | 1.71 | 2.53 | 1.51 | 5.46 | 30.65 | 97.40 | 0.0484 | 413 | 58 |
| | c-be | 12.97 | 26.62 | 2.82 | 11.40 | 2.17 | 1.97 | 1.98 | 1.37 | 4.79 | 29.83 | 95.92 | 0.0386 | 314 | 74 |
| | c-be | 12.49 | 28.30 | 3.30 | 11.88 | 2.10 | 1.48 | 1.07 | 1.43 | 5.33 | 31.17 | 98.53 | 0.0229 | 83 | 140 |
| | r | 11.78 | 26.21 | 3.26 | 11.07 | 1.98 | 1.82 | 4.04 | 1.28 | 4.57 | 30.90 | 96.92 | 0.0786 | 626 | 37 |
| | r | 12.23 | 26.11 | 2.83 | 11.08 | 1.95 | 1.98 | 4.01 | 1.30 | 4.64 | 30.46 | 96.59 | 0.0778 | 621 | 37 |
| | r | 12.27 | 26.73 | 2.72 | 10.87 | 2.02 | 1.49 | 3.63 | 1.41 | 5.16 | 30.21 | 96.52 | 0.0773 | 619 | 41 |
| | r | 12.54 | 26.45 | 2.93 | 11.13 | 2.10 | 1.85 | 3.99 | 1.30 | 4.76 | 30.28 | 97.34 | 0.0764 | 614 | 37 |
| | r | 12.19 | 27.33 | 3.20 | 11.54 | 1.99 | 1.76 | 3.90 | 1.25 | 4.53 | 30.53 | 98.23 | 0.0744 | 602 | 38 |
| | r | 12.62 | 25.84 | 2.67 | 11.03 | 1.98 | 1.76 | 3.72 | 1.48 | 4.98 | 30.71 | 96.80 | 0.0714 | 584 | 39 |
| J | c | 12.10 | 25.57 | 2.55 | 11.24 | 2.31 | 1.74 | 2.66 | 1.59 | 5.22 | 30.76 | 95.73 | 0.0579 | 492 | 56 |
| M10 | c | 13.56 | 29.12 | 3.36 | 12.76 | 2.65 | 1.79 | 2.61 | 0.45 | 1.20 | 30.96 | 98.46 | 0.0554 | 472 | 57 |
| | r | 12.69 | 27.14 | 2.61 | 11.15 | 2.13 | 1.68 | 3.67 | 1.23 | 4.81 | 30.80 | 97.91 | 0.0775 | 620 | 40 |
| | r | 12.58 | 26.91 | 2.92 | 11.08 | 2.19 | 1.37 | 3.58 | 1.18 | 4.50 | 30.20 | 96.51 | 0.0764 | 614 | 41 |
| | r | 12.27 | 25.99 | 2.75 | 10.96 | 2.51 | 1.87 | 3.39 | 1.41 | 5.22 | 30.14 | 96.50 | 0.0723 | 589 | 44 |
| K | c | 13.01 | 27.64 | 3.06 | 11.54 | 2.19 | 1.41 | 2.46 | 1.07 | 3.83 | 30.56 | 96.77 | 0.0530 | 453 | 60 |
| L | c | 13.48 | 29.10 | 3.17 | 11.64 | 2.31 | 2.08 | 3.16 | 0.55 | 1.80 | 31.29 | 98.58 | 0.0644 | 538 | 46 |
| | c | 12.05 | 25.34 | 2.53 | 11.11 | 2.36 | 1.55 | 2.49 | 1.58 | 5.23 | 29.99 | 94.23 | 0.0549 | 468 | 59 |
| | c | 12.02 | 25.77 | 2.96 | 11.05 | 2.25 | 1.83 | 2.74 | 1.58 | 4.97 | 30.09 | 95.28 | 0.0532 | 455 | 53 |
| | c | 15.13 | 29.46 | 2.90 | 11.88 | 2.24 | 1.81 | 2.09 | 0.50 | 1.08 | 29.80 | 96.90 | 0.0432 | 363 | 70 |
| | c-be | 12.21 | 26.76 | 3.07 | 11.92 | 2.21 | 1.69 | 1.22 | 1.39 | 5.18 | 30.04 | 95.70 | 0.0241 | 107 | 120 |
| | r | 12.23 | 27.08 | 2.75 | 10.98 | 2.15 | 1.57 | 3.54 | 1.27 | 4.57 | 29.37 | 95.51 | 0.0757 | 609 | 42 |
| | r | 12.36 | 26.56 | 3.03 | 10.59 | 2.01 | 2.04 | 3.94 | 1.34 | 4.90 | 30.63 | 97.40 | 0.0755 | 609 | 37 |
| | r | 12.28 | 26.52 | 2.59 | 11.27 | 1.95 | 1.96 | 3.81 | 1.26 | 4.59 | 30.22 | 96.46 | 0.0741 | 600 | 39 |
| | r | 11.96 | 26.95 | 2.70 | 11.10 | 1.71 | 1.58 | 3.60 | 1.33 | 4.68 | 29.43 | 95.05 | 0.0703 | 577 | 41 |
| N | c | 12.89 | 27.44 | 2.88 | 11.87 | 2.26 | 1.30 | 2.69 | 1.17 | 3.95 | 30.50 | 96.95 | 0.0575 | 488 | 55 |
| | r | 12.32 | 27.03 | 2.68 | 10.76 | 2.18 | 1.20 | 3.85 | 1.31 | 4.78 | 30.03 | 96.14 | 0.0821 | 645 | 38 |
| O | c | 12.49 | 26.54 | 2.78 | 11.25 | 2.16 | 1.40 | 2.70 | 1.35 | 4.96 | 29.96 | 95.58 | 0.0584 | 495 | 55 |
| | r | 12.50 | 27.41 | 2.74 | 10.90 | 2.07 | 1.52 | 3.16 | 1.24 | 4.80 | 30.51 | 96.86 | 0.0676 | 560 | 47 |
| P | c | 9.11 | 22.09 | 2.53 | 10.28 | 2.99 | 2.31 | 3.73 | 2.11 | 5.92 | 30.37 | 91.44 | 0.0847 | 659 | 40 |
| | c | 12.51 | 25.94 | 3.06 | 10.67 | 2.33 | 1.31 | 2.34 | 1.67 | 5.01 | 30.24 | 95.08 | 0.0509 | 435 | 63 |
| | r | 12.36 | 27.01 | 3.15 | 11.05 | 2.17 | 1.29 | 3.74 | 1.29 | 5.00 | 30.87 | 97.93 | 0.0789 | 628 | 39 |
| Q | c | 13.26 | 27.53 | 2.86 | 10.77 | 2.13 | 1.49 | 3.59 | 1.28 | 4.43 | 30.97 | 98.31 | 0.0753 | 607 | 41 |
| | r | 11.19 | 25.13 | 2.88 | 10.64 | 2.33 | 1.80 | 3.86 | 1.63 | 6.44 | 29.86 | 95.75 | 0.0827 | 648 | 38 |
| M4 | c | 13.16 | 27.53 | 2.74 | 10.73 | 2.10 | 1.25 | 2.66 | 1.02 | 6.05 | 29.23 | 96.47 | 0.0572 | 486 | 55 |
| | c | 14.26 | 29.01 | 2.83 | 11.87 | 1.87 | 1.23 | 1.94 | 0.82 | 4.10 | 29.93 | 97.86 | 0.0412 | 342 | 77 |
| | r | 12.50 | 26.52 | 2.66 | 11.18 | 2.23 | 1.68 | 4.02 | 1.40 | 5.17 | 30.47 | 97.84 | 0.0841 | 656 | 37 |
| | r | 11.60 | 24.85 | 2.69 | 11.06 | 2.53 | 1.90 | 3.83 | 1.58 | 6.18 | 30.68 | 96.91 | 0.0817 | 643 | 39 |
| | r | 11.98 | 26.36 | 2.59 | 11.35 | 2.66 | 1.58 | 3.81 | 1.36 | 4.97 | 31.43 | 98.09 | 0.0807 | 638 | 39 |
| M5 | c | 11.54 | 25.77 | 2.74 | 11.24 | 2.14 | 1.56 | 2.72 | 1.68 | 5.21 | 30.77 | 95.38 | 0.0594 | 503 | 54 |
| | c | 11.75 | 25.93 | 2.93 | 10.86 | 1.90 | 1.64 | 2.76 | 1.94 | 5.72 | 29.94 | 95.39 | 0.0521 | 446 | 53 |
| | c | 13.12 | 27.23 | 2.91 | 11.37 | 2.30 | 1.73 | 2.71 | 1.48 | 4.90 | 30.61 | 98.36 | 0.0511 | 437 | 54 |
| | c | 12.18 | 26.12 | 3.21 | 10.81 | 1.96 | 1.84 | 2.59 | 1.55 | 5.22 | 29.65 | 95.14 | 0.0501 | 428 | 56 |
| | r | 12.87 | 26.02 | 3.01 | 10.54 | 2.14 | 1.52 | 3.61 | 1.46 | 5.18 | 30.62 | 96.96 | 0.0767 | 615 | 41 |
| | r | 12.16 | 26.12 | 2.91 | 10.71 | 2.02 | 1.85 | 3.92 | 1.38 | 5.33 | 30.96 | 97.38 | 0.0752 | 607 | 38 |
| | r | 11.96 | 26.31 | 2.86 | 11.12 | 1.95 | 1.77 | 3.62 | 1.44 | 5.08 | 30.21 | 96.34 | 0.0696 | 573 | 41 |
| | r | 12.60 | 27.20 | 3.02 | 10.70 | 2.13 | 1.68 | 3.55 | 1.30 | 4.73 | 31.10 | 98.02 | 0.0683 | 564 | 41 |
| | r | 12.95 | 27.10 | 2.91 | 11.24 | 2.04 | 1.57 | 3.49 | 1.30 | 4.43 | 30.20 | 97.23 | 0.0671 | 557 | 42 |
| | r | 12.44 | 26.13 | 2.76 | 10.61 | 2.08 | 1.76 | 3.33 | 1.38 | 4.85 | 28.93 | 94.28 | 0.0652 | 544 | 44 |
| | r | 12.70 | 27.33 | 2.98 | 10.65 | 1.83 | 1.60 | 3.32 | 1.23 | 4.74 | 29.53 | 95.92 | 0.0647 | 540 | 44 |
| | r | 12.64 | 26.76 | 2.94 | 11.29 | 1.99 | 1.69 | 3.06 | 1.35 | 4.78 | 28.75 | 95.25 | 0.0592 | 501 | 48 |

**Table 3** (Continued)

| Grain[a] | Location[b] | $La_2O_3$[c] | $Ce_2O_3$[c] | $Pr_2O_3$[c] | $Nd_2O_3$[c] | $Sm_2O_3$[c] | $Gd_2O_3$[c] | $Y_2O_3$[c] | CaO[c] | $ThO_2$[c] | $P_2O_5$[c] | Total | $Y_{mz}$[d] | T[e] (°C) | 2σ error in T[f](°C) |
|---|---|---|---|---|---|---|---|---|---|---|---|---|---|---|---|
| R | c | 12.06 | 25.76 | 3.02 | 10.79 | 2.35 | 1.50 | 2.76 | 1.61 | 4.84 | 30.72 | 95.40 | 0.0601 | 508 | 53 |
| | c | 11.99 | 27.09 | 3.07 | 10.71 | 2.13 | 1.70 | 2.84 | 1.65 | 5.88 | 30.63 | 97.69 | 0.0534 | 456 | 51 |
| | c | 11.72 | 26.09 | 2.90 | 10.99 | 2.29 | 1.69 | 2.77 | 1.68 | 5.70 | 30.35 | 96.18 | 0.0528 | 451 | 53 |
| | c | 12.19 | 25.81 | 2.94 | 10.65 | 2.21 | 2.04 | 2.62 | 1.56 | 5.42 | 29.95 | 95.40 | 0.0507 | 433 | 56 |
| | c | 12.49 | 25.85 | 3.02 | 10.65 | 2.21 | 1.59 | 2.55 | 1.77 | 4.69 | 30.13 | 94.96 | 0.0491 | 420 | 57 |
| | r | 13.11 | 26.81 | 2.53 | 10.94 | 2.25 | 1.47 | 3.28 | 1.32 | 5.23 | 31.50 | 98.45 | 0.0695 | 572 | 44 |
| | r | 13.40 | 27.04 | 2.85 | 10.83 | 1.94 | 1.41 | 2.94 | 1.29 | 4.98 | 29.50 | 96.19 | 0.0570 | 485 | 50 |

[a] Grain names are arbitrarily assigned (A–R) except for grains that were dated (M1–M10; see Table 1)
[b] Location refers to analysis location within grain: *h* homogeneous grain; *c* core; *c-be* bright edge of core; *r* rim
[c] Measurements made on the electron microprobe
[d] $Y_{mz}$ is the mole fraction Y in monazite calculated assuming a total cationic site occupancy of 1
[e] Temperature calculated from Eq. (1) assuming a pressure of 5.09 ± 0.37 kbar (2σ; Hubbard 1989)
[f] Errors in T determined by propagating microprobe analytical uncertainties, and pressure uncertainty through all calculations

**Table 4** Compositions and calculated Nd partitioning temperatures for xenotimes in sample 98E5

| Grain[a] | $Ce_2O_3$[b] | $Nd_2O_3$[b] | $Sm_2O_3$[b] | $Gd_2O_3$[b] | $Y_2O_3$[b] | CaO[b] | $ThO_2$[b] | $P_2O_5$[b] | Total | $Nd_{xn}$[c] | T[d] (°C) | T[e] (°C) |
|---|---|---|---|---|---|---|---|---|---|---|---|---|
| X5 | 0.050 | 0.146 | 0.598 | 2.393 | 42.66 | 0.134 | 0.207 | 34.03 | 80.21 | 0.0019 | 550 | 560 |
| X7 | 0.081 | 0.132 | 0.436 | 1.879 | 42.16 | 0.064 | 0.021 | 33.88 | 78.65 | 0.0018 | 525 | – |
| X10 | 0.043 | 0.118 | 0.420 | 2.239 | 42.45 | 0.089 | 0.202 | 33.67 | 79.23 | 0.0016 | – | 515 |
| X11 | 0.074 | 0.146 | 0.408 | 2.028 | 42.41 | 0.037 | 0.016 | 34.43 | 79.55 | 0.0019 | – | 540 |

[a] Grain names assigned to dated grains (Table 1)
[b] Measurements made on the electron microprobe. La and Pr concentrations were below the detection limit
[c] $Nd_{xn}$ is the mole fraction Nd in xenotime assuming a total cationic site occupancy of 1
[d] Temperature calculated from empirical partition coefficients ($D = Nd_{mz}/Nd_{xn}$; Andrehs and Heinrich 1998) assuming equilibrium between M6 and X5 ($D = 82$), X7 ($D = 91$)
[e] Temperature calculated from empirical partition coefficients ($D = Nd_{mz}/Nd_{xn}$; Andrehs and Heinrich 1998) assuming equilibrium between M8 and X5 ($D = 77$), X10 ($D = 95$), X11 ($D = 85$)

## Thermometry results

Temperatures calculated for 98E5 monazites with the YMX thermometer range widely – from a high of 677 ± 37 °C to a low of 83 ± 140 °C. While temperatures at the lower end of the spectrum are geologically unrealistic and probably mean that the analyzed monazite and xenotime were not in equilibrium at the time of crystallization, most calculated temperatures are above 350 °C and are at least geologically plausible.

A direct relationship exists between the internal structure of monazites, as revealed by BSE imaging, and the distribution of YMX temperatures (Fig. 3). The highest temperature variations occur in grains that show complex internal zoning and consist of an inherited core, a neoblastic rim, and an intervening bright, high-U + Th band (e.g., grains I and L). All of the geologically implausible temperatures were calculated from analyses in the bright bands, a finding consistent with interpreting these bands as intracrystalline reaction boundaries that developed without an opportunity for the monazite to achieve equilibrium with xenotime in the matrix. YMX temperatures for the inherited cores range from 659 ± 40 to 342 ± 77 °C, with an average of 470 °C and an uncertainty (two standard errors of the mean, or 2SE) of 24 °C. Much, but not all, of the scatter in core temperatures of individual grains can be explained by analytical imprecision. YMX temperatures for the neoblastic rims of these crystals are generally higher and more tightly clustered, ranging from 656 ± 37 to 485 ± 50 °C with an average of 595 °C (2SE = 15 °C). All YMX temperature variation within the rims of single grains is within the limits of analytical imprecision.

Individual unzoned and weakly zoned monazites yield a wider variety of YMX temperatures than the neoblastic rims of conspicuously zoned grains – 677 ± 37 to 472 ± 57 °C – but have a statistically indistinguishable average 586 °C (2SE = 33 °C). The low temperature was calculated for a spot in the core of grain M10 that appeared slightly darker in the BSE image than the rest of the grain and may be anomalous; other analyses from the grain indicate a narrow range of YMX temperatures (589–620 °C).

## Interpretation of YMX temperatures

The geological significance of the temperatures in Table 3 depends heavily on whether or not each analysis represents the chemical composition of monazite that was in equilibrium with xenotime. In the previous section, we argued that this was not the case for the "bright band" analyses, and we now consider the significance of the rest of the data in the context

of the U–Pb results for 98E5. Most of the near-concordant monazite analyses shown in Fig. 4b (M1, M6, and M8–M10) correspond to apparently unzoned or very weakly zoned grains that yield YMX temperatures ranging from 677 ± 37 to 472 ± 57 °C. Because $^{207}Pb/^{235}U$ dates for unzoned xenotimes in 98E5 range from older to younger than the $^{207}Pb/^{235}U$ dates for the near-concordant monazites, one simple – but potentially erroneous – interpretation is that xenotime was part of the equilibrium assemblage throughout the growth history of the near-concordant monazites and that all of the YMX temperatures for these grains are robust. However, there is no simple relationship between the $^{207}Pb/^{235}U$ dates for these monazites and their YMX temperatures. We might expect a simple relationship if (1) the dates represent growth ages, (2) the YMX calculations indicate the temperature at the time of monazite growth, and (3) temperatures evolve in a relatively systematic way during regional metamorphism and anatexis.

A more conservative interpretation is suggested if we regard as robust only those temperatures calculated for unzoned or weakly zoned monazites with $^{207}Pb/^{235}U$ dates statistically indistinguishable from unzoned xenotimes. There are only two such grains in our data set: M8 (22.30 ± 0.20 Ma), with a temperature of 641 ± 39 °C, and M6 (22.17 ± 0.06 Ma), which yields a temperature of 535 ± 49 °C. In order to explore the significance of these YMX temperatures further, we can use the compositions of the monazites and their coeval xenotimes (X5 and X7 for M6; X5, X10, and X11 for M8) to estimate temperatures independently using empirically derived monazite–xenotime Nd distribution coefficients (Andrehs and Heinrich 1998). The M6–X5–X3 subpopulation – which has a weighted mean $^{207}Pb/^{235}U$ date of 22.11 ± 0.22 (MSWD = 2.07) – corroborates the YMX temperature for M6 (535 ± 49 °C) by providing Nd-partitioning temperatures from 525 to 550 °C (Table 4). In contrast, the Nd-partitioning temperatures for the M8–X5–X10–X11 subpopulation (weighted mean $^{207}Pb/^{235}U$ date = 22.364 ± 0.097, MSWD = 0.077) range from 515 to 560 °C and are significantly different from the M8 YMX temperature (641 ± 39 °C).

There are at least three possible explanations for the disagreement among calculated M8–X5–X10–X11 temperatures. The first is that M8, although coeval with xenotime, was simply not in equilibrium with it. In this case, the YMX and Nd-partitioning temperatures are all geologically meaningless. The second possibility, given the limited availability of REE partitioning data for monazite and xenotime, is that the empirical temperature–composition relationships derived by Andrehs and Heinrich (1998) require further refinement, and that the YMX temperature may be correct despite a lack of corroboration from the Nd-partitioning calculation. A third possibility is that the Nd-partitioning temperatures are correct for 98E5 at 22.364 Ma and that the YMX calibration of Gratz and Heinrich (1997) is not applicable to the M8 monazite. For example, Eq. (1) was derived from experimental data for the simple (Ce, Y)$PO_4$ binary and it is not well known how high thorium and uranium concentrations may affect Y-partitioning behavior between more chemically complex natural xenotimes and monazites. Because M8 contains a particularly high concentration of both thorium and uranium (Table 1), this problem may impact the reliability of the 641 ± 39 °C estimate. Given the consistency of Nd-partitioning temperatures for both sub-populations and the YMX temperature for M6, we regard the third explanation as the most likely. We suspect that the Nd-partitioning temperatures are more robust for the M6–X5–X3 subpopulation for two reasons. First, the calibration of Andrehs and Heinrich (1998) is empirical, and thus more likely to compensate for natural compositional variability in monazite. Second, Nd concentrations in monazite are much higher than Y concentrations, such that Y-partitioning may be more sensitive to compositional complexities.

The significance of the generally low YMX temperatures for inherited cores remains unclear. Inherited monazite and xenotime may have been in chemical equilibrium at ~466 Ma, judging by the coincidence of the upper intercepts of U–Pb discordia defined by cores and overgrowths of each mineral (Fig. 4a). If this were the case and the monazite core YMX temperatures are reliable, the fact that only one temperature – 659 ± 40 °C for a single core spot in monazite grain P – is high enough to be a reasonable magmatic value suggests that the inherited monazites did not crystallize from the granitic melt of the orthogneiss protolith, but instead represent one or more episodes of subsolidus mineral growth. The lack of corroborating evidence for the simultaneous crystallization of xenotime and monazite and our poor definition of the monazite and xenotime discordia counsel against attaching too much significance to this observation at present, but additional study may show that monazite–xenotime thermochronometry provides an opportunity to "see through" high-grade metamorphism and extract time–temperature information from inherited accessory mineral suites.

## Monazite–xenotime thermochronology of the Namche Migmatitic Orthogneiss

Armed with an array of petrographic observations and trace-element partitioning constraints, we can make well-informed choices among the several alternative interpretations of the near-concordant U–Pb isotopic data for 98E5. Because the preponderance of evidence suggests that the Himalayan leucogranites are products of muscovite- and/or biotite-dehydration melting at temperatures substantially above 650 °C (Harris et al. 1995; Scalliet et al. 1995), the robust 535 ± 48 °C YMX temperature for M6 argues strongly against interpreting the geochronological data as indicative of melting at

~22.2 Ma. One possibility is that anatexis occurred after that time, perhaps at ~17.6 Ma as indicated by the X8 date. However, a leucogranitic dike that transects, and thus postdates the leucosome–melanosome layering in the 98E5 outcrop, yields preliminary U–Pb monazite data indicating an intrusive age of ~17–18 Ma (Viskupic and Hodges, unpublished data), and the most probable scenario, therefore, is that a later thermal event during dike intrusion led to subsolidus crystallization of xenotime in 98E5 at ~17.6 Ma.

Following this line of reasoning, partial melting occurred in 98E5 prior to ~22.2 Ma. Based on limited experimental evidence for phase relations during the crystallization of Himalayan leucogranites (Scalliet et al. 1995) and on petrographic observations of the textural relationships between unzoned to weakly zoned monazites and major phases in 98E5, any "magmatic" monazites in this sample should have crystallized over a temperature range from perhaps as high as 800 °C to perhaps as low as 650 °C. Of the YMX temperatures calculated for dated unzoned monazites, only one – the 677 ± 37 °C value for M1 – falls within this range. Although this temperature cannot be regarded as completely robust (because no dated xenotime has the same age as M1), we tentatively regard the $^{207}Pb/^{235}U$ date of M1 (25.39 ± 0.11 Ma) as the best available constraint on the age of leucosome crystallization in 98E5. This hypothesis could be tested through a more comprehensive survey of the trace-element geochemistry of unzoned and weakly zoned xenotimes in the sample. Given the composition of M1, a xenotime in equilibrium with it at 677 °C should have a mole-fraction Nd content of ~0.0043 (Andrehs and Heinrich 1998). If xenotimes of approximately this composition are found to exist in 98E5, we would predict their $^{207}Pb/^{235}U$ dates to be ~25.4 Ma.

Until such time-intensive studies are undertaken, we regard the best interpretation of the 98E5 data to be as follows. The igneous protolith of the orthogneiss crystallized at or before ~466 Ma as part of a regionally important magmatic event that has been widely documented in the Himalayan metamorphic core (e.g., Le Fort et al. 1986). Metamorphism of this rock during the Himalayan orogeny began at or before 28.37 Ma (the $^{207}Pb/^{235}U$ date of crystal X13), presumably during the well-documented Eohimalayan metamorphic event (Hodges 2000). This metamorphism culminated at the structural level of 98E5 with anatectic melting that began at least as early as ~25.4 Ma. Because grain M9 yields only a slightly lower YMX temperature (622 ± 41 °C) than M1, the anatectic event may have persisted to at least ~24.75 Ma. A conspicuous gap in U–Pb accessory mineral dates occurs between ~24.75 (M9) and ~23.31 Ma (X12), which we interpret to mean that a distinctive metamorphic event was responsible for accessory mineral crystallization between ~23.31 (X12) and ~22.00 Ma (X7). This interpretation is supported by previously published U–Pb geochronological data from the Everest region and elsewhere in the central Himalayan orogen that indicate widespread high-temperature, intermediate to low-pressure regional metamorphism over this interval (Hodges et al. 1992; Parrish and Hodges 1993; Hodges et al. 1996; Coleman 1998; Simpson et al. 2000). A second gap in U–Pb dates implies that xenotime crystallization at ~17.6 Ma resulted from a third thermal event related to the intrusion of crosscutting leucogranitic dikes at the level of 98E5. Additional U–Pb data from the region (Hodges et al. 1998; Murphy and Harrison 1999; Searle et al. 1997) document that leucogranitic intrusion was common in the structurally higher Rongbuk Formation–Black Gneiss succession over the 16- to 18-Ma interval.

## Tectonic implications

Monazite–xenotime thermochronometry of the Namche Migmatitic Orthogneiss suggests that the partial melting event (or events) responsible for distributed leucogranitic leucosomes at deep structural levels in the Everest region are older than ~22.2 Ma and probably of Late Oligocene age. Only the oldest dated leucogranite plutons in the region (e.g., the Makalu pluton, Schärer 1984) might be attributed to this phase of anatexis. Others, such as the 20.5–21.3-Ma Everest granite about 20 km to the northeast of Namche Bazaar (Simpson et al. 2000) and the 16–18 Ma leucogranites that are abundant at high structural levels (Searle et al. 1997; Hodges et al. 1998; Murphy and Harrison 1999) must represent products of separate melting events. Many models have been proposed for the generation of Himalayan leucogranites (as reviewed by Hodges 1998), but the necessity of having a mechanism for repetitive melting events affecting the same column of crust over a ~10-million year period reduces the number of viable models to those that involve the rapid and continual addition of heat to the orogen through long-term shear heating (Harrison et al. 1998) or underplating by materials rich in heat-producing elements (Huerta et al. 1999).

Our data also reveal a major difference in the Early Miocene time–temperature histories of upper and middle structural levels of the Himalayan metamorphic core in the Everest region. Although the structural level represented by 98E5 had cooled to 535 °C by 22.11 Ma, rocks at Kala Pattar (Fig. 1), roughly 25 km to the northeast of and perhaps 3–5 km structurally higher than Namche Bazaar, were subjected to cordierite–sillimanite-grade metamorphism at temperatures of > 620 °C at roughly the same time (Simpson et al. 2000). This inconsistency implies either a large-scale thermal inversion or the existence of a major post-22.11-Ma structural discontinuity between the two localities. Given the arguments of Searle (1999a) for the existence of the Khumbu thrust, we prefer the latter interpretation.

## Conclusions

Integrated application of U–Pb geochronology and accessory phase thermometry to a sample from the Nepalese Himalaya illustrates that monazite–xenotime thermochronometry is a powerful tool for reconstructing the thermal histories of high-temperature metamorphic terrains. The combination of YMX thermometry as described by Gratz and Heinrich (1997) and semi-quantitative temperature estimation based on rare-earth element partitioning between monazite and xenotime (Andrehs and Heinrich 1998) allows for robust temperature estimates that are not overly sensitive to analytical uncertainties. These estimates are a tremendous resource for interpreting complex U–Th–Pb geochronological data sets such as those typically obtained through the study of orogenic granites.

Although conventional U–Pb methods, such as those applied here, can be used successfully for monazite–xenotime thermochronometry, there would be an obvious advantage to augmenting monazite–xenotime trace-element thermometry with U–Th–Pb data obtained through techniques having higher spatial resolution. Ion microprobes have been used with great success to date portions of single monazite grains with the $^{232}Th$–$^{208}Pb$ decay scheme (Harrison et al. 1995; Grove and Harrison 1999), but this approach has not been widely applied to xenotime; as yet, the only published ion microprobe dates for xenotimes are based on SHRIMP U–Pb methods (e.g., McNaughton et al. 1999). Although electron microprobe U–Th–Pb chemical dating of monazite has received much attention in recent years (e.g., Crowley and Ghent 1999; Williams et al. 1999), low Pb concentrations limit this application in Cenozoic monazites, and large corrections for yttrium-lead peak overlaps virtually preclude the application of this approach to dating a high-Y mineral such as xenotime. At present, the most effective approach to monazite–xenotime thermochronometry may be a combination of (1) BSE and X-ray mapping of thin sections to evaluate the textural relationships among major and accessory phases and to identify candidate grains for detailed work; (2) systematic measurement of major and trace-element abundances in monazites for YMX thermometry and, when possible, chemical dating; (3) reconnaissance ion microprobe dating of monazite to evaluate core-overgrowth age relationships in situations when chemical dating is inappropriate; and (4) conventional U–Th–Pb analysis of unzoned monazites and xenotimes for high-precision geochronology.

**Acknowledgements** This work was funded by a US National Science Foundation grant to K.V. Hodges and S.A. Bowring. We are grateful to Sam Bowring for use of the U–Pb laboratory at MIT, Mark Schmitz for help with U–Pb analyses and interpretation of U–Pb data, and to Neel Chatterjee for assistance with quantitative analysis of monazite and xenotime on the electron probe. Critical reviews by Frank Spear and Wilhelm Heinrich greatly improved the manuscript.

## References

Amli R, Griffin WL (1975) Microprobe analysis of REE minerals using empirical correction factors. Am Mineral 60:599–606

Andrehs G, Heinrich W (1998) Experimental determination of REE distributions between monazite and xenotime: potential for temperature-calibrated geochronology. Chem Geol 149:83–96

Ashwal LD, Tucker RD, Zinner EK (1999) Slow cooling of deep crustal granulites and Pb-loss in zircon. Geochim Cosmochim Acta 63:2839–2851

Ashworth JR, McLellan E (1985) Textures. In: Ashworth JR (ed) Migmatites. Blackie, Glasgow, pp 180–204

Bordet P (1961) Recherches géologiques dans l'Himalaya du Népal, région du Makalu. Edition du Centre National de la Recherche Scientifique, Paris

Brunel M, Kienast JR (1986) Etude petrostructurale des chevauchements ductile himalayens sur la transversale de L'Everest–Makalu (Nepal oriental). Can J Earth Sci 23:1117–1137

Burchfiel BC, Chen Z, Hodges KV, Liu Y, Royden LH, Deng C, Xu J (1992) The south Tibetan detachment system, Himalayan orogen: extension contemporaneous with and parallel to shortening in a collisional mountain belt. Geological Society of America, Boulder

Carosi R, Lombardo B, Musumeci G, Pertusati PC (1999) Geology of the higher Himalayan crystallines in Khumbu Himal (eastern Nepal). J Asian Earth Sci 17:785–803

Coleman ME (1998) U–Pb constraints on Oligocene–Miocene deformation and anatexis within the central Himalaya, Marsyandi valley, Nepal. Am J Sci 298:553–571

Copeland P, Parrish RR, Harrison TM (1988) Identification of inherited radiogenic Pb in monazite and its implications for U–Pb systematics. Nature 333:760–763

Crowley JL, Ghent ED (1999) An electron microprobe study of the U–Th–Pb systematics of metamorphosed monazite: the role of Pb diffusion versus overgrowth and recrystallization. Chem Geol 157:285–302

Ferrara G, Lombardo B, Tonarini S (1983) Rb/Sr geochronology of granites and gneisses from the Mount Everest region, Nepal Himalaya. Geol Rundsch 72:119–136

Gratz R, Heinrich W (1997) Monazite–xenotime thermobarometry: experimental calibration of the miscibility gap in the binary system $CePO_4$–$YPO_4$. Am Mineral 82:772–780

Gratz R, Heinrich W (1998) Monazite–xenotime thermometry III. Experimental calibration of the partitioning of gadolinium between monazite and xenotime. Eur J Mineral 10:579–588

Grove M, Harrison TM (1999) Monazite Th–Pb age depth profiling. Geology 27:487–490

Harris N, Ayres M, Massey J (1995) Geochemistry of granitic melts produced during the incongruent melting of muscovite; implications for the extraction of Himalayan leucogranite magmas. J Geophys Res 100:15767–15777

Harrison TM, McKeegan KD, Akers W, Ryerson FJ (1994) Prograde thermochronometry using SIMS analysis of monazite. In: Lanphere MA, Dalrymple GB, Turrin BD (eds) Abstracts of 8th International Conference on Geochronology, cosmochronology, and isotope geology, no 128. US Geological Survey Circular 1107, Denver, CO

Harrison TM, McKeegan KD, LeFort P (1995) Detection of inherited monazite in the Manaslu leucogranite by $^{208}Pb/^{232}Th$ ion microprobe dating: crystallization age and tectonic implications. Earth Planet Sci Lett 133:271–282

Harrison TM, Grove M, Lovera OM, Catlos EJ (1998) A model for the origin of Himalayan anatexis and inverted metamorphism. J Geophys Res 103:27017–27032

Hawkins DP, Bowring SA (1997) U–Pb systematics of monazite and xenotime: case studies from the Paleoproterozoic of the Grand Canyon, Arizona. Contrib Mineral Petrol 127:87–103

Heinrich W, Andrehs G, Franz G (1997) Monazite–xenotime miscibility gap thermometry. I. An empirical calibration. J Metamorph Geol 15:3–16

Hodges KV (1998) The thermodynamics of Himalayan orogenesis. In: Treloar PJ, O'Brien P (eds) What drives metamorphism and metamorphic reactions? Geol Soc Lond Spec Publ 138:7–22

Hodges KV (2000) Tectonics of the Himalaya and southern Tibet from two perspectives. Geol Soc Am Bull 112:324–350

Hodges KV, Parrish R, Housh T, Lux D, Burchfiel BC, Royden L, Chen Z (1992) Simultaneous Miocene extension and shortening in the Himalayan orogen. Science 258:1466–1470

Hodges KV, Parrish RR, Searle MP (1996) Tectonic evolution of the central Annapurna Range, Nepalese Himalayas. Tectonics 15:1264–1291

Hodges K, Bowring S, Davidek K, Hawkins D, Krol M (1998) Evidence for rapid displacement on Himalayan normal faults and the importance of tectonic denudation in the evolution of mountain ranges. Geology 26:483–486

Hubbard MS (1989) Thermobarometric constraints on the thermal history of the Main Central Thrust Zone and Tibetan Slab, eastern Nepal Himalaya. J Metamorph Geol 7:19–30

Huerta AD, Royden LH, Hodges KV (1999) The effects of accretion, erosion and radiogenic heat on the metamorphic evolution of collisional orogens. J Metamorph Geol 17:349–366

Le Fort P, Debon F, Pêcher A, Sonet J, Vidal P (1986) The 500 Ma magmatic event in Alpine southern Asia, a thermal episode at Gondwana scale. Sci Terre Mém 47:191–209

Lee JKW, Williams IS, Ellis DJ (1997) Pb, U and Th diffusion in natural zircon. Nature 390:159–162

Lombard A (1958) Un itinéraire géologique dans l'est du Népal (Massif du Mont Everest). Mém Soc Helvétique Sci Naturalles 82:104

Lombardo B, Pertusati P, Borghi S (1993) Geology and tectonomagmatic evolution of the eastern Himalaya along the Chomolungma–Makalu transect. In: Treloar PJ, Searle MP (eds) Himalayan tectonics. Geol Soc Lond Spec Publ 47: 341–355

McNaughton NJ, Rasmussen B, Fletcher IR (1999) SHRIMP U–Pb dating of diagenetic xenotime in siliciclastic sedimentary rocks. Science 285:79–80

Mu AT, Wen SH, Wang YK, Chang PK, Yin CH (1973) Stratigraphy of the Mount Jolmo Lungma region in Southern Tibet, China. Sci Sin16:96–111

Murphy MA, Harrison TM (1999) Relationship between leucogranites and the Qomolangma detachment in the Rongbuk Valley, south Tibet. Geology 27:831–834

Noble SR, Searle MP (1995) Age of crustal melting and leucogranite formation from U–Pb zircon and monazite dating in the western Himalaya, Zanskar, India. Geology 23:1135–1138

Parrish R (1990) U–Pb dating of monazite and its application to geological problems. Can J Earth Sci 27:1431–1450

Parrish RR, Hodges KV (1993) Miocene (22 ± 1 Ma) metamorphism and two-stage thrusting in the Greater Himalayan sequence, Annapurna Sanctuary, Nepal. Geol Soc Am Abstr Prog 25:A174

Pognante U, Benna P (1993) Metamorphic zonation, migmatization and leucogranites along the Everest transect of eastern Nepal and Tibet: record of an exhumation history. In: Treloar PJ, Searle MP (eds) Himalayan tectonics. The Geological Society, London, pp 323–340

Scalliet B, Pichavant M, Roux J (1995) Experimental crystallization of leucogranite magmas. J Petrol 36:663–705

Schärer U (1984) The effect of initial $^{230}$Th disequilibrium on young U–Pb ages: the Makalu case, Himalaya. Earth Planet Sci Lett 67:191–204

Schneider DA, Edwards MA, Kidd WSF, Zeitler PK, Coath CD (1999) Early Miocene anatexis identified in the western syntaxis, Pakistan Himalaya. Earth Planet Sci Lett 167:121–129

Searle MP (1999a) Extensional and compressional faults in the Everest–Lhotse massif, Khumbu Himalaya, Nepal. J Geol Soc Lond 156:227–240

Searle MP (1999b) Emplacement of Himalayan leucogranites by magma injection along giant sill complexes: examples from the Cho Oyu, Gyachung Kang and Everest leucogranites (Nepal Himalaya). J Asian Earth Sci 17:773–783

Searle MP, Parrish RR, Hodges KV, Hurford A, Ayres MW, Whitehouse MJ (1997) Shisha Pangma leucogranite, South Tibetan Himalaya; field relations, geochemistry, age, origin, and emplacement. J Geol 105:295–317

Searle MP, Noble SR, Hurford AJ, Rex DC (1999) Age of crustal melting, emplacement and exhumation history of the Shivling leucogranite, Garhwal Himalaya. Geol Mag 136: 513–525

Simpson RL, Parrish RR, Searle MP, Waters DJ (2000) Two episodes of monazite crystallization during metamorphism and crustal melting in the Everest region of the Nepalese Himalaya. Geology 28:403–406

Smith HA, Giletti BJ (1997) Lead diffusion in monazite. Geochim Cosmochim Acta 61:1047–1055

Spear FS, Kohn MJ, Cheney JT (1999) P–T paths from anatectic pelites. Contrib Mineral Petrol 134:17–32

Suzuki K, Adachi M, Kajizuka I (1994) Electron microprobe observations of Pb diffusion in metamorphosed detrital monazite. Earth Planet Sci Lett 128:391–405

Tonarini S, Lombardo B, Ferrara G, Marcassa P (1994) Partial melting in the Namche Migmatite of Khumbu Himal (Nepal Himalaya). Mineral Petrogr Acta 37:277–294

Walker J, Martin MW, Bowring SA, Searle MP, Waters DJ, Hodges KV (1999) Metamorphism, melting, and extension: age constraints from the High Himalayan Slab of southeast Zanskar and northwest Lahaul. J Geol 107:473–495

Wendt I, Carl C (1991) The statistical distribution of the mean squared weighted deviation. Chem Geol 86:275–285

Williams ML, Jercinovic MJ, Terry MP (1999) Age mapping and dating of monazite on the electron microprobe: deconvoluting multistage tectonic histories. Geology 27:961–1056

Yin CH, Kuo ST (1978) Stratigraphy of the Mount Jolmo Lungma and its north slope. Sci Sin 21:629–644

Zeitler PK, Chamberlain CP, Smith HA (1993) Synchronous anatexis, metamorphism, and rapid denudation at Nanga Parbat (Pakistan Himalaya). Geology 21:347–350

# Chapter 2

## Thermal and Intrusive History of the upper Greater Himalayan Sequence in the Everest Region, Eastern Nepal: Implications for the Timescales of Melt Generation and the Thermal Evolution of the Himalayan Metamorphic Core

**Abstract**

Studies of anatexis and melt migration in the Himalaya can provide important insights regarding the role of granitic magmatism in the evolution of collisional orogens. In the Everest region of the Nepalese Himalaya, where granitic magmatism and progressive deformation were intimately related, $^{40}Ar/^{39}Ar$ and U-Pb geochronology provide evidence for a complex thermal history marked by multiple episodes of granite intrusion. The oldest mobilized melt in the area formed syn-deformational granitic sills that have U-Pb crystallization ages of 21.334 ± 0.025 Ma and 21.796 ± 0.047 Ma. Preserved in these same granites, however, is a record of earlier, nearly continuous, magmatic crystallization of xenotime, monazite and zircon between ca. 26 and ca. 23 Ma. This pattern of accessory phase crystallization likely reflects incremental melting and crystallization in the source region of the sills before ultimate melt migration.

$^{40}Ar/^{39}Ar$ dates of biotite from the granite sills suggest they experienced rapid cooling after emplacement, cooling below ~370°C by 19 Ma. Although these rocks in the upper structural levels of the Himalayan metamorphic core were relatively cool, melting elsewhere was still taking place, as evidenced by post-deformational crosscutting granite dikes with U-Pb crystallization ages of 18.00 ± 0.18 Ma, 18.275 ± 0.065 Ma and 17.47-18.33 Ma. These crystallization ages are concordant with $^{40}Ar/^{39}Ar$ biotite dates from the same samples, suggesting that the final melt phases underwent rapid cooling.

The melting history recorded in the Everest region requires that anatectic temperatures were periodically reached or maintained for a period of almost 10 million years starting at ca. 26 Ma. The beginning of crustal melting in the Everest region predates the earliest known movement on both the Main Central thrust and the South Tibetan fault systems, but is temporally associated with the implied pressure decrease between "Eohimalayan" and "Neohimalayan" metamorphism suggesting that the earliest melting may be related to decompression.

**Introduction**

The temporal and spatial generation of granitc melts in collisional orogens reflects changing orogenic thermal structures. These thermal structures are influenced by tectonic displacement of crustal geotherms and the accretion of crust enriched in radiogenic heat producing elements beneath the orogen (Huerta et al., 1998). The generation and subsequent mobilization of the melts themselves, however, must also influence orogenic thermal, and potentially structural, evolution.

The Himalayan orogen offers a remarkable natural laboratory in which to investigate the influences of anatexis on the thermal structure of a developing collisional orogen. Spectacular exposures through the Himalayan metamorphic core reveal leucogranitic melts at all scales, ranging from centimeter-scale leucosomes in anatexites to plutons and batholiths that crop out over tens of square kilometers. Perhaps the largest volume of these crustal melts is exposed in the Everest region of eastern Nepal. In the Everest region, the Greater Himalayan Sequence consists of three main rock types: upper amphibolite to granulite facies migmatitic ortho- and paragneisses; upper amphibolite facies metapelitic and calc-silicate gneisses and schists; and Miocene leucogranites. Near the base of the Greater Himalayan Sequence, discontinuous,

centimeter-scale leucosomes characterize metapelitic anatexites. In the middle of the sequence, dikes and sills of leucogranite, ranging from centimeters up to several meters wide, attest to the segregation and mobilization of melt at progressively higher structural levels. Near the top of the Greater Himalayan Sequence, plutons and batholiths of leucogranite crop out. The largest of these include the Makalu and the Nuptse plutons (Figure 1).

Models of the thermal structure of the Himalayan orogen have implied that the upper Greater Himalayan Sequence experienced a relatively simple thermal history characterized by one or two pulses of granite emplacement (Harris and Massey, 1994; Harrison et al. 1998, 1999). Field relationships, however, indicate multiple phases of leucogranite intrusion. These relationships are supported by geochronologic studies that report a wide range of crystallization ages (ca. 24-12 Ma) for granites in the Greater Himalayan Sequence throughout the orogen (see review in Chapter 4). However, important questions about the temporal and spatial generation of granitic melts remain unanswered. How frequent were episodes of anatexis and intrusion? Was melt generation continuous or episodic? What were the durations of intrusive events? What was the thermal evolution of the country rocks during the intervals between intrusive events? Such questions can best be addressed with detailed geologic, thermochronologic, and geochronologic studies of multiple generations of granitic melts and their country rocks at the outcrop scale. In this paper, I establish the thermal and intrusive history of the upper Greater Himalayan Sequence in one small area, the Everest region of eastern Nepal, which displays evidence for multiple generations of granitic intrusions.

**Evolution of the Greater Himalayan Sequence in the Everest Region**

The Greater Himalayan Sequence is tectonically bound below by north-dipping reverse faults of the Main Central Thrust (MCT) system, and above by north-dipping principally normal faults of the South Tibetan Fault (STF) system. Movement along the STF and MCT was contemporaneous during the Early Miocene, but both fault systems appear to have had long and episodic slip histories throughout much of the past 20 million years (Hodges, 2000). In the Everest region, motion on the MCT began at least as early as 20 Ma (Hubbard & Harrison, 1989), and deformation related to slip on the Qomolangma detachment (STF) was ongoing at 16-17 Ma (Hodges et al., 1998; Murphy & Harrison, 1999).

Petrologic and thermobarometric studies of the Greater Himalayan Sequence in the Everest region have reported two phases of metamorphism. Pognante and Benna (1993) described an early metamorphism (T=550-560 °C, P=8-10 kb) caused by subduction and crustal thickening during continental collision. Later, the crust underwent partial melting during a second metamorphic event (T=650-750°C, P=4-7 kb). Simpson et al. (2000) placed constraints on the timing of these two events in the Everest region by dating metamorphic monazite. They determined peak sillimanite-grade metamorphism at 32.2 ± 0.4 Ma, and later high temperature, low-pressure (620°C, 4 kb) metamorphism at 22.7 ± 0.2 Ma. These two phases of metamorphism will be referred to as Eohimalayan (early, high pressure), and Neohimalayan (late, high temperature, low pressure) metamorphism after Hodges, et al. (1994).

**Sampling Strategy**

This study focuses on three outcrops where multiple generations of leucogranitic dikes and sills intrude ortho- and para-gneisses in the upper Greater Himalayan Sequence in the Everest region, one near the village of Namche Bazaar, and two near the village of Gokyo (Figure 1). Although granites are pervasive at high structural levels in the Everest region, these outcrops were chosen for detailed study due to their good exposure, accessibility, sample freshness, and evidence for polyphase injection of leucogranitic melts. Outcrops were first mapped and photographed with the goal of establishing relative age relationships to guide geochronologic data interpretation. Critical samples of the granites and their country rocks were then collected for U-Pb and $^{40}Ar/^{39}Ar$ dating to determine the timescales of melt injection and cooling.

*Outcrop 1: Namche Bazaar*

The structurally lowest outcrop sampled is approximately 1km north of Namche Bazaar. The country rock and an undeformed cross-cutting dike were sampled. The country rock (98E5; Viskupic & Hodges, 2001) is characteristic of the Namche migmatitic orthogneiss, a conspicuously banded, biotite-rich gneiss with ~10% leucogranitic leucosome distributed as millimeter- to centimeter-scale vein-like segregations. These leucosomes contain K-feldspar, quartz, plagioclase, and cordierite, and are rimmed by thin biotite and sillimanite selvages. The leucosomes are interpreted to be the result of *in situ* melting. The alignment of biotite and fibrolitic sillimanite defines the gneissic foliation of the rock ($S_1$). Sample 98E6 is a 1 meter-wide leucogranite dike that cuts across the $S_1$ fabric. Its mineralogy includes quartz, microcline,

muscovite, minor biotite, rare tourmaline, and accessory monazite, xenotime, and zircon. Most monazite and xenotime crystals are subhedral to euhedral.

*Outcrop 2: Gokyo Ri*

A second outcrop located along the base of Gokyo Ri is structurally high in the Greater Himalayan Sequence. Four samples, representative of the country rock and three intrusive phases, were collected from this outcrop (Figure 2). Sample 00SK07 is the paragneiss country rock; its foliation ($S_1$) is defined by the alignment of abundant (~25%) red-brown biotite. The quartz grains show slight undulatory extinction, and the feldspars show little to no alteration. Accessory phases include rutile, monazite, apatite and zircon. Sample 00SK09 was collected from a sill concordant to and containing the $S_1$ schistosity suggesting intrusion was pre- or syn-kinematic with respect to $S_1$ formation. Subsequent deformation of $S_1$ is evidenced by the boudinage of such concordant sills ($B_2$). The mineralogy of 00SK09 includes plagioclase, quartz, K-feldspar, tourmaline, cordierite, minor biotite, and accessory monazite, xenotime, apatite and zircon. Tourmaline grains are highly pleochroic and occur along grain boundaries and as inclusions in plagioclase. Quartz grains are small and irregular in shape, and show slight undulatory extinction. Plagioclase is subhedral and unaltered. Samples 00SK08 and 00SK10 are coarse grained, unfoliated granites. Sample 00SK08 was collected from a sill parallel to $S_1$ that did not contain the $S_1$ foliation. Sample 00SK10 was collected from a dike that clearly cut $S_1$. Where the dike of 00SK10 and the sill of 00SK08 were observed to meet, no clear crosscutting relationships were seen, but instead the two granites pooled together. This relationship, along with the lack of $S_1$ schistosity or $B_2$ boudinage in the 00SK08 sill, suggests that it was post-kinematic, like dike 00SK10. The mineralogy of 00SK08 includes quartz, plagioclase,

microcline, cordierite, minor biotite and muscovite, and accessory monazite, and zircon. The feldspars are slightly altered to sericite. Quartz shows undulatory extinction and subgrain boundaries. The red-brown biotite grains are elongated, but not aligned, and show no evidence for alteration. The mineralogy of sample 00SK10 includes quartz, plagioclase, K-feldspar, tourmaline, minor biotite, and accessory monazite and zircon. The plagioclase is slightly altered, and the green-brown biotite shows some chloritization.

*Outcrop 3: The 5$^{th}$ Lake*

The structurally highest outcrop sampled was along the southern edge of what is locally known as Gokyo's "fifth" lake (Figure 3). This outcrop is also at the approximate location of the trace of the Khumbu Thrust proposed by Searle (1999), although no direct structural evidence for the fault was observed during this study. Sample 01SK53 is the augen orthogneiss country rock containing the $S_1$ schistosity. Its mineralogy includes quartz, plagioclase, K-feldspar, minor biotite, and accessory monazite, xenotime, and zircon. Sample 01SK54 is a granite sill, concordant to and containing the $S_1$ schistosity, suggesting it was pre- to syn-kinematic with respect to $S_1$ development. There is no evidence for $B_2$ at this outcrop. The mineralogy of sill 01SK54 includes quartz, plagioclase, K-feldspar, minor biotite, rare garnet, and accessory monazite, xenotime, and zircon. Sample 01SK55 is from a granite dike that cuts across $S_1$ and the 01SK54 sill. Its mineralogy includes quartz, plagioclase, K-feldspar, minor biotite, minor tourmaline, rare garnet included in feldspar and accessory monazite, xenotime and zircon.

**Results and Discussion**

Details of the analytical methods used are described in Appendix A. Results from U-Pb geochronology, and $^{40}Ar/^{39}Ar$ geochronology are organized and presented by outcrop. Himalayan leucogranites are notorious for containing xenocrystic monazite, zircon, and rarely xenotime. The characterization and avoidance of such pre-Himalayan "inheritance" is critical to accurately determining granite crystallization ages. In this vein, only single grains or grain fragments of monazite and xenotime were dated, and almost all dated grains were characterized using backscattered electron (BSE) images. Overall, the U-Pb results show protracted accessory mineral crystallization, the timing of which is consistent with the cross-cutting relationships observed. Surprisingly, $^{40}Ar/^{39}Ar$ cooling ages for samples from single outcrops are distinct and also agree with the cross cutting relationships observed, suggesting that subsequent intrusions did not reset Ar systematics in previously crystallized minerals in the host rocks.

Outcrop 1: Namche Bazaar

The U-Pb systematics of the migmatitic orthogneiss country rock at this outcrop (98E5) were studied in detail by Viskupic and Hodges (2001). The sample showed accessory phase growth between ca. 28 and ca. 18 Ma. Quantitative thermometry based on the partitioning of yttrium (Y) between monazite and xenotime (Gratz & Heinrich, 1997) and semi-quantitative thermometry based on Nd partitioning between monazite and xenotime (Andrehs & Heinrich, 1998) were used to interpret the U-Pb data. The authors suggested that the country rock reached temperatures appropriate for partial melting (> 650 °C) at ca. 25 Ma, and had cooled to ~530 °C by 22 Ma.

Four monazites from the undeformed dike (98E6) that cuts across the $S_1$ schistosity of 98E5 were dated (Figure 4, Table 1). Two of the grains were imaged (m5, m12) and they showed essentially homogeneous centers with patchy zoning towards the rim (Figure 5), consistent with there being no pre-Himalayan inherited component. All four monazites dated plot above the concordia curve, which is typical in young, Th-rich minerals. Fractionation of U and Th between crystallizing minerals and melts can cause the two U decay series to be in disequilibrium. Th-rich minerals such as monazite can incorporate excess $^{230}Th$, which leads to an excess of $^{206}Pb$ (Schärer, 1984), causing the isotopic data to plot above the concordia curve (reverse or negative discordance). Thorium-poor minerals such as zircon and xenotime also can exhibit disequilibrium due to a deficit of $^{206}Pb$ due to $^{230}Th$ deficiency. Uranium-thorium disequilibrium in zircon and xenotime can cause isotopic data to plot below the concordia curve (normal or positive discordance), although the degree of disequilibrium, and therefore of discordance, is not as great as in monazite. In order to interpret such discordant data, the $^{207}Pb/^{235}U$ dates are taken to be the most reliable estimates of the timing of crystallization of individual grains since they are not affected by initial U-Th disequilibrium.

The four grains from dike 98E6 have a weighted mean $^{207}Pb/^{235}U$ date of 18.00 ± 0.18 Ma (MSWD=1.08; Wendt & Carl, 1991). One xenotime from the dike was also dated. Backscattered electron imaging of grain x6 revealed a homogeneous center with some embayed, oscillatory zoning towards the rim. It has a $^{207}Pb/^{235}U$ date of 17.576 ± 0.045 Ma, slightly younger than the four monazites analyzed. Collectively, the monazite and xenotime data suggest that the dike from which 98E6 was collected crystallized at ~17.6-18.0 Ma.

The similarity between this age and the date obtained on the single youngest xenotime in 98E5, suggests that the ca. 18 Ma xenotime in 98E5 may have grown during a local reheating

event related to intrusion of the 98E6 dike. Alternatively, the young xenotime may have crystallized during the waning stages of regional metamorphism at temperatures below 530°C.

Outcrop 2: Gokyo Ri

In backscattered electron images, monazites from gneiss 00SK07 (Figure 6) include low-contrast grains with patchy concentric zoning (m3b, m6) to high-contrast grains with rounded domains (m5). The latter population may represent intergrowths of smaller grains. $^{207}Pb/^{235}U$ dates for 00SK07 monazites range from 22.64 ± 0.47 to 344.94 ± 0.29 Ma (Figure 7, Table 1). The timing of country rock metamorphism is poorly constrained by a crude linear array of discordant data suggestive of an inherited component with a ca. 465 Ma age and a metamorphic component with a ca. 23 Ma age. This interpretation is consistent with the conclusions of Hodges et al. (1992), Simpson et al., (2000), and Viskupic and Hodges (2001) that prograde Neohimalayan metamorphism in the upper Greater Himalayan Sequence peaked in Early Miocene time.

Monazites and xenotimes from sill 00SK09 show a range of internal structures. Homogeneous growth zoning (m3) and sector zoning (m4) were most often seen in BSE images of monazites (Figure 8). Xenotimes display more variable internal structures. A few xenotimes show irregular geometric zoning (x3) or patchy concentric zoning (x2). The majority of xenotimes show cores with speckled or flame-like structures, often rich in inclusions of quartz, alkali feldspar, sillimanite, biotite, and sometimes uraninite and monazite, surrounded by homogeneous or oscillatory zoned rims (x1, x5, x6). The shapes of the speckled cores generally mimic the overall grain shapes, with some evidence for minor resorbtion of the core prior to rim growth.

This flame-like texture is also seen in unusual zircon-xenotime intergrowths. Backscattered electron images of these intergrowths are shown in Figure 9, where the darker phase is zircon, and the lighter phase is xenotime. In both phases, speckled, inclusion-rich, cores can be seen. In these intergrowths, as in the single xenotimes imaged, the shapes of the cores mimic the shapes of the grains, and there appears to be only minor resorbtion of the core prior to rim growth. In three dimensions, the intergrowths look like crosses; a xenotime with two zircon termini protruding from opposite sides, or a zircon with two xenotime termini protruding from opposite sides, depending on which grain is larger. Similar intergrowths of zircon and xenotime have been described previously in granitic rocks. Köppel (1974) noted intergrowths of zircon and xenotime in a sample of postmetamorphic granite from the Ivrea Zone, and Wark and Miller (1993) identified zircon-xenotime intergrowths in granites and aplites from the Sweetwater Wash pluton. Backscattered electron images of the Sweetwater Wash pluton intergrowths show them to have the same morphology as the intergrowths from sample 00SK09, but no internal zoning is evident. Finally, Bea (1996) described zircon-xenotime intergrowths, citing them in the Ronda and Albuquerque leucogranites. Such intergrowths have not been observed in metamorphic accessory mineral suites, suggesting that they are related exclusively to magmatic processes. Since the magmatic zircon-xenotime intergrowths in 00SK09 have the same internal structures as most single xenotimes, it seems likely that xenotimes with core that have flame-like zoning also are magmatic.

Three xenotimes (x1, x5, x6) with flame-structured cores were cut with an obsidian blade in an effort to isolate the core and rim components (indicated by dashed lines in Figure 8). The fragments have $^{207}Pb/^{235}U$ dates that range from 23.81 ± 0.11 to 24.327 ± 0.084 Ma for x1, 23.81 ± 0.11 to 24.566 ± 0.093 Ma for x5, and 24.576 ± 0.026 to 24.846 ± 0.025 Ma for x6 (Figure 10,

Table 1). Although the core and rim components were not completely separated from each other, the less than one million-year difference in $^{207}Pb/^{235}U$ dates of fragments from the same grains demonstrates that there was not a significant time lapse between core and rim growth. It also demonstrates that the cores are not a pre-Himalayan inherited component from the source rock or country rock. In addition, all of the cores and all of the rims did not crystallize at the same time. For example, rim-rich x6a is older than core-rich x1a.

One fragment of xenotime was cut from a zircon-xenotime intergrowth (x8, Figure 9), and has a $^{207}Pb/^{235}U$ date of 23.615 ± 0.046 Ma, slightly younger than fragments from xenotimes with the same flame-structured cores. Additional xenotimes, and one monazite have $^{207}Pb/^{235}U$ dates that range from 23.624 ± 0.050 (x2) to 25.396 ± 0.055 Ma (x3), completely overlapping the range of dates recorded by the xenotime fragments (Figure 10). Four multigrain fractions of zircon also were analyzed. Fractions z6, z7, and z8 were made up of inclusion-rich zircons, similar to the zircons intergrown with xenotime. These three fractions have $^{207}Pb/^{235}U$ dates that range from 24.214 ± 0.027 Ma (z6) to 25.64 ± 0.10 Ma (z8). The final zircon fraction (z5) was made up of three clear, inclusion-free grains, and has a $^{207}Pb/^{235}U$ date of 21.795 ± 0.046 Ma, much younger than other grains analyzed.

There are three alternative interpretations for the nearly concordant xenotime and zircon analyses with $^{207}Pb/^{235}U$ dates that range from ~23.6 to 25.6 Ma. The first interpretation is that all grains crystallizaed at ca. 26 Ma and subsequently lost variable amounts of Pb by volume diffusion. The second interpretation is that the dates represent two component mixing between grains that crystallized at ca. 26 Ma and ca. 23 Ma. The third interpretation is that the grains crystallized episodically over that time interval.

*Diffusive Pb Loss*

Diffusive Pb loss in monazite has been a common explanation for discordance in their U-Pb systematics (e.g. Parrish, 1990). In the Himalayan literature, diffusive Pb loss was called upon in early studies to explain analyses that were nearly concordant, but "too young" (e.g. Schärer, 1984). Because young (Cenozoic) analyses plot on a relatively straight part of the concordia curve, Pb loss, no matter how recent, moves them on a trajectory subparallel to the concordia curve, resulting in analyses that remain nearly concordant (i.e. they might look like the data for 00SK09). This makes data interpretation especially subjective.

The first estimates for the closure temperature of Pb diffusion in monazite were based on studies of monazites in well characterized metamorphic or igneous rocks, and ranged from 630 to 750°C (Köppel & Grunenfelder, 1975; Köppel et al., 1980; Kingsbury et al., 1993; Copeland et al., 1988). The closure temperature for Pb diffusion in xenotime was poorly constrained to be $\geq$ 650°C (Heaman & Parrish, 1991), but similar to that of monazite. Electron microprobe measurements of natural Pb diffusion gradients in the rims of monazites (Suzuki et al., 1994) yielded similar closure temperatures, as did in-diffusion experiments on several natural monazites (Smith & Giletti, 1997). However, more recent studies have demonstrated the preservation of unaltered monazite U-Pb systematics through temperatures in excess of 750°C (Spear & Parrish, 1996; Schaltegger, et al., 1999; Rubatto, et al., 2001), and even in excess of 900°C (Braun, et al., 1998) and 1000°C (Schmitz & Bowring, in press). Two such studies also addressed the closure temperature of Pb in xenotime, and estimated the Pb closure temperatures for monazite and xenotime to be in excess of 800°C (Kamber, et al., 1998) and 1100°C (Asami, et al., 2002).

With the advent of improved microbeam techniques for analyzing the chemistry of phosphate accessory minerals, it has become increasingly clear that many grains preserve complex internal zoning patterns in U, Th, and Pb (Cocherie, et al., 1998; Crowley & Ghent, 1999). The persistence of these patterns in crystals that have experienced subsequent high-temperature metamorphism offers evidence that the diffusive mobility of Pb in monazite is extremely limited at most temperatures accessible in the continental crust. Many recent studies have emphasized the importance of fluid-rock interactions and dissolution-precipitation of monazite in explaining discordance (Hawkins & Bowring, 1997, 1999; Braun, et al., 1998; Crowley & Ghent, 1999). Pb-loss mechanisms in monazite were investigated in an experimental study by Teufel and Heinrich (1997) whose results underscored the importance of dissolution-precipitation of monazite in the presence of a fluid phase, rather than Pb volume diffusion, for resetting U-Pb isotope systematics. In addition, the most recent Pb diffusion experiments on synthetic monazite (Cherniak et al., 2000), measured a much higher activation energy for Pb volume diffusion than previous experiments, and suggest that the closure temperature for Pb diffusion in monazite may be similar to, or even higher than, that for zircon (>1000°C; Cherniak & Watson, 2000).

In light of the most recent studies of Pb diffusion in monazite and xenotime, it is unlikely that the U-Pb systematics of sample 00SK09 can be explained by diffusive Pb loss. Magmatic temperatures for these rocks are likely to be ~650-700 °C (Clemens & Vielzeuf, 1987), far below reasonable estimates for the closure temperature for Pb in both monazite and xenotime. Another argument against diffusive Pb loss in 00SK09 accessory phases is the absence of a correlation between grain size and date. If diffusive Pb loss affected the U-Pb systematics in this rock, we would expect that small grains would be more affected, and therefore appear to be younger.

Since Pb loss by volume diffusion did not disturb the U-Pb systematics of sample 00SK09, and there is no evidence for alteration in the presence of a fluid that might have disturbed the U-Pb systematics, Pb loss by any mechanism is not an appropriate explanation for the observed data.

*Two-Component Mixing*

Another possible interpretation of the near concordant dates between 23 and 26 Ma in granite 00SK09 is that they represent mixtures of two different age components, one at 26 Ma (or slightly older), and one at 23 Ma (or slightly younger). Given the core-rim relationships observed in accessory phases in both samples, a reasonable hypothesis would be that the cores formed at ca. 26 Ma, and the rims at ca. 23 Ma. Several observations suggest that this is not the case. First, the observed dates would be expected to cluster near the two end-members depending on whether they are core-rich or rim-rich. The data for sample 00SK09, however, spread evenly between ca. 23 and ca. 26 Ma. Second, several grains from sample 00SK09 that showed core-rim relationships (x1, x5, x6) were cut in an attempt to isolate the two components. In all cases, $^{207}Pb/^{235}U$ dates for cores and rims from the same grains were different by less than 1 Ma. Core-rich fragments were all older than rim-rich fragments from the same grains, but not necessarily older than rim-rich fragments from other grains. For example, rim-rich fragment x6a has the same $^{207}Pb/^{235}U$ date as core-rich fragment x5a, and is *older* than core-rich fragment x1a. This suggests that all the cores and all the rims did not form at the same times (i.e. 26 and 23 Ma, respectively). In addition, grains that did not show distinct core-rim relationships (x2, x3, x9, x10, m3) also have $^{207}Pb/^{235}U$ dates that span the entire age range in question. These relationships suggest that xenotime was growing throughout the 26 to 23 Ma time interval and that the measured dates are not simple mixtures of two end members.

In order to explore the possibility of mixing in a quantitative way, a simple two-component mixing model was made to try to reproduce the U-Pb systematics observed in sample 00SK09. Older xenotimes in 00SK09 generally have lower Th/U ratios and higher U concentrations (Table 1). Mixing between a core with 40000 ppm U and a Th/U of 0.008, and a rim with 6500 ppm U and a Th/U of 0.308 was considered. A mixing curve between these two end members, along with the data for xenotimes in sample 00SK09 (Table 1), is shown in Figure 11. The mixing model does not fit the data well, but changing the compositions of the end members does not result in a better fit between the model and the data. Assuming the rim component was 23 Ma, and the core component 26 Ma, a Pb/U mixing model was calculated assuming the same U concentrations used in the Th/U model. Poor agreement between the Pb/U mixing model (Figure 12) and the observed data suggests that the observed data are not the result of mixing between two different end members.

*Protracted Accessory Phase Growth*

Given the results of the mixing models, and the fact that diffusive loss of radiogenic Pb in 00SK09 can be disregarded as an important process, the spread in accessory phase dates is interpreted to represent real variation in the crystallization ages of igneous accessory phases. The nearly concordant xenotime and zircon analyses and the one reversely discordant monazite analysis that have $^{207}Pb/^{235}U$ dates ranging from ca. 23.6 to 25.6 Ma indicate magmatic accessory phase growth during that time interval, while the youngest zircon fraction (z5) gives the best estimate of the timing of sill crystallization at 21.795 ± 0.046 Ma. I am not suggesting that the sill remained a partial melt for 3 million years, but rather that the early accessory phase growth is

the result of episodic to semi-continuous production and crystallization of small volumes of melt in the source region that were later entrained in the partial melt that crystallized sill 00SK09.

Other Outcrop 2 Samples

In granite sample 00SK08, most of the monazites are fairly homogeneous in BSE images (Figure 13), with faint oscillatory zoning near the rims (m2, m3). Large inclusions of plagioclase (in m5) and quartz (in m6) also occur. A few grains exhibit patchy zoning (m7). Grains m2 and m3 are unusually normally discordant with $^{207}Pb/^{235}U$ dates of 19.14 ± 0.41 and 19.58 ± 0.23 Ma, respectively (Figure 14, Table 1). Both of these grains, however, had large concentrations of common Pb, making them especially sensitive to the common Pb correction used. Using a more radiogenic common Pb composition than that assumed from the model of Stacey and Kramers (1975) would shift these analyses toward younger $^{207}Pb/^{235}U$ dates, while the $^{206}Pb/^{238}U$ dates would remain largely unchanged, resulting in more concordant analyses. Three other nearly concordant monazites have $^{207}Pb/^{235}U$ dates that range from 18.36 ± 0.13 (m7) to 18.664 ± 0.070 Ma (m6). Grains m6 and m7 contained less common Pb, and are therefore less sensitive to the common Pb correction used. Due to the uncertainties in the common Pb correction for these grains, the youngest date (m7, 18.36 Ma) is considered a minimum estimate of the age of crystallization of the sill from which 00SK08 was collected.

The youngest intrusive phase at the Gokyo Ri outcrop is the undeformed dike 00SK10 that cuts across the $S_1$ schistosity. Grains from this sample were not imaged, but the sample has pre-Himalayan inherited components as evidenced by four normally discordant analyses (m7, m8, m10, m11) with $^{207}Pb/^{235}U$ dates that range from 29.06 ± 0.26 Ma (m8) to 50.77 ± 0.31 Ma (m11) (Figure 15, Table 1). One slightly reversely discordant monazite (m6) has a $^{207}Pb/^{235}U$

date of 18.275 ± 0.065 Ma, which I interpret to be the best estimate of the crystallization age of the dike. Regression of these five monazite analyses does not yield a statistically meaningful discordia, but its implied upper intercept (ca. 440 Ma) is consistent with other evidence for the existence of an Ordovician inherited component in leucogranites of the Everest region (Simpson et al., 2000).

$^{40}Ar/^{39}Ar$ analyses of biotites from Outcrop 2 yielded statistically significant plateaus (Figure 16, Table 2) corresponding to dates of 23.76 ± 0.27 Ma (country rock 00SK07), 20.29 ± 0.21 Ma (granite sill 00SK08), 19.97 ± 0.44 Ma (boudinaged granite sill 00SK09), and 17.97 ± 0.52 Ma (granite dike 00SK10). Calculated closure temperatures for biotite in each sample are reported in Table 3, and range from 377 to 400°C assuming a cooling rate of 100°C/my. The isochron dates for each sample are consistent with the plateau dates. However, that consistency depends on the first step in each spectrum with a high non-radiogenic gas component. This observation, combined with the fact that the $^{40}Ar/^{39}Ar$ date for sample 00SK08 is 2 million years older than the interpreted crystallization age of the granite, and that the $^{40}Ar/^{39}Ar$ date for sample 00SK07 is slightly older than the interpreted age of metamorphism, requires that at least some of the samples contain a component of unresolved excess $^{40}Ar$. As a consequence, all of the biotite dates may be unreliable. Nevertheless, the relative $^{40}Ar/^{39}Ar$ dates agree with the crosscutting relationships observed, suggesting that the $^{40}Ar/^{39}Ar$ cooling ages of the country rock and early intrusive phases were not reset by subsequent intrusions.

Combining the results of $^{40}Ar/^{39}Ar$ biotite and U-Pb analyses suggests country rock metamorphism and the formation of $S_1$ schistosity at 22.64 Ma, followed closely by crystallization of granite sill 00SK09 at 21.8 Ma. This sill contained monazite, xenotime and zircon that had crystallized from earlier crustal melts between ca. 26 Ma and ca. 23 Ma.

$^{40}Ar/^{39}Ar$ biotite data from 00SK09 suggest the sill cooled through ~375°C by 19.97 Ma if these data are not contaminated by excess $^{40}Ar$. Sill 00SK08 intruded next, with a minimum crystallization age of 18.36 Ma, but likely not earlier than 19.6 Ma. Intrusion of 00SK08 does not appear to have strongly affected the $^{40}Ar/^{39}Ar$ systematics of biotite from 00SK07 or 00SK09. Final intrusion and crystallization of cross-cutting dike 00SK10 took place at 18.28 Ma. The concordance of U-Pb monazite and $^{40}Ar/^{39}Ar$ biotite dates in sample 00SK10 implies that the dike underwent rapid cooling through 380°C.

Outcrop 3: Gokyo's 5$^{th}$ Lake

Backscattered electron images of monazites from country rock 01SK53 show relatively simple sector or oscillatory zoning, while the xenotimes have more irregular patchy or sector zoning (Figure 17). Eight monazite analyses and one xenotime analysis cluster near concordia at ca. 19 Ma (Figure 18) showing both normal and reverse discordance. Their $^{207}Pb/^{235}U$ dates range from 18.28 ± 0.17 Ma (m8) to 19.75 ± 0.23 Ma (m7). The positions of these analyses relative to the concordia curve are insensitive to the common Pb correction used since they all have high ratios of radiogenic Pb/common Pb (Table 1). Two older, essentially concordant, xenotimes have $^{207}Pb/^{235}U$ dates of 21.020 ± 0.071 Ma (x1) and 24.36 ± 0.26 Ma (x2). The relationship between these dates and metamorphic fabric development is discussed below.

Monazites from sill 01SK54 display sector zoning (m1), but xenotime internal structures are more patchy and irregular (x1, x5, x3) or feathery (x4, x6) (Figure 19). One xenotime (x4) has a speckled core similar to those seen in 00SK09 xenotimes. U-Pb systematics for samples 01SK54 and 00SK09 are also similar. Six nearly concordant 01SK54 xenotimes have $^{207}Pb/^{235}U$ dates that range from 23.91 ± 0.12 Ma (x11) to 26.251 ± 0.026 Ma (x6), while one much

younger concordant xenotime (x1) and three reversely discordant monazites (m1, m4, m7) have a weighted mean $^{207}Pb/^{235}U$ date of 21.334 ± 0.025 Ma (MSWD= 0.91) (Figure 20, Table 1). Unlike sample 00SK09, the zircon in sample 01SK54 contains a pre-Himalayan inherited component. Two multigrain fractions of zircon are highly discordant (z1, z3) with $^{207}Pb/^{206}Pb$ dates of 477 Ma and 403 Ma, respectively. These results are consistent with the inferred age of inherited monazite analyzed in other samples during this study.

A mixing model similar to the one described for sample 00SK09 was derived for sample 01SK54 in order to determine if the spread in dates between 23.91 and 26.25 Ma could be described by two-component mixing. The mixing model for 01SK54 was equally as unsuccessful as the model for 00SK09 in describing the observed data. Following the logic used to interpret the 00SK09 data, the 01SK54 data are interpreted to represent magmatic crystallization of xenotime and monazite between 26.25 and 23.91 Ma, with those accessory minerals later entrained in melt that intruded as a sill and crystallized at 21.334 ± 0.025 Ma.

The monazite in crosscutting dike 01SK55 is either homogeneous or sector zoned, while the xenotime shows more irregular, patchy zoning (Figure 21). One nearly concordant xenotime and seven reversely discordant monazite analyses have $^{207}Pb/^{235}U$ dates that range from 17.467 ± 0.052 Ma (m4) to 18.328 ± 0.035 Ma (m6) (Figure 22, Table 1), suggesting dike crystallization between 17.47 and 18.33 Ma. Sample 01SK55 also contains zircon with a pre-Himalayan inherited component. Three zircon fractions analyzed have $^{207}Pb/^{206}Pb$ dates that range from 391 Ma to 475 Ma.

$^{40}Ar/^{39}Ar$ analyses of biotite from Outcrop 3 samples yielded plateaus corresponding to cooling ages of 20.53 ± 0.23 (gneiss 01SK53), 19.27 ± 0.63 (granite sill 01SK54), and 17.71 ± 0.15 Ma (granite dike 01SK55) (Figure 23, Table 2). The isochron dates for each sample are

consistent with the plateau dates. However, as with the samples from the Gokyo Ri outcrop, the biotite may contain a component of excess $^{40}Ar$. Because the dates agree with the crosscutting relationships observed, any excess $^{40}Ar$ contamination is likely to be small, and the $^{40}Ar/^{39}Ar$ cooling ages of the country rock and early intrusive phases do not appear to have been reset by subsequent intrusions.

The inverse isochron date of gneiss 01SK53 (20.73 Ma) is approximately the same age as one of the older xenotimes from 01SK53 (21.02 Ma), but is considerably older than all of the monazite dates (18.28-19.75 Ma). The timing of metamorphism and $S_1$ formation at this outcrop is not clear. Granite sill 01SK54 is pre- to syn-kinematic with respect to the formation of $S_1$, and has a crystallization age of 21.33 ± 0.03 Ma. The biotite $^{40}Ar/^{39}Ar$ data for sill 01SK54 suggests cooling through 378°C by 19.27 Ma, unless there is a component of excess $^{40}Ar$ in the biotite. Because the biotite date is not older than the crystallization age of 01SK54, there is no a priori reason to assume that it contains excess $^{40}Ar$ contamination. However, the biotite date is older than many of the U-Pb monazite dates in country rock 01SK53.

There are two possible interpretations of the combined $^{40}Ar/^{39}Ar$ and U-Pb data for samples 01SK53 and 01SK54. The first interpretation is that metamorphism of gneiss 01SK53 and the development of $S_1$ occurred between 21.02 and 24.36 Ma, consistent with the older U-Pb xenotime dates from that sample. This interpretation would make sill 01SK54 syn-kinematic with respect to $S_1$ development, and requires that the young monazite growth in 01SK53 be related to either local reheating, or to low temperature growth during the waning stages of regional metamorphism. A second interpretation is that metamorphism took place sometime between 18.28 and 19.75 Ma, making sill 01SK54 pre-kinematic with respect to the development of $S_1$, and unlikely to have cooled to ~378°C by 19.27 Ma as the biotite data suggest. Given the

consistency between the biotite and U-Pb data from granite 01SK54, and the evidence for earliest Miocene metamorphism at the nearby Gokyo Ri outcrop, I consider the first interpretation most likely.

After intrusion of granite 01SK54 at 21.33 Ma and subsequent cooling to ~378°C by 19.27 Ma, cross-cutting granite 01SK55 intruded between 17.47 and 18.33 Ma, and cooled rapidly, as evidenced by the concordance of U-Pb and $^{40}Ar/^{39}Ar$ dates. The inverse isochron and initial $^{40}Ar/^{36}Ar$ are well defined for the 01SK55 biotite, suggesting that no excess $^{40}Ar$ was present.

**Implications for the Timescales of Crustal Melting**

Evidence for near continuous growth of magmatic xenotime, monazite and zircon in small igneous bodies, such as those from which 00SK09 and 01SK54 were collected, suggests incremental melting and crystallization in the leucogranite source region over a period of several million years, during which the melt did not mobilize. Eventually, melt was capable of migrating from the source region, perhaps when a sufficiently high melt fraction was generated (Sawyer, 1994). This migrating melt entrained minerals from earlier crustal melts. Since 00SK09 and 01SK54 were both collected from syn-kinematic sills, it is also possible that deformational processes assisted melt migration (Rushmer, 1995; Rutter & Neumann, 1995). In the part of the Greater Himalayan Sequence represented by the outcrops at Gokyo Ri and the 5$^{th}$ Lake, this happened at ca. 21-22 Ma. All accessory phases older than ca. 21-22 Ma are then in some sense xenocrystic, although they are intimately related to the production of the melt.

**Implications for Greater Himalayan Sequence Thermal Evolution**

The combination of data from the three outcrops examined for this study demonstrates that the upper Greater Himalayan Sequence had a complex thermal history involving country rock metamorphism and the intrusion of at least two generations of granitic melts. The interpreted age of country rock metamorphism at the Gokyo Ri outcrop, 22.64 ± 0.47 Ma, corresponds to the timing of Neohimalayan metamorphism (22.64 ± 0.47 Ma) determined by Simpson et al. (2000). The timing of country rock metamorphism at the 5$^{th}$ Lake outcrop is interpreted to be between 21.02 and 24.36 Ma.

All three outcrops studied show evidence for crustal melting starting at ca. 26 Ma, which is temporally associated with the implied decompression between high-pressure Eohimalayan and low-pressure Neohimalayan metamorphism. The migmatitic orthogneiss at the Namche Bazaar outcrop experienced temperatures consistent with anatexis (~670°C) between ca. 24.8 and 25.5 Ma (Viskupic & Hodges, 2001). At the Gokyo Ri and 5$^{th}$ Lake outcrops, sills 00SK09 and 01SK54 preserve records of near continuous magmatic accessory phase crystallization between ca. 26 Ma and ca. 23 Ma.

Samples 00SK09 and 01SK54 from the Gokyo Ri and 5$^{th}$ Lake outcrops demonstrate that granitic melt had begun to mobilize in the upper Greater Himalayan Sequence by 21.8-21.3 Ma. $^{40}Ar/^{39}Ar$ data suggest that sills of this generation at this structural level cooled quickly, to below ~380°C, within 2-3 Ma. Nevertheless, melting continued at deeper structural levels for several million years afterwards, as evidenced by the 17.47 Ma to 18.33 Ma ages of post-deformational dikes in the Gokyo Ri, 5$^{th}$ Lake, and Namche Bazaar outcrops. $^{40}Ar/^{39}Ar$ dates of biotites from these granites are concordant with U-Pb crystallization ages, again suggesting rapid cooling.

There is no evidence that intrusion of these small, late-stage dikes caused substantial heating of their country rocks; the $^{40}Ar/^{39}Ar$ systematics of gneisses and older granites in the outcrops into which the post-deformational dikes were emplaced are undisturbed.

The $^{40}Ar/^{39}Ar$ and U-Pb data from this study suggest that the upper Greater Himalayan Sequence in the Everest region experienced rapid cooling between ca. 21 Ma and ca. 19 Ma. If that cooling was the result of movement along the South Tibetan Fault system, decompression could have aided post-19 Ma melt generation. While this in an interesting hypothesis, there are no independent data that constrain the motion on the STF here at 20 Ma. Dating of mylonitized granites from the Rongbuk Valley on the north side of Mount Everest at 16.2-16.8 Ma (Hodges, et al., 1998; Murphy & Harrison, 1999) constrain movement on the STF in the Everest region at 16-17 Ma.

Granite geochronology presented here and in previous studies demonstrates that crustal anatexis in the Everest region took place over a period of roughly 10 million years. However, the thermal structure of the Greater Himalayan Sequence during this period was complicated; while some structural levels were undergoing partial melting at temperatures in excess of 650°C, others had cooled well below 400°C. In outcrops such as those examined as part of this study, where granites of different generations were intruded as thin dikes and sills, the influx of granitic magma was not responsible for substantial advection of heat. Areas where large plutons intruded likely experienced a much different thermal history.

**Acknowledgements**
This work was funded by a National Science Foundation grant to KV Hodges and SA Bowring.

## Appendix A
## Analytical Techniques

### *$^{40}Ar/^{39}Ar$ Techniques*

Biotite was separated from coarsely crushed samples (>500 μm) for $^{40}Ar/^{39}Ar$ using standard magnetic methods followed by hand picking of subhedral to euhedral grains. Resulting mineral separates were approximately 99% pure. Grains were washed in distilled water, acetone, and ethanol in an ultrasonic bath and then packaged in Al foil. Two to four individual sample packets were placed in Al disks, and up to eight disks were stacked for irradiation at the McMaster University reactor.

K, Ca, and Cl production factors during irradiation were determined by including packets of synthetic, reagent grade $K_2SO_4$, $CaF_2$, and KCl salts with the samples. Fast neutron flux was monitored using Fish Canyon sanidine (28.02 Ma, Renne et al., 1998), and Taylor Creek Rhyolite sanidine (TCR-2; 27.87 ± 0.04 Ma, Duffield & Dalrymple, 1990), and the results were used to calculate the irradiation parameter, *J*, (e.g. McDougall and Harrison, 1999). The mean *J* calculated for a disk was assigned to all samples in that disk. A conservative 2% uncertainty in *J* (at 2σ) was assumed for all samples in order to account for potential heterogeneities in the monitor materials and neutron flux.

Gas extraction was accomplished by incremental heating in a double-vacuum resistance furnace. Additional details of the extraction line and gas purification are given by Hodges et al. (1994). The furnace contributes the dominant component of the operational blank which is therefore strongly temperature dependent. Furnace system blanks were measured as a function of temperature prior to each sample analysis.

$^{40}Ar/^{39}Ar$ model ages for each gas extraction step were calculated assuming an initial $^{40}Ar/^{39}Ar$ value of 295.5 and are assigned a $2\sigma$ uncertainty that reflects propagated errors in all correction factors and *J*. Release spectra illustrate model ages for incremental heating analyses as a function of the amount of $^{39}Ar_K$ in each step. Plateau ages determined from the release spectra are defined as the error-weighted mean age of at least three consecutive increments that define 50% or more of the total $^{30}Ar_K$ released and have model ages that overlap at the $2\sigma$ confidence level when the error in *J* is ignored. Age estimates also were derived from linear fits of the data on $^{36}Ar/^{40}Ar$ verses $^{39}Ar/^{40}Ar$ isotope correlation diagrams. For all samples, the two methods of data analysis yield dates that are indistinguishable at the $2\sigma$ confidence level. We have therefore chosen to use the plateau ages as the best estimate of the closure age of the sample since the errors associated with the plateau age are slightly smaller.

Closure temperatures for biotites were calculated using the equations of Dodson (1973) and diffusion parameters (see Table 3) for biotite from the experimental results of Grove and Harrison (1996) and Harrison et al. (1985).

*U-Pb Techniques*

U-Pb analyses of monazite, xenotime, and zircon were made by isotope dilution thermal ionization mass spectrometry (IDTIMS). All analyses of monazite and xenotime were conducted with single grains or grain fragments. Analyzed zircon fractions contained 1 to 4 grains. Prior to dissolution, most monazite and xenotime grains were mounted in epoxy and polished for backscattered electron (BSE) imaging. Backscattered electron images were made on a JEOL Superprobe 733 at MIT operating at an accelerating voltage of 15 to 20 kV and a beam current of 10 to 15 nA. Mineral inclusions were identified by energy dispersive analysis (EDS) under the

same operating conditions. BSE images were made in order to examine the internal structures of the crystals and to try to avoid grains with possibly inherited cores. In cases where cores were observed, single grains were cut with an obsidian blade in an attempt to isolate the core and rim components. After grains were plucked from the epoxy mounts, they were washed in acetone and warm water, and dissolved in HCl with a mixed $^{205}Pb$-$^{233}U$-$^{235}U$ tracer. Zircons were divided into different populations based on color, morphology, and inclusion characteristics, and were air abraded (Krogh, 1982) for approximately 40 hours or until all crystal faces were removed. After abrasion, zircons were washed in warm 30% $HNO_3$ for several hours and were then placed in an ultrasonic bath. Zircons were dissolved in HF with a mixed $^{205}Pb$-$^{233}U$-$^{235}U$ tracer. Uranium and Pb from all minerals were isolated by anion exchange chromatography and analyzed on a VG Sector 54 mass spectrometer at MIT. Lead was analyzed either: (1) in static mode, using Faraday detectors for all isotopes except $^{204}Pb$, which was measured simultaneously with the Daly detector in ion counting mode; or (2) by peak-jumping using a Daly detector in ion counting mode. Uranium was analyzed as an oxide in static mode using faraday collectors. Details of fractionation and blank corrections are given in Table 1.

## References


Andrehs, G., Heinrich, W. (1998) Experimental determination of REE distributions between monazite and xenotime: potential for temperature-calibrated geochronology. Chemical Geology, v. 149, p. 83-96.

Asami, M., Suzuki, K., Grew, E.S. (2002) Chemical Th-U-total Pb dating by electron microprobe analysis of monazite, xenotime and zircon from the Archean Napier Complex, East Antarctica: evidence for ultra-high-temperature metamorphism at 2400 Ma. Precambrian Research, v. 114, p. 249-275.

Bea, F. (1996) Residence of REE, Y, Th, and U in granites and crustal protoliths; implications for the chemistry of crustal melts. Journal of Petrology, v. 37, p. 521-552.

Braun, I., Montel, J.-M., Micollet, C. (1998) Electron microprobe dating of monazites from high-grade gneisses and pegmatites of the Kerala Khondalite Belt, southern India. Chemical Geology, v. 146, p. 65-85.

Carosi R., Lombardo B., Musumeci G., Pertusati P.C. (1999) Geology of the higher Himalayan crystallines in Khumbu Himal (eastern Nepal). Journal of Asian Earth Sciences, v. 17, p. 785-803.

Cherniak, D.J., Watson, E.B., Harrison, T.M., Grove, M. (2000) Pb diffusion in monazite: a progress report on a combined RBS/SIMS study [abs.]. EOS (Transactions, American Geophysical Union), v. 81, p. S25.

Cherniak, D.J., Watson, E.B. (2000) Pb diffusion in zircon. Chemical Geology, v. 172, p. 5-24.

Clemens, J.D., Vielzeuf, D. (1987) Constraints on melting and magma production in the crust. Earth and Planetary Science Letters, v.86, p. 287-306.

Cocherie, A., Legendre, O., Peucat, J.J., Kouamelan, A.N. (1998) Geochronology of polygenetic monazites constrained by in situ electron microprobe Th-U-total lead determination: Implications for lead behavior in monazite. Geochim. Cosmochim. Act. v. 62, p. 2475-2497.

Copeland, P., Parrish, R.R., Harrison, T.M. (1988) Identification of inherited radiogenic Pb in monazite and its implications for U-Pb systematics. Nature, v. 333, p. 760-763.

Crowley, J.L., Ghent, E.D. (1999) An electron microprobe study of the U-Th-Pb systematics of metamorphosed monazite: the role of Pb diffusion versus overgrowth and recrystallization. Chemical Geology, v. 157, p. 285-302.

Dodson, M.H. (1973) Closure temperature in cooling geochronoligical and petrological systems. Contributions to Mineralogy and Petrology, v. 40, p. 259-274.

Duffield, W.A., Dalrymple, G.B. (1990) The Taylor Creek rhyolite of New Mexico- a rapidly emplaced field of lava domes and flows. Bulletin of Volcanology, v. 52, p. 475-487.

Gratz, R., Heinrich, W. (1997) Monazite-xenotime thermobarometry: experimental calibration of the miscibility gap in the binary system $CePO_4$-$YPO_4$. American Mineralogist, v. 82, p. 772-780.

Grove, M., Harrison, T.M. (1996) $^{40}Ar^*$ diffusion in Fe-rich biotite. American Mineralogist, v. 81, 940-951.

Harris N., Massey J. (1994) Decompression and anatexis of Himalayan metapelites. Tectonics, v. 13, p. 1537-1546.

Harrison, T.M., Duncan, I., McDougall, I. (1985) Diffusion of 40Ar in biotite: Temperature, pressure, and compositional effects. Geochimica et Cosmochimica Acta, v. 49, p. 2461-2468.

Harrison T.M., Grove M., Lovera O.M., Catlos E.J. (1998) A model for the origin of Himalayan anatexis and inverted metamorphism. Journal of Geophysical Research, v. 103, p. 27017-27032.

Harrison, T.M., Grove, M., Lovera, O.M., Catlos, E.J., D'Andrea, J. (1999) The origin of Himalayan anatexis and inverted metamorphism: models and constraints. Journal of Asian Earth Sciences, v. 17, p. 755-772.

Hawkins, D.P., Bowring, S.A. (1997) U-Pb systematics of monazite and xenotime: case studies from the Paleoproterozoic of the Grand Canyon, Arizona. Contributions to Mineralogy and Petrology, v. 127, p. 87-103.

Hawkins, D.P., Bowring, S.A. (1999) U-Pb monazite, xenotime and titanite geochronological constraints on the prograde to post-peak metamorphic thermal history of Paleoproterozoic migmatites from the Grand Canyon, Arizona. Contributions to Mineralogy and Petrology, v. 134, p. 150-169.

Heaman, L., Parrish, R.R. (1991) U-Pb geochronology of accessory minerals. In: Heaman, L., Ludden, J.N. (eds.) Short Course Handbook on Applications of Radiogenic Isotope Systems to Problems in Geology. Mineralogical Association of Canada, Toronto. p. 59-102.

Hodges, K.V. (2000) Tectonics of the Himalaya and southern Tibet from two perspectives. Geological Society of America Bulletin, v. 112, p. 324-350.

Hodges, K., Bowring, S., Davidek, K., Hawkins, D., Krol, M (1998) Evidence for rapid displacement on Himalayan normal faults and the importance of tectonic denudation in the evolution of mountain ranges. Geology, v. 26 p. 483-486.

Hodges, K.V., Hames, W.E., Olszewski, W.J., Burchfiel, B.C., Royden, L.H., Chen, Z. (1994) Thermobarometric and $^{40}Ar/^{39}Ar$ geochronologic constraints on Eohimalayan metamorphism in the Dinggye area, southern Tibet. Contributions to Mineralogy and Petrology, v. 117, p. 151-163.

Hodges K.V., Parrish R.R., Housh T.B., Lux D.R., Burchfiel B.C., Royden L.H., Chen, Z. (1992) Simultaneous Miocene extension and shortening in the Himalayan orogen. Science, v. 258, p. 1466-1470.

Hubbard, M.S., Harrison, T.M. (1989) $^{40}Ar/^{39}Ar$ age constraints on deformation and metamorphism in the Main Central Thrust zone and Tibetan slab, eastern Nepal Himalaya. Tectonics, v. 8, p. 865-880.

Huerta A.D., Royden L.H., Hodges K.V. (1998) The thermal structure of collisional orogens as a response to accretion, erosion, and radiogenic heating. Journal of Geophysical Research, v. 103, p. 15287-15302.

Kamber, B.S., Frei, R., Gibb, A.J. (1998) Pitfalls and new approaches in granulite chronometry. An example from the Limpopo Belt, Zimbabwe. Precambrian Research, v. 91, p. 269-285.

Kingsbury, J.A., Miller, C.F., Wooden, J.L., Harrison, T.M. (1993) Monazite paragenesis and U-Pb systematics in rocks of the eastern Mojave Desert, California, USA: implications for thermochronometry. Chemical Geology, v. 110, p. 147-167.

Köppel, V. (1974) Isotopic U-Pb ages of monazites and zircons from the crust-mantle transition and adjacent units of the Ivrea and Ceneri Zones (Southern Alps, Italy). Contributions to Mineralogy and Petrology v. 43, p. 55-70.

Köppel, V., Grunenfelder, M. (1975) Concordant U-Pb ages of monazite and xenotime from the Central Alps and the timing of the high temperature Alpine metamorphism, a preliminary report. Schweiz. Mineral. petrog. Mitt. v. 55, p. 129-132.

Köppel, V., Gunthert, A., Grunenfelder, M. (1980) Patterns of U-Pb zircon and monazite ages in polymetamorphic units of the Swiss Central Alps. Schweiz. Mineral. petrogr. Mitt. v. 61, p. 97-119.

Krogh T.E. (1982) Improved accuracy of U-Pb ages by the creation of more concordant systems using an air abrasion technique. Geochim Cosmoshim Acta, v. 46, pl 637-649.

McDougall I., Harrison T.M. (1999) Geochronology and Thermochronology by the $^{40}Ar/^{39}Ar$ Method ($2^{nd}$ Ed.). New York, Oxford University Press, 269 p.

Murphy, M.A., Harrison, T.M. (1999) Relationship between leucogranites and the Qomolangma detachment in the Rongbuk Valley, south Tibet. Geology, v. 27, p. 831-834.

Parrish, R.R. (1990) U-Pb dating of monazite and its application to geological problems. Canadian Journal of Earth Sciences, v. 27, p. 1431-1450.

Pognante, U., Benna, P. (1993) Metamorphic zonation, migmatization and leucogranites along the Everest transect of eastern Nepal and Tibet: record of an exhumation history. In Treloar, P.J., Searle, M.P. (eds). Himalayan Tectonics. Geological Society Special Publication no. 74, p. 323-340.

Renne, P.R., Swisher, C.C., Deino, A.L., Karner, D.B., Owens, T.L., DePaolo, D.J. (1998) Intercalibration of standards, absolute ages and uncertainties in $^{40}Ar/^{39}Ar$ dating. Chemical Geology, v. 145, p. 117-152.

Rubatto, D., Williams, I.S., Buick, I.S. (2001) Zircon and monazite response to prograde metamorphism in the Reynolds Range, central Australia. Contributions to Mineralogy and Petrology v. 140, p. 458-468.

Rushmer, T. (1995) An experimental deformation study of partially molten amphibolite: Application to low-melt fraction segregation. Journal of Geophysical Research, v. 100, p. 15681-15695.

Rutter, E., Neumann, D. (1995) Experimental deformation of partially molten Westerly Granite under fluid-absent conditions, with implications for the extraction of granitic magmas. Journal of Geophysical Research, v. 100, p. 15697-15715.

Sawyer, E. (1994) Melt segregation in the continental crust. Geology, v. 22, p. 1019-1022.

Schaltegger, U., Fanning, C.M., Gunther, P., Maurin, J.C., Schulmann, K., Gebauer, D. (1999) Growth, annealing and recrystallization of zircon and preservation of monazite in high-grade metamorphism: conventional and in-situ U-Pb, isotope, cathodoluminesence and microchemical evidence. Contributions to Mineralogy and Petrology, v. 134, p. 186-201.

Schärer, U. (1984) The effect of initial $^{230}Th$ disequilibrium on young U-Pb ages: the Makalu case, Himalaya. Contributions to Mineralogy and Petrology, v. 67, p. 191-204

Schmitz, M.D., Bowring, S.A. (in press) Ultrahigh-temperature metamorphism in the lower crust during Neoarchean Ventersdorp rifting and magmatism, Kaapvaal Craton, southern Africa. Geological Society of America Bulletin.

Searle, M.P. (1999) Extensional and compressional faults in the Everest-Lhotse massif, Khumbu Himalaya, Nepal. Journal of the Geological Society of London, v. 156, p. 227-240.

Simpson, R.L, Parrish, R.R., Searle, M.P., Waters, D.J. (2000) Two episodes of monazite crystallization during metamorphism and crustal melting in the Everest region of the Nepalese Himalaya. Geology, v. 28, p. 403-406.

Smith, H.A., Giletti, B.J. (1997) Lead diffusion in monazite. Geochim. Cosmocim. Act. v. 61, p. 1047-1055.

Spear, F.S., Parrish, R.R. (1996) Petrology and Cooling rates of the Valhalla Complex, British Columbia, Canada. Journal of Petrology, v. 37, p. 733-765.

Stacey, I.S., Kramers, J.D. (1975) Approximation of terrestrial lead isotope evolution by a two-stage model. Earth and Planetary Science Letters, v. 26, p. 207-221.

Suzuki, K., Adachi, M., Kajizuka, I. (1994) Electron microprobe observations of Pb diffusion in metamorphosed detrital monazites. Earth and Planetary Science Letters, v. 128, p. 391-405.

Teufel, S., Heinrich, W. (1997) Partial resetting of the U-Pb isotope system in monazite through hydrothermal experiments: An SEM and U-Pb isotope study. Chemical Geology, v. 137, p. 273-281.

Viskupic K., Hodges, K.V. (2001) Monazite-xenotime thermochronometry: methodology and an example from the Nepalese Himalaya. Contributions to Mineralogy and Petrology, v. 141, p. 233-247.

Wark, D.A., Miller, C.F. (1993) Accessory mineral behavior during differentiation of a granite suite: monazite, xenotime and zircon in the Sweetwater Wash pluton, southeastern California, U.S.A. Chemical Geology, v. 110, p. 49-67.

Wendt, I., Carl, C. (1991) The statistical distribution of the mean squared weighted deviation. Chemical Geology, v. 86, p. 275-285.

**Table 1.** U-Pb geocronologic data.

| Sample | Fractions[a] | Weight[b] (mg) | Composition U[c] (ppm) | Th[c] U | Pb[c] (ppm) | Pb*/Pbc[d] | Pbc[e] (pg) | Isotopic Ratios 206 Pb*[f] 204 Pb | 208 Pb[g] 206 Pb | 206 Pb[g] 238 U | % err | 207 Pb[g] 235 U | % err | 207 Pb[g] 206 Pb | % err | corr. coef. | Dates (Ma) 206 Pb 238 U | 207 Pb[h] 235 U | error (Ma) | 207 Pb 206 Pb |
|---|---|---|---|---|---|---|---|---|---|---|---|---|---|---|---|---|---|---|---|---|
| *Namche Bazaar* | | | | | | | | | | | | | | | | | | | | |
| 98E6 | m12 (1) | 0.0096 | 3115 | 7.06 | 26.0 | 25.6 | 9.52 | 605.8 | 2.184 | 0.002919 | (.30) | 0.01799 | (.40) | 0.04469 | (.26) | 0.761 | 18.79 | 18.102 | 0.073 | -72.4 |
| | m5 (1) | 0.0048 | 2470 | 6.86 | 21.4 | 8.37 | 11.2 | 215.7 | 2.103 | 0.002940 | (.72) | 0.01795 | (1.72) | 0.04430 | (1.49) | 0.509 | 18.92 | 18.07 | 0.31 | -94.1 |
| | m2 (1) | 0.0007 | 16942 | 8.56 | 166 | 10.4 | 10.8 | 227.2 | 2.641 | 0.002888 | (.70) | 0.01775 | (1.69) | 0.04458 | (1.46) | 0.514 | 18.59 | 17.86 | 0.30 | -78.8 |
| | m3 (1) | 0.0002 | 22291 | 8.33 | 238 | 3.22 | 9.28 | 84.11 | 2.609 | 0.002828 | (2.35) | 0.01765 | (3.87) | 0.04526 | (2.95) | 0.648 | 18.20 | 17.76 | 0.69 | -41.4 |
| | x6 (1) | 0.0117 | 8716 | 0.204 | 30.3 | 2.83 | 93.4 | 207.4 | 0.0660 | 0.002713 | (.10) | 0.01746 | (.26) | 0.04667 | (.23) | 0.473 | 17.47 | 17.576 | 0.045 | 32.6 |
| *Gokyo Ri* | | | | | | | | | | | | | | | | | | | | |
| 00SK07 | m2a (f) | 0.0041 | 9559 | 1.06 | 658 | 464 | 5.83 | 22580 | 0.4735 | 0.052156 | (.07) | 0.40454 | (.08) | 0.05625 | (.04) | 0.855 | 327.7 | 344.94 | 0.29 | 462 |
| | m2b (f) | 0.0043 | 5376 | 1.80 | 325 | 1.18 | 638 | 70.74 | 0.6249 | 0.022647 | (.30) | 0.16748 | (1.64) | 0.05363 | (1.52) | 0.472 | 144.4 | 157.2 | 2.6 | 356 |
| | m5 (1) | 0.0031 | 2755 | 0.428 | 56.3 | 19.8 | 8.54 | 1239 | 0.1530 | 0.019108 | (.17) | 0.14415 | (.20) | 0.05471 | (.11) | 0.832 | 122.02 | 136.73 | 0.27 | 401 |
| | m10 (1) | 0.0031 | 6204 | 3.36 | 186 | 45.8 | 12.5 | 1519 | 1.208 | 0.015127 | (.10) | 0.11305 | (.12) | 0.05420 | (.07) | 0.823 | 96.79 | 108.75 | 0.13 | 379 |
| | m7 (1) | 0.0028 | 12015 | 7.24 | 547 | 180 | 8.38 | 3686 | 2.588 | 0.014404 | (.11) | 0.10678 | (.15) | 0.05377 | (.10) | 0.746 | 92.19 | 103.02 | 0.15 | 361 |
| | m6 (1) | 0.0072 | 1326 | 16.7 | 92.5 | 65.1 | 10.1 | 700.2 | 6.008 | 0.011286 | (.24) | 0.08349 | (.30) | 0.05365 | (.16) | 0.830 | 72.35 | 81.42 | 0.24 | 356 |
| | m9 (1) | 0.0247 | 482 | 5.04 | 13.0 | 7.46 | 38.5 | 213.6 | 1.778 | 0.009873 | (.22) | 0.07115 | (.52) | 0.05227 | (.45) | 0.514 | 63.33 | 69.79 | 0.36 | 297 |
| | m3b (f) | 0.0005 | 8533 | 3.90 | 177 | 2.06 | 27.7 | 83.11 | 1.317 | 0.007109 | (.76) | 0.04847 | (1.20) | 0.04945 | (.89) | 0.672 | 45.67 | 48.06 | 0.58 | 169 |
| | m8 (1) | 0.0045 | 4530 | 5.86 | 96.8 | 2.21 | 138 | 73.07 | 1.950 | 0.005717 | (.18) | 0.03831 | (.67) | 0.04860 | (.62) | 0.414 | 36.75 | 38.18 | 0 26 | 129 |
| | m4 (1) | 0.0142 | 4410 | 4.07 | 45.7 | 28.5 | 22.1 | 884.5 | 1.384 | 0.004791 | (.20) | 0.03274 | (.25) | 0.04955 | (.14) | 0.813 | 30.81 | 32.708 | 0.081 | 174 |
| | m11(1) | 0.0017 | 2197 | 4.04 | 19.1 | 2.91 | 9.24 | 111.4 | 1.285 | 0.003553 | (1.73) | 0.02255 | (2.06) | 0.04603 | (1.04) | 0.864 | 22.86 | 22.64 | 0.47 | -0.7 |
| 00SK08 | m3 (1) | 0.0097 | 1781 | 8.80 | 23.7 | 3.01 | 58.3 | 75.37 | 2.872 | 0.002992 | (.39) | 0.01947 | (1.16) | 0.04719 | (1.05) | 0.447 | 19.26 | 19.58 | 0.23 | 58.9 |
| | m2 (1) | 0.0032 | 2036 | 6.17 | 24.1 | 1.65 | 30.2 | 58.34 | 2.032 | 0.002896 | (.99) | 0.01902 | (2.14) | 0.04764 | (1.83) | 0.525 | 18.64 | 19.14 | 0.41 | 81.6 |
| | m6 (1) | 0.0069 | 5900 | 5.69 | 48.9 | 6.11 | 48.2 | 175.8 | 1.827 | 0.002899 | (.20) | 0.01855 | (.38) | 0.04641 | (.30) | 0.587 | 18.66 | 18.664 | 0.070 | 18.9 |
| | m5 (1) | 0.0111 | 621.3 | 4.56 | 8.21 | 0.832 | 51.5 | 43.32 | 1.452 | 0.002886 | (.78) | 0.01831 | (2.41) | 0.04602 | (2.17) | 0.4499 | 18.58 | 18.43 | 0.44 | -1.4 |
| | m7 (1) | 0.0051 | 4664 | 4.03 | 37.98 | 2.29 | 60.1 | 91.30 | 1.291 | 0.002860 | (.31) | 0.01825 | (.70) | 0.04627 | (.60) | 0.521 | 18.41 | 18.36 | 0.13 | 11.7 |
| 00SK09 | z8 (3) | 0.0110 | 2061.8 | 0.007 | 7.76 | 10.9 | 7.47 | 793.3 | 0.0021 | 0.003983 | (.29) | 0.0256 | (.38) | 0.04658 | (.24) | 0.780 | 25.62 | 25.64 | 0.10 | 27.5 |
| | x3 (1) | 0.0378 | 20138 | 0.050 | 88.0 | 4.56 | 599 | 337.8 | 0.0160 | 0.003928 | (.17) | 0.0253 | (.22) | 0.04677 | (.13) | 0.804 | 25.27 | 25.396 | 0.055 | 37.3 |
| | x10a (f) | 0.0075 | 15238 | 0.144 | 66.4 | 5.38 | 79.0 | 384.9 | 0.0461 | 0.003940 | (.07) | 0.0253 | (.16) | 0.04651 | (.13) | 0.526 | 25.35 | 25.335 | 0.039 | 24.0 |
| | z7 (2) | 0.0041 | 4738 | 0.006 | 16.8 | 16.4 | 4.16 | 1188 | 0.0020 | 0.003907 | (.35) | 0.0251 | (.39) | 0.04655 | (.16) | 0 906 | 25.13 | 25.15 | 0.10 | 26.4 |
| | x6b (f) | 0.0043 | 28249 | 0.110 | 103 | 49.9 | 8.71 | 3459 | 0.0352 | 0.003861 | (.08) | 0.0248 | (.10) | 0.04653 | (.07) | 0.754 | 24.84 | 24.846 | 0.025 | 25.3 |
| | x6a (f) | 0.0147 | 13534 | 0.124 | 51.5 | 13.9 | 51.2 | 969.1 | 0.0397 | 0.003817 | (.07) | 0.0245 | (.10) | 0.04655 | (.08) | 0.684 | 24.56 | 24.576 | 0.026 | 26.2 |
| | x5a (f) | 0.0163 | 11186 | 0.135 | 51.0 | 3.61 | 181 | 264.7 | 0.0432 | 0.003826 | (.13) | 0.0245 | (.38) | 0.04642 | (.34) | 0.444 | 24.62 | 24.566 | 0.093 | 19.5 |
| | x1a (f) | 0.0024 | 9765 | 0.136 | 39.7 | 5.31 | 15.7 | 381.1 | 0.0437 | 0.003782 | (.29) | 0.0242 | (.35) | 0.04650 | (.19) | 0.841 | 24.33 | 24.327 | 0.084 | 23.7 |
| | x9 (1) | 0.0203 | 18144 | 0.119 | 64.4 | 70.04 | 18.5 | 4822 | 0.0383 | 0.003764 | (.06) | 0.0241 | (.08) | 0.04652 | (.05) | 0.801 | 24.22 | 24.226 | 0.018 | 24.8 |
| | z6 (4) | 0.0061 | 6482 | 0.009 | 21.9 | 40.2 | 3.33 | 2889 | 0.0030 | 0.003751 | (.08) | 0.0241 | (.11) | 0.04666 | (.07) | 0.753 | 24.13 | 24.214 | 0.027 | 32.0 |
| | m3 (1) | 0.0165 | 5313 | 4.36 | 53.2 | 4.63 | 156 | 167.5 | 1.259 | 0.004157 | (.17) | 0.0240 | (.92) | 0.04179 | (.87) | 0.378 | 26.74 | 24.04 | 0.22 | -238.9 |
| | x1c (f) | 0.0021 | 15342 | 0.128 | 112 | 0.892 | 125 | 79.66 | 0.0409 | 0.003739 | (.19) | 0.0240 | (1.17) | 0.04647 | (1.09) | 0.459 | 24.06 | 24.04 | 0.28 | 22.1 |
| | x5b (f) | 0.0034 | 16956 | 0.138 | 98.1 | 1.46 | 136 | 118.1 | 0.0442 | 0.003702 | (.12) | 0.0237 | (.45) | 0.04649 | (.42) | 0.407 | 23.82 | 23.81 | 0.11 | 22.9 |
| | x1b (f) | 0.0007 | 19587 | 0.132 | 95.0 | 2.15 | 22.8 | 165.5 | 0.0421 | 0.003720 | (.45) | 0.0237 | (.60) | 0.04626 | (.38) | 0.775 | 23.93 | 23.81 | 0.14 | 11.3 |
| | x2 (1) | 0.0578 | 6681 | 0.177 | 25.0 | 13.6 | 99.2 | 932.9 | 0.0565 | 0.003680 | (.10) | 0.0235 | (.21) | 0.04639 | (.18) | 0.517 | 23.68 | 23.624 | 0.050 | 18.0 |
| | x8 (f) | 0.0027 | 17411 | 0.157 | 63.8 | 12.1 | 13.5 | 842.7 | 0.0505 | 0.003665 | (.15) | 0.0235 | (.19) | 0.04657 | (.11) | 0.809 | 23.58 | 23.615 | 0.046 | 27.0 |
| | z5 (3) | 0.0234 | 939 | 0.004 | 2.86 | 19.6 | 3.42 | 1417 | 0.0014 | 0.003379 | (.15) | 0.0217 | (.21) | 0.04657 | (.15) | 0.709 | 21.74 | 21.796 | 0.047 | 27.4 |
| 00SK10B | m11 (1) | 0.0024 | 4096 | 5.50 | 93.8 | 3.83 | 47.3 | 111.8 | 1.987 | 0.007019 | (.32) | 0.0513 | (.60) | 0.05297 | (.49) | 0.593 | 45.09 | 50.77 | 0.31 | 327.6 |
| | m7 (1) | 0.0040 | 6333 | 4.53 | 100 | 9.90 | 37.2 | 296.1 | 1.587 | 0.006343 | (.16) | 0.0448 | (.26) | 0.05124 | (.19) | 0.661 | 40.76 | 44.52 | 0.11 | 251.8 |
| | m10 (1) | 0.0041 | 3594 | 2.71 | 29.4 | 6.46 | 16.7 | 263.4 | 0.9084 | 0.004322 | (.39) | 0.0290 | (.64) | 0.04873 | (.49) | 0.650 | 27.804 | 29.07 | 0.19 | 135.0 |
| | m8 (1) | 0.0027 | 3224 | 8.39 | 50.9 | 8.27 | 15.1 | 177.6 | 2.800 | 0.004340 | (.64) | 0.0290 | (.91) | 0.04852 | (.62) | 0.736 | 27.91 | 29.06 | 0.26 | 124.6 |
| | m6 (1) | 0.0086 | 7352 | 5.20 | 55.9 | 6.96 | 60.7 | 209.8 | 1.647 | 0.002879 | (.14) | 0.0182 | (.36) | 0.04574 | (.32) | 0.476 | 18.54 | 18.275 | 0.065 | -15.8 |

| Sample | Fractions[a] | Weight[b] (mg) | Composition U[c] (ppm) | Th[g] U | Pb[c] (ppm) | Pb*/Pbc[d] | Pbc[e] (pg) | Isotopic Ratios 206 Pb*[f] 204 Pb | 208 Pb[g] 206 Pb | 206 Pb[g] 238 U | % err | 207 Pb[g] 235 U | % err | 207 Pb[g] 206 Pb | % err | corr. coef. | Dates (Ma) 206 Pb 238 U | 207 Pb[h] 235 U | error (Ma) | 207 Pb 206 Pb |
|---|---|---|---|---|---|---|---|---|---|---|---|---|---|---|---|---|---|---|---|---|
| *5th Lake* | | | | | | | | | | | | | | | | | | | | |
| 00SK53 | x2 (1) | 0.0044 | 10679 | 0.702 | 77.1 | 1.33 | 148 | 96.06 | 0.2244 | 0.003802 | (.18) | 0.0243 | (1.06) | 0.04632 | (.99) | 0.420 | 24.46 | 24.36 | 0.26 | 14.4 |
| | x1 (1) | 0.0043 | 16818 | 0.993 | 72.1 | 7.32 | 37.7 | 415.9 | 0.3211 | 0.003239 | (.13) | 0.0209 | (.34) | 0.04684 | (.30) | 0.466 | 20.85 | 21.020 | 0.071 | 40.9 |
| | m7 (1) | 0.0045 | 6074 | 13.4 | 121 | 2.39 | 161 | 50.90 | 4.413 | 0.002992 | (.22) | 0.0196 | (1.17) | 0.04760 | (1.09) | 0.414 | 19.26 | 19.75 | 0.23 | 79.6 |
| | m1 (1) | 0.0077 | 3491 | 14.2 | 53.9 | 14.1 | 27.6 | 201.6 | 4.651 | 0.002946 | (.36) | 0.0193 | (1.29) | 0.04754 | (1.19) | 0.421 | 18.96 | 19.42 | 0.25 | 76.2 |
| | x3 (1) | 0.0077 | 16780 | 1.02 | 60.3 | 55.00 | 8.33 | 2995 | 0.3282 | 0.003002 | (.08) | 0.0193 | (.11) | 0.04659 | (.07) | 0.795 | 19.33 | 19.400 | 0.021 | 28.5 |
| | m3 (1) | 0.0062 | 4744 | 15.5 | 77.6 | 14.6 | 31.2 | 193.00 | 5.130 | 0.002881 | (.41) | 0.0190 | (1.30) | 0.04784 | (1.18) | 0.440 | 18.55 | 19.12 | 0.25 | 91 3 |
| | m4 (1) | 0.0096 | 4556 | 17.7 | 80.8 | 33.98 | 22.3 | 391.2 | 5.687 | 0.002966 | (.20) | 0.0190 | (.31) | 0.04644 | (.23) | 0.676 | 19.09 | 19.103 | 0.059 | 20.6 |
| | m5 (1) | 0.0067 | 3257 | 10.8 | 37.9 | 47.6 | 5.30 | 799.00 | 3.479 | 0.002952 | (.40) | 0.0189 | (.46) | 0.04647 | (.21) | 0.887 | 19.004 | 19.030 | 0.088 | 22.3 |
| | m6 (1) | 0.0062 | 5307 | 12.6 | 69.4 | 60.4 | 7.08 | 918.3 | 3.9296 | 0.003010 | (.26) | 0.0187 | (.33) | 0.04508 | (.19) | 0.823 | 19.38 | 18.822 | 0.062 | -51.3 |
| | m9 (1) | 0.0132 | 2846 | 14.7 | 42.2 | 33.0 | 16.5 | 448.5 | 4.622 | 0.002952 | (.24) | 0.0186 | (.38) | 0.04558 | (.29) | 0.646 | 19.000 | 18.663 | 0.072 | -24.6 |
| | m8 (1) | 0.0048 | 2631 | 14.6 | 38.7 | 18.4 | 9.74 | 264.9 | 4.493 | 0.002963 | (.67) | 0.0182 | (.94) | 0.04446 | (.65) | 0.726 | 19.07 | 18.28 | 0.17 | -85.1 |
| 00SK54 | z1 (2) | 0.0062 | 753 | 0.191 | 34.8 | 12.1 | 16.7 | 794.8 | 0.107 | 0.043333 | (.20) | 0.3392 | (.62) | 0.05677 | (.55) | 0.463 | 273.5 | 296.5 | 1.8 | 482.4 |
| | z3 (4) | 0.0043 | 3958 | 0.155 | 83.8 | 17.2 | 20.0 | 1169 | 0.055 | 0.021179 | (.15) | 0.1602 | (.24) | 0.05488 | (.18) | 0.652 | 135.1 | 150.92 | 0.37 | 407.2 |
| | x6 (1) | 0.0104 | 19805 | 0.608 | 92.2 | 14.4 | 62.7 | 880.2 | 0.195 | 0.004090 | (.06) | 0.0262 | (.10) | 0.04644 | (.08) | 0.624 | 26.31 | 26.251 | 0.026 | 20.5 |
| | x4 (1) | 0.0129 | 12981 | 0.549 | 55.7 | 91.2 | 7.81 | 5580 | 0.175 | 0.004062 | (.06) | 0.0259 | (.08) | 0.04624 | (.05) | 0.775 | 26.13 | 25.962 | 0.021 | 10.2 |
| | x3 (1) | 0.0079 | 14080 | 0.573 | 59.0 | 27.1 | 16.7 | 1656 | 0.183 | 0.003848 | (.08) | 0.0246 | (.13) | 0.04638 | (.10) | 0.662 | 24.76 | 24.682 | 0.033 | 17.5 |
| | x7 (1) | 0.0051 | 32114 | 0.587 | 143 | 9.64 | 69.0 | 598.1 | 0.189 | 0.003805 | (.07) | 0.0244 | (.15) | 0.04656 | (.12) | 0.532 | 24.48 | 24.506 | 0.036 | 26.8 |
| | x5 (1) | 0.0070 | 25112 | 0.567 | 102 | 56.4 | 12.4 | 3432 | 0.182 | 0.003788 | (.06) | 0.0243 | (.08) | 0.04657 | (.05) | 0.763 | 24.37 | 24.397 | 0.019 | 27.0 |
| | x11(1) | 0.0071 | 14574 | 0.392 | 96.1 | 1.26 | 302 | 98.54 | 0.128 | 0.003660 | (.09) | 0.0238 | (.51) | 0.04722 | (.48) | 0.413 | 23.55 | 23.91 | 0.12 | 60.4 |
| | m1 (1) | 0.0094 | 7498 | 10.7 | 103 | 41.6 | 22.7 | 808.1 | 2.854 | 0.003982 | (.15) | 0.0213 | (.37) | 0.03877 | (.34) | 0.402 | 25.62 | 21.388 | 0.080 | -432.4 |
| | m7 (1) | 0.0082 | 4140 | 9.99 | 59.1 | 8.24 | 53.0 | 184.0 | 2.643 | 0.004027 | (.18) | 0.0213 | (.40) | 0.03829 | (.34) | 0.506 | 25.905 | 21.358 | 0.085 | -465.2 |
| | x1 (1) | 0.0116 | 11976 | 0.496 | 47.6 | 6.19 | 77.6 | 399.8 | 0.159 | 0.003320 | (.07) | 0.0212 | (.14) | 0.04636 | (.11) | 0.566 | 21.37 | 21.325 | 0.030 | 16.3 |
| | m4 (1) | 0.0045 | 7100 | 10.9 | 108 | 7.88 | 54.5 | 166.8 | 2.892 | 0.003987 | (.19) | 0.0212 | (.48) | 0.03858 | (.42) | 0.469 | 25.65 | 21.311 | 0.102 | -445.1 |
| 01SK55 | z2 (2) | 0.0052 | 1705 | 0.088 | 67.3 | 125 | 2.79 | 8482 | 0.051 | 0.041489 | (.06) | 0.3236 | (.09) | 0.05657 | (.07) | 0.633 | 262.1 | 284.66 | 0.25 | 474.7 |
| | z4 (1) | 0.0076 | 1610 | 0.139 | 51.4 | 58.4 | 6.62 | 3779 | 0.101 | 0.031834 | (.09) | 0.2464 | (.12) | 0.05613 | (.08) | 0.761 | 202.0 | 223.63 | 0.26 | 457.5 |
| | z1(1) | 0.0059 | 1052 | 0.305 | 19.2 | 12.1 | 8.97 | 790.2 | 0.109 | 0.017350 | (.25) | 0.1303 | (.54) | 0.05448 | (.45) | 0.550 | 110.9 | 124.4 | 0.67 | 390.7 |
| | m6 (1) | 0.0369 | 5280 | 12.7 | 74.1 | 18.3 | 142 | 337.9 | 3.201 | 0.003634 | (.07) | 0.0182 | (.19) | 0.03635 | (.17) | 0.432 | 23.39 | 18.328 | 0.035 | -604.6 |
| | m7 (1) | 0.0395 | 3143 | 12.4 | 44.9 | 8.81 | 181 | 173.9 | 3.154 | 0.003543 | (.08) | 0.0179 | (.32) | 0.03667 | (.30) | 0.361 | 22.797 | 18.027 | 0.057 | -580.7 |
| | x2 (f) | 0.0055 | 18945 | 0.292 | 67.9 | 2.99 | 94.2 | 213.8 | 0.094 | 0.002766 | (.11) | 0.0177 | (.41) | 0.04649 | (.38) | 0.410 | 17.81 | 17.846 | 0.073 | 23.0 |
| | m1 (1) | 0.0200 | 6975 | 13.4 | 99.4 | 15.5 | 120 | 274.2 | 3.441 | 0.003459 | (.19) | 0.0177 | (.65) | 0.03716 | (.60) | 0.396 | 22.26 | 17.84 | 0.12 | -545.0 |
| | m5 (f) | 0.0029 | 9876 | 12.0 | 129 | 15.0 | 23.7 | 298.5 | 2.938 | 0.003589 | (.26) | 0.0176 | (.73) | 0.03548 | (.65) | 0.440 | 23.09 | 17.67 | 0.13 | -670.8 |
| | m3 (f) | 0.0077 | 5666 | 12.7 | 78.3 | 11.9 | 46.9 | 225.1 | 3.221 | 0.003478 | (.27) | 0.0176 | (2.11) | 0.03661 | (2.01) | 0.433 | 22.38 | 17.67 | 0.37 | -585.4 |
| | m2 (f) | 0.0091 | 6884 | 14.3 | 99.9 | 25.4 | 34.3 | 421.03 | 3.634 | 0.003468 | (.14) | 0.0176 | (.63) | 0.03671 | (.59) | 0.363 | 22.32 | 17.67 | 0.11 | -577.9 |
| | m4 (f) | 0.0085 | 7484 | 11.6 | 91.6 | 32.1 | 23.7 | 636.8 | 2.806 | 0.003589 | (.13) | 0.0174 | (.30) | 0.03507 | (.26) | 0.480 | 23.09 | 17.467 | 0.052 | -703.4 |

(a) Fractions are designated by mineral: m monazite; x xenotime. Fractions were either single grains (1), fragments of grains(f), or multigrain fractions of zircons (# of grains)

(b) Sample weights, estimated using sample dimensions determined from a grided video monitor, are known to within 20% based on comporisons of estimated and measured weights

(c) Compositions expressed as ppm U, ppm total Pb, and Th/U. Th/U ratios were calculated from the 208Pb/206Pb ratios.

(d) Ratio of radiogenic Pb to common Pb.

(e) Total common Pb

(f) Measured ratio corrected for fractionation and spike only; Pb fractionation is 0.12 ± 0.04% per amu for multicollector Faraday analyses and 0.15 ± 0.04% per amu for single collector Daly analysis based on repeated analyses of NBS-981

(g) Isotopic ratios are corrected for fractionation, spike, blank, and initial common Pb. U blank = 1 pg ± 50%; data were reduced using a Pb blank of 3.5 pg ± 50%

(h) Uncertainties in millions of years at the 2s confidence interval

Table 2 . $^{40}Ar/^{39}Ar$ biotite analyses.

| T (K) | $^{36}Ar/^{40}Ar$ | Error $^{36}Ar/^{40}Ar$ | $^{39}Ar/^{40}Ar$ | Error $^{39}Ar/^{40}Ar$ | Moles $^{39}Ar_K$ | Cumulative % $^{39}Ar_K$ | % $^{40}Ar^*$ | Age (Ma) | Age Error (w/ J) | Age Error (w/o J) |
|---|---|---|---|---|---|---|---|---|---|---|
| 00SK07 biotite (Jvalue = 0.003175 ± 2.06e-5) | | | | | | | | | | |
| 873 | 1.14E-03 | 6.48E-05 | 0.165263 | 0.0017903 | 8.69E-13 | 23.37 | 66.27 | 22.84 | 0.76 | 0.703 |
| 973 | 4.37E-05 | 7.66E-05 | 0.237308 | 0.0035572 | 4.67E-13 | 35.91 | 98.59 | 23.67 | 0.67 | 0.59 |
| 1073 | 7.35E-05 | 8.87E-05 | 0.239399 | 0.0055348 | 3.03E-13 | 44.05 | 97.71 | 23.26 | 0.81 | 0.75 |
| 1098 | 1.10E-05 | 5.70E-04 | 0.241269 | 0.0077017 | 8.75E-14 | 46.404 | 99.56 | 23.51 | 3.99 | 4.0 |
| 1123 | 1.69E-04 | 7.35E-04 | 0.219352 | 0.0049112 | 9.17E-14 | 48.87 | 94.90 | 24.6 | 5.6 | 5.6 |
| 1148 | 2.19E-05 | 2.27E-04 | 0.220121 | 0.0050006 | 1.60E-13 | 53.16 | 99.24 | 25.7 | 1.8 | 1.8 |
| 1173 | 1.95E-05 | 5.43E-05 | 0.234391 | 0.0027650 | 3.40E-13 | 62.31 | 99.31 | 24.13 | 0.55 | 0.46 |
| 1198 | 2.30E-06 | 7.94E-05 | 0.234578 | 0.0043764 | 3.89E-13 | 72.78 | 99.81 | 24.24 | 0.74 | 0.67 |
| 1223 | 5.59E-05 | 9.79E-05 | 0.238116 | 0.0054452 | 3.59E-13 | 82.43 | 98.23 | 23.50 | 0.85 | 0.796 |
| 1248 | 2.75E-06 | 1.19E-04 | 0.236670 | 0.0055395 | 3.33E-13 | 91.39 | 99.80 | 24.02 | 0.98 | 0.93 |
| 1273 | 5.89E-05 | 1.59E-04 | 0.237849 | 0.0066174 | 2.50E-13 | 98.11 | 98.14 | 23.5 | 1.3 | 1.2 |
| 1323 | 2.70E-05 | 1.11E-03 | 0.213967 | 0.0059970 | 7.03E-14 | 100.00 | 99.095 | 26.4 | 8.7 | 8.7 |
| 00SK08 biotite (Jvalue = 0.003175 ± 2.07e-5) | | | | | | | | | | |
| 873 | 1.49E-03 | 1.82E-04 | 0.155384 | 0.0013033 | 1.53E-12 | 34.16 | 56.03 | 20.55 | 1.99 | 1.97 |
| 923 | 3.36E-04 | 1.53E-04 | 0.257155 | 0.0037083 | 2.64E-13 | 40.05 | 89.96 | 19.95 | 1.05 | 1.01 |
| 973 | 2.74E-05 | 3.60E-05 | 0.273285 | 0.0040774 | 4.73E-13 | 50.62 | 99.05 | 20.67 | 0.40 | 0.29 |
| 1023 | 3.26E-06 | 7.85E-05 | 0.279377 | 0.0034663 | 3.44E-13 | 58.301 | 99.76 | 20.37 | 0.55 | 0.48 |
| 1073 | 2.65E-04 | 3.61E-04 | 0.277837 | 0.0062278 | 1.24E-13 | 61.06 | 92.03 | 18.90 | 2.2 | 2.2 |
| 1098 | 3.85E-04 | 6.65E-04 | 0.259440 | 0.0142407 | 9.19E-14 | 63.11 | 88.50 | 19.5 | 4.4 | 4.4 |
| 1123 | 3.19E-04 | 4.16E-04 | 0.279840 | 0.0093186 | 8.30E-14 | 64.97 | 90.45 | 18.4 | 2.5 | 2.5 |
| 1148 | 2.30E-04 | 3.05E-04 | 0.277882 | 0.0082957 | 1.24E-13 | 67.74 | 93.07 | 19.1 | 1.9 | 1.9 |
| 1173 | 9.03E-05 | 8.95E-05 | 0.268457 | 0.0047497 | 1.95E-13 | 72.096 | 97.20 | 20.65 | 0.65 | 0.59 |
| 1198 | 1.17E-04 | 1.62E-04 | 0.270829 | 0.0039234 | 2.18E-13 | 76.97 | 96.41 | 20.3 | 1.1 | 1.04 |
| 1223 | 2.73E-04 | 1.80E-04 | 0.265517 | 0.0051088 | 2.15E-13 | 81.77 | 91.801 | 19.7 | 1.2 | 1.1 |
| 1248 | 1.20E-04 | 7.29E-05 | 0.269595 | 0.0070832 | 2.19E-13 | 86.66 | 96.34 | 20.38 | 0.67 | 0.61 |
| 1273 | 1.29E-04 | 1.10E-04 | 0.276808 | 0.0057326 | 4.19E-13 | 96.02 | 96.06 | 19.80 | 0.78 | 0.74 |
| 1323 | 5.91E-06 | 6.75E-05 | 0.287359 | 0.0085405 | 1.78E-13 | 100.00 | 99.68 | 19.79 | 0.63 | 0.57 |
| 00SK09 biotite (Jvalue = 0.003233 ± 5.9e-5) | | | | | | | | | | |
| 873 | 1.64E-03 | 5.00E-05 | 0.148968 | 0.0012218 | 1.18E-12 | 34.604 | 51.39 | 20.02 | 0.94 | 0.600 |
| 973 | 2.94E-05 | 1.98E-04 | 0.287303 | 0.0048127 | 4.39E-13 | 47.53 | 98.99 | 20.0 | 1.4 | 1.2 |
| 1073 | 1.22E-04 | 1.51E-04 | 0.278999 | 0.0063916 | 3.07E-13 | 56.57 | 96.25 | 20.0 | 1.2 | 0.98 |
| 1098 | 3.55E-04 | 5.42E-04 | 0.281404 | 0.0063997 | 8.39E-14 | 59.04 | 89.38 | 18.5 | 3.4 | 3.3 |
| 1123 | 6.48E-05 | 3.95E-04 | 0.286409 | 0.0027976 | 8.91E-14 | 61.66 | 97.94 | 19.9 | 2.5 | 2.4 |
| 1148 | 2.52E-05 | 3.01E-04 | 0.288452 | 0.0042036 | 1.25E-13 | 65.35 | 99.11 | 20.0 | 1.9 | 1.8 |
| 1173 | 2.30E-05 | 8.08E-04 | 0.285719 | 0.0043670 | 1.59E-13 | 70.04 | 99.18 | 20.2 | 4.9 | 4.8 |
| 1198 | 8.35E-05 | 8.40E-04 | 0.280365 | 0.0044056 | 2.05E-13 | 76.09 | 97.396 | 20.2 | 5.2 | 5.1 |
| 1223 | 1.84E-04 | 1.22E-04 | 0.272665 | 0.0046807 | 2.49E-13 | 83.42 | 94.43 | 20.1 | 1.1 | 0.81 |
| 1248 | 2.86E-04 | 1.70E-04 | 0.271520 | 0.0045930 | 2.60E-13 | 91.07 | 91.41 | 19.6 | 1.3 | 1.1 |
| 1273 | 1.03E-04 | 1.50E-04 | 0.279066 | 0.0043833 | 2.11E-13 | 97.29 | 96.83 | 20.2 | 1.2 | 0.95 |
| 1323 | 1.89E-04 | 8.02E-04 | 0.279341 | 0.0033857 | 9.19E-14 | 100.00 | 94.29 | 19.6 | 4.9 | 4.9 |

| T (K) | $^{36}Ar/^{40}Ar$ | Error $^{36}Ar/^{40}Ar$ | $^{39}Ar/^{40}Ar$ | Error $^{39}Ar/^{40}Ar$ | Moles $^{39}Ar_K$ | Cumulative % $^{39}Ar_K$ | % $^{40}Ar^*$ | Age (Ma) | Age Error (w/ J) | Age Error (w/o J) |
|---|---|---|---|---|---|---|---|---|---|---|
| 00SK10 biotite (Jvalue = 0.003233 ± 5.9e-5) | | | | | | | | | | |
| 873 | 1.91E-03 | 5.61E-05 | 0.145924 | 0.0020158 | 5.46E-13 | 28.95 | 43.38 | 17.27 | 0.98 | 0.75 |
| 923 | 3.39E-04 | 1.82E-04 | 0.311708 | 0.0055339 | 1.98E-13 | 39.47 | 89.83 | 16.8 | 1.2 | 1.03 |
| 973 | 4.20E-04 | 2.81E-04 | 0.283457 | 0.0053189 | 2.05E-13 | 50.36 | 87.48 | 17.9 | 1.8 | 1.7 |
| 1073 | 5.31E-04 | 1.83E-04 | 0.253400 | 0.0049077 | 1.86E-13 | 60.23 | 84.22 | 19.3 | 1.4 | 1.3 |
| 1098 | 4.84E-04 | 4.09E-04 | 0.264894 | 0.0086058 | 7.89E-14 | 64.42 | 85.58 | 18.8 | 2.8 | 2.7 |
| 1123 | 1.17E-04 | 2.77E-04 | 0.279540 | 0.0086122 | 9.02E-14 | 69.197 | 96.41 | 20.0 | 1.9 | 1.8 |
| 1148 | 3.23E-04 | 3.03E-04 | 0.288791 | 0.0091916 | 1.35E-13 | 76.35 | 90.33 | 18.18 | 1.96 | 1.8 |
| 1173 | 3.08E-04 | 3.56E-04 | 0.289145 | 0.0080383 | 1.50E-13 | 84.29 | 90.76 | 18.2 | 2.2 | 2.1 |
| 1198 | 5.12E-05 | 1.45E-03 | 0.290918 | 0.0086346 | 1.14E-13 | 90.33 | 98.35 | 19.6 | 8.6 | 8.5 |
| 1223 | 1.75E-04 | 3.67E-04 | 0.297883 | 0.0078274 | 7.95E-14 | 94.54 | 94.68 | 18.5 | 2.3 | 2.1 |
| 1248 | 6.94E-05 | 2.36E-03 | 0.299848 | 0.0055417 | 4.66E-14 | 97.01 | 97.801 | 19 | 13 | 13 |
| 1273 | 1.11E-04 | 1.07E-03 | 0.300369 | 0.0100242 | 2.77E-14 | 98.48 | 96.59 | 18.7 | 6.1 | 6.1 |
| 1323 | 2.78E-04 | 4.84E-04 | 0.290140 | 0.0085441 | 2.88E-14 | 100.00 | 91.66 | 18.36 | 2.98 | 2.9 |
| 01SK53 biotite (Jvalue = 0.001633 ± 1.56e-5) | | | | | | | | | | |
| 973 | 1.00E-03 | 1.23E-04 | 0.108174 | 0.0015857 | 1.15E-13 | 5.43 | 70.298 | 19.1 | 1.1 | 1.02 |
| 1023 | 2.46E-04 | 2.02E-04 | 0.132952 | 0.0015676 | 2.07E-13 | 15.21 | 92.67 | 20.4 | 1.4 | 1.3 |
| 1073 | 2.56E-05 | 1.02E-04 | 0.139934 | 0.0009650 | 2.88E-13 | 28.79 | 99.17 | 20.77 | 0.75 | 0.64 |
| 1123 | 1.54E-05 | 5.12E-05 | 0.140899 | 0.0010936 | 2.42E-13 | 40.18 | 99.47 | 20.69 | 0.51 | 0.32 |
| 1173 | 2.63E-05 | 1.59E-04 | 0.140083 | 0.0005806 | 1.51E-13 | 47.29 | 99.15 | 20.7 | 1.1 | 0.98 |
| 1223 | 7.69E-05 | 1.31E-04 | 0.138874 | 0.0005405 | 8.61E-14 | 51.35 | 97.66 | 20.612 | 0.902 | 0.81 |
| 1273 | 1.73E-04 | 1.60E-04 | 0.132273 | 0.0008266 | 9.16E-14 | 55.67 | 94.83 | 21.0 | 1.1 | 1.04 |
| 1323 | 1.18E-04 | 3.65E-05 | 0.137260 | 0.0009431 | 5.87E-13 | 83.33 | 96.45 | 20.60 | 0.46 | 0.24 |
| 1373 | 1.39E-04 | 7.19E-05 | 0.136507 | 0.0010370 | 2.39E-13 | 94.61 | 95.81 | 20.57 | 0.61 | 0.47 |
| 1423 | 2.00E-04 | 1.68E-04 | 0.137727 | 0.0006996 | 7.96E-14 | 98.36 | 94.04 | 20.0 | 1.1 | 1.1 |
| 1473 | 4.83E-04 | 3.53E-04 | 0.135552 | 0.0012623 | 3.49E-14 | 100.00 | 85.66 | 18.5 | 2.3 | 2.2 |
| 01SK54 biotite (Jvalue = 0.001666 ± 1.55e-5) | | | | | | | | | | |
| 973 | 2.05E-03 | 4.02E-04 | 0.050910 | 0.0003925 | 3.63E-14 | 4.66 | 39.31 | 23.1 | 6.9 | 6.9 |
| 1023 | 8.18E-04 | 1.94E-04 | 0.124326 | 0.0004218 | 7.61E-14 | 14.42 | 75.79 | 18.2 | 1.4 | 1.4 |
| 1073 | 1.85E-04 | 2.09E-04 | 0.147273 | 0.0004199 | 1.28E-13 | 30.81 | 94.47 | 19.2 | 1.3 | 1.2 |
| 1123 | 1.62E-04 | 9.57E-04 | 0.151884 | 0.0007584 | 1.23E-13 | 46.54 | 95.14 | 18.7 | 5.6 | 5.5 |
| 1173 | 1.06E-04 | 2.67E-04 | 0.150097 | 0.0004390 | 7.08E-14 | 55.62 | 96.802 | 19.3 | 1.6 | 1.6 |
| 1223 | 1.34E-04 | 4.10E-04 | 0.145433 | 0.0005387 | 4.45E-14 | 61.33 | 95.98 | 19.7 | 2.5 | 2.5 |
| 1248 | 1.85E-04 | 4.55E-04 | 0.141751 | 0.0005733 | 2.93E-14 | 65.09 | 94.45 | 19.9 | 2.8 | 2.8 |
| 1273 | 1.86E-04 | 1.23E-03 | 0.140965 | 0.0051177 | 3.46E-14 | 69.52 | 94.44 | 20.0 | 7.7 | 7.7 |
| 1323 | 8.01E-05 | 3.66E-04 | 0.144252 | 0.0005017 | 1.02E-13 | 82.59 | 97.56 | 20.2 | 2.3 | 2.2 |
| 1373 | 1.21E-04 | 2.71E-04 | 0.144251 | 0.0004690 | 7.80E-14 | 92.602 | 96.37 | 20.0 | 1.7 | 1.6 |
| 1423 | 4.97E-04 | 5.73E-04 | 0.143672 | 0.0010146 | 3.70E-14 | 97.34 | 85.27 | 17.8 | 3.5 | 3.5 |
| 1473 | 2.58E-04 | 8.06E-04 | 0.141223 | 0.0020264 | 2.07E-14 | 100.00 | 92.302 | 19.55 | 5.03 | 5.02 |
| 01SK55 biotite (Jvalue = 0.001602 ± 4.39e-6) | | | | | | | | | | |
| 923 | 2.72E-03 | 6.18E-05 | 0.033201 | 0.0005486 | 7.00E-14 | 3.54 | 19.56 | 16.9 | 1.6 | 1.6 |
| 973 | 1.45E-03 | 1.11E-04 | 0.093581 | 0.0006462 | 1.66E-13 | 11.95 | 57.15 | 17.57 | 1.02 | 1.02 |
| 1023 | 4.46E-04 | 8.02E-05 | 0.143494 | 0.0013645 | 3.16E-13 | 27.92 | 86.74 | 17.395 | 0.495 | 0.49 |
| 1073 | 2.02E-04 | 6.60E-05 | 0.154173 | 0.0010845 | 3.79E-13 | 47.09 | 93.94 | 17.53 | 0.38 | 0.37 |
| 1123 | 2.08E-04 | 6.34E-05 | 0.154041 | 0.0007219 | 2.29E-13 | 58.65 | 93.79 | 17.52 | 0.36 | 0.35 |
| 1173 | 4.04E-04 | 3.45E-04 | 0.147144 | 0.0006698 | 1.11E-13 | 64.26 | 88.00 | 17.21 | 1.99 | 2.0 |
| 1223 | 5.79E-04 | 2.43E-04 | 0.139678 | 0.0002928 | 7.20E-14 | 67.89 | 82.82 | 17.1 | 1.5 | 1.5 |
| 1273 | 5.60E-04 | 2.00E-04 | 0.137414 | 0.0007154 | 1.36E-13 | 74.75 | 83.41 | 17.5 | 1.2 | 1.2 |
| 1323 | 2.79E-04 | 3.26E-05 | 0.147588 | 0.0003891 | 4.02E-13 | 95.08 | 91.695 | 17.88 | 0.21 | 0.19 |
| 1373 | 3.40E-04 | 1.11E-04 | 0.141944 | 0.0004122 | 9.73E-14 | 100.00 | 89.88 | 18.22 | 0.67 | 0.66 |

Table 3 . Estimates of biotite closure temperatures.

| Sample | half grain size ($\mu$m) | cooling rate (°C/Myr) | $T_c$ (°C) |
|---|---|---|---|
| 00SK07 | 410 | 100 | 393 |
| 00SK08 | 325 | 100 | 385 |
| 00SK09 | 255 | 100 | 377 |
| 00SK10 | 280 | 100 | 380 |
| 01SK53 | 490 | 100 | 400 |
| 01SK54 | 260 | 100 | 378 |
| 01SK55 | 348 | 100 | 384 |

Closure temperatures calculated using a cylindrical geometry, activation energy of 47 kcal/mol, activation volume 14 $cm^3$, and frequency factor 0.77 $cm^2/s$. Diffusion parameters from Grove & Harrison (1996) and Harrison et al. (1985)

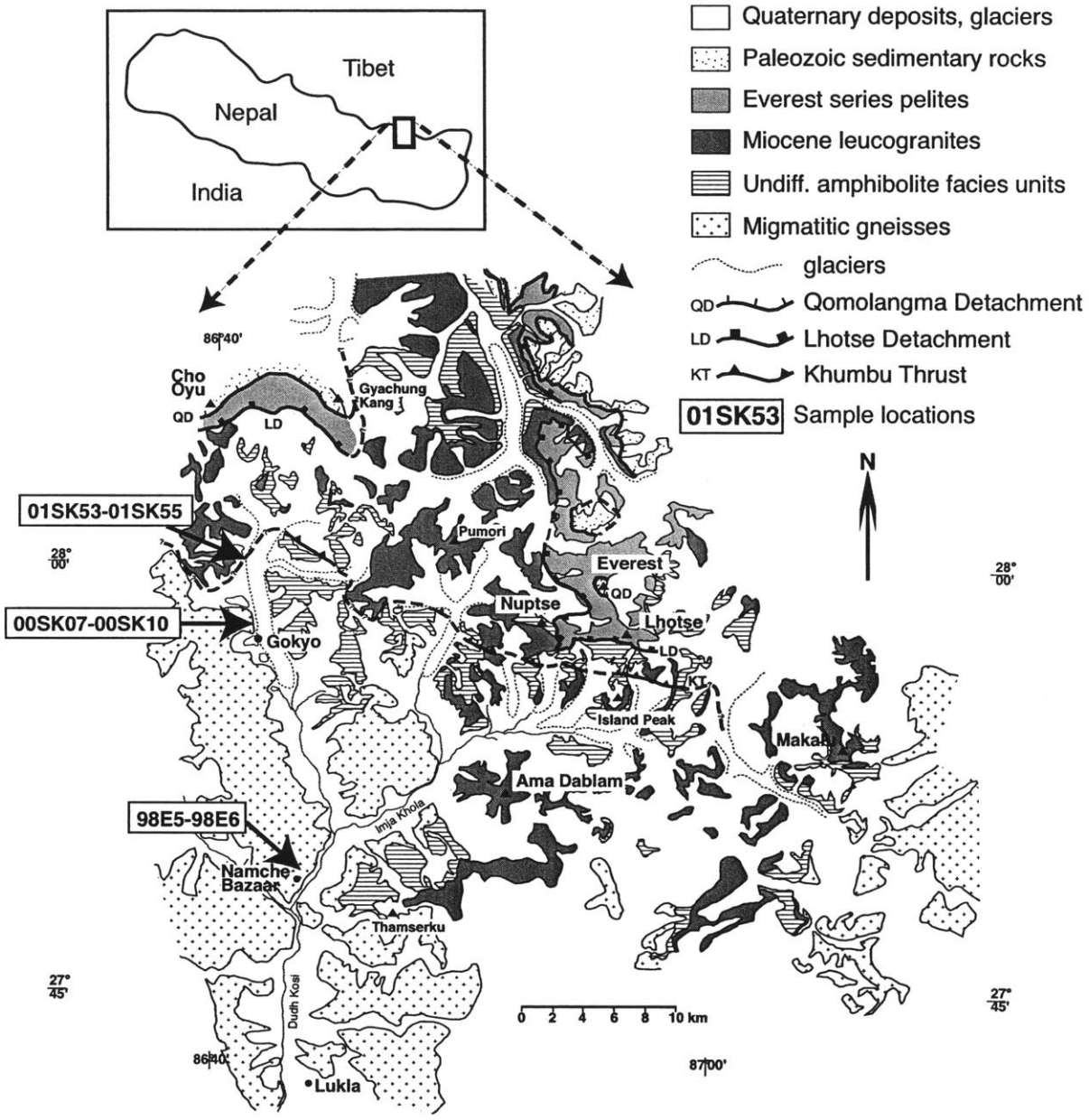


**Figure 1**. Geologic sketch map of the Everest region, modified after Carosi, et al. (1999), and Searle (1999)

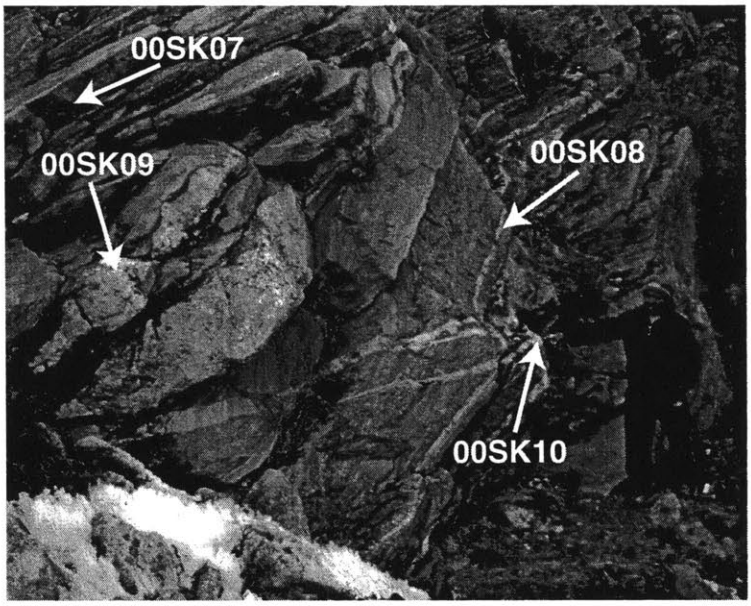


**Figure 2.** Photograph of the Gokyo Ri outcrop. Arrows point to exact sample collection locations.

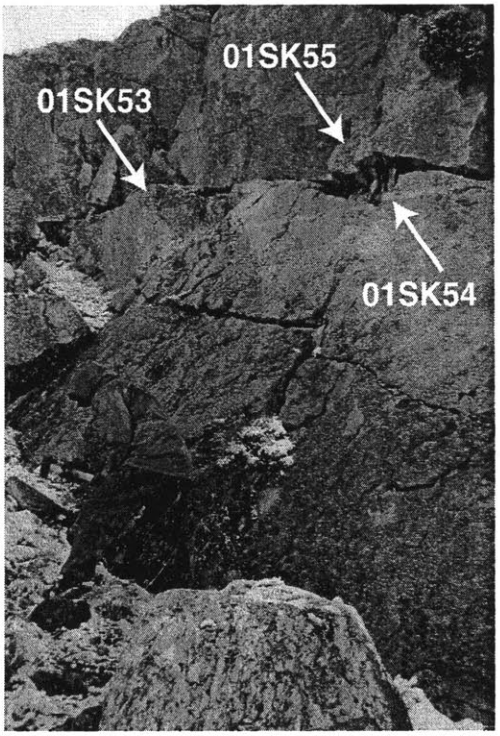


**Figure 3.** Photograph of the 5th Lake outcrop. Arrows point to exact sample collection locations.

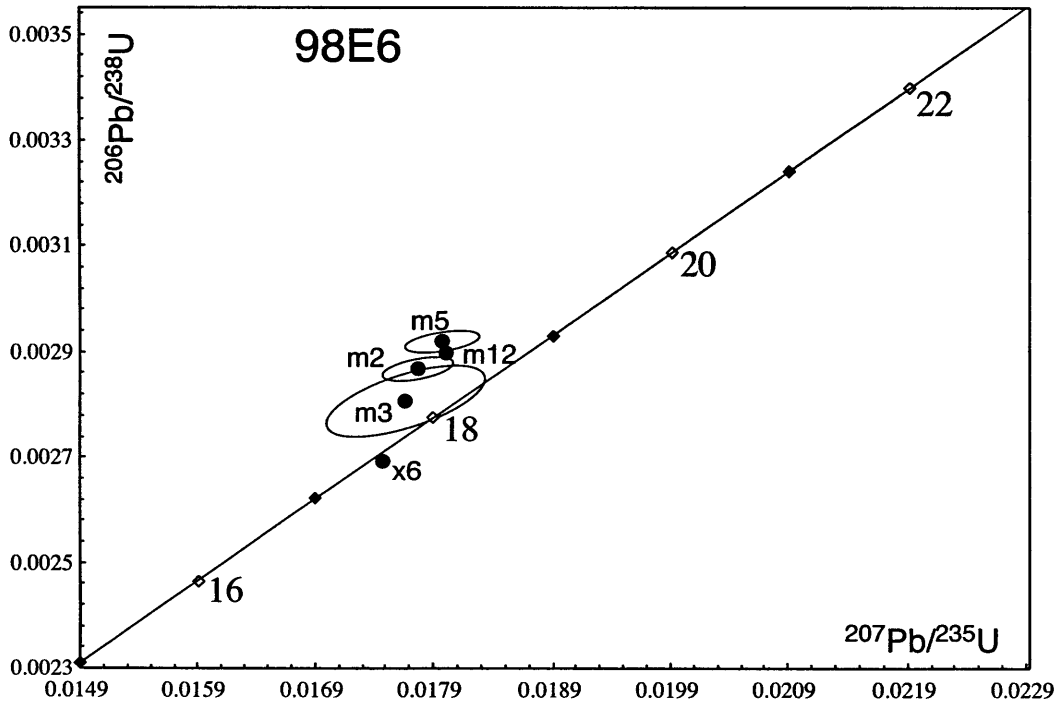


**Figure 4.** U-Pb concordia diagram for sample 98E5, an undeformed crosscutting dike at the Namche Bazaar outcrop.

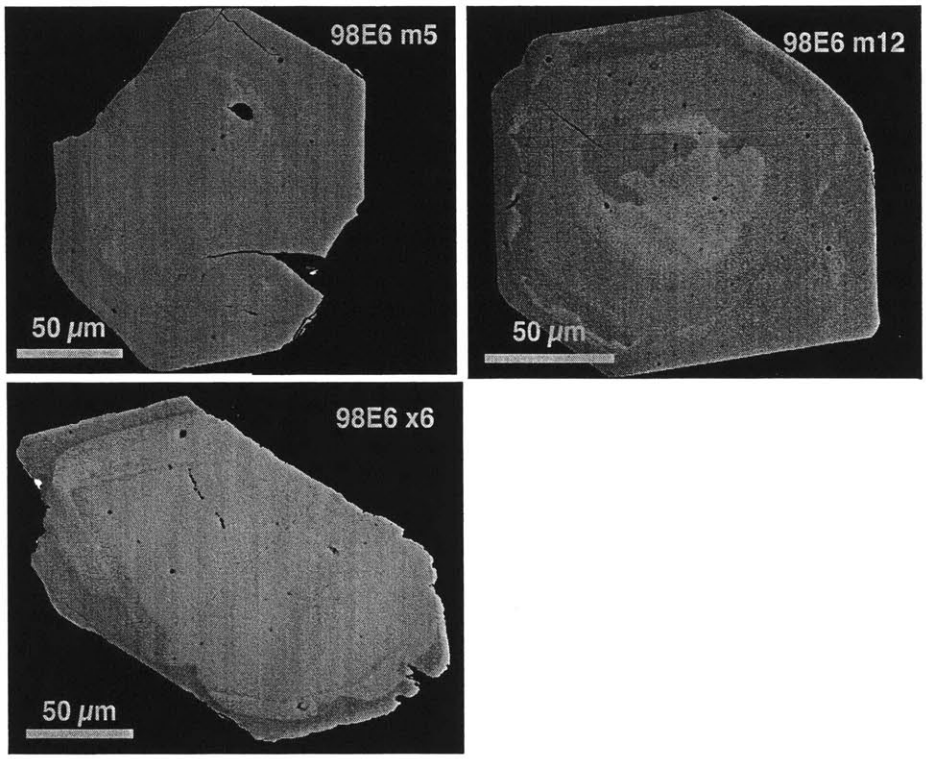


**Figure 5.** BSE images of monazite and xenotime grains from leucogranite dike 98E6 that were dated by U-Pb geochronology.

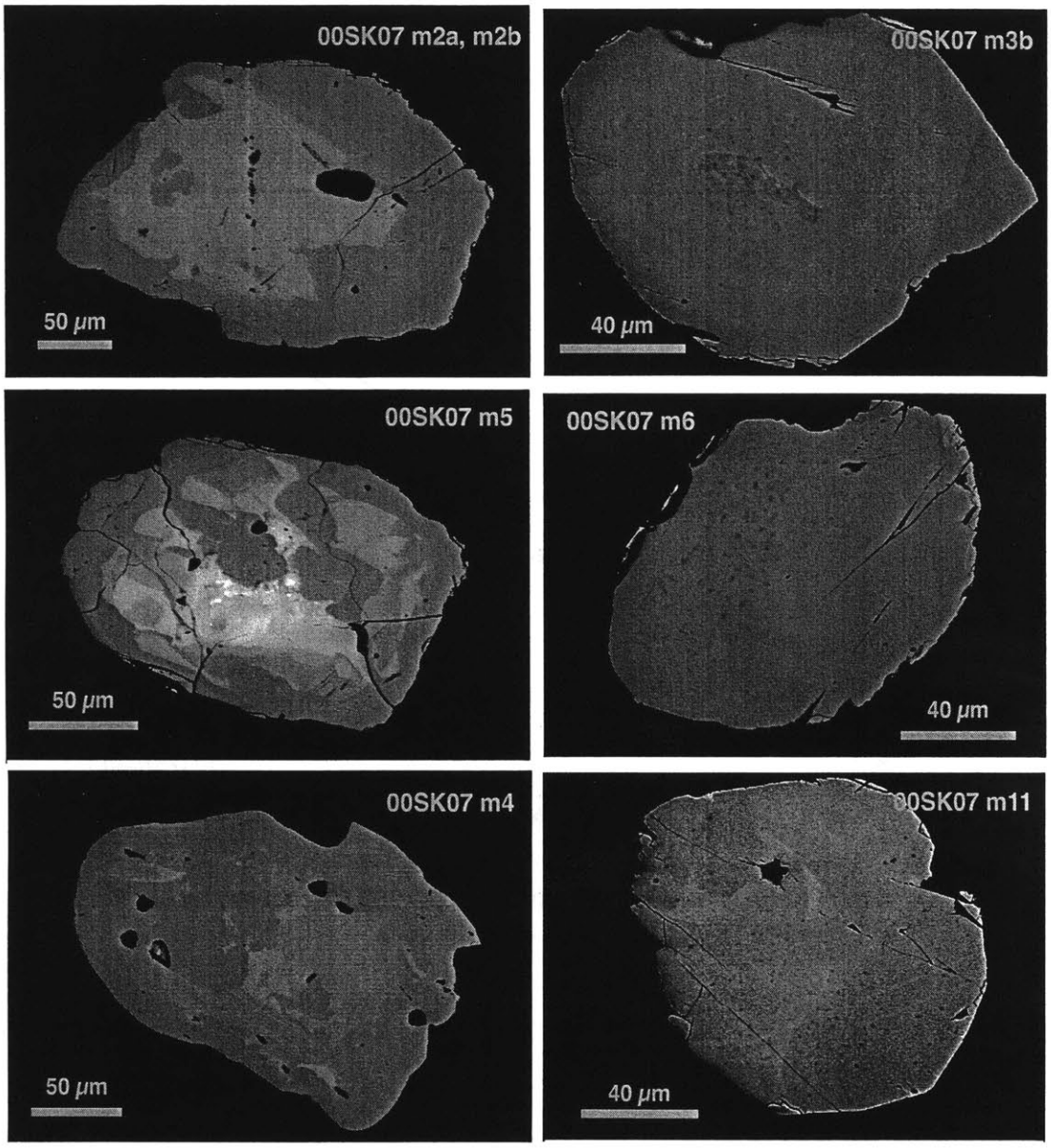


**Figure 6.** BSE images of monazite grains from paragneiss 00SK07 that were dated by U-Pb IDTIMS.

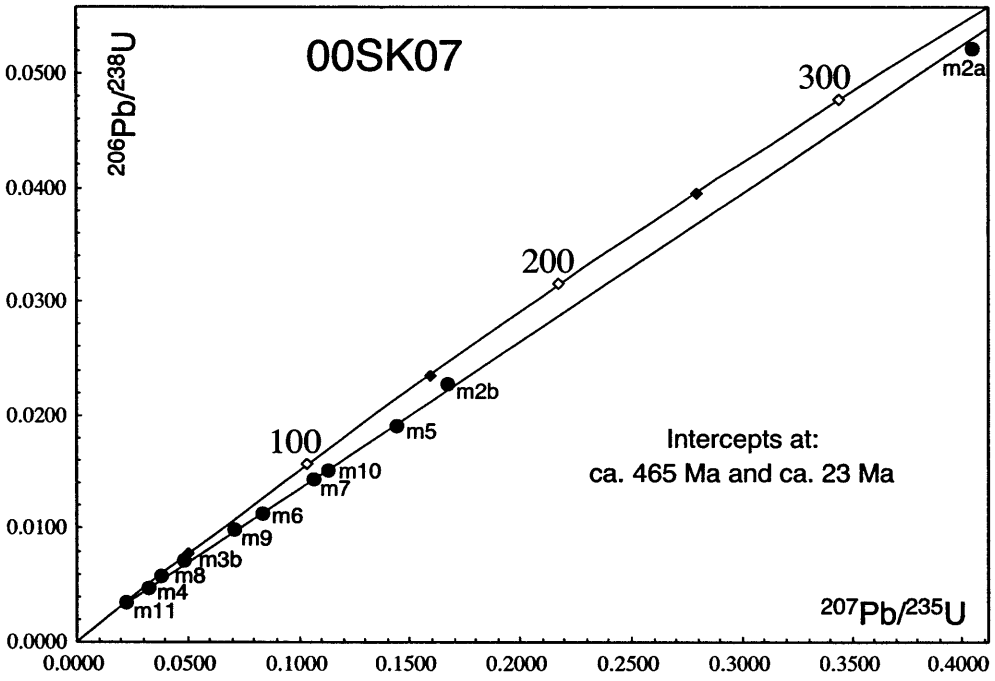


**Figure 7.** U-Pb concordia diagram for sample 00SK07, country rock at the Gokyo Ri outcrop.

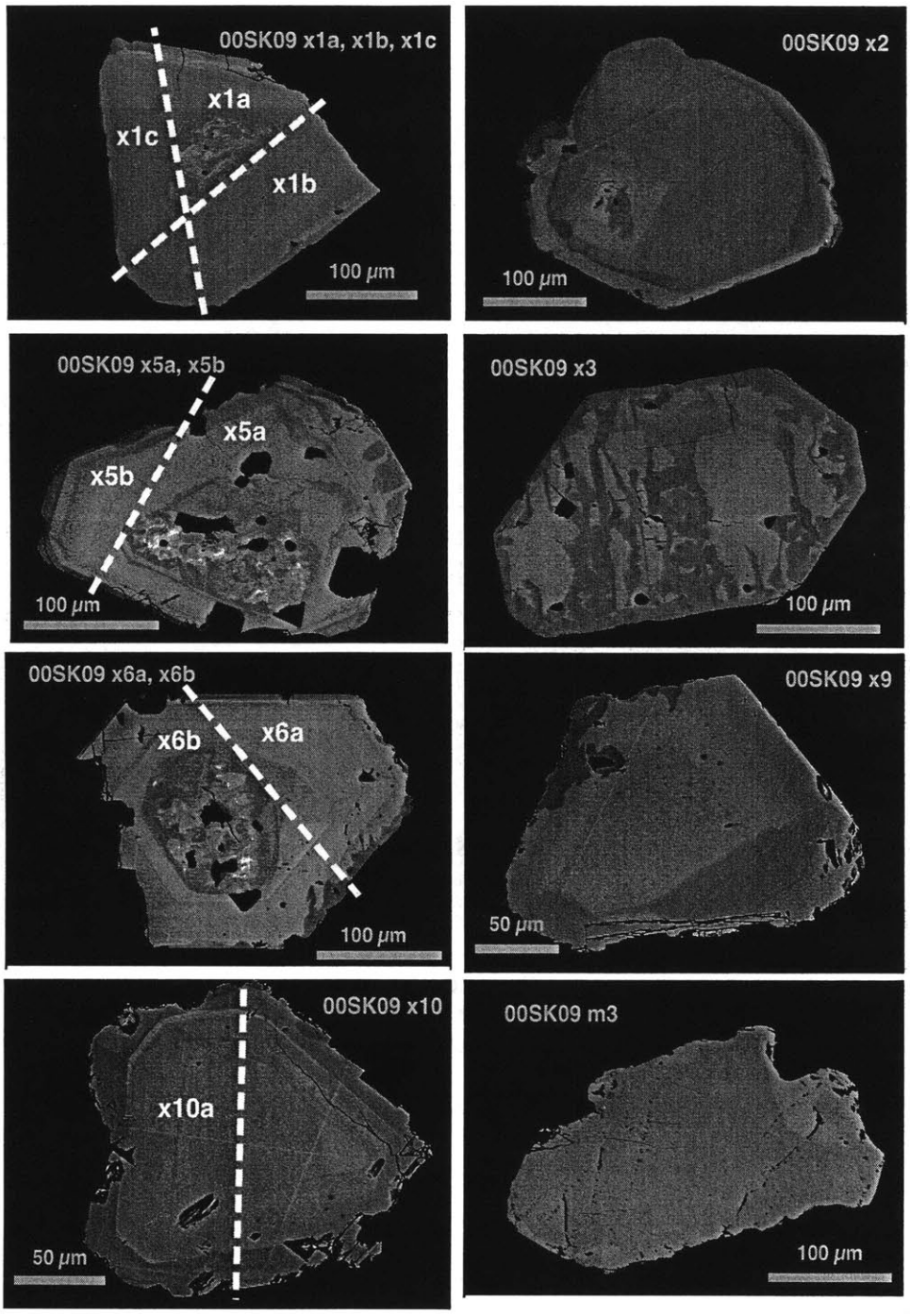


**Figure 8.** BSE images of monazite and xenotime grains from leucogranite sill 00SK09 that were used for U-Pb geochronology. Dashed white lines indicate where grains werecut with an obsidian blade.

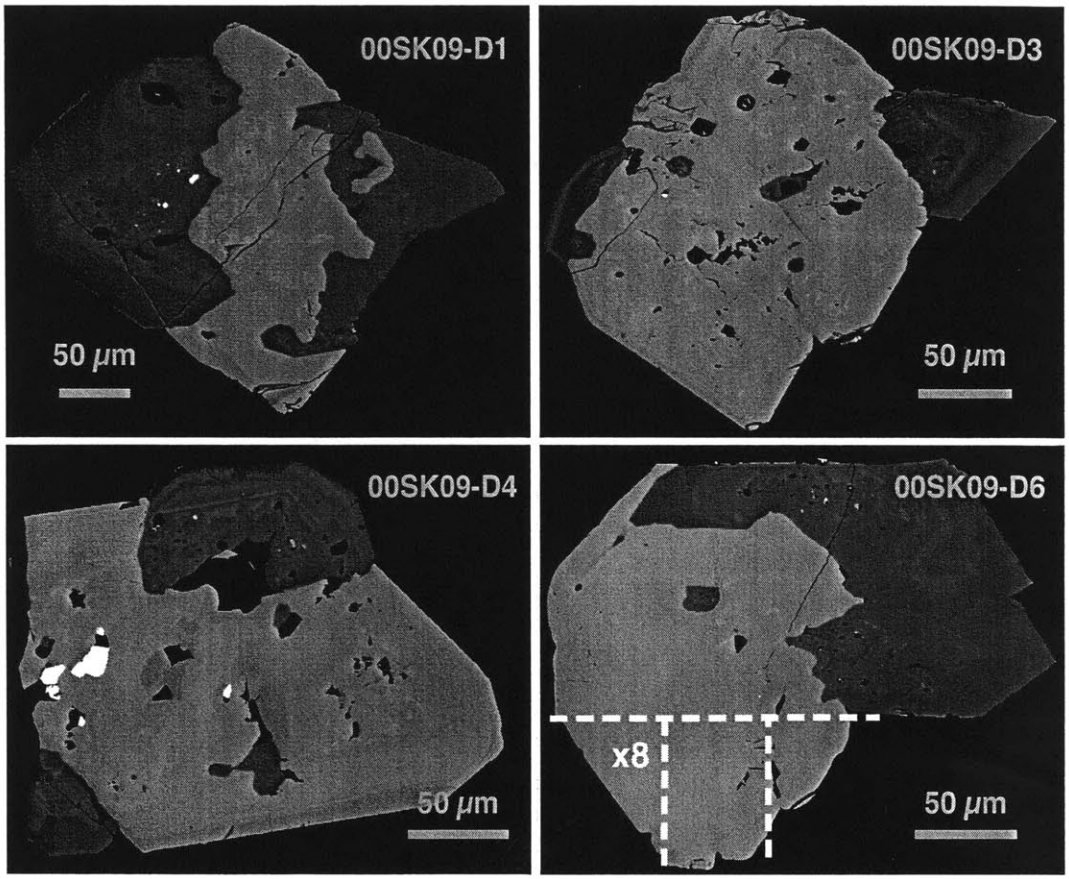


**Figure 9.** BSE images of zircon-xenotime intergrowths from leucogranite sill 00SK09. Zircon is the darker phase, and xenotime is the lighter phase. Bright white inclusions are monazite and uraninite. Fragment x8 was cut from one of the intergrowths as indicated by the dashed white lines.

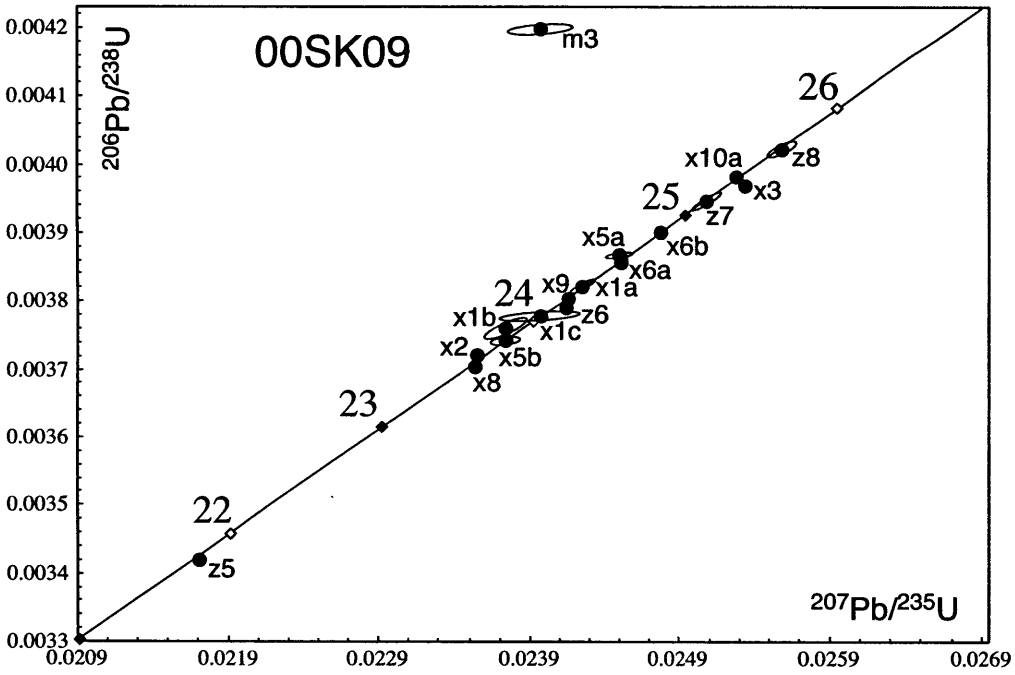


**Figure 10.** U-Pb concordia diagram for sample 00SK09, a boudinaged sill concordant to the foliation of 00SK07 at the Gokyo Ri outcrop.

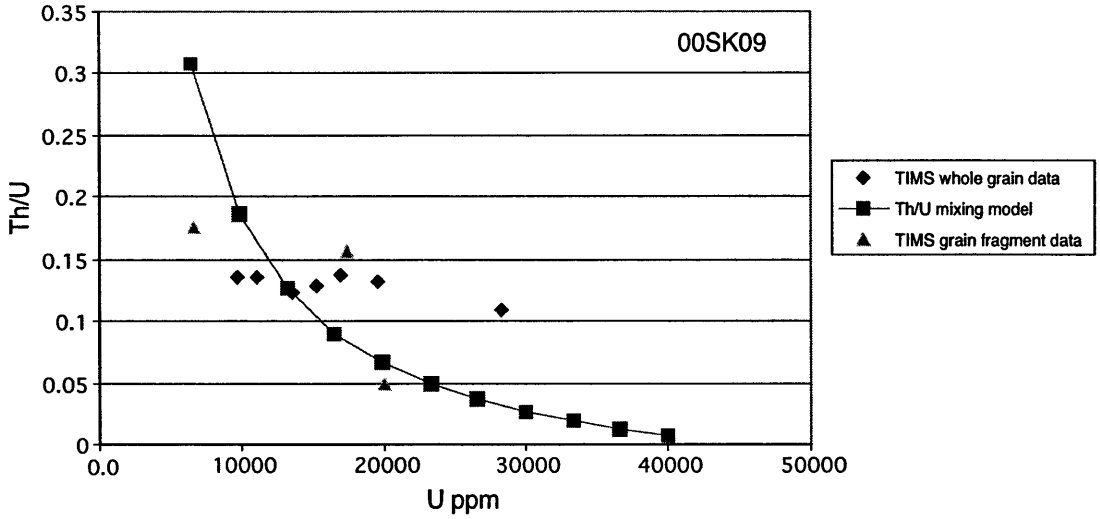


**Figure 11.** Th/U mixing model for leucogranite 00SK09 calculated assuming a core component with 40000 ppm U and Th/U 0.008 and a rim with 6500 ppm U and Th/U 0.308.

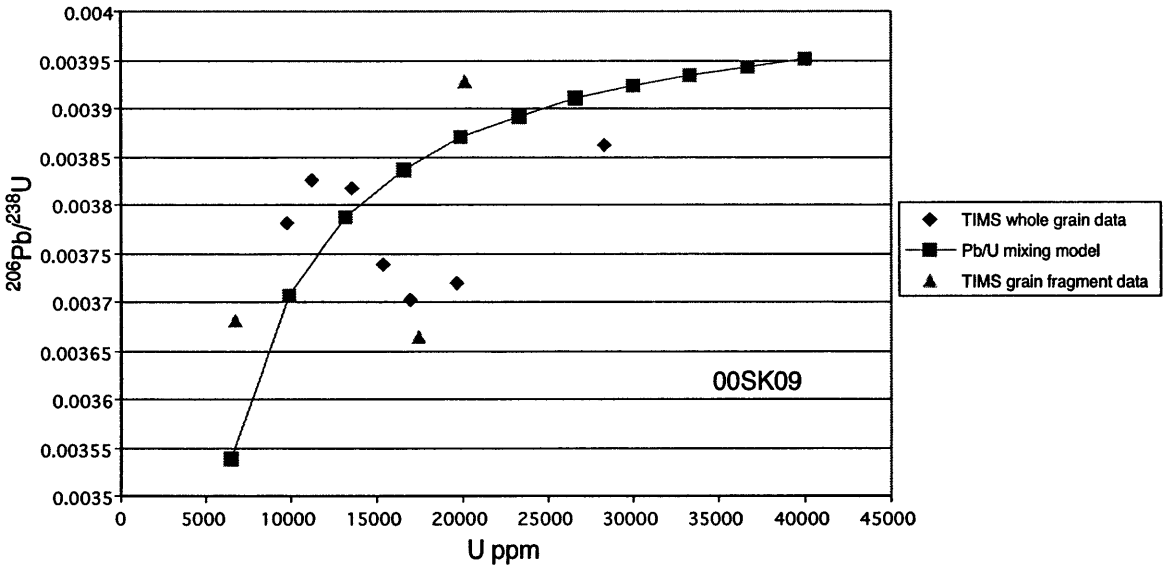


**Figure 12.** Pb/U mixing model for leucogranite 00SK09 calculated assuming a 26 Ma core component and a 23 Ma rim component.

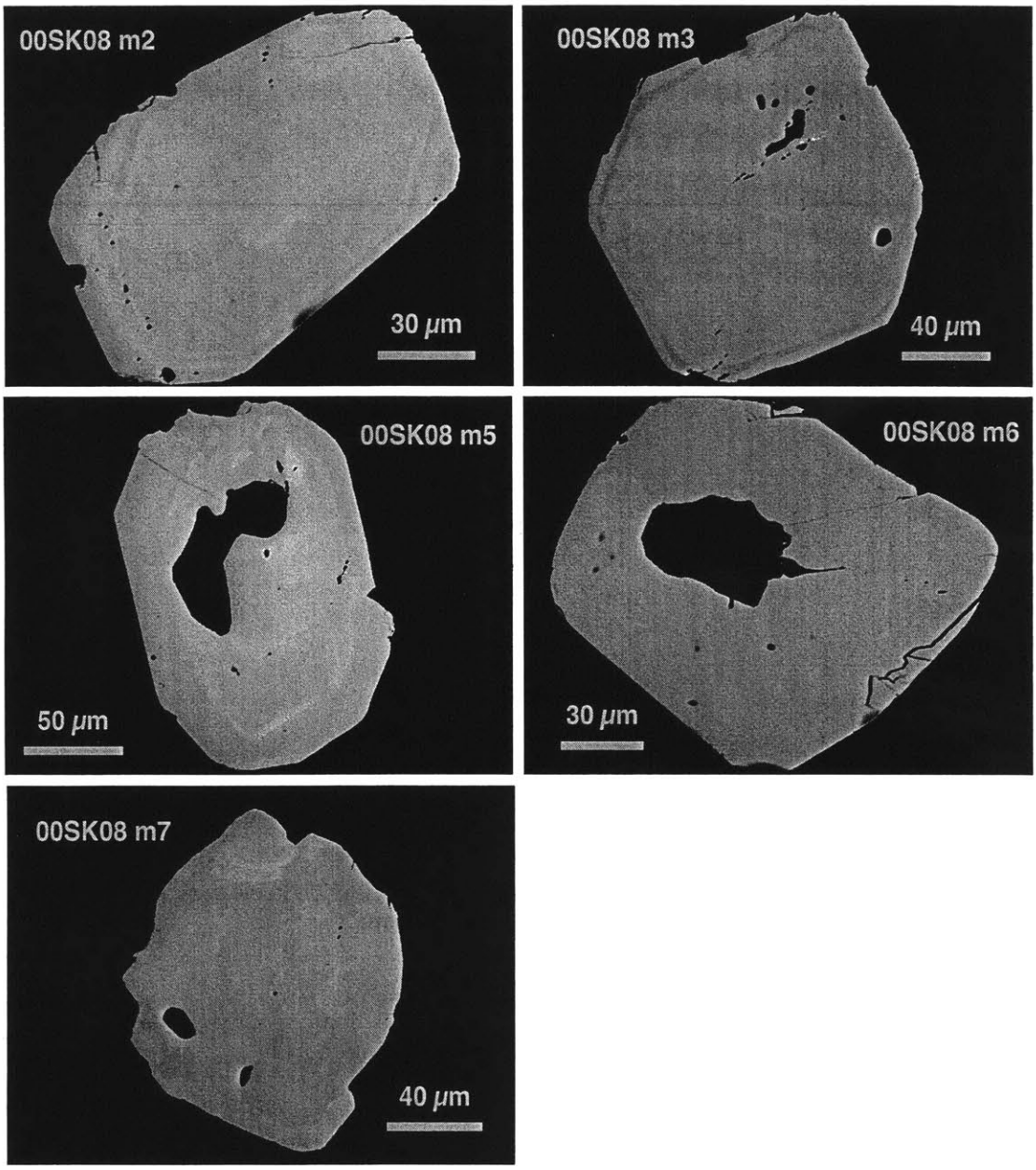


**Figure 13.** BSE images of monazite grains from leucogranite sill 00SK08 that were dated by U-Pb IDTIMS. The large black spots in grains m5, m6, amd m7 are inclusions of plagioclase, quartz, and K-feldspar respectively.

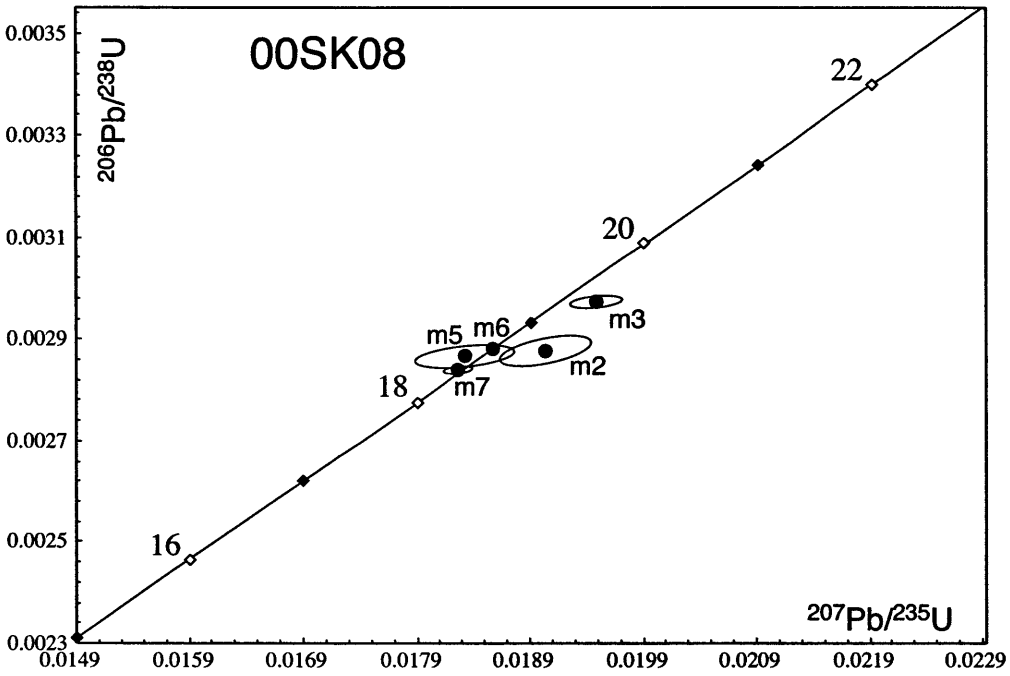


**Figure 14.** U-Pb concordia diagram for sample 00SK08, a sill concordant to the foliation of 00SK07 at the Gokyo Ri outcrop.

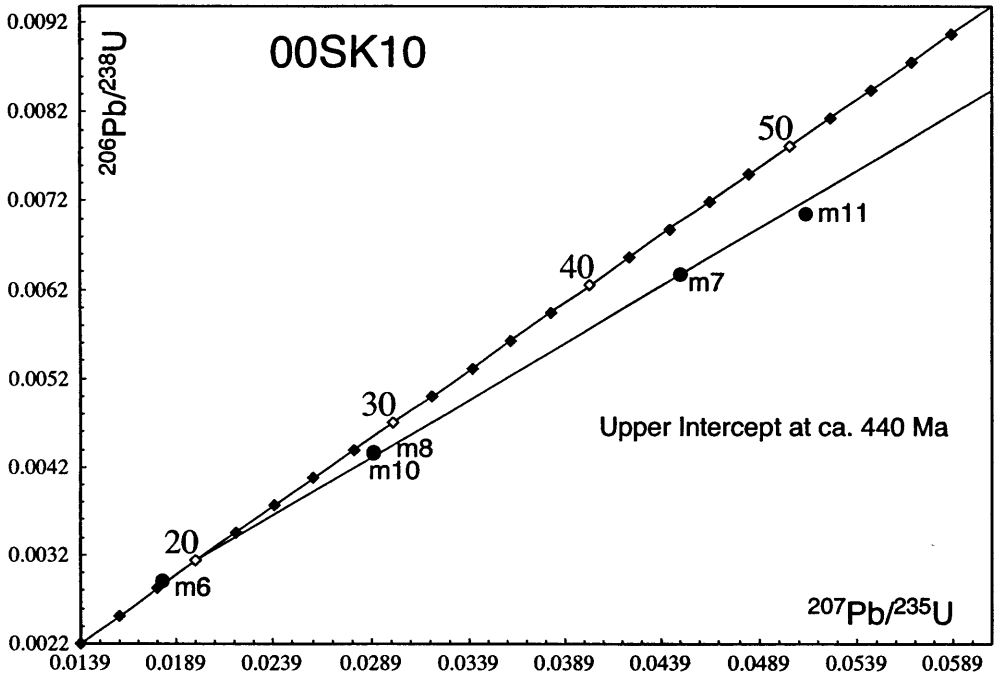


**Figure 15.** U-Pb concordia diagram for sample 00SK10, an undeformed crosscutting dike at the Gokyo Ri outcrop.

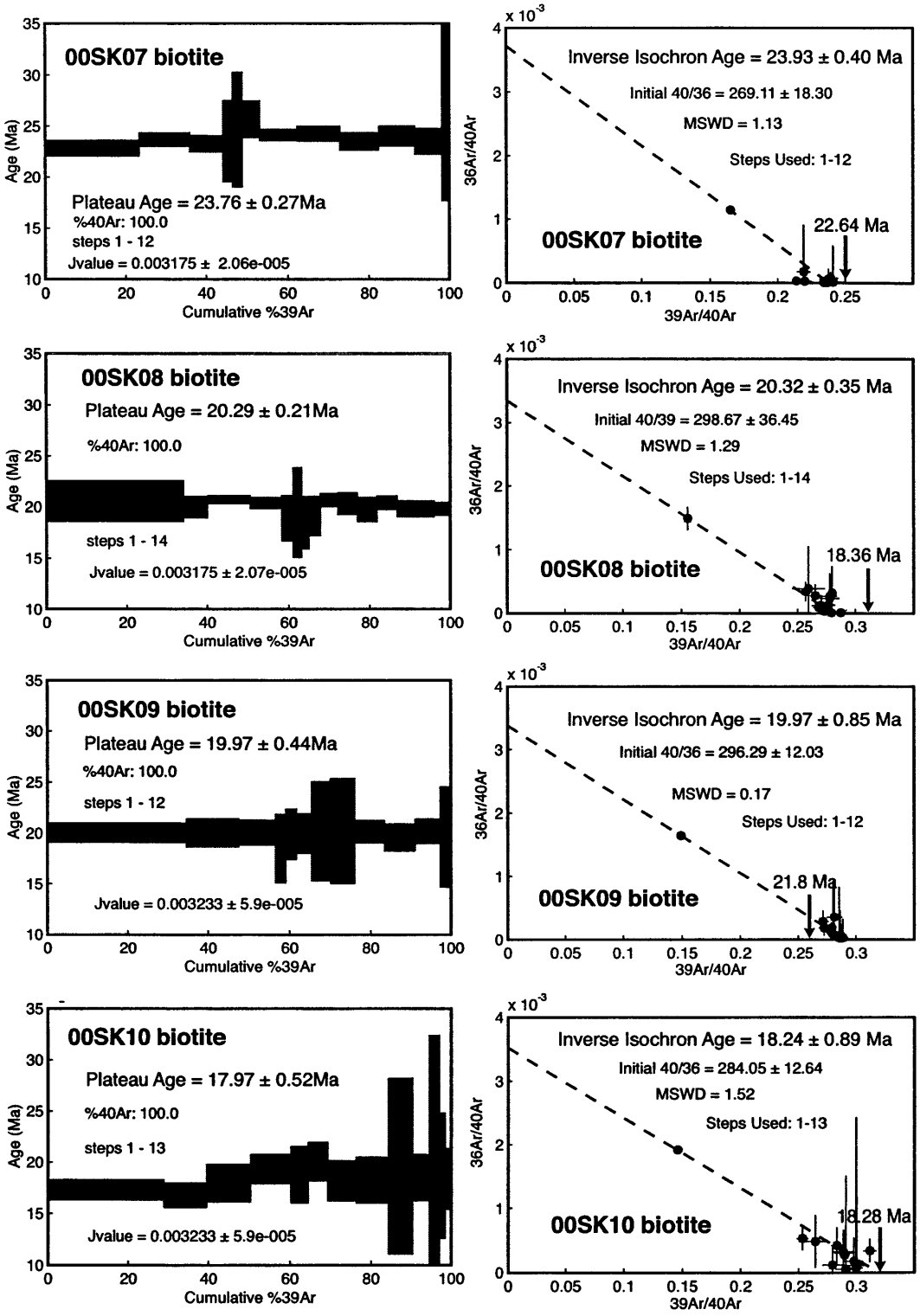


**Figure 16.** $^{40}Ar/^{39}Ar$ release spectra and inverse isochron diagrams for biotites from the Gokyo Ri outcrop. $^{40}Ar/^{39}Ar$ ratios corresponding to the U-Pb crystallization age of each sample are indicated with arrows on the inverse isochron diagrams.

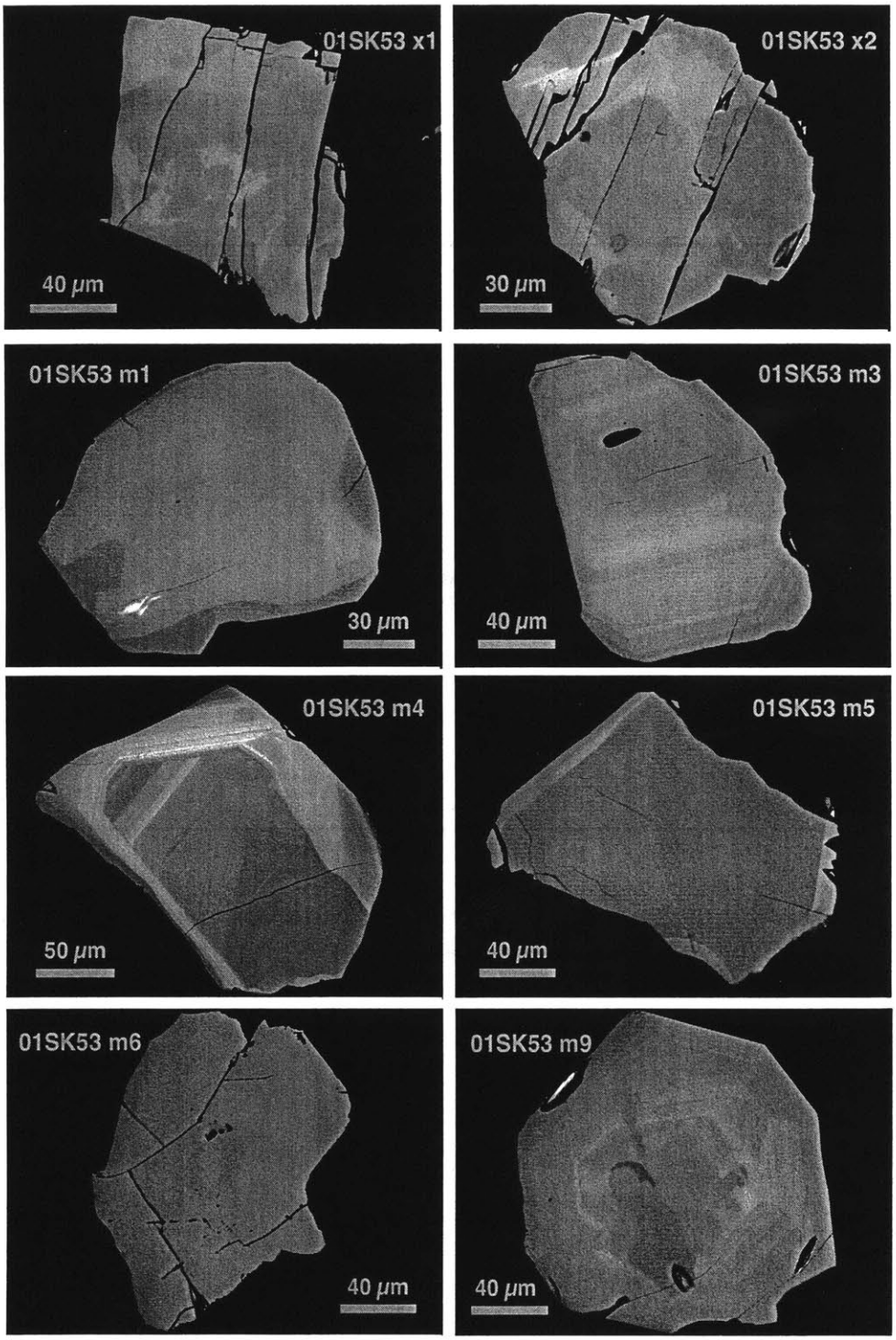


**Figure 17.** BSE images of monazite and xenotime grains from orthogneiss country rock 01SK54 that were dated by U-Pb geochronology.

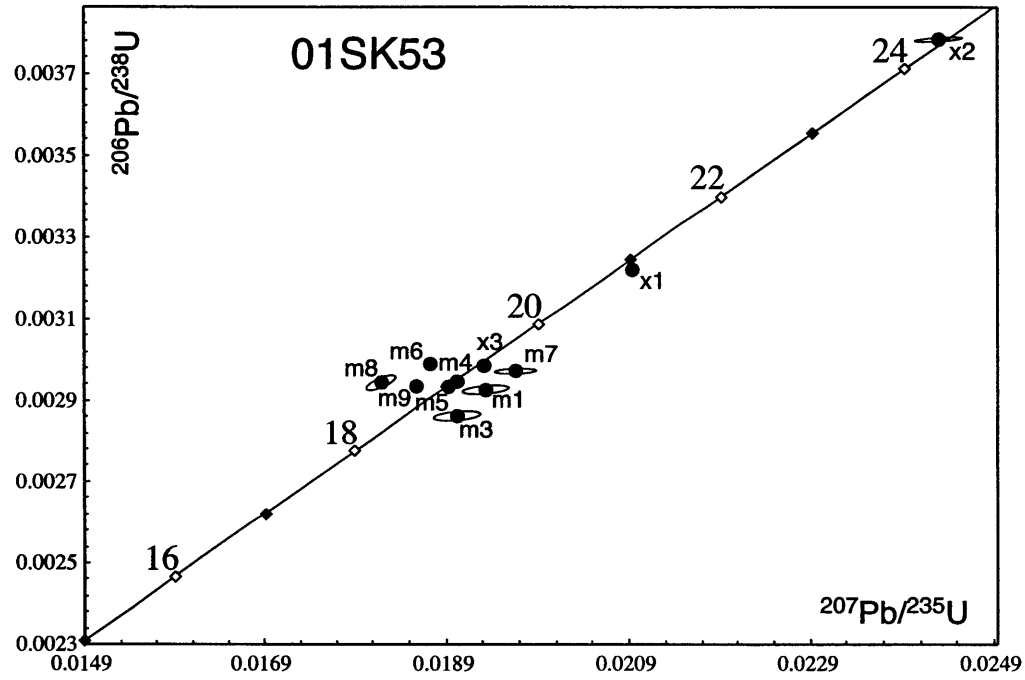


**Figure 18.** U-Pb concordia diagram for sample 01SK53, the orthogneiss country rock at the 5th Lake outcrop.

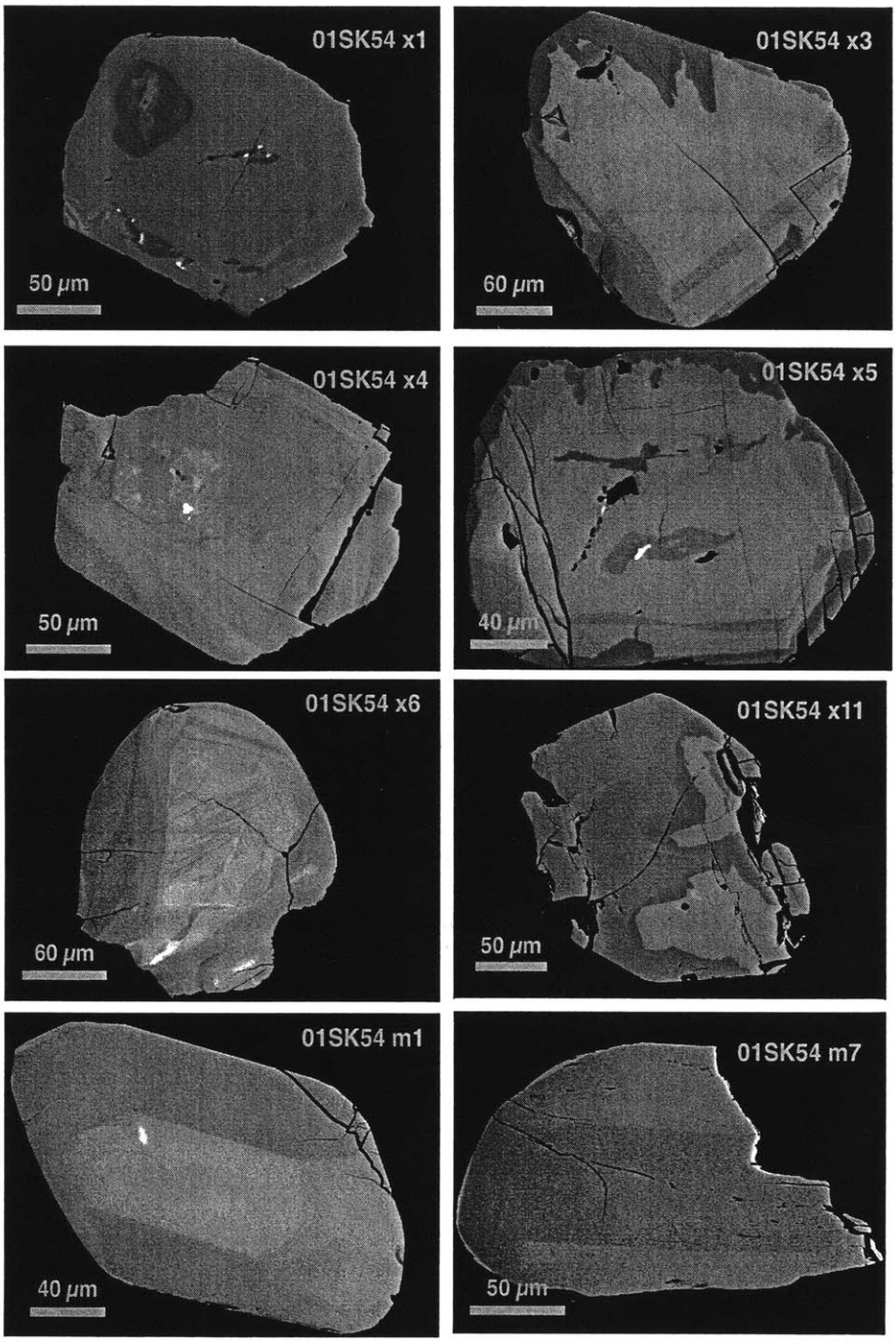


**Figure 19.** BSE images of monazite and xenotime grains from leucogranite sill 01SK54 that were dated by U-Pb geochronology.

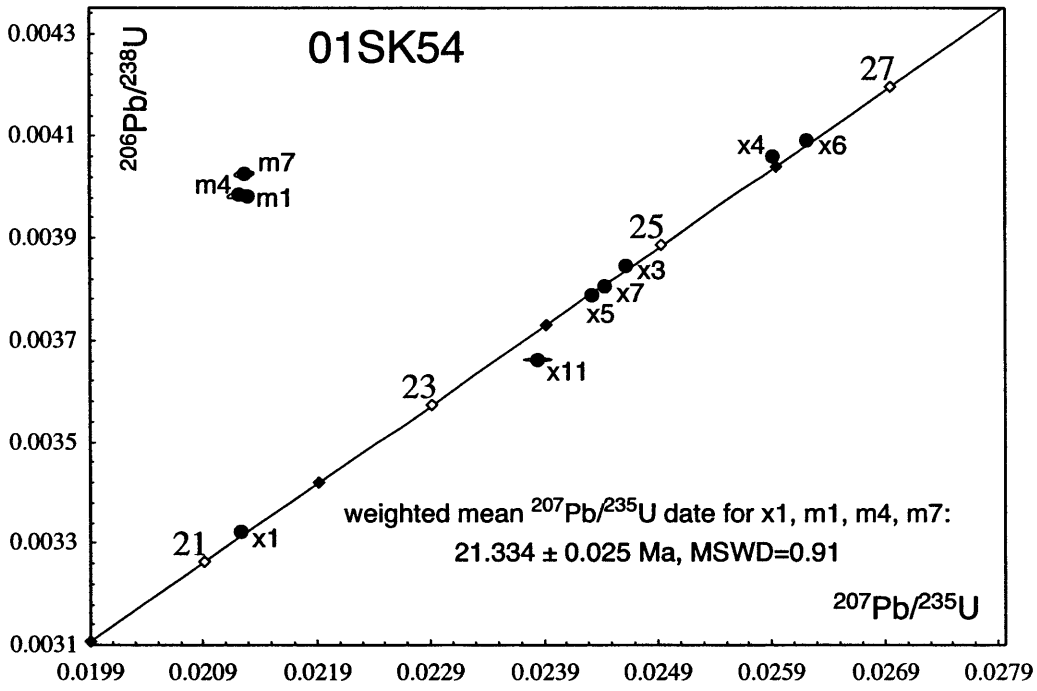


**Figure 20.** U-Pb concordia diagram for sample 01SK54, a leucogranite sill concordant to the foliation of 01SK53 at the 5th Lake outcrop.

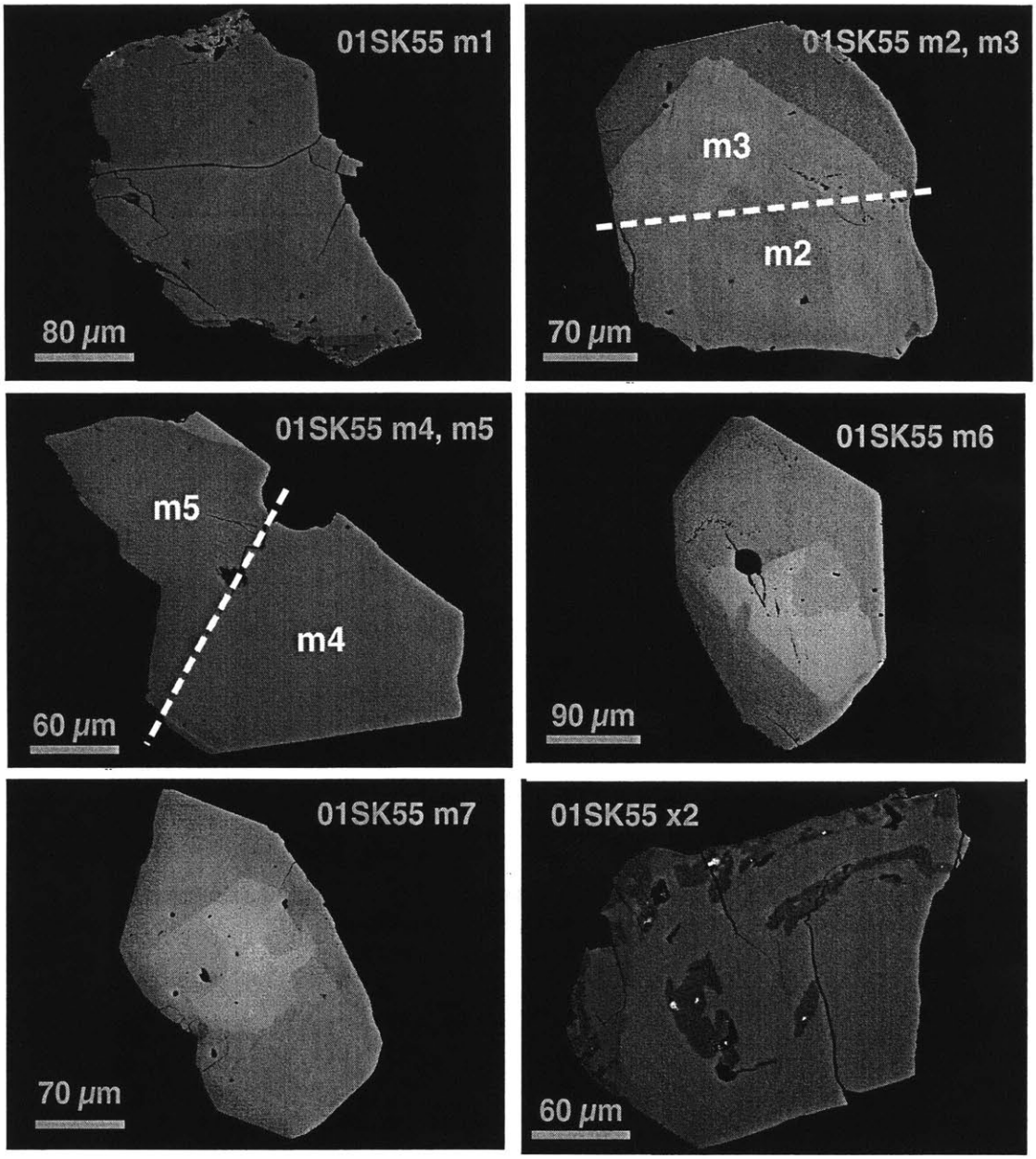


**Figure 21.** BSE images of monazite and xenotime from leucogranite dike 01SK55 that were dated by U-Pb geochronology. Dashed white lines indicate where individual grains were cur with an obsidian blade.

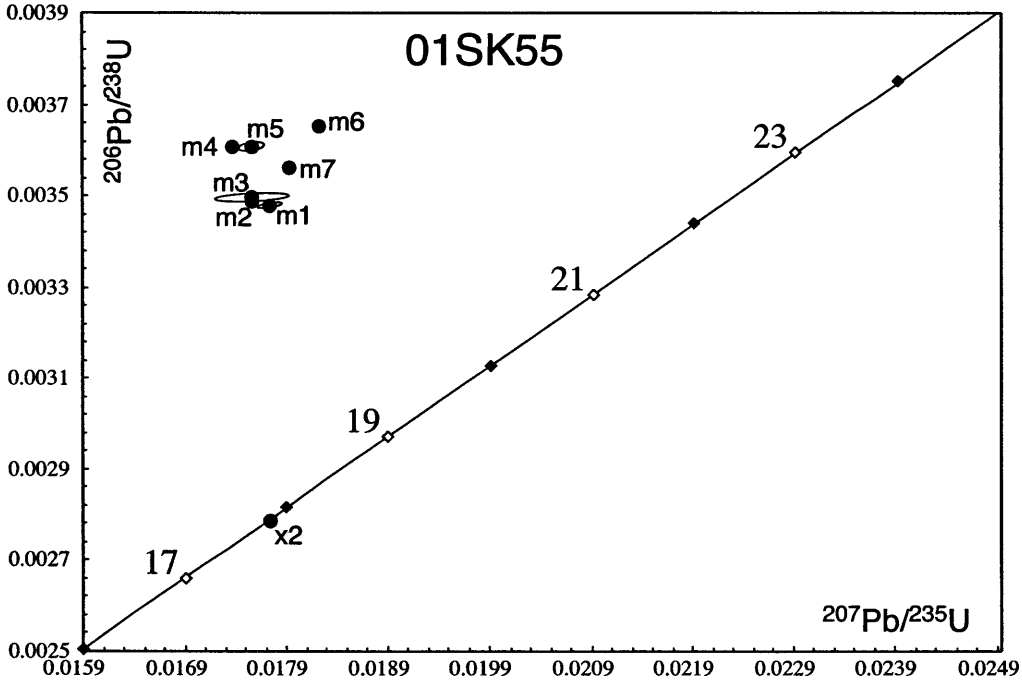


**Figure 22.** U-Pb concordia diagram for sample 10SK55, and undeformed, crosscutting dike at the 5th Lake outcrop.

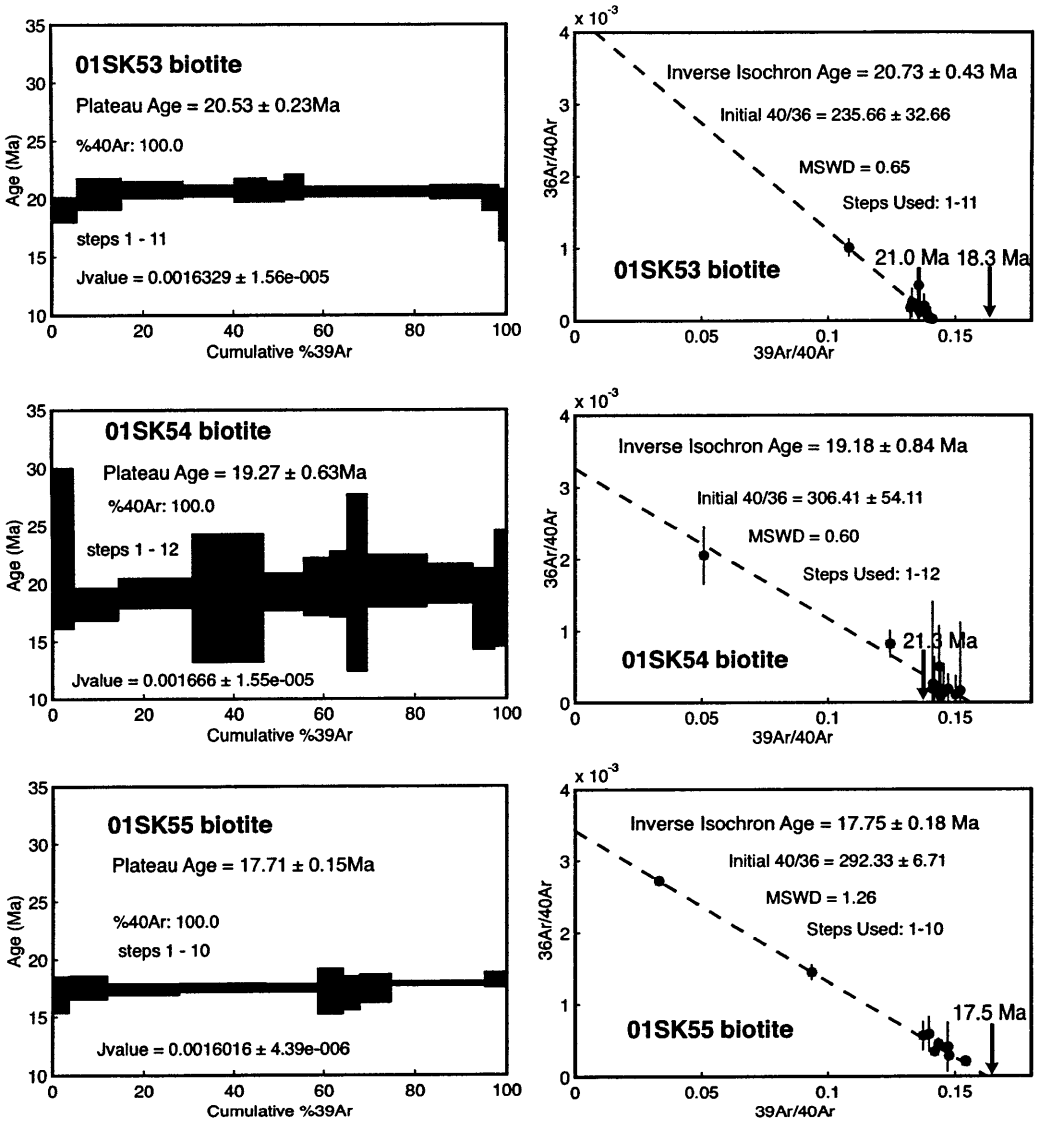


**Figure 23.** $^{40}Ar/^{39}Ar$ release spectra and inverse isochron diagrams for biotites from the 5th Lake outcrop. $^{40}Ar/^{39}Ar$ ratios corresponding to the U-Pb crystallization age of each sample are indicated with arrows on the inverse isochron diagrams.

# Chapter 3

## Investigating Himalayan Leucogranite Melt Generation and Source Characteristics using Nd and Sr Isotopic Signatures in Accessory Phases

**Abstract**

The Nd isotopic systematics of dated monazite, xenotime and host rock samples from four outcrops at different structural levels within the metamorphic core of the Himalayan orogen have been examined to provide constraints on the processes of leucogranite melt generation. Monazite and host rock Nd isotopic compositions are generally indistinguishable while xenotime Nd isotopic compositions, based on a more limited data set, are consistently more radiogenic. The similarity of monazite and host rock isotopic compositions reflects the predominant role that monazite plays in controlling the Nd isotopic composition of its host rock. The slightly more radiogenic xenotime Nd isotopic compositions may reflect local isotopic heterogeneities in low-temperature leucogranitic melts. If an inhomogeneous distribution of high Sm/Nd accessory phases (such as xenotime or apatite) in a source rock prior to melting leads to local variations in Sm/Nd and $^{143}Nd/^{144}Nd$ in the melt that is produced, xenotime crystallizing from high $^{143}Nd/^{144}Nd$ domains of the melt likely will have $^{143}Nd/^{144}Nd$ higher than that of the average melt.

Strontium isotopic compositions of single apatite grains generally agree with host rock isotopic compositions, especially in granites. One exception is a granite that shows extreme heterogeneity in apatite Sr isotopic compositions as well as heterogeneous and highly radiogenic Nd isotopic whole-rock and monazite signatures. The gneiss that the granite intrudes also has

unusually radiogenic Nd, that suggests the granite may have been locally derived or entrained Nd-rich phases from the country rock during emplacement.

Because granite whole-rock samples are mixtures of crystallized melt and xenocrystic minerals, the isotopic signatures of whole-rock samples may not accurately reflect the isotopic signatures of crustal melts. In contrast, demonstrably magmatic accessory phases that concentrate the elements of interest provide a better record of melt isotopic compositions.

## Introduction

Neodymium and Sr isotopic tracer studies are often used to link crustal melts with potential source regions. Such studies assume the melt and source rocks were in isotopic equilibrium and use the coincidence of whole-rock isotopic signatures to suggest a genetic link between source rock and melt. This technique, however, can be hampered by variability in the Nd and Sr isotopic compositions among different samples collected from the same granite body. For example, whole-rock isotopic studies of the Manaslu pluton in the central Nepal Himalaya have documented variations in $\varepsilon_{Nd(20Ma)}$ between –12.9 and –17.1 (Vidal et al., 1984; Deniel et al., 1987), and variations in $^{87}Sr/^{86}Sr_{(20Ma)}$ between 0.74012 and 0.76372 (Vidal et al., 1982, 1984; Deniel et al., 1987) at the pluton scale. Variations at the meter scale were found to be on the order of $\pm$ 2 $\varepsilon_{Nd}$ units and $\pm$ 0.005 $^{87}Sr/^{86}Sr$. These variations are significantly larger than typical analytical uncertainties of $\pm$ 0.5 $\varepsilon_{Nd}$ and $\pm$ 0.0003 $^{87}Sr/^{86}Sr$, and could result from: 1) melting of an isotopically heterogeneous source; 2) incomplete mixing of granites that were in isotopic equilibrium with a homogeneous source with others that were not; or 3) a combination of the two.

In crustal rocks, Rb and Sr are concentrated in major rock-forming minerals such as micas and plagioclase, but a small percentage (~1%) of the whole-rock Sr budget is found in apatite (Harris & Ayres, 1998). Samarium and Nd, on the other hand, are concentrated almost entirely in accessory phosphates, such as monazite and xenotime (e.g. Bea, 1996; Wark & Miller, 1993). Because monazite is a common xenocrystic (inherited) phase in crustal melts such as the Himalayan leucogranites (e.g. Copeland et al., 1988), and xenocrystic xenotime also has been documented (Viskupic & Hodges, 2001), a potential cause of Nd isotopic heterogeneity in anatectic granites is the presence of xenocrystic accessory phases. If xenocrystic accessory phases contribute to the Nd isotopic budget of the host granite, the whole-rock Nd isotopic signature of the granite will not be the same as the melt. The potential of inherited accessory phases to compromise the value of Nd isotopic studies in exploring the melting process makes investigation of the isotopic signatures of individual accessory minerals and how they relate to the isotopic signatures of the granites in which they occur extremely important.

The focus of this study was on the causes of isotopic heterogeneity among petrographically similar granitic rocks in the Himalayan orogen by examining the isotopic systematics of well-characterized phosphate accessory minerals and addressing the following questions: 1) What is the degree of isotopic equilibrium between host rocks and the accessory phases in them, and what can we learn about the melting process from these observations? 2) What is the range of isotopic compositions preserved within accessory phases in discrete melt batches on the hand sample scale, and are those ranges distinguishable from whole-rock isotopic compositions? 3) How does this study at the outcrop/handsample scale relate to the broader isotope systematics of the Himalayan metamorphic core?

**Sr and Nd Isotopic Studies of Himalayan Leucogranites**

Numerous radiogenic isotope studies of Himalayan crustal rocks have sought to understand the origin of the Himalayan leucogranites, a discontinuous chain of plutons and batholiths that crop out along the crest of the Himalayan range. These bodies are part of the Himalayan metamorphic core known as the Greater Himalayan Sequence, that includes orthogneisses, paragneisses, migmatites, and smaller-scale leucogranite dikes and sills. A summary of all whole-rock Sr isotopic studies of the Greater Himalayan Sequence is given in Figures 1 and 2. The metamorphic rocks and the leucogranites show a large degree of heterogeneity in their $^{87}Sr/^{86}Sr$ ratios (calculated at t=20Ma). Although the range in $^{87}Sr/^{86}Sr$ ratios for the schists and gneisses is much greater than that for the leucogranites, the majority of ratios for the metamorphic rocks are between 0.72 and 0.80, and directly overlap the range of granite ratios. This observation led to the suggestion that the Greater Himalayan Sequence metasedimentary rocks are likely to have been the source rocks for the leucogranites (Vidal et al., 1982; Deniel et al., 1987; Guillot & Le Fort, 1995). However, the large degree of isotopic variability in both the granites and the potential source rocks precludes the identification of specific rock types as the leucogranite sources based on isotopic compositions alone.

A compilation of Nd whole-rock isotopic results is shown in Figure 3. The break between lower and higher $^{143}Nd/^{144}Nd$ ratios (calculated at 20 Ma) approximately corresponds to the transition between the Lesser Himalayan Sequence and the Greater Himalayan Sequence as marked by the Main Central Thrust system (Hodges, 2000). Although the Lesser Himalayan Sequence generally has lower $^{143}Nd/^{144}Nd$ ratios, there is some overlap between Lesser and Greater Himalayan isotopic signatures. There is complete overlap between the Nd isotopic

signatures of the Greater Himalayan schists and gneisses and the Himalayan leucogranites, but the schists and gneisses show greater variability in $\varepsilon_{Nd}$ than the leucogranites.

Heterogeneities in Nd and Sr isotopic signatures in the Himalayan leucogranites are hypothesized to result from $^{87}Sr/^{86}Sr$ and $^{143}Nd/^{144}Nd$ heterogeneity in the source region at the time of melting (Vidal et al., 1982; Deniel et al., 1987; Scaillet et al., 1990). Such models imply that leucogranites are the result of the coalescence of isotopically distinct batches of melt that remain unmixed (Vidal et al., 1982; Deniel et al., 1987). Pre-Himalayan (ca. 450-500 Ma) zircon, monazite and xenotime have all been identified in Greater Himalayan Sequence metamorphic rocks and leucogranites (Copeland et al., 1988; Noble & Searle, 1995; Walker et al., 1999; Hodges et al., 1996; Parrish & Hodges, 1996; Searle et al., 1997; Coleman, 1998; Hodges et al., 1998; Simpson et al., 2000; Catlos et al., 2001; Viskupic & Hodges, 2001; Viskupic, Chapter 3). Therefore, the leucogranite source regions are likely to contain accessory phases with a variety of isotopic signatures, including pre-Himalayan inherited phases and metamorphic phases that grew at various times during the Himalayan orogeny. As a consequence, the Himalayan leucogranites and the presumed Greater Himalayan source rocks provide an excellent opportunity to examine the hypothesis that Sr and Nd isotopic heterogeneities in granites and anatexites are related to an inhomogeneous distribution of inherited accessory minerals that do not participate in the anatectic process.

## Accessory Phases and the Nd Isotopic Signatures of Granites

The isotopic composition of a crustal melt will be determined by the phases in the source region that participate in the melting reactions and the degree that small increments of melt with different isotopic compositions are subsequently homogenized (Knesel & Davidson, 2002). Two

studies have found evidence for inherited $^{143}Nd/^{144}Nd$ signatures in accessory zircons (Paterson et al., 1992; von Blanckenburg, 1992), that suggest inherited isotopic signatures in xenocrystic accessory phases may influence whole-rock signatures of partial melts. Exactly how an inherited accessory phase will affect the whole-rock signature depends on the Sm/Nd ratio of the accessory phase, the time elapsed since the accessory phase and the host rock were last in equilibrium, and the relative control that phase has on the whole-rock Nd budget.

Representative rare earth element diagrams for monazite, apatite and xenotime are shown in Figure 4. Monazite is enriched in the light rare earth elements (LREE), has the highest concentrations of Sm and Nd, and has the lowest Sm/Nd ratio of the three phases. Xenotime is enriched in the heavy rare earth elements (HREE), has much lower concentrations of Sm and Nd than monazite, and has a high Sm/Nd ratio. Apatite has the lowest Sm and Nd concentrations of the three phases, and a Sm/Nd ratio intermediate to those of monazite and xenotime.

A hypothetical example of how accessory phases contribute to the whole-rock Sm and Nd budget of a gneiss approximating the mineralogy and composition of a Greater Himalayan Sequence gneiss is given in Table 1. Although monazite makes up only 0.032 wt.% of the gneiss in this example, it contains 98% of the total whole-rock Nd and 94% of the whole-rock Sm. Inclusion of the accessory phosphates xenotime and apatite accounts for nearly 99% of the whole-rock Nd budget and nearly 97% of the whole-rock Sm budget. In order to illustrate how accessory phases contribute to the Nd isotopic composition of a whole-rock and to explore how they may contribute to the Nd isotopic composition of a crustal melt, the mineral compositions in Table 1 were used to make a Nd evolution model assuming the phases last equilibrated to a $^{143}Nd/^{144}Nd$ ratio of 0.51153 at 450 Ma, a value representative of the Greater Himalayan Sequence metasedimentary gneisses at that time. Results of the model are shown in Figure 5 and

the $^{143}Nd/^{144}Nd$ ratios of the minerals at 20 Ma are given in Table 1. The control of monazite on the whole-rock isotopic signature is clearly shown; monazite and the whole-rock $^{143}Nd/^{144}Nd$ ratios evolve along almost the same trajectory, resulting in Nd isotopic compositions at 20 Ma that would not be distinguishable given typical precision limits for Nd isotopic analyses. In contrast, xenotime, zircon and apatite, evolve to much more radiogenic Nd isotopic compositions due to their high Sm/Nd ratios.

*The Significance of Monazite*

Most researchers attribute granites such as those found in the Himalaya to muscovite dehydration melting through a reaction such as:

muscovite + quartz + plagioclase = K-feldspar + sillimanite + melt (1)

(e.g. Thompson, 1982; Harris & Inger, 1992; Harris et al., 1995). The minerals taking part in this reaction contain negligible quantities of Sm and Nd (Table 1) and cannot account for observed LREE concentrations in Himalayan leucogranites (Harris & Inger, 1992; Inger & Harris, 1993). The partial or complete dissolution of REE-rich accessory phases therefore must take place. It is already established that monazite exerts the most control over a rock's Sm and Nd budgets. Thus, if we assume monazite is the only REE-rich accessory phase involved in the melting process, the melt will inherit the Nd isotopic signature of the monazite–essentially the same Nd isotopic signature of the whole-rock. The proportion of monazite in the source rock involved in the melting reaction will change the concentrations of Sm and Nd in the melt, but will not significantly change the Nd isotopic composition of the melt, unless a mixed population of monazites of various ages is present in the source and monazites of a specific age are more likely to be involved in the melting process than others. As little as 0.1% monazite dissolution

will contribute enough Sm and Nd to the melt to overwhelm the minor contributions of these elements from the major rock-forming minerals. Variations in the proportion of ca. 450 Ma monazite versus younger metamorphic monazite involved in the melting process will also not significantly change the Nd isotopic composition of the resulting melt because the 450 Ma monazite has a Nd isotopic composition that is indistinguishable from the whole-rock Nd isotopic composition with which we assumed the younger metamorphic monazite would be in equilibrium. It follows that the entrainment of xenocrystic monazite into the melt will influence the whole-rock Nd isotopic composition in the same way that dissolving monazite affects the Nd isotopic composition of the melt.

*The Role of Garnet*

Garnet is a common mineral in suspected source rocks for crustal melts and, because this mineral is relatively rich in rare earth elements, it is worthwhile to consider how it may influence the Nd isotopic signatures of granites. For typical pelitic compositions in regional metamorphic terrains such as the Himalayan metamorphic core, garnet is not a reactant in melt reactions at appropriate pressure-temperature conditions (Spear et al., 1999). In this case, garnet in the source rock would have no influence on the Nd isotopic character of a melt unless it was entrained as xenocrysts or dissolved in the melt. In the case of the Himalayan leucogranites, garnets that are found as accessory phases are typically high in Mn and are probably of magmatic origin (e.g., Hodges & Silverberg, 1988). In the case of garnet dissolution, the influence of garnet depends critically on the elapsed time between primary garnet crystallization and melting. In the Greater Himalayan Sequence, most research suggests that garnets are of Himalayan age

and therefore would not have had time to evolve to significantly high $^{143}Nd/^{144}Nd$ to strongly influence the Nd isotopic composition of a Himalayan-aged leucogranite magma.

*The Significance of Xenotime and Apatite*

Because both xenotime and apatite have high Sm/Nd ratios and, in a hypothetical source region, could have Nd isotopic compositions different from those of monazite, their participation in the anatectic process most likely would alter the Nd isotopic composition of the melt. The dissolution or entrainment of inherited xenotime or apatite would result in a more radiogenic Nd isotopic composition in an anatectic melt than the source rock. The degree that dissolving apatite or xenotime can alter the Nd isotopic composition of a melt depends on how radiogenic their Nd isotopic signatures might be and on the relative proportions of xenotime, apatite and monazite dissolving in the melt. If relatively little monazite dissolves, the dissolution of xenotime or apatite will contribute proportionally more Sm and Nd to the melt and would have a greater affect on the melt isotopic composition. This is illustrated in Figure 6, which shows the resulting Nd isotopic compositions of two-component mixtures of xenotime-monazite, and apatite-monazite. The affects of apatite dissolution or entrainment are less profound and are likely to be insignificant since, to date, no pre-Himalayan apatite has been found in the Greater Himalayan Sequence. Pre-Himalayan xenotime is not common, although it has been documented as a xenocrystic phase (Viskupic & Hodges, 2001). As a consequence, it is likely that phosphates other than monazite had little influence on the *bulk* Nd isotopic signatures of most Himalayan leucogranites. Nevertheless, preliminary analyses of the Nd isotopic compositions of magmatic xenotimes from these rocks, presented below, suggest that pre-magmatic xenotime and/or apatite may have had local effects on the $^{143}Nd/^{144}Nd$ of melts.

**Testing the Hypothesis**

To determine if isotopic heterogeneities observed on the meter scale reflect the coalescence of isotopically distinct batches of melt that remain unmixed, or if they reflect the heterogeneous distribution of isotopically distinct accessory phases, samples of potentially different melt batches are needed. Because different intrusive phases may be difficult to recognize within a pluton, granite samples from individual dikes and sills represent the best choices for isotopic characterization. The isotopic signature of a crustal melt is influenced by conditions of melt transport and emplacement as well as by the processes governing anatexis. Interaction with wall rocks during transport could influence the isotopic signature of a partial melt if accessory phases are entrained. Examining the isotope systematics of different melts on the outcrop scale rather than the pluton scale allows a more detailed investigation of isotopic differences based on relative age, structural level, and country rock characteristics. More importantly, determining the isotopic signature of individual accessory phases, especially if their age relations are known, provides better constraints on the origins of leucogranite isotopic heterogeneities and on the leucogranites themselves.

For this study, whole-rock Nd and Sr isotopic signatures from leucogranite dikes and sills, and metamorphic country rocks in the Greater Himalayan Sequence were determined. Detailed geochronologic studies of the same rocks from three of these outcrops were previously reported in Chapter 2 and by Viskupic and Hodges (2001). This allowed the determination of Nd isotopic signatures of well-characterized, previously dated grains of monazite and xenotime. In addition, apatites were separated from several of the rocks for Sr isotopic analysis. Although apatite does not control a rock's Sr budget, determining Sr isotopic signatures for individual

apatite grains provides an independent way to investigate isotopic variations at the sub-handsample scale.

**Sample Descriptions**

The samples examined come from four outcrops at different structural levels in the Greater Himalayan Sequence of the Everest region of eastern Nepal. A pelitic gneiss (01SK30) sampled from the Main Central Thrust zone comes from the structurally lowest outcrop studied, and has not been previously described. The gneiss is biotite- and muscovite-rich with euhedral garnets up to 4 mm in diameter. The foliation is defined by the alignment of the micas and fibrolitic sillimanite. Augen of plagioclase feldspar are approximately 5 mm in width, and are aligned with the dominant foliation. Quartz and rare K-feldspar are also present. All other samples come from three outcrops in the mid-upper Greater Himalayan Sequence and were described in Chapter 2. A summary of the sample locations, lithologies, ages, and the presence or absence of inherited accessory phases is given in Table 2. Results from these samples will be discussed, outcrop by outcrop, from the structurally lowest to the structurally highest. The country rock samples 01SK30, 98E5, and 01SK53 will be referred to as gneisses, leucogranite sills 00SK09 and 01SK54 will be referred to as "early sills", and leucogranite dikes 98E6, 00SK10, and 01SK55 will be referred to as "late-stage" granites or crosscutting dikes. Sill 00SK08 is also considered a late-stage granite based on geochronology (Table 1), even though it does not crosscut the country rock metamorphic fabric.

## Results

Details of the analytical methods used can be found in Appendix A. Whole-rock major and trace element concentrations are reported in Table 3, and plotted in Figure 7. The granites are all peraluminous, with $Al_2O_3$ >13 wt.%, and $SiO_2$ between 72 and 76 wt.%. No covariation between $SiO_2$ and other major elements is observed. As has been described previously, the leucogranites are depleted in rare earth elements (REE) relative to the gneisses of the Greater Himalayan Sequence (Vidal et al., 1982; Deniel et al., 1987; Le Fort et al., 1987; Ayres & Harris, 1997), and show varying degrees of LREE enrichment. Leucogranite sills 00SK09 and 01SK54 have the flattest REE patterns, consistent with the observation that both samples contain an abundance of xenotime.

Results from Nd and Sr isotopic analyses are reported in Tables 4 and 5, and plotted in Figures 8 and 9. All $^{143}Nd/^{144}Nd$ ratios, $\varepsilon_{Nd}$ values, and whole-rock $^{87}Sr/^{86}Sr$ ratios were calculated at the previously determined whole-rock crystallization ages reported in Table 2. The apatite $^{87}Sr/^{86}Sr$ ratios are reported as measured without age correction; apatite Rb/Sr ratios are sufficiently low (<0.02) that in over 20 million years, their $^{87}Sr/^{86}Sr$ ratios will not change significantly. Errors reported in the tables, figures, and throughout the text are given at the 95% confidence level.

### *Lower Greater Himalayan Sequence Gneiss*

The whole-rock sample and two single grain monazites from gneiss sample 01SK30 were analyzed for Nd. $^{143}Nd/^{144}Nd$ values for the whole-rock (0.512178 ± 0.00001) and grain m1 (0.512180 ± 0.00001) agree within analytical uncertainty, but grain m2, has a lower $^{143}Nd/^{144}Nd$

ratio (0.512139 ± 0.000012) that differs from the whole-rock value by ca. 4σ. Both monazite grains and the whole-rock sample have $^{143}Nd/^{144}Nd$ ratios that are higher than almost all such published Himalayan whole-rock ratios (Figure 3). Four single apatite grains from gneiss sample 01SK30 were analyzed for Sr (Figure 8). The $^{87}Sr/^{86}Sr$ initial ratios vary from 0.76702 ± 0.00003 to 0.77364 ± 0.00002, suggesting substantial heterogeneity in Sr isotopes on the hand sample scale (centimeter to decimeter). The 01SK30 $^{87}Sr/^{86}Sr$ ratios agree well with the majority of published Sr data from the Greater Himalayan Sequence (Figure 1).

*Namche Bazaar*

Monazites from the migmatitic orthogneiss 98E5 show remarkable consistency in their Nd isotopic compositions. Seven monazites, including three that contain an inherited component ($^{207}Pb/^{206}Pb$ dates range from 250 to 452 Ma), and the host rock sample have $^{143}Nd/^{144}Nd$ ratios that range from 0.511888 ± 16 to 0.511905 ± 16 and agree within 2σ uncertainty. In contrast, two xenotimes from gneiss 98E5 have $^{143}Nd/^{144}Nd$ ratios that are nominally more radiogenic (0.511924 ± 18 and 0.511925 ± 12) than those of the monazites and host rock.

Whole-rock and apatite Sr isotopic compositions in gneiss 98E5 are more heterogeneous, with $^{87}Sr/^{86}Sr$ ratios ranging from 0.76697 ± 0.00003 to 0.76921 ± 0.00002 with the whole-rock sample and only one of the single apatites (a4) having $^{87}Sr/^{86}Sr$ ratios that are indistinguishable at the 2σ level.

In the late-stage crosscutting dike 98E6, three monazites, one xenotime, and the host rock sample have $^{143}Nd/^{144}Nd$ ratios that agree within analytical uncertainty (ranging from 0.511929 ± 0.000075 to 0.511898 ± 0.00002), while a fourth monazite has a significantly lower ratio

(0.511804 ± 0.000012). Note that the $^{143}Nd/^{144}Nd$ compositions for crosscutting leucogranite 98E6 are slightly, but resolvably, lower than those of gneiss 98E5.

*Gokyo Ri*

Neodymium isotopic signatures were determined for three granites from the Gokyo Ri outcrop; two sills, and one crosscutting dike. One monazite and two xenotimes from the oldest sill, 00SK09, were analyzed. The $^{143}Nd/^{144}Nd$ ratio of the monazite (0.511891 ± 0.000014) is indistinguishable from that of the whole-rock (0.511870 ± 0.000011) at the 2σ level. The two xenotimes have more radiogenic Nd isotopic compositions (0.511903 ± 0.000014, and 0.511920 ± 0.000012). The isotopic compositions of these monazites and xenotimes are similar to those measured in gneiss 98E5 at the Namche Bazaar outcrop.

Strontium was measured in the 00SK09 whole-rock sample as well as three single apatites. One of the apatites (a3, $^{87}Sr/^{86}Sr$ =0.75740 ± 0.00003) has an indistinguishable $^{87}Sr/^{86}Sr$ ratio from the whole-rock (0.75740 ± 0.00002), but the other two apatites have $^{87}Sr/^{86}Sr$ ratios that are higher by at least 4σ (0.75760 ± 0.00002 and 0.75852 ± 0.00002).

All three monazites analyzed from late stage dike 00SK10 contain an inherited component (Chapter 3). Two of the monazites have different $^{143}Nd/^{144}Nd$ ratios at the 2σ level (0.511798 ± 0.000014 and 0.511847 ± 0.000025), but they both have $^{143}Nd/^{144}Nd$ ratios that are indistinguishable from that of the third monazite (0.511818 ± 0.000012) at the 2σ level. One monazite from late-stage granite 00SK08 was analyzed. Its $^{143}Nd/^{144}Nd$ ratio of 0.511837 ± 0.00001 is indistinguishable from monazite analyses from late-stage granite 00SK10 (from the same outcrop) and late-stage dike 98E6 (from the Namche Bazaar outcrop). Note again that the

late-stage granites (00SK10, 00SK08) have slightly, but resolvably, less radiogenic Nd isotopic compositions than the early sill (00SK09).

*Gokyo's 5th Lake*

The $^{143}Nd/^{144}Nd$ ratios of all samples from the 5th Lake outcrop are different than those from Gokyo Ri and Namche Bazaar. Gneiss 01SK53 has a whole-rock $^{143}Nd/^{144}Nd$ ratio of 0.512072 ± 0.00001, higher than almost all whole-rock ratios in the Himalayan literature. A single monazite from gneiss 01SK53 has a similarly high $^{143}Nd/^{144}Nd$ ratio of 0.512088 ± 0.00001 that is indistinguishable from the whole-rock value at the 2σ level.

The whole-rock $^{143}Nd/^{144}Nd$ ratio from early sill 01SK54 is 0.512271 ± 0.00001, and is higher than any such ratio reported for a granite in the Himalaya. Unlike the other samples studied, the single monazite analyzed from this sample had an extremely high $^{143}Nd/^{144}Nd$ ratio (0.512140 ± 0.000015) that is much higher than the whole-rock ratio (Figure 3).

The apatite Sr isotopic compositions for sill 01SK54 also are heterogeneous and different than other Himalayan granites. Five single apatites have $^{87}Sr/^{86}Sr$ ratios that vary from 0.80606 ± 0.00003 to 0.81592 ± 0.00002. Most Himalayan leucogranites have $^{87}Sr/^{86}Sr$ ratios between 0.74 and 0.78 (Figure 2).

Late-stage dike 01SK55 also has more radiogenic Nd than most Himalayan leucogranites, but is less radiogenic than the country rock and early sill from the same outcrop. The whole-rock $^{143}Nd/^{144}Nd$ ratio is 0.512001 ± 0.000020, and two single monazites have ratios of 0.511989 ± 0.00001 and 0.512020 ± 0.00001 that are indistinguishable from the whole-rock ratio at the 2σ level.

Five apatites from dike 01SK55 have $^{87}Sr/^{86}Sr$ ratios that range from 0.77603 ± 3 to 0.77709 ± 2. Their Sr isotopic compositions do not agree within analytical uncertainty, but are more homogeneous than the apatite $^{87}Sr/^{86}Sr$ ratios measured for gneisses 98E5 and 01SK30.

## Discussion

*Inherited Monazite, Magmatic Monazite, and Host Rock Nd Isotopic Signatures*

Overall, monazites and their host rocks have indistinguishable Nd isotopic compositions, except in the case of sample 01SK54 which will be discussed separately. For example, migmatitic orthogneiss sample 98E5 contains both inherited and non-inherited monazite that have the same Nd isotopic compositions as their host rock. As postulated earlier, this observation is consistent with monazite being the principal host for Sm and Nd.

Although most monazites have the same $^{143}Nd/^{144}Nd$ ratios as their host rocks, a few examples of differences between individual monazites and their host rocks were observed. In all three cases (00SK30 m2, 98E6 m12, 01SK54 m7) the monazite is less radiogenic than the whole-rock by greater than 4σ. These discrepancies indicate that although the Nd isotopic signature of a whole-rock may be similar to that of monazite, the whole-rock isotopic signature is given by the weighted mean of the isotopic compositions of the constituent phases, some of which may be xenocrystic. The simplest explanation for the less radiogenic monazites is that they crystallized from a melt that was isotopically heterogeneous on a scale smaller than that represented by the hand sample. In order for this explanation to be correct, complementary phases with more radiogenic Nd isotopic compositions must also be present in the host rock. Evidence for the existence of such radiogenic phases will be discussed in the next section.

*Xenotime Nd Isotopic Signatures*

Although few xenotimes were analyzed in this study, those that were (from gneiss 98E5 and granites 98E6 and 00SK09) have Nd isotopic compositions that are consistently more radiogenic than their host rocks and coexisting monazites. Relative probability distributions for these data indicate a roughly 80% probability that this difference is statistically significant, provided that the analyzed compositions are representative of the populations of monazite and xenotime in each sample. There are two potential explanations for this finding. The first is that older inclusions exist in the analyzed xenotimes. This possibility is extremely unlikely because backscattered electron images and U-Pb data for these grains yield no evidence for inheritance (Chapters 1 and 2). The alternative (and preferred) explanation is that the xenotimes crystallized from zones of melt that had locally high $^{143}Nd/^{144}Nd$, perhaps due to the dissolution of older, high Sm/Nd accessory phases.

The LREEs incorporated in magmatic xenotime are most likely derived from the dissolution of monazite, apatite, or xenotime. The Nd isotopic compositions of magmatic and inherited monazite were measured in sample 98E5. Both were less radiogenic than the coexisting xenotime. It is therefore possible that the LREEs in the magmatic xenotime were partially derived from the dissolution of minerals with high Sm/Nd ratios that could have evolved to more radiogenic Nd isotopic compositions, such as older inherited xenotime or possibly apatite. The mixing curves in Figure 6 illustrate the relative proportions of xenotime or apatite Nd needed to locally "dilute" the monazite Nd isotopic composition.

Local dissolution and reprecipitation of phosphate accessory phases has been demonstrated experimentally. Monazite precipitation along the margins of dissolving apatite

crystals has been observed even when the bulk melt was not monazite-saturated (Wolf & London, 1995). Experimental studies also suggest that P derived from the dissolution of monazite or xenotime remains associated with the REEs derived from the dissolving accessory phases (Montel, 1993; Wolf & London, 1995) so that reprecipitation of locally dissolved monazite, xenotime, and apatite is likely. Such processes lend themselves to the preservation of isotopic heterogeneities among accessory phosphates in a single hand sample because they imply that chemical equilibrium may only be reached on a local scale.

*Isotopic Differences between the Gneisses and Early Sills and the Late Granites*

In the three outcrops intruded by granites, the country rock gneisses (98E5, 01SK53) and the early leucogranite sills (00SK09, 01SK54) have more radiogenic Nd isotopic compositions than the late-stage granites at the same outcrops (98E6, 00SK08, 00SK10, 01SK55). A similar trend is seen in the Shisha Pangma and Manaslu plutons. Searle et al. (1997) identified two phases of the Shisha Pangma pluton. The older phase (20.2 Ma) has a $^{143}Nd/^{144}Nd$ ratio of 0.511834 ± 0.000015 and the younger phase (17.3 Ma) has a $^{143}Nd/^{144}Nd$ ratio of 0.511758 ± 0.000015 (ratios calculated at 17 Ma for both samples). Similarly, Harrison et al. (1999) identified two phases of the Manaslu pluton. $^{143}Nd/^{144}Nd$ whole-rock ratios in the older phase (22.9 Ma) range from 0.511880 to 0.511929 (n=4, average $^{143}Nd/^{144}Nd$ = 0.511907), while one sample of the younger phase (19.3 Ma) has a $^{143}Nd/^{144}Nd$ ratio of 0.511874 (ratios calculated at 19.3 Ma for both samples). Given the limited amount of data, it is difficult to comment on this apparent trend other than to hypothesize that it could reflect a change in source composition with time or varying degrees of accessory inheritance. Unfortunately, most Nd isotopic studies have not included geochronologic studies, so a potential change in isotopic composition with time

cannot be further evaluated without more combined Nd and U-Pb isotopic investigations. Another possibility is that the older phases contain greater proportions of high Sm/Nd phases such as inherited xenotime, although this hypothesis is not supported for the samples examined in this study.

*Differences in Isotopic Composition as a Function of Structural Level*

Overall, rocks from the Namche Bazaar (98E5, 98E6) and Gokyo Ri (00SK08, 00SK09, 00SK10) outcrops have Nd isotopic compositions that are similar to those reported from other Himalayan leucogranites and gneisses. However, rocks from the lower Greater Himalayan Sequence (01SK30) and the 5$^{th}$ Lake outcrop (01SK53, 01SK54, 01SK55) are much more radiogenic. These differences in $^{143}Nd/^{144}Nd$ are not fully supported by differences in Sm/Nd ratios, suggesting some initial source heterogeneity. The Nd isotopic signature of late-stage granite 01SK55 is most similar to the less radiogenic Nd isotopic compositions at the other outcrops studied. One possible explanation for the more radiogenic Nd signature of 01SK55 is that it incorporated radiogenic Nd from the country rock (01SK53) during emplacement. This explanation requires that REE rich phases from the country rock were entrained in the dike during transport and that these xenocrystic phases subsequently dissolved and altered the isotopic composition of the melt. Entrainment alone of accessory phases from the country rock could account for the more radiogenic whole-rock 01SK55 Nd isotopic composition. However, this mechanism would necessitate the dissolution of the entrained accessory phases since magmatic monazites in granite 01SK55 have similarly radiogenic Nd isotopic compositions.

The whole-rock and monazite Nd isotopic signatures of leucogranite sill 01SK54 are even more radiogenic, also suggesting local contamination by the country rock or even a local

melt source. The discrepancy between the whole-rock and the monazite Nd isotopic compositions in 01SK54 and the heterogeneity in the apatite Sr isotopic compositions are consistent with the melt being locally derived. A clue to the origin of the extremely radiogenic whole-rock Nd isotopic composition may also lie in the melt's bulk composition: Sample 01SK54 has a flatter REE pattern than the other samples studied (Figure 6), it has the highest Sm/Nd ratio of all the samples studied, and it is observed to contain an equal to higher proportion of xenotime than monazite. These observations suggest that the radiogenic whole-rock $^{143}Nd/^{144}Nd$ ratio is the result of a levering effect by xenotime, with high Sm/Nd ratios and highly radiogenic Nd signatures. This hypothesis needs to be tested with single-grain xenotime Nd analyses. The absence of such a radiogenic Nd signature in the larger Himalayan leucogranite plutons (Figure 3) suggests that there may only be a small volume of such radiogenic melts and that they exert little leverage of the compositions of large plutons.

*Sr Isotopic Systematics*

In addition to the Sr isotopic heterogeneity observed in leucogranite 01SK54, Sr isotopic heterogeneity was also observed in gneiss 01SK30. The other three samples analyzed (98E5, 00SK09, 01SK55) show more homogeneous apatite Sr systematics and some agreement between apatite and whole-rock Sr signatures. Overall, there is less variation in Sr isotopic compositions within samples than between them. This suggests that apatite can be a faithful recorder of whole-rock $^{87}Sr/^{86}Sr$ ratios, and that Sr isotopic signatures can be homogeneous at the hand-sample scale. Although large degrees of Sr isotopic heterogeneity are observed in Himalayan leucogranites, there is some suggestion that Sr isotopic signatures can be homogenous on a scale of meters to tens of meters. Deniel et al. (1987) measured whole-rock $^{87}Sr/^{86}Sr$ ratios in

leucogranite samples from several 100 m outcrop sections in the Manaslu pluton. In one such section, 6 of the 11 Sr isotopic compositions were indistinguishable at the 2σ uncertainty level, suggesting homogenization at the tens of meters scale.

*Implications for Monazite-Xenotime Thermometry*

Viskupic and Hodges (2001) used quantitative monazite-xenotime thermometry based on the partitioning of Y between monazite and xenotime (Gratz & Heinrich, 1997) and temperature estimates based on empirical studies of Nd partitioning between monazite and xenotime (Andrehs & Heinrich, 1998) to investigate the thermal history of migmatitic orthogneiss 98E5. Application of both thermometers presumes that monazite and xenotime were in chemical equilibrium, which Viskupic and Hodges (2001) evaluated by comparing the results of the independent Y and Nd thermometers and by establishing with U-Pb geochronology if monazite and xenotime were crystallizing at the same time. Calculated temperatures were considered robust when they were based on the chemistries of coeval monazite and xenotime and when the Y and Nd thermometers were in agreement.

Results from this study, however, suggest that volumes of melt smaller than those represented by a hand sample can be chemically heterogeneous, and that monazite and xenotime that crystallized in the same hand sample at the same time may not be in chemical equilibrium. While this conclusion does not negate the results of Viskupic and Hodges (2001), it does suggest caution in applying such thermometers to accessory phases that have been separated from their host rock. In the application of traditional thermobarometers, chemical compositions are measured on minerals in thin sections, often immediately adjacent to each other, where chemical equilibrium is more likely to have been achieved and where textural relationships can be

evaluated. A similar approach should be used when applying accessory phase thermometers so that the spatial and textural relationships between monazite and xenotime can be observed.

**Conclusions**

1) Demonstrably magmatic monazite almost always records the whole-rock Nd isotopic signature. This may not be true in granites that contain large proportions of xenocrystic accessory minerals of variable ages that do not equilibrate with the melt.
2) Demonstrably magmatic xenotimes in the studied samples record more radiogenic Nd isotopic signatures than their host rocks and coexisting monazites, suggesting crystallization from a locally more radiogenic melt. The dissolution of inherited xenotime or apatite and local regrowth of xenotime during the melting process is one mechanism by which this may occur.
3) Heterogeneities recorded in monazite and xenotime Nd isotopic compositions, and in apatite Sr compositions, support a model for melt generation where accessory phases grow from locally derived sources without there being a well mixed, isotopically heterogeneous melt.
4) There is some suggestion that the Nd isotopic systematics of leucogranite melts can be affected by the country rocks they intrude as a result of the entrainment of REE-rich phases during transport and emplacement. This effect of local host rock on leucogranite melt isotopic composition must be considered in future isotopic studies.
5) Relationships between Nd isotopic composition and age of melt may define a change in source composition with time if additional studies support the observations made here. This progression to less radiogenic Nd isotopic compositions with time could be the result of declining concentrations in the source region of high Sm/Nd phases such as apatite and

xenotime, resulting in less leverage on the melt composition of their more radiogenic components.

6) Granitic whole-rocks are physical and chemical mixtures of crystallized melt and minerals entrained from the melt source region and from the surrounding country rocks during transport and emplacement. Arguably the most reliable way to isotopically fingerprint crustal melts, therefore, is to study the isotopic systematics of demonstrably magmatic accessory phases that concentrate the elements of interest such as monazite, xenotime, and apatite.

## Appendix A
## Analytical Methods

Monazite, xenotime, and apatite were separated from whole-rock samples by standard crushing, magnetic, and heavy liquid separation techniques, followed by hand selection under a picking microscope. Monazite and xenotime grains were dissolved in Teflon microcapsules in 12M HCl at 180°C for 48 hours, followed by conversion to 6M HCl at 180°C for 24 hours. Since all of the monazites and xenotimes were dated by U-Pb IDTIMS (see details in Chapter 3), Pb and U were first separated from the mineral solutions using miniaturized HBr and HCl-based anion exchange chromatography. All of the mineral solutions except the Pb and U elutions were collected for Nd chemistry. Xenotime, and one monazite, solutions were spiked with a mixed $^{149}Sm$-$^{150}Nd$ tracer and fluxed at 150°C for 3-4 days, followed by repeated drying and redissolving in 6M HCl. The remaining monazite solutions were not spiked. Whole-rock powders were spiked with a mixed $^{149}Sm$-$^{150}Nd$ tracer and dissolved in HF-$HNO_3$ in teflon pressure vessels at 220°C for three days, followed by conversion to 6M HCl and fluxing at

150°C for 48 hours. The separation and purification of Sm and Nd for whole-rock and accessory phase samples were accomplished with a standard two-stage cation exchange HDEHP reverse chromatography procedure.

An aliquot of each whole-rock solution was spiked with a mixed $^{87}Rb$-$^{84}Sr$ tracer and fluxed at 150°C for 3-4 days, followed by repeated drying and dissolving in 6M HCl. Single apatite grains were dissolved in 12M HCl in Teflon beakers at 150°C for 4-5 days. The separation and purification of Rb and Sr were accomplished with a combination of cation and Sr-selective crown ether ion exchange chromatography.

All isotopic measurements were made on the MIT VG Sector 54 thermal ionization mass spectrometer. Samarium was loaded on single Ta filaments with 1 μl of 1M $H_3PO_4$ and analyzed as metal ions in static multicollector mode with a $^{152}Sm$ ion beam of $1.5x10^{-11}$ A. Neodymium was loaded on triple Re filaments with 1 μl of 0.1M $H_3PO_4$ and analyzed as metal ions in dynamic multicollector mode with a $^{144}Nd$ ion beam of $1.0x10^{-10}$ A. Samarium and Nd data were fractionation-corrected with an exponential law, normalizing to $^{152}Sm/^{147}Sm = 1.783$ and $^{146}Nd/^{144}Nd = 0.7219$, respectively. Strontium was loaded on single Re filaments with 1μl of 1M $H_3PO_4$ and 1μl $TaCl_5$ and analyzed as metal ions in dynamic multicollector mode with a $^{88}Sr$ ion beam of $1.5x10^{-10}$ A. Strontium data was fractionation-corrected with an exponential law, normalizing to $^{86}Sr/^{88}Sr = 0.1194$. Rubidium was loaded on single Re filaments with 1μl of 1M $H_3PO_4$ and analyzed as metal ions in static multicollector mode with a $^{87}Rb$ ion beam of $5x10^{-13}$ A.

Separate aliquots of the whole-rock powders were used to determine major and trace element concentrations by XRF and ICPMS, respectively (Actlabs).

**Acknowledgements**

This study was supported by an NSF grant to K.V. Hodges and S.A. Bowring.

## References

Ahmad, T., Harris, N., Bickle, M., Chapman, H., Bunbury, J., Prince, C. (2000) Isotopic constraints on the structural relationships between the Lesser Himalayan Series and the High Himalayan Crystalline Series, Garhwal Himalaya. Geological Society of America Bulletin, v. 112, p. 467-477.

Andrehs, G., Heinrich, W. (1998) Experimental determination of REE distributions between monazite and xenotime: potential for temperature-calibrated geochronology. Chemical Geology, v. 149, p. 83-96.

Ayres, M.W. (1997) Trace-element behaviour during high-grade metamorphism and anatexis of the Himalayas. PhD thesis, The Open University, U.K.

Ayres, M., Harris, N. (1997) REE fractionation and Nd-isotope disequilibrium during crustal anatexis: constraints from Himalayan leucogranites. Chemical Geology, v.139, p.249-269.

Bea, F. (1996) Residence of REE, Y, Th and U in granites and crustal protoliths: implications for the chemistry of crustal melts. Journal of Petrology, v. 37, p. 521-552.

Coleman, M.E. (1998) U-Pb constraints on Oligocene-Miocene deformation and anatexis within the central Himalaya, Marsyandi Valley, Nepal. American Journal of Science, v. 298, p. 553-571.

Catlos, E.J., Harrison, T.M., Kohn, M.J., Grove, M., Ryerson, F.J., Manning, C.E., Upreti, B.N. (2001) Geochronologic and thermobarometric constraints on the evolution of the Main Central Thrust, central Nepal Himalaya. Journal of Geophysical Research, v. 106, p. 16177-16204.

Copeland, P., Parrish, R.R., Harrison, T.M., (1988) Identification of inherited radiogenic Pb in monazite and its implications for U-Pb systematics. Nature, v. 333. p. 760-763.

Deniel, C., Vidal, Ph., Fernandez, A., Le Fort, P., Peucat, J.-J. (1987) Isotopic study of the Manaslu granite (Himalaya, Nepal): inferences on the age and source of Himalayan leucogranites. Contributions to Mineralogy and Petrology, v. 98, p. 78-92.

Dietrich, V., Gansser, A. (1981) The leucogranites of the Bhutan Himalaya (Crustal anatexis versus mantle melting). Schweiz. mineral. petrogr. Mitt., v. 61, p. 177-202.

Ferrara, G., Lombardo, B., Tonarini, S. (1983) Rb/Sr geochonology of granites and gneisses from the Mount Everest region, Nepal Himalaya. Geologische Rundschau, v. 72, p. 119-136.

Ferrara, G., Lombardo, B., Tonarini, S., Turi, B. (1991) Sr, Nd and O isotopic characterization of the Gophu La and Gumburanjun leucogranites (High Himalaya). Schweiz. min. pet. Mitt. v. 71, p. 35-51.

Gratz, R., Heinrich, W. (1997) Monazite-xenotime thermobarometry: experimental calibration of the miscibility gap in the binary system $CePO_4$-$YPO_4$. American Mineralogist, v. 82, p. 772-780.

Guillot, S., Le Fort, P. (1995) Geochemical constraints on the bimodal origin of the High Himalayan leucogranites. Lithos, v. 35, p. 221-234.

Harris, N., Ayres, M. (1998) The implications of Sr-isotope disequilibrium for rates of prograde metamorphism and melt extraction in anatectic terrains. In: Treloar, P.J, O'Brien, (eds) What Drives Metamorphism and Metamorphic Reactions? Geological Society, London, Special Publications, v. 138, p. 171-182.

Harris, N., Ayres, M., Massey, J. (1995) Geochemistry of granitic melts produced during the incongruent melting of muscovite: Implications for the extraction of Himalayan leucogranite magmas. Journal of Geophysical Research, v.106, p.15,767-15,777.

Harris, N., Inger, S. (1992) Trace element modelling of pelite-derived granites. Contributions to Mineralogy and Petrology, v. 110, p. 46-56.

Harrison, T.M., Grove, M., McKeegan, K.D., Coath, C.D., Lovera, O.M., Le Fort, P. (1999) Origin and episodic emplacement of the Manaslu intrusive complex, central Himalaya. Journal of Petrology, v. 40, p. 3-19.

Harrison, T.M., Watson, E.B. (1983) Kinetics of zircon dissolution and zirconium diffusion in granitic melts of variable water content. Contributions to Mineralogy and Petrology, v. 84, p. 66-72.

Hodges, K.V. (2000) Tectonics of the Himalaya and southern Tibet from two perspectives. Geological Society of America Bulletin, v. 112, p. 324-350.

Hodges, K., Bowring, S., Davidek, K., Hawkins, D., Krol, M. (1998) Evidence for rapid displacement on Himalayan normal faults and the importance of tectonic denudation in the evolution of mountain ranges. Geology, v. 26, p. 483-486.

Hodges, K.V., Parrish, R.R., Searle, M.P. (1996) Tectonic evolution of the central Annapurna Range, Nepalese Himalayas. Tectonics, v. 15, p. 1264-1291.

Hodges, K.V., Silverberg, D.S. (1988) Thermal evolution of the Greater Himalaya, Garhwal, India. Tectonics, v. 7, p. 583-600.

Inger, S., Harris, N (1993) Geochemical constraints on leucogranite mamgmatism in the Langtang Valley, Nepal, Himalaya. Journal of Petrology, v. 34, p. 345-368.

Knesel, K.M., Davidson, J.P. (2002) Insights into collisional magmatism from isotopic fingerprints of melting reactions. Science, v. 296, p. 2206-2208.

Le Fort, P., Cuney, M., Deniel, C., France-Lanord, C., Sheppard, S.M.F., Upreti, B.N., Vidal, P.(1987) Crustal generation of Himalayan leucogranites. Tectonophysics, v. 134, p. 39-57.

Montel, J.-M. (1993) A model for monazite/melt equilibrium and application to the generation of granitic magmas. Chemical Geology, v.110, p. 127-146.

Noble, S.R., Searle, M.P. (1995) Age of crustal melting and leucogranite formation from U-Pb zircon and monazite dating in the western Himalaya, Zanskar, India. Geology, v. 23, p. 1135-1138.

Parrish, R.R., Hodges, K.V. (1996) Isotopic constraints on the age and provenance of the Lesser and Greater Himalayan Sequences, Nepalese Himalaya. GSA Bulletin, v. 108, p. 904-911.

Paterson, B.A., Rogers, G., Stephens, W.E. (1992) Evidence for inherited Sm-Nd isotopes in granitoid zircons. Contributions to Mineralogy and Petrology, v.111, p.378-390.

Robinson, D.M., DeCelles, P.G., Patchett, P.J., Garzione, C.N. (2001) The kinetic evolution of the Nepalese Himalaya interpreted from Nd isotopes. Earth and Planetary Science Letters, v. 192, p. 507-521.

Scaillet, B., France-Lanord, C., Le Fort, P. (1990) Badrinath-Gangotri plutons (Garhwal, India): petrological and geochemical evidence for fractionation processes in a high Himalayan leucogranite. Journal of Volcanology and Geothermal Research, v. 44, p. 163-188.

Searle, M.P., Parrish, R.R., Hodges, K.V., Hurford, A., Ayres, M.W., Whitehouse, M.J. (1997) Shisha Pangma leucogranite, south Tibetan Himalaya: field relations, geochemistry, age, origin, and emplacement. Journal of Geology, v. 105, p. 295-317.

Simpson, R.L., Parrish, R.R., Searle, M.P., Waters, D.J. (2000) Two episodes of monazite crystallization during metamorphism and crustal melting in the Everest region of the Nepalese Himalaya. Geology, v. 28, p. 403-406.

Spear, F.S., Kohn, M.J., Cheney, J.T. (1999) P-T paths from anatectic pelites. Contributions to Mineralogy and Petrology, v. 134, p. 17-32.

Sun, S.-s., McDonough, W.F. (1989) Chemical and isotopic systematics of oceanic basalts: implications for mantle composition and processes. In Saunders, A.D., Norry, M.J. (eds.) Magmatism in the Ocean Basins, Geological Society Special Publication no.42, p. 313-345.

Thompson, A.B. (1982) Dehydration melting of pelitic rocks and the generation of $H_2O$ undersaturated granitic liquids. American Journal of Science, v. 282, p. 1567-1595.

Vidal, Ph., Bernard-Griffiths, J., Cocherie, A., Le Fort, P., Peucat, J.J., Sheppard, S.M.F. (1984) Geochemical comparison between Himalayan and Hercynian leucogranites. Physics of the Earth and Planetary Interiors, v. 35, p. 179-190.

Vidal, Ph., Cocherie, A., Le Fort, P. (1982) Geochemical investigations of the origin of the Manaslu leucogranite (Himalaya, Nepal). Geochim. Cosmochim. Acta v. 46, p. 2279-2292.

Viskupic, K., Hodges, K.V. (2001) Monazite-xenotime thermochronometry: methodology and an example from the Nepalese Himalaya. Contributions to Mineralogy and Petrology, v. 141, p. 233-247.

von Blanckenburg, F. (1992) Combined high-precision chronometry and geochemical tracing using accessory minerals: applied to the Central-Alpine Bergell intrusion (central Europe). Chemical Geology, v.100, p.19-40.

Walker, J.D., Martin, M.W., Bowring, S.A., Searle, M.P., Waters, D.J., Hodges, K.V. (1999) Metamorphism, melting, and extension: Age constraints from the High Himalayan slab of southeast Zanskar and northwest Lahaul. Journal of Geology, v. 107, p. 473-495.

Wark, D.A., Miller, C.F. (1993) Accessory mineral behavior during differentiation of a granite suite: monazite, xenotime and zircon in the Sweetwater Wash pluton, southeastern California, U.S.A., Chemical Geology, v. 110, p. 49-67.

Wolf, M.B., London, D. (1995) Incongruent dissolution of REE- and Sr-rich apatite in peraluminous granitic liquids: Differential apatite, monazite, and xenotime solubilities during anatexis. American Mineralogist, v.80, p. 765-775.

Table 1. Hypothetical contributions of minerals to a whole rock Nd and Sm budget.

| Mineral | Sm (ppm)[a] | Nd (ppm)[a] | Sm/Nd | $^{147}Sm/^{144}Nd$ | wt% in gneiss [b] | % of WR Nd | % of WR Sm | $^{143}Nd/^{144}Nd$ t=20Ma[c] |
|---|---|---|---|---|---|---|---|---|
| monazite | 19530 | 95000 | 0.206 | 0.130 | 0.032 | 98 | 94 | 0.511896 |
| xenotime | 3300 | 3000 | 1.10 | 0.696 | 0.004 | 0.39 | 2.0 | 0.513489 |
| apatite | 198 | 412 | 0.481 | 0.304 | 0.03 | 0.40 | 0.90 | 0.512386 |
| zircon | 3.0 | 5.9 | 0.514 | 0.325 | 0.03 | 0.01 | 0.01 | 0.512445 |
| garnet | 1.2 | 0.3 | 4.14 | 2.62 | 10 | 0.09 | 1.7 | 0.518897 |
| biotite | 0.21 | 0.42 | 0.500 | 0.316 | 12 | 0.16 | 0.38 | 0.512420 |
| plagioclase | 0.11 | 0.63 | 0.176 | 0.111 | 16 | 0.32 | 0.27 | 0.511843 |
| K-feldspar | 0.11 | 0.38 | 0.289 | 0.183 | 2 | 0.02 | 0.03 | 0.512046 |
| muscovite | 0.08 | 0.29 | 0.276 | 0.174 | 26 | 0.24 | 0.31 | 0.512021 |
| quartz | 0 | 0 | - | - | 28 | 0 | 0 | - |
| silimanite | 0 | 0 | - | - | 5 | 0 | 0 | - |
| Whole Rock | 6.6 | 31 | 0.214 | 0.136 | 99.1 | | | 0.511909 |

(a) Mineral compositions from Bea (1996), Ayres (1997), Ayres and Harris (1997), and this work

(b) weight % of each mineral in a hypothetical source rock gneiss having 31 ppm Nd and 6.6 ppm Sm

(c) Nd isotopic composition of each mineral at 20 Ma assuming the minerals last equilibrated with a whole rock $^{143}Nd/^{144}Nd$ ratio of 0.51153 at t=450 Ma (see Fig. 5). Typical errors in $^{143}Nd/^{144}Nd$ are ± 0.000012

Table 2 . Summary of rock types and previous geochronology

| Sample | Outcrop | Location [a] | Lithology [b] | Dates (Ma)[c] | Age[c] | Inheritance [c] |
|---|---|---|---|---|---|---|
| 01SK30 | MCT zone | MCT zone | pellitic gneiss | 23.4 | min age metamorphism | n.d |
| 98E5 | Namche | mid-upper GHS | migmatitic orthogneiss | 25 | onset of in situ melting | m, x ca. 460 Ma |
| 98E6 | Namche | mid-upper GHS | 2m+tur granite | 18.0 | dike crystallization | none |
| 00SK08 | Gokyo Ri | upper GHS | 2m granite sill | 18.4 | min age dike crystallization | none |
| 00SK09 | Gokyo Ri | upper GHS | 2m granite sill | 21.8 | sill crystallization | none |
| 00SK10 | Gokyo Ri | upper GHS | bt+tur granite | 18.3 | sill crystallization | m ca. 440 Ma |
| 01SK53 | 5th Lake | upper GHS | augen orthogneiss | 19 | latest metamorphism | none |
| 01SK54 | 5th Lake | upper GHS | bt granite | 21.3 | sill crystallization | z, Ordovician |
| 01SK55 | 5th Lake | upper GHS | bt+tur granite | 17.5 | min age dike crystallization | m ca. 500 Ma |

(a) MCT= Main Central Thrust, GHS= Greater Himalayan sequence

(b) 2m= 2 mica

(c) For discussion of geochronology and its interpretation, see Viskupic and Hodges (2001) and Viskupic (Chapter 3)

Table 3 . Whole rock geochemical data.

| | Gneisses | | | Leucogranites | | | |
|---|---|---|---|---|---|---|---|
| | 01SK30 | 98E5 | 01SK53 | 98E6 | 00SK09 | 01SK54 | 01SK55 |
| Major elements (wt.%) [a] | | | | | | | |
| $SiO_2$ | 65.89 | 67.29 | 73.38 | 72.91 | 74.53 | 75.54 | 73.28 |
| $Al_2O_3$ | 17.69 | 15.10 | 12.80 | 14.83 | 15.14 | 13.26 | 14.86 |
| $Fe_2O_3$ | 5.53 | 5.99 | 3.34 | 1.26 | 0.58 | 0.31 | 0.15 |
| MnO | 0.146 | 0.066 | 0.046 | 0.024 | 0.004 | 0.006 | 0.002 |
| MgO | 1.52 | 2.65 | 0.82 | 0.31 | 0.42 | 0.08 | 0.06 |
| CaO | 0.55 | 1.13 | 1.55 | 0.77 | 1.07 | 0.70 | 0.71 |
| $Na_2O$ | 2.79 | 2.21 | 2.65 | 3.52 | 6.32 | 2.62 | 2.98 |
| $K_2O$ | 3.35 | 3.45 | 4.70 | 4.70 | 0.93 | 6.86 | 7.66 |
| $TiO_2$ | 0.728 | 0.756 | 0.513 | 0.156 | 0.096 | 0.045 | 0.024 |
| $P_2O_5$ | 0.10 | 0.14 | 0.11 | 0.16 | 0.07 | 0.08 | 0.05 |
| LOI | 1.92 | 1.50 | 0.44 | 1.04 | 0.54 | 0.31 | 0.27 |
| TOTAL | 100.21 | 100.28 | 100.35 | 99.67 | 99.68 | 99.80 | 100.03 |
| Trace elements (ppm) [b] | | | | | | | |
| Rb | 172 | 252 | 296 | 298 | 28 | 281 | 309 |
| Sr | 104 | 67 | 54 | 94 | 92 | 53 | 90 |
| Y | 40 | 35 | 58 | 13 | 17 | 15 | 3 |
| Zr | 231 | 199 | 246 | 48 | 22 | 37 | 0 |
| Nb | 19 | 16 | 19 | 15 | 11 | 6 | 4 |
| Cs | 10.9 | 11.6 | 11.1 | 27.0 | 3.2 | 3.8 | 5.4 |
| Ba | 699 | 311 | 638 | 343 | 137 | 690 | 492 |
| La | 45.5 | 40.2 | 48.5 | 12.3 | 7.8 | 6.8 | 2.5 |
| Ce | 88.6 | 75.2 | 91.4 | 23.2 | 13.0 | 13.2 | 3.5 |
| Pr | 11.5 | 9.48 | 11.4 | 2.93 | 1.43 | 1.71 | 0.38 |
| Nd | 41.5 | 33.8 | 39.5 | 10.2 | 4.5 | 5.8 | 1.2 |
| Sm | 8.3 | 7.0 | 8.2 | 2.4 | 1.1 | 1.6 | 0.3 |
| Eu | 1.52 | 1.14 | 1.06 | 0.61 | 0.71 | 0.71 | 0.83 |
| Gd | 7.2 | 6.3 | 7.7 | 2.2 | 1.4 | 1.6 | 0.3 |
| Tb | 1.2 | 1.1 | 1.4 | 0.4 | 0.4 | 0.4 | 0.0 |
| Dy | 7.0 | 6.4 | 9.2 | 2.1 | 2.4 | 2.5 | 0.5 |
| Ho | 1.5 | 1.3 | 2.0 | 0.4 | 0.5 | 0.5 | 0.0 |
| Er | 4.4 | 3.8 | 6.0 | 1.2 | 1.6 | 1.6 | 0.3 |
| Tm | 0.64 | 0.54 | 0.88 | 0.16 | 0.22 | 0.27 | 0.0 |
| Yb | 4.1 | 3.3 | 5.3 | 1.0 | 1.4 | 1.8 | 0.3 |
| Lu | 0.58 | 0.48 | 0.76 | 0.14 | 0.19 | 0.29 | 0.0 |
| Hf | 6.6 | 5.8 | 7.3 | 1.8 | 0.8 | 2.4 | 0.0 |
| Ta | 1.3 | 1.4 | 1.6 | 4.4 | 0.0 | 0.1 | 0.2 |
| Pb | 17 | 25 | 21 | 16 | 24 | 27 | 32 |
| Th | 15.6 | 15.4 | 28.2 | 5.3 | 0.9 | 5.3 | 0.4 |
| U | 3.1 | 4.3 | 7.0 | 3.4 | 1.5 | 12.7 | 1.5 |
| $T_{zrn}$ (°C) [c] | | | | 704 | 648 | 675 | 475 |
| $T_{mnz}$ (°C) [d] | | | | 713 | 665 | 649 | 573 |

(a) Major elements determined by XRF
(b) Trace elements determined by ICPMS
(c) Zircon saturation temperature calculated from Harrison and Watson (1983)
(d) Monazite saturation temperature calculated from Montel (1993)

Table 4 . Nd isotopic data for monazites, xeotimes, and whole rock samples.

| Sample | grain [a] | age [b] (Ma) | t (Ma) [c] WR age | $^{147}Sm$ [d] / $^{144}Nd$ | $^{143}Nd$ / $^{144}Nd(o)$ | 2σ err | Epsilon Nd(o) | $^{143}Nd$ [e] / $^{144}Nd(t)$ | Epsilon [e] Nd(t) |
|---|---|---|---|---|---|---|---|---|---|
| MCT zone | | | | | | | | | |
| 01SK30 | m1 | 24.7 | 23.4 | 0.130* | 0.512198 | ±10 | -8.6 | 0.512178 | -8.4 |
| 01SK30 | m2 | 23.4 | 23.4 | 0.130* | 0.512156 | ±12 | -9.4 | 0.512136 | -9.2 |
| 01SK30 | WR | 23.4 | 23.4 | 0.106 | 0.512192 | ±10 | -8.7 | 0.512176 | -8.4 |
| Namche Bazaar | | | | | | | | | |
| 98E5 | m1 | 25.4 | 22.0 | 0.130* | 0.511924 | ±28 | -13.9 | 0.511905 | -13.7 |
| 98E5 | m5a | 250 | 22.0 | 0.130* | 0.511909 | ±16 | -14.2 | 0.511890 | -14.0 |
| 98E5 | m5b | 452 | 22.0 | 0.130* | 0.511924 | ±10 | -13.9 | 0.511905 | -13.7 |
| 98E5 | m6 | 22.2 | 22.0 | 0.130* | 0.511906 | ±16 | -14.3 | 0.511888 | -14.1 |
| 98E5 | m7 | 450 | 22.0 | 0.130* | 0.511924 | ±50 | -13.9 | 0.511905 | -13.7 |
| 98E5 | m9 | 24.7 | 22.0 | 0.130* | 0.511911 | ±16 | -14.2 | 0.511892 | -14.0 |
| 98E5 | m10 | 25.7 | 22.0 | 0.130* | 0.511909 | ±20 | -14.2 | 0.511890 | -14.0 |
| 98E5 | x12 | 23.3 | 22.0 | 0.684* | 0.512025 | ±18 | -12.0 | 0.511924 | -13.4 |
| 98E5 | x13 | 28.4 | 22.0 | 0.684 | 0.512023 | ±12 | -12.0 | 0.511925 | -13.4 |
| 98E5 | WR | 22.0 | 22.0 | 0.123 | 0.511894 | ±10 | -14.5 | 0.511876 | -14.3 |
| 98E6 | m1 | 18.8 | 17.6 | 0.130* | 0.511881 | ±12 | -14.8 | 0.511866 | -14.6 |
| 98E6 | m2 | 17.9 | 17.6 | 0.130* | 0.511870 | ±52 | -15.0 | 0.511855 | -14.8 |
| 98E6 | m3 | 17.8 | 17.6 | 0.130* | 0.511844 | ±75 | -15.5 | 0.511829 | -15.3 |
| 98E6 | m12 | 18.1 | 17.6 | 0.127 | 0.511819 | ±12 | -16.0 | 0.511804 | -15.8 |
| 98E6 | x6 | 17.6 | 17.6 | 0.857 | 0.511997 | ±20 | -12.5 | 0.511898 | -14.0 |
| 98E6 | WR | 17.6 | 17.6 | 0.141 | 0.511887 | ±10 | -14.6 | 0.511871 | -14.5 |
| Gokyo Ri | | | | | | | | | |
| 00SK08 | m8 | 17.5 | 17.5 | 0.130* | 0.511852 | ±10 | -15.3 | 0.511837 | -15.2 |
| 00SK09 | m4 | 18.3 | 21.8 | 0.130* | 0.511910 | ±14 | -14.2 | 0.511891 | -14.0 |
| 00SK09 | x6a | 24.6 | 21.8 | 1.06 | 0.512054 | ±14 | -11.4 | 0.511903 | -13.8 |
| 00SK09 | x9 | 24.2 | 21.8 | 1.07 | 0.512072 | ±12 | -11.0 | 0.511920 | -13.5 |
| 00SK09 | WR | 21.8 | 21.8 | 0.156 | 0.511892 | ±11 | -14.6 | 0.511870 | -14.4 |
| 00SK10 | m10 | 135 | 18.3 | 0.130* | 0.511814 | ±14 | -16.1 | 0.511798 | -15.9 |
| 00SK10 | m11 | 327 | 18.3 | 0.130* | 0.511863 | ±25 | -15.1 | 0.511847 | -15.0 |
| 00SK10 | m12 | 593 | 18.3 | 0.130* | 0.511834 | ±12 | -15.7 | 0.511818 | -15.5 |
| Gokyo's 5th Lake | | | | | | | | | |
| 01SK53 | m9 | 18.7 | 18.7 | 0.130* | 0.512104 | ±10 | -10.4 | 0.512088 | -10.3 |
| 01SK53 | WR | 18.7 | 18.7 | 0.125 | 0.512087 | ±10 | -10.7 | 0.512072 | -10.6 |
| 01SK54 | m7 | 21.3 | 21.3 | 0.130* | 0.512159 | ±15 | -9.4 | 0.512140 | -9.2 |
| 01SK54 | WR | 21.3 | 21.3 | 0.168 | 0.512294 | ±10 | -6.7 | 0.512271 | -6.6 |
| 01SK55 | m6 | 18.2 | 17.5 | 0.130* | 0.512004 | ±10 | -12.4 | 0.511989 | -12.2 |
| 01SK55 | m7 | 18.0 | 17.5 | 0.130* | 0.512034 | ±10 | -11.8 | 0.512020 | -11.6 |
| 01SK55 | WR | 18.0 | 17.5 | 0.148 | 0.512018 | ±20 | -12.1 | 0.512001 | -12.0 |

(a) Grains are labeled "m" for monazite and "x" for xenotime. WR is the whole rock.

(b) Ages from Viskupic (Chapters 1 and 2). Ages for inherited grains are the approximate upper intercept ages. Monazites from sample 01SK30 have not yet been dated; n.d. = not determin

(c) Whole rock crystallization ages used to calculate $^{143}Nd/^{144}Nd$ (t)for comparison of mineral isotopic signatures

(d) Internal errors in measured $^{147}Sm/^{144}Nd$ are <0.1% (2σ s.d.). Numbers with "*" indicate estimated values based on other grains analyzed during this study.

(e) Calculated at the whole rock crystallization ages for each sample

Table 5 . Sr isotopic data for whole rocks and apatites.

| Sample | grain [a] | $^{87}Rb/^{86}Sr$ | $^{87}Sr/^{86}Sr$ | 2s err | $^{87}Sr/^{86}Sr(t)$ [b] |
|---|---|---|---|---|---|
| MCT zone | | | | | |
| 01SK30 | a1 | | 0.76702 | ±3 | |
| 01SK30 | a2 | | 0.76813 | ±3 | |
| 01SK30 | a3 | | 0.77364 | ±2 | |
| 01SK30 | a4 | | 0.77008 | ±2 | |
| Namche Bazaar | | | | | |
| 98E5 | a1 | | 0.76830 | ±3 | |
| 98E5 | a2 | | 0.76921 | ±2 | |
| 98E5 | a4 | | 0.76697 | ±3 | |
| 98E5 | WR | 10.6 | 0.77196 | ±2 | 0.76864 |
| Gokyo Ri | | | | | |
| 00SK09 | a1 | | 0.75852 | ±2 | |
| 00SK09 | a2 | | 0.75760 | ±2 | |
| 00SK09 | a3 | | 0.75740 | ±3 | |
| 00SK09 | WR | 0.859 | 0.75767 | ±2 | 0.75740 |
| 5th Lake | | | | | |
| 01SK54 | a1 | | 0.80149 | ±5 | |
| 01SK54 | a2 | | 0.80980 | ±6 | |
| 01SK54 | a3 | | 0.80606 | ±3 | |
| 01SK54 | a4 | | 0.81592 | ±2 | |
| 01SK54 | a5 | | 0.80728 | ±12 | |
| 01SK55 | a1 | | 0.77705 | ±2 | |
| 01SK55 | a2 | | 0.77709 | ±2 | |
| 01SK55 | a3 | | 0.77603 | ±3 | |
| 01SK55 | a4 | | 0.77693 | ±2 | |
| 01SK55 | a5 | | 0.77697 | ±2 | |

(a) Samples are labeled "a" for apatite and WR for the whole rock.
(b) Ratios calculated at the whole rock crystallization ages given in Table 2.

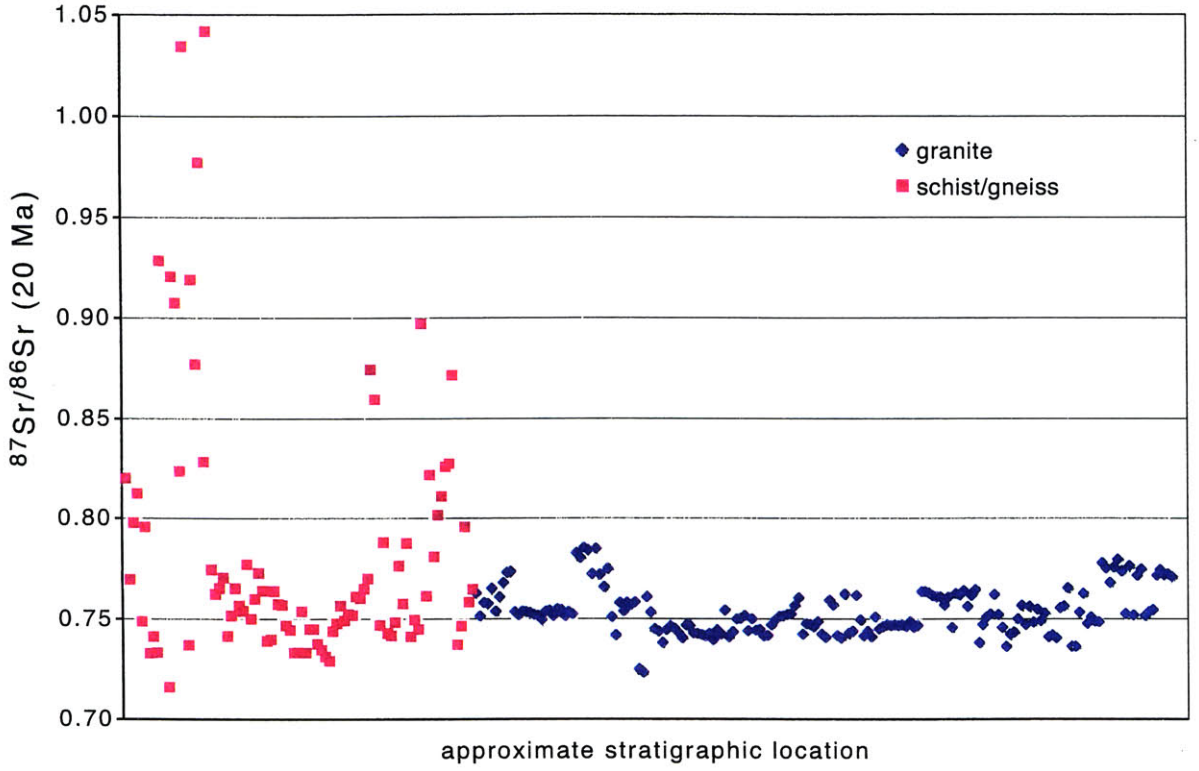


**Figure 1.** Sr isotopic signatures at 20 Ma for Greater Himalayan sequence schists, gneisses, and leucogranites. The x-axis roughly refers to stratigraphic location with the base of the Greater Himalayan sequence at the left, and the High Himalayan leucogranite at the top of the Greater Himalayan sequence at the right. Analyses from: Dietrich & Gansser (1981), Vidal et al. (1982), Ferrara et al. (1983), Deniel et al. (1987), Scaillet et al. (1990), Ferrara et al. (1991), Inger & Harris (1993), Ayres (1997), Searle et al. (1997), Ahmad et al. (2000).

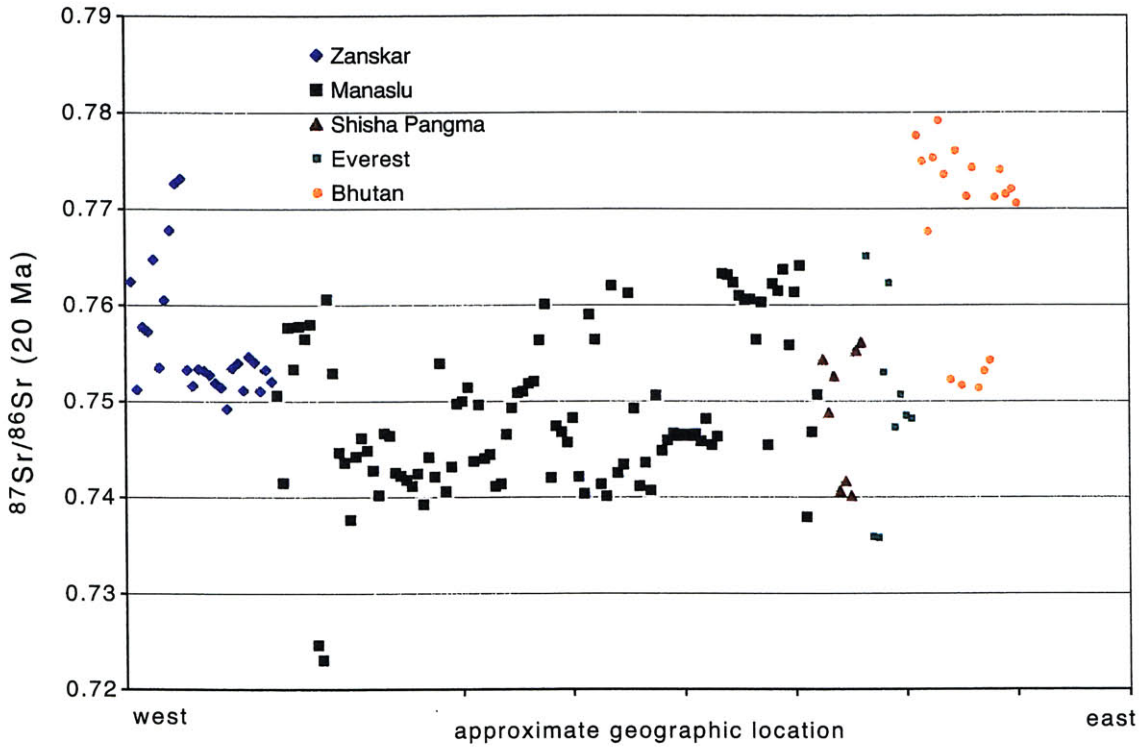


**Figure 2.** Sr isotopic signatures at 20 Ma for the High Himalayan leucogranites. X-axis refers roughly to geographic location from the western Himalaya on the left to the eastern Himalaya on the right. References in the caption of Figure 1.

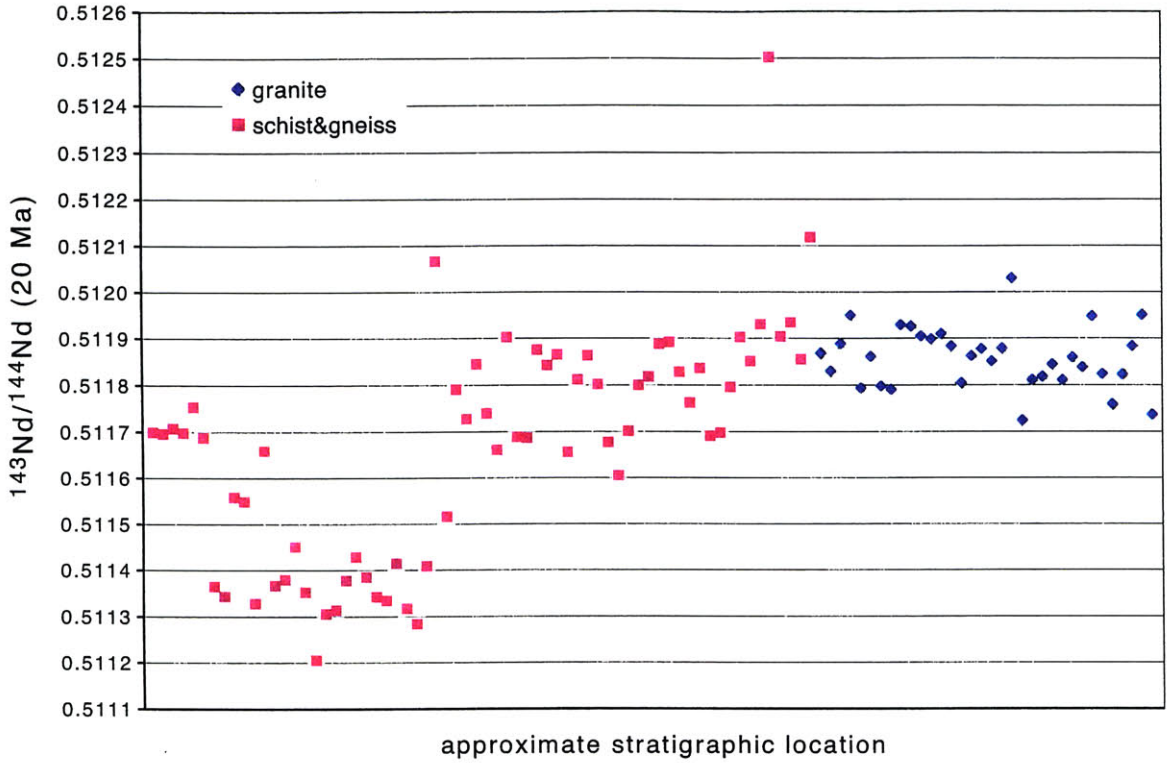


**Figure 3.** Nd isotopic signatures calculated at 20 Ma for Greater Himalayan sequence schists, gneisses, and leucogranites. The x-axis refers to the approximate stratigraphic location of the analyses, starting with the Lesser Himalayan sequence at the left, and ending with the High Himalayan leucogranites at the right. Analyses from: Vidal et al. (1984), Deniel et al. (1987), Ferrara et al. (1991), Inger & Harris (1993), Parrish & Hodges,(1996), Searle et al. (1997), Ahmad et al. (2000), Robinson et al. (2001).

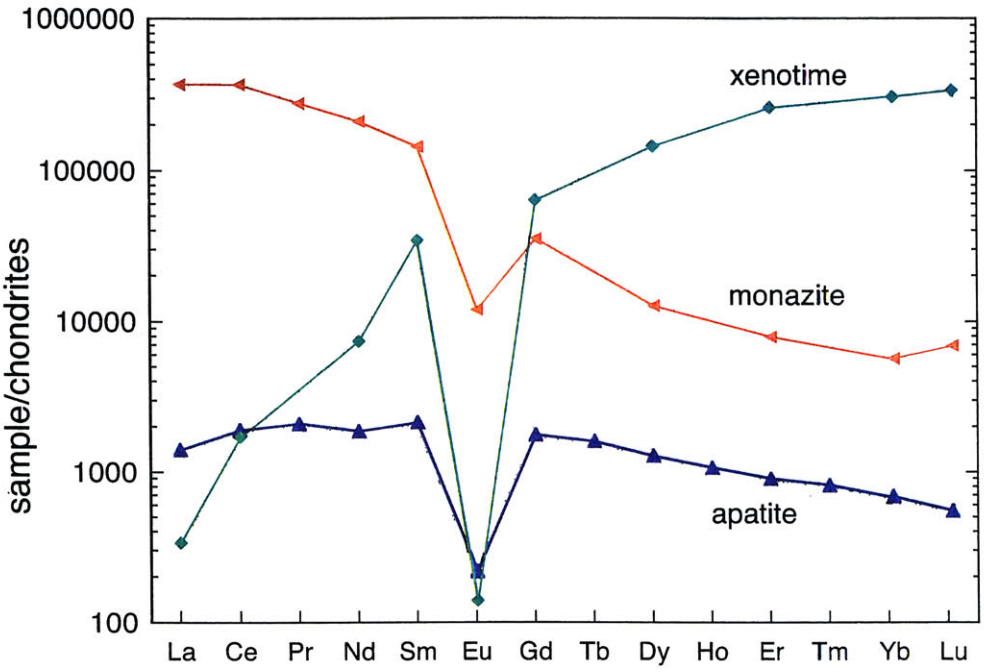


**Figure 4.** Representative REE diagrams for monazite, xenotime, and apatite. Analyses from Bea (1996) for grains from a two mica granite. Chondrite values from Sun and McDonough (1989).

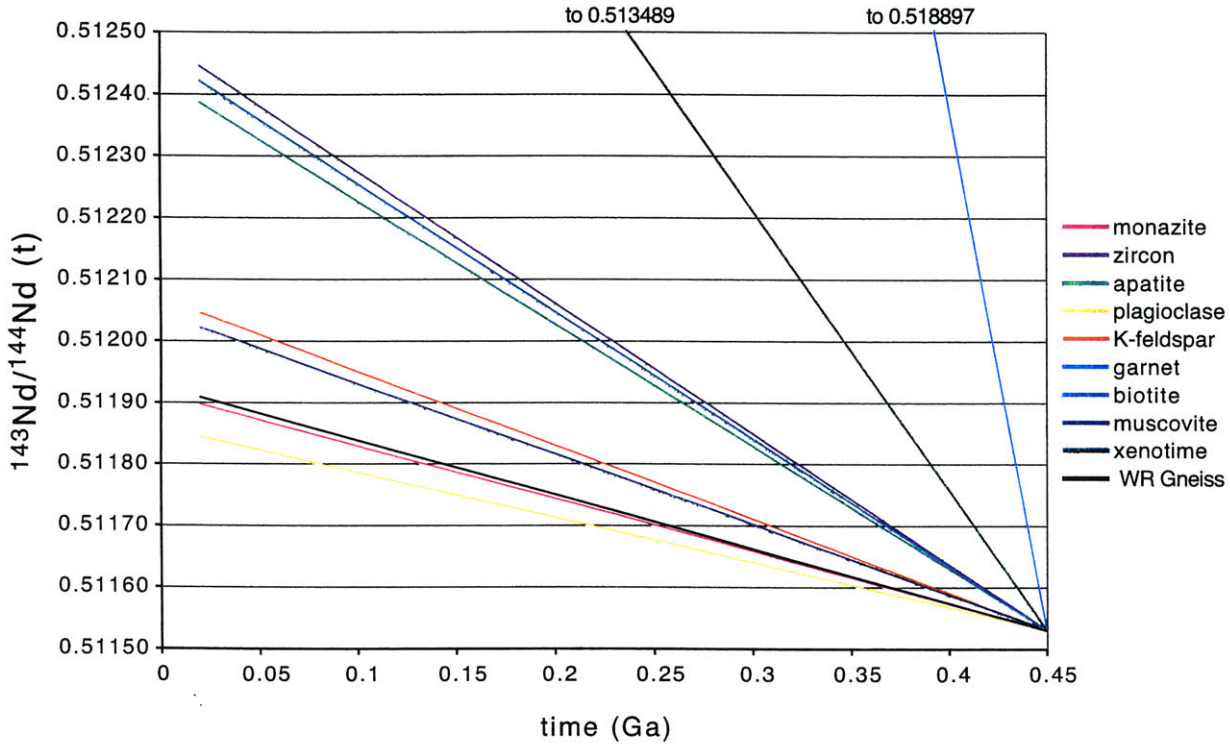


**Figure 5.** Nd isotopic evolution of the whole rock gneiss and its constituate minerals described in Table 1. All phases were in equilibrium at 450 Ma with a $^{143}Nd/^{144}Nd$ ratio of 0.51153.

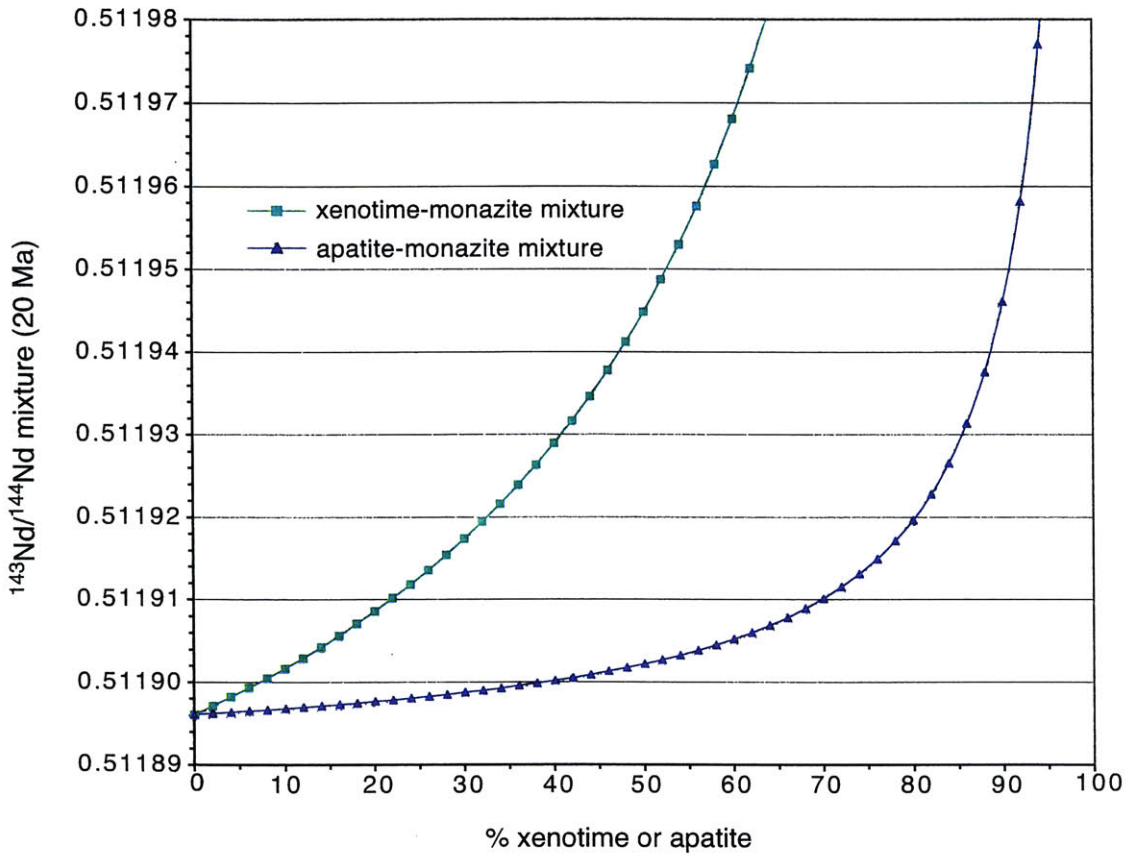


**Figure 6.** Model predicting the $^{143}Nd/^{144}Nd$ ratio of mixtures resulting from the combination of low Sm/Nd monazite with higher Sm/Nd apatite or xenotime. Details of model in text. Mineral compositions are from Table 1.

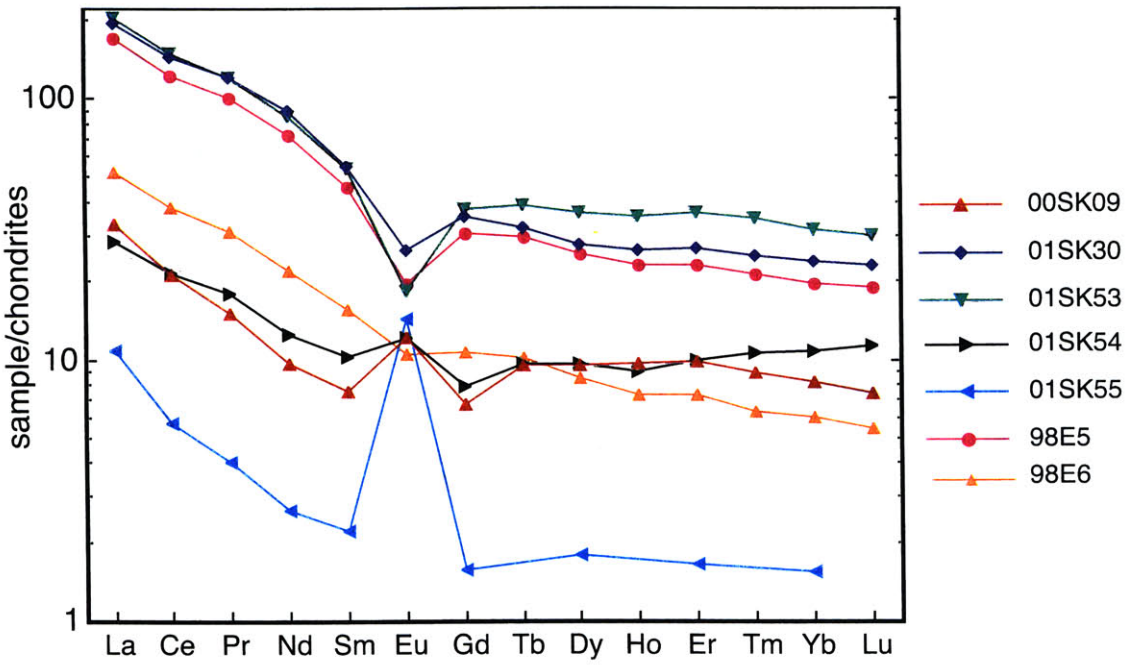


**Figure 7**. REE diagrams for whole rock leucogranite and gneiss samples. Chondrite values from Sun and McDonough (1989).

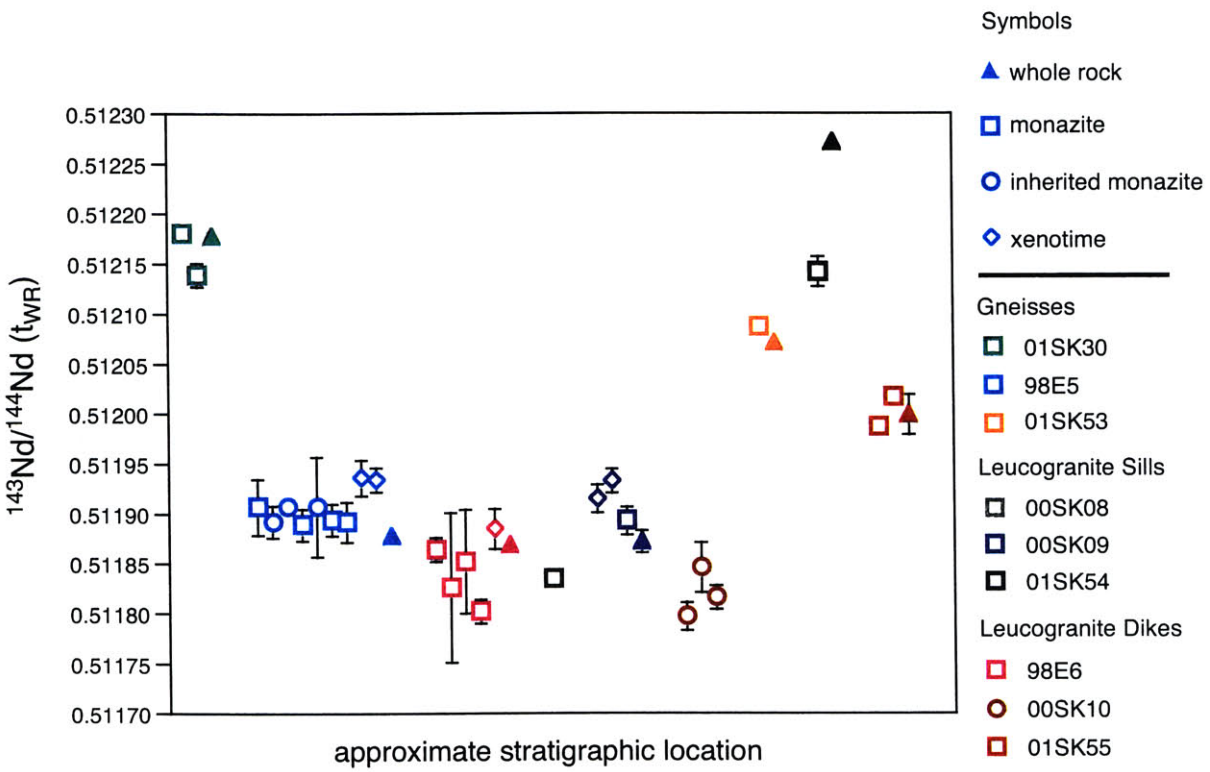


**Figure 8.** $^{143}Nd/^{144}Nd$ ratios calculated at the whole rock ages given in Table 2. Samples are ordered from lowest structural level on the left to highest structural level on the right.

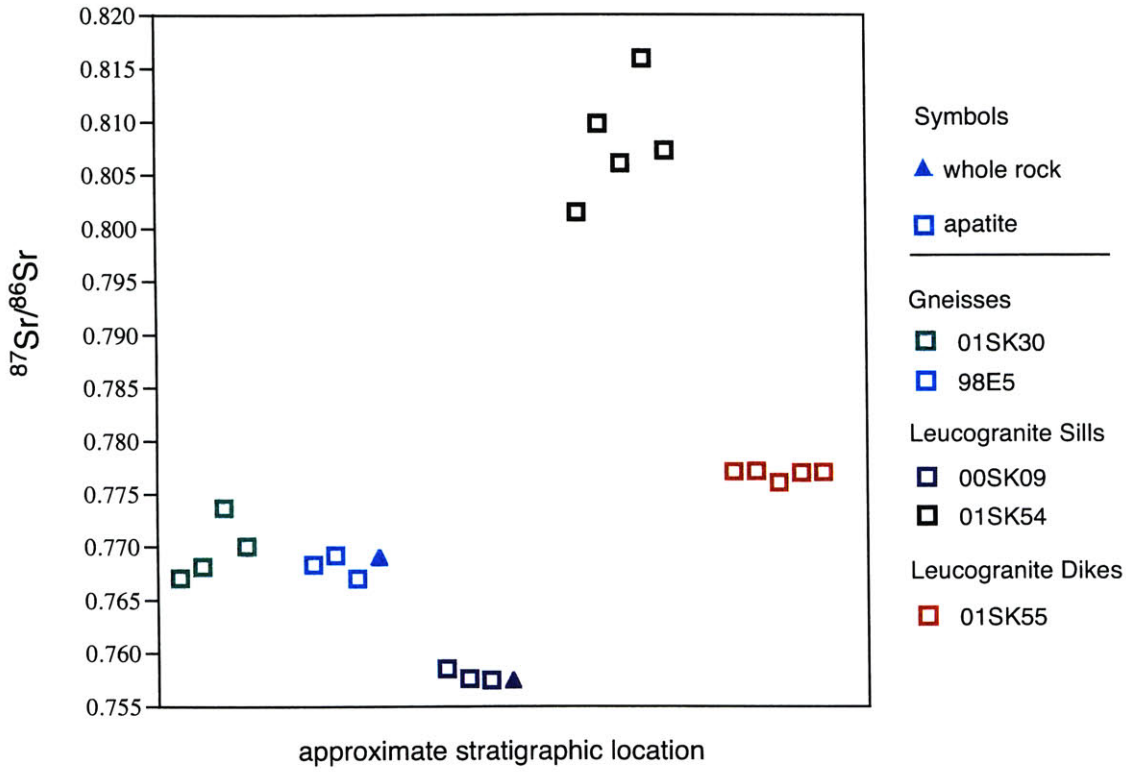


**Figure 9.** $^{87}Sr/^{86}Sr$ ratios calculated at whole rock ages given in Table 2 for each sample, and reported at 0 Ma for single apatites.

# Chapter 4

## Timescales of Melt Production in the Himalayan Orogen: A Review of Himalayan Leucogranite U-Th-Pb Age Determinations


### Abstract

Crustal anatexis is an important process during collisional orogenesis, but the timescales of melt generation, segregation, and transport are difficult to constrain. This paper is a comprehensive review of U-Th-Pb geochronologic studies of Himalayan leucogranites that, in some cases, involves new geochronological interpretations based on current knowledge about diffusive Pb loss, inheritance of xenocrystic accessory phases, and accessory phase growth. The resulting compilation of data highlights the semi-continuous crystallization of Himalayan leucogranites over a broad time interval from ca. 26 Ma to ca.16 Ma with additional crystallization at ca. 14 Ma and ca. 12 Ma. This protracted period of melt crystallization suggests that anatectic temperatures in the metamorphic core of the orogen were episodically reached or maintained over a period of at least 10 million years.


### Introduction

One of the Himalayan orogen's most defining features is a discontinuous chain of plutons and batholiths that extend along the crest of the range for nearly 2000 km (Figure 1). In addition to these plutons, the mid-upper structural level gneisses of the Himalayan metamorphic core host an extensive network of leucogranitic dikes and sills, as well as migmatitic leucosomes, making granitic rocks a ubiquitous part of the metamorphic core of the orogen known as the Greater Himalayan Sequence. The Greater Himalayan Sequence is tectonically bound below by north-dipping reverse faults of the Main Central Thrust (MCT) system, and above by north-dipping

primarily normal faults of the South Tibetan Fault (STF) system (Figure 1). Most theories of melt generation for the Himalayan leucogranites focus on the thermal consequences of movement on these two major fault systems. Some emphasize fluxing of melting by fluid infiltration associated with thrusting and metamorphism along the MCT (Le Fort, 1981; Le Fort et al., 1987; France-Lanord et al., 1998). Others emphasize the role of shear heating along the MCT (Arita, 1983; Molnar et al., 1983; Molnar & England, 1990; England et al., 1992; England & Molnar, 1993; Harrison et al., 1998). Noting that tectonic denudation associated with slip on the STF system was substantial, some researchers have suggested that the leucogranites are the products of decompression melting (e.g., Harris & Massey, 1994). Not all models of Himalayan anatexis depend directly on slip along the STF and MCT systems, however. The accretion of rocks with unusually high concentrations of radioactive heat producing elements to the base of the Himalayan orogenic wedge could have played an important role in generating the high geothermal gradients necessary for melting of the middle crust (e.g., Huerta et al., 1996). Moreover, it has been suggested that the focusing of heat due to contrasts in thermal conductivity between the Greater Himalayan Sequence and overlying unmetamorphosed rocks, a second-order effect of juxtaposition of the footwall and hangingwall of the STF system, may have influenced the localization of anatectic melts (Pinet & Jaupart, 1987).

The commonly inferred relationship between tectonic activity and anatexis in the Himalaya emphasizes the need to understand the timescales of melt generation in order to understand the tectonic evolution of the orogen. Unfortunately, the leucogranite products of this melting are notoriously difficult to date. Complications in geochronological data interpretation arise from the compounded effects of isotopic disequilibrium in low temperature melts, the incorporation of xenocrystic accessory minerals, the potential for protracted mineral growth, and

the often complex growth histories recorded in single accessory phase grains. As a consequence, many published "ages" for Himalayan granites are highly interpretive and were published over a time period when our understanding of isotopic systematics in granites was evolving rapidly.

The goal of this paper is to review geochronologic studies of the Himalayan leucogranites in the context of our current understanding of accessory phase isotopic systematics. The result substantially improves our understanding of the evolution of Himalayan anatexis in time and space, and helps inform future models of the thermal evolution of the orogen.

**Himalayan Leucogranite Characteristics**

Leucogranites in the Himalaya are present at all scales, from centimeter scale leucosomes, to batholithic bodies outcropping over tens of square kilometers. In general, the proportion of granitc rocks increases at structurally higher levels, with migmatitic leucosomes common in the lower Greater Himalayan Sequence, dikes and sills common in the middle to upper Greater Himalayan Sequence, and large plutons and batholiths outcropping near the top of the Greater Himalayan Sequence. Detailed mapping near the top of the Greater Himalayan Sequence has revealed that the granites are not restricted to the Greater Himalayan Sequence but have, in some cases, intruded into the overlying weakly to unmetamorphosed rocks of the Tibetan Sedimentary Sequence (Guillot et al., 1993; Vannay & Hodges, 1996; Hodges et al., 1996; Coleman, 1998). Crosscutting relationships show that multiple generations of leucogranites exist. The leucogranites generally contain the assemblage Qtz + Kfs + Pl + Ms ± Bt ± Tur ± Grt ± Sil ± Crd (mineral abbreviations after Kretz, 1983), and have sometimes been subdivided into three mineralogical groups: Ms + Bt granites with little or no tourmaline; Tur + Ms granites; and Ms + Bt + Tur granites (Scaillet et al., 1990; Hodges et al., 1993; Inger &

Harris, 1993; Guillot & Le Fort, 1995). There is little difference in major element chemistry between the three groups, and all samples contain 70-75 wt.% $SiO_2$ and >13 wt.% $Al_2O_3$.

**Geochronological Studies of Himalayan Leucogranites**

The earliest attempts to date Himalayan leucogranites relied on Rb-Sr (e.g. Hamet & Allegre, 1975; Ferrara et al., 1983) and K-Ar methods (e.g. Wager, 1965). The heterogeneity of Himalayan granite Sr isotopic compositions is well-documented (Vidal et al., 1982; Deniel et al., 1987; Scaillet et al., 1990), and today the Rb-Sr geochronologic technique is rarely employed for such studies because the high variability of $^{87}Sr/^{86}Sr$ initial ratios among the granites precludes the calculation of whole-rock isochron dates. Both K-Ar and $^{40}Ar/^{39}Ar$ techniques continue to be used principally for cooling history studies (Maluski et al., 1988; Hodges et al., 1994; Searle et al., 1997; Hodges et al., 1998; Searle et al.; 1999; Walker et al., 1999; Godin et al., 2001), with the exception of one attempt at indirect dating of the Manaslu pluton by dating rapidly cooled minerals in the contact aureole (Guillot et al., 1994).

The most useful method for determining crystallization ages of granitic rocks is U-Th-Pb dating of accessory minerals like zircon, monazite, and xenotime. As will be emphasized later in the paper, all three minerals have closure temperatures above typical magmatic temperatures for the Himalayan leucogranites (ca. 650-750°C, Clemens & Vielzeuf, 1987; Patino Douce & Harris, 1998; Scaillet et al., 1995), and therefore can robustly record crystallization ages. Dating leucogranites with the U-Th-Pb isotopic system is not without problems, however. The low temperatures of Himalayan anatexis, and the peraluminous chemistry of the resulting melts, often result in the incorporation of xenocrystic ("inherited") accessory phases in the leucogranites. Most leucogranites have such inherited zircon, many have inherited monazite (e.g. Copeland, et al., 1988), and a few have inherited xenotime (e.g. Viskupic & Hodges, 2001). Separating young

magmatic accessory phases from older xenocrystic components is one of the challenges of U-Th-Pb geochronology. Another challenge unique to young (Cenozoic) samples is initial U-Th disequilibrium caused by the incorporation of excess $^{230}$Th into Th-rich minerals such as monazite (Schärer, 1984). This excess $^{230}$Th decays to $^{206}$Pb causing discordance between $^{207}$Pb/$^{235}$U and $^{206}$Pb/$^{238}$U dates. The resulting analyses plot above the concordia curve and are said to be reversely or negatively discordant. Mattinson (1973) first introduced the concept of initial U-Th disequilibrium with a description of $^{230}$Th exclusion in Th-poor zircon. Thorium-poor xenotime can likewise have a deficit of $^{230}$Th leading to a deficit of $^{206}$Pb, although the degree of disequilibrium, and therefore the degree of discordance, in zircon and xenotime is much less than that for monazite. Zircon and xenotime, therefore, usually plot slightly below the concordia curve and are said to be normally or positively discordant. U-Pb dates can be corrected for disequilibrium by estimating the degree of U-Th fractionation between the mineral and melt (see Schärer, 1984, or Parrish, 1990 for a detailed discussion). More commonly, the $^{207}$Pb/$^{235}$U date is taken as the best estimate of the timing of crystallization since it is not affected by initial U-Th disequilibrium. Using $^{232}$Th-$^{208}$Pb systematics instead of U-Pb avoids the problem of U-Th disequilibrium.

Two main U-Th-Pb techniques have been used to date Himalayan leucogranites. Conventional isotope dilution thermal ionization mass spectrometry (IDTIMS) is used to determine $^{207}$Pb/$^{235}$U, $^{206}$Pb/$^{238}$U, and (less commonly) $^{208}$Pb/$^{232}$Th dates. Ion microprobe secondary ion mass spectrometry (IMSIMS) provides an alternative to IDTIMS that avoids the need to dissolve crystals and chemically separate U, Th, and Pb prior to analysis. Although IMSIMS can be used to determine $^{207}$Pb/$^{235}$U and $^{206}$Pb/$^{238}$U dates, most applications to

Himalayan samples have focused on $^{208}Pb/^{232}Th$ dating of monazite (e.g., Harrison et al., 1995; Harrison et al., 1999).

*Thermal Ionization Mass Spectrometry*

The advantages to using the IDTIMS technique are precision (approaching 0.1%), the variety of phases (monazite, zircon, xenotime, uraninite, sphene, apatite) routinely analyzed, and the ability to use two independent U-Pb decay chains ($^{235}U$-$^{207}Pb$ and $^{238}U$-$^{206}Pb$) to check for internal consistency. Even though young monazites usually show some degree of reverse discordance, the concordia construction and measurement of two independent U-Pb decay chains is extremely advantageous for identifying the presence of pre-Himalayan inheritance. If a monazite, xenotime, or zircon contains a pre-Himalayan inherited component, it will almost always show unusual normal discordance (unless the inherited component is extremely small, as may be the case in multigrain fractions where only one or two grains have inherited components).

The main disadvantage of the IDTIMS technique is low spatial resolution. Accessory phases are separated from a sample using heavy liquid and magnetic techniques and are then dissolved with an isotopic tracer. Often, multigrain fractions of minerals (especially zircon) are analyzed, although it is possible to precisely analyze fragments of single grains (e.g. Viskupic & Hodges, 2001). Lack of spatial resolution can be effectively compensated for with a combination of imaging and microsampling of single grains. Individual grains can be imaged using backscattered electron (BSE) imaging (monazite and xenotime) and cathodoluminescence imaging (zircon and xenotime) techniques either *in situ* (in thin section) or on grains mounted in epoxy resin. Imaging of grains allows their petrographic context to be explored and often gives

important clues about petrogenesis and the presence of inherited components that can aid U-Pb data interpretation (Hawkins & Bowring, 1997, 1999; Simpson et al. 2000, Viskupic & Hodges, 2001; Chapter 2). Examples of BSE images of Himalayan monazite and xenotime are shown in Figure 2. The xenotime and monazite in Figures 2a and 2b have irregularly shaped cores suggesting the presence of xenocrystic components, while the monazites in Figure 2c and 2d show sector zoning and oscillatory zoning, respectively, indicative of magmatic growth. Clearly high spatial resolution is advantageous and even necessary when trying to precisely date accessory phases such as those shown in Figures 2a and 2b.

It has recently been suggested that the U-Pb IDTIMS technique for dating monazite also suffers from instrumental limitations in an inability to precisely measure the small amounts of U in monazite (Catlos et al., 2001, 2002). For example, Catlos, et al. (2002) cite Overstreet (1967) in suggesting that U is rarely present in monazites in concentrations greater than 0.5 wt.%, which they argue is too little U to be measured by IDTIMS. However, several IDTIMS laboratories report precise measurements of U by IDTIMS in Tertiary monazite single crystals and crystal fragments (e.g. Viskupic & Hodges, 2001). Furthermore, U concentrations are much lower in zircons (typically only a few hundred ppm) than in monazites, yet U-Pb dating of zircons by IDTIMS is arguably the most precise method of dating available. For example, a 50μm x 50μm sphere with only 150 ppm U has enough U to measure at the 1 $^{0}/_{000}$ level.

*Ion Microprobe Secondary Ion Mass Spectrometry*

The main advantage of using the $^{208}Pb/^{232}Th$ IMSIMS technique for dating Himalayan monazites is its high spatial resolution—spot sizes are typically 10x15 μm (Harrison et al., 1995). Unfortunately, IMSIMS is much less precise than IDTIMS, reflecting an inevitable

tradeoff between high spatial resolution and high precision. The precision of IMSIMS is limited to $\geq$ 2% by the reproducibility of measurements on a standard monazite used to make a calibration curve (Harrison et al., 1995, 1999, 2002).

In an ideal IMSIMS study, BSE images of monazite grains in thin sections would be made in order to determine petrographic context and to help identify inherited components. The same grains would then be dated using IMSIMS. Unfortunately, in most published IMSIMS studies of Himalayan leucogranites, grains have been separated from the rock and mounted in epoxy resin much the same way grains are separated for IDTIMS analyses. If the grains are not imaged, spot analyses can overlap different age domains (e.g. Harrison et al., 1995; 1999) resulting in data that are difficult to interpret. Th-Pb monazite data also are difficult to interpret when the results from a single sample are inconsistent with a single population (Harrison et al., 2002). Since many Himalayan leucogranites contain inherited monazite, this is frequently the case.

**Case Studies**

The relative strengths and weaknesses of the techniques outlined above, as well as some of the general challenges in leucogranite geochronology, are highlighted in the following case studies of efforts to date Himalayan leucogranites. These studies were published over nearly 20 years. During those years, two important advances were made that changed the way U-Th-Pb accessory phase data are interpreted. The identification of inherited radiogenic Pb in monazite, and then in xenotime, reinforced the idea that accessory phases can be chemically zoned, complex minerals, that often need to be examined at the subgrain scale. More recently, experimental and empirical studies of Pb diffusion rates have demonstrated that closure

temperatures for Pb in monazite and xenotime are likely in excess of 1000°C (Cherniak et al., 2000; Kamber et al., 1998; Asami et al., 2002), making them similar to, or even higher than the closure temperature for Pb in zircon (Cherniak & Watson, 2000).

Figure 1 shows the locations of leucogranites discussed in the following case studies, and Table 1 shows IDTIMS and IMSIMS data for them. There is a discrepancy in the way errors in IDTIMS and IMSIMS data are reported in most publications containing Himalayan leucogranite data: IDTIMS data are traditionally reported at the ~95% confidence level, whereas IMSIMS data are usually reported at the ~68% confidence level. In order to avoid confusion, all errors have been quoted in this paper at the two standard deviations ($2\sigma$) level, or, in the case of average dates for multiple analyses, at the two standard errors of the mean (2SE) level. As always, the standard error of the mean is calculated as the standard deviation of a collection of averaged dates divided by the square root of the number of averaged dates.

*Manaslu Pluton*

The Manaslu pluton in Central Nepal is the most extensively studied of the Himalayan leucogranites (Le Fort, 1975, 1981; Vidal, 1982; Deniel, et al., 1987; France-Lanord et al., 1988; Guillot et al., 1993, 1994, 1995). The main body of the granite is a sheet approximately 10 km thick, with a much thinner sill, the "Chhokang arm", extending to the east for approximately 50 km. The base of the pluton is concordant with the foliation of the surrounding gneisses, and does not display a metamorphic aureole (Vidal, et al., 1982). The upper contact, however, is discordant with the surrounding Tibetan Sedimentary sequence and produced an amphibolite-facies contact aureole (Guillot et al., 1994).

The first attempt to date the Manalsu pluton using U-Th-Pb geochronology was made by Deniel et al. (1987) who analyzed one multigrain fraction of monazite by U-Pb IDTIMS, which had a $^{206}Pb/^{238}U$ date of 26.6 Ma and a $^{207}Pb/^{235}U$ date of 25.7 Ma. Based on this analysis, Deniel et al. (1987) suggested that magmatic activity began at 25.5 ± 0.5 Ma.

Another attempt to date the Manaslu pluton was made by Harrison et al. (1995) using the $^{208}Pb/^{232}Th$ IMSIMS dating technique. Harrison et al. (1995) made 28 IMSIMS analyses on 18 grains of monazite from a biotite + muscovite + tourmaline leucogranite collected near the base of the Manaslu pluton. Four spot analyses on one grain gave pre-Himalayan inherited ages > 560 Ma. The remaining 24 analyses ranged from 18.6 ± 2.0 Ma (2σ) to 25.6 ± 1.8 Ma (2σ) in a roughly normal distribution with a mean $^{208}Pb/^{232}Th$ date of 22.4 ± 0.5 Ma (2SE). This date is in agreement with the minimum crystallization age suggested by Guillot et al. (1994) on the basis of $^{40}Ar/^{39}Ar$ dating of hornblendes from the contact aureole of the pluton, and was interpreted by Harrison et al. (1995) as the crystallization age of the pluton. The large distribution of dates for individual $^{208}Pb/^{232}Th$ spot analyses was regarded as the consequence of analytical uncertainties alone based on the agreement of the weighted mean date (22.7 ± 0.3 Ma) with the unweighted mean date for the distribution (Harrison et al., 1995).

Harrison et al. (1999) conducted a more comprehensive IMSIMS study of the Manalsu pluton. They determined 158 Th-Pb dates on an unspecified number of monazites from 11 samples of both two-mica and two-mica + tourmaline leucogranites distributed throughout the Manaslu pluton on a scale of tens of kilometers. The data are not reported, but it appears that most of the measured dates ranged between ca. 17 Ma and ca. 37 Ma with a second distribution of dates that ranged between ca. 100 Ma and ca. 620 Ma. From these data, Harrison et al. (1999) distinguished two pulses of magmatism, the Larkya La and Bimtang phases, both of which

contain two-mica and two-mica + tourmaline granites. The Larkya La phase (7 samples) showed a bimodal distribution of dates, with Himalayan-aged dates as old as 38 Ma (the young end of range cannot be determined from the limited data reported), and pre-Himalayan dates ranging from 99 to 613 Ma. Attributing all dates older than ca. 31 Ma to the presence of inheritance led to the interpretation that the Larkya La phase crystallized at 22.9 ± 0.6 Ma (2SE). The Bimtang phase (4 samples) does not contain an obvious pre-Himalayan inherited component, and had a younger mean distribution of dates that ranged up to 33 Ma (young end of range cannot be determined). Dates older than 23 Ma were interpreted to result from overlap of the ion microprobe beam on both core and rim components or from diffusive Pb loss (Harrison et al., 1999), and the crystallization age of the Bimtang phase was interpreted to be 19.3 ± 0.3 Ma (2SE). Because such a large range of dates are preserved in Manaslu monazites, and because errors associated with individual IMSIMS spot analyses are large (ca. ± 1Ma) it is difficult to know whether the dates reflect episodic crystallization in discrete batches at ca. 23 and ca. 19 Ma, as suggested by Harrison et al. (1999), or whether they reflect a more protracted magmatic history.

*Rongbuk Granites*

Dating of granites from the Rongbuk Valley north of Mt. Everest has been controversial due to the debated relationship between the granites and the Qomolangma detachment, a strand of the STF. The most intensively studied granitic body from this area is the Rongbuk granite of Burchfiel et al. (1992), a weakly foliated, two mica + tourmaline granite that was mapped initially as a coherent pluton which cut the mylonitic foliation in footwall rocks of the Qomolangma detachment. Based on their observations and the presence of roof pendants of

Tibetan Sedimentary Sequence rocks within the granite (which contain skarn mineralization consistent with contact metamorphism), Burchfiel et al. (1992) concluded that the granite had intruded across the Qomolangma detachment and into its hanging wall. Burchfiel and coworkers collected sample Δ33 of the Rongbuk granite for U-Pb geochronology.

The first geochronologic study of Rongbuk granite Δ33 was published by Copeland et al. (1988), who used conventional IDTIMS to analyze multigrain fractions of monazite and zircon, as well as a few single zircon crystals. All of the zircon fractions, except for one single grain analysis, contained a pre-Himalayan inherited component. A single concordant zircon had an imprecise $^{206}Pb/^{238}U$ date of 19.5 ± 0.8 Ma. Three multigrain monazite fractions were highly normally discordant and had $^{207}Pb/^{206}Pb$ dates ranging from 157-417 Ma with an upper intercept of 471 ± 10 Ma (MSWD = 19.7; Wendt & Carl, 1991), demonstrating the existence of pre-Himalayan inherited monazite in the sample. The youngest monazite fraction was reversely discordant with a $^{207}Pb/^{235}U$ date of ca. 21Ma, while four other monazite fractions were reversely discordant with $^{207}Pb/^{235}U$ dates between 22 and 26 Ma. Based on these data, Copeland et al. (1988) regarded the crystallization age of the Rongbuk granite to be 20 ± 1 Ma, in agreement with the single concordant zircon and the youngest monazite fraction.

In an effort to further constrain the crystallization age of the Rongbuk granite, Hodges et al. (1992) analyzed four multigrain fractions of Δ33 xenotime by IDTIMS. All of the fractions were essentially concordant, with $^{207}Pb/^{235}U$ dates ranging from 20.6 ± 0.1 to 21.6 ± 0.1 Ma. Hodges et al. (1992) noted that $^{40}Ar/^{39}Ar$ and U-Pb cooling ages for nearby Greater Himalayan Sequence country rocks were younger than the youngest xenotime dates in the post-metamorphic Rongbuk granite, and suggested that the crystallization age of the granite was about 19.5 Ma (the

zircon date reported by Copeland et al., 1988), with the older xenotime dates representing varying degrees of inheritance.

Harrison et al. (1995) measured thirty IMSIMS Th-Pb dates on an unspecified number of Δ33 monazite grains. Although the data were not reported, a histogram of the $^{208}Pb/^{232}Th$ dates was shown, from which it appears that the dates ranged from 18 to 26 Ma, with two older single analyses at 29 and 37 Ma. The dominant peak in the histogram is at 22 Ma, but there is apparently another, smaller, peak at 26 Ma. From this complicated distribution of dates, Harrison et al. assumed that any analyses older than 25 Ma (there are 8 of them) were the result of inheritance. From the remaining 24 analyses, they calculated a mean date of 22 Ma with an uncertainty of about 2 Ma (2SE). Because xenotimes as old as 21.6 Ma had been reported earlier by Hodges et al. (1992), and apparently because they considered xenotime as unlikely to have been an inherited phase, Harrison et al. (1992) cited asymmetric uncertainty bounds of –0.5 and + 1.0 Ma for the age of Δ33.

Hodges et al. (1998) used U-Pb IDTIMS analyses of a granite sill that is cut across by the Rongbuk granite to place further constraints on its age of crystallization. Sample R113 is from a prominent 100-150m thick mylonitized granite sill exposed along the eastern wall of the Rongbuk valley for ~10 km (Hodges et al., 1998). The sill is about 200 m below the Qomolangma detachment, and the sill is cut by the Rongbuk granite (Hodges et al., 1992, 1998). Three multigrain monazite fractions, one single zircon, and five single xenotimes all yielded $^{207}Pb/^{235}U$ dates between 16.57 and 16.74 Ma. The weighted mean $^{207}Pb/^{235}U$ date for these nine analyses was 16.67 ± 0.04 Ma (MSWD=0.75), and was considered to be the crystallization age of the granite sill. Given the relative age relationships between the sill and the Rongbuk granite, this date also corresponded to a maximum age for the Rongbuk granite, leading Hodges et al.

(1998) to conclude that all previously dated monazite, xenotime, and zircon grains from Δ33 contained xenocrystic components.

Murphy and Harrison (1999) dated three granite samples from the Rongbuk Valley using IMSIMS: a mylonitic sill immediately beneath the Qomolangma detachment, a dike that had been deflected into parallelism with the shear zone foliation, and a "crosscutting dike" that presumably postdated the other two samples. Murphy and Harrison (1999) reported ten $^{208}Pb/^{232}Th$ dates for eight grains from a sample of the mylonitic sill (likely the same sill represented by sample R113 of Hodges et al., 1998), that ranged from 14.8 ± 0.6 Ma to 17.8 ± 0.4 Ma. From this distribution, they reported a crystallization age of 16.2 ± 0.8 Ma (2SE) for the sill. Thirteen analyses on 11 grains from the deflected dike ranged from 15.1 ± 0.4 Ma to 23.9 ± 0.8 Ma. A histogram of the data shows peaks at ~17 and ~23.5 Ma. Presumably attributing the older dates to inheritance, the authors interpreted the crystallization age of the deflected dike as 16.4 ± 0.6 Ma. The latest crosscutting dike was interpreted to have a crystallization age of 16.8 ± 0.8 Ma based on ten dates of ten grains that ranged from 15.2 ± 0.6 Ma to 19.6 ± 0.6 Ma.

Even without the controversy surrounding the geologic relationships in the Rongbuk Valley, the Δ33 data sets are difficult to interpret due to the wide range of U-Pb and Th-Pb dates reported. Perhaps the most comprehensive Δ33 geochronologic data set is an unpublished U-Pb IDTIMS study of monazite, xenotime, zircon, and uraninite by S.A Bowring and K.V. Hodges, which will be summarized here. Zircon is the only phase to clearly show the presence of pre-Himalayan inheritance with four multigrain fractions having $^{207}Pb/^{206}Pb$ dates that range from 297 to 499 Ma. One additional zircon fraction is essentially concordant with a $^{207}Pb/^{235}U$ date of 20.61 ± 0.8 Ma. Eight single grain xenotime fractions were analyzed. The oldest fraction has a $^{207}Pb/^{235}U$ date of 24.2 Ma, but is highly normally discordant, which could indicate the presence

of an inherited component. Six of the remaining seven xenotime analyses are essentially concordant with $^{207}Pb/^{235}U$ dates that range from 21.37 to 20.78 Ma. The youngest xenotime is normally discordant and has a $^{207}Pb/^{235}U$ date of 20.58 ± 0.08 Ma. All ten single grain monazite fractions analyzed are reversely discordant. The oldest has a $^{207}Pb/^{235}U$ date of 25.16 Ma. Three single monazites have $^{207}Pb/^{235}U$ dates that range from 23.2 to 23.6 Ma, and five others have $^{207}Pb/^{235}U$ dates that range from 21.68 to 21.18 Ma. The youngest monazite has a $^{207}Pb/^{235}U$ date of 20.51 ± 0.12 Ma. Thirteen single grains or grain fragments of uraninite also were analyzed. All analyses are normally discordant by approximately the same degree, forming a line subparallel to the concordia curve due to their spread in apparent ages. The oldest uraninite has an imprecise $^{207}Pb/^{235}U$ date of 22.14 ± 0.52. Another uraninite fragment has a $^{207}Pb/^{235}U$ date of 21.96 Ma. The remaining eleven analyses have $^{207}Pb/^{235}U$ dates that range from 21.20 to 20.30 Ma.

As a whole, the Δ33 data set of Bowring and Hodges (unpublished) shows a wide range of apparent ages for monazite, xenotime, uraninite, and zircon, with no obvious indication of what the crystallization age of Δ33 might be. The youngest monazite, xenotime, and zircon $^{207}Pb/^{235}U$ dates have a weighted mean of 20.57 ± 0.11 Ma (MSWD=1.02) suggesting a minimum age of crystallization if it is assumed that these accessory phases may have undergone diffusive Pb loss. Given the high closure temperatures for Pb in all three phases, and the concordance of $^{207}Pb/^{235}U$ dates for three analyses of three different accessory phases, this seems unlikely. The $^{207}Pb/^{235}U$ dates are therefore interpreted to represent crystallization ages of the minerals. In addition to monazite, xenotime, and zircon crystallization at 20.57 Ma, uraninite was also crystallizing, suggesting the melt was multiply saturated in P, LREE, HREE, U, and Zr. Although it seems reasonable to interpret the crystallization age of Δ33 to be 20.57 ± 0.11 Ma, it

is not the only possible interpretation of the data, especially given the constraint of Hodges et al. (1998) that Δ33 should be younger than 16.7 Ma. The saga of Δ33 illustrates the limitations of blind single grain analyses by U-Pb IDTIMS. Unfortunately, the data of Bowring and Hodges (unpublished) were obtained in the late 1990's before it became routine in the MIT lab to image grains selected for dating. Without such imformation, a robust interpretation of the crystallization age of the Rongbuk granite remains elusive.

*Zanskar, Gumburanjon*

The geology of the Gumburanjon leucogranite in southeast Zanskar was studied in detail by Walker et al. (1999) who used U-Pb geochronology by IDTIMS to determine the crystallization age of the pluton. Single grain analyses of four uraninites and two monazites from one sample of the main granite had $^{207}Pb/^{235}U$ dates that ranged from 21.2 to 21.8 Ma, with the uraninite being younger than the monazite. The weighted mean $^{207}Pb/^{235}U$ date of the uraninite, 21.4 ± 0.1 Ma (MSWD=1.3), was taken to be the crystallization age of the granite. Three additional monazites analyzed from this sample contained a ca. 460 Ma inherited component. A second sample of the main Gumburanjon leucogranite also contained inherited monazite, but two uraninites, one xenotime, and one monazite had a weighted mean $^{207}Pb/^{235}U$ date of 21.3 ± 0.1 Ma (MSWD=2.3) which agreed with U-Pb results from the first sample, and was taken to be the crystallization age of the granite. The crystallization age of a final leucogranite dike that cuts across the mylonitic fabric in the Zanskar Shear Zone (a local strand of the STF) was determined to be 22.1 ± 0.4 Ma, the weighted mean $^{207}Pb/^{235}U$ date of three monazite analyses. One additional monazite analysis contained an inherited component, and two normally discordant uraninite analyses had $^{207}Pb/^{235}U$ dates of 22.3 and 22.0 Ma, which are in

agreement with the weighted mean monazite date. Based on the results from these three samples, Walker et al. (1999) concluded that the Gumburanjon leucogranite was emplaced and crystallized ca. 21-22 Ma.

*Gangotri and Shivling*

Harrison et al. (1997) determined crystallization ages for the Gangotri and Shivling granites in the Garhwal Himalaya, India, of 22.4 ± 0.5 and 21.9 ± 0.5 Ma, respectively, using the Th-Pb IMSIMS technique. Unfortunately, only a summary table giving one representative analysis for each granite was reported, so this data cannot be further evaluated.

Searle et al. (1999) dated monazites from a two mica + tourmaline sample from the Shivling leucogranite by U-Pb IDTIMS. Three reversely discordant single grain euhedral monazite fractions had a weighted mean $^{207}Pb/^{235}U$ date of 23.0 ± 0.2 Ma (MSWD=0.3) which was taken to be the crystallization age of the granite. One additional reversely discordant euhedral single monazite analysis was slightly older, however, it contained visible inclusions and was interpreted to have an inherited component. A multigrain fraction of rounded monazites was concordant at ca. 36 Ma and was interpreted to be either an inherited metamorphic component from the source rock or a mixture of ca. 460 Ma inheritance and 23 Ma magmatic monazite (Searle, et al., 1999).

*Shisha Pangma and Nyalam*

The Shisha Pangma (Xixabangma) pluton of southern Tibet was studied in detail by Searle et al. (1997), and determined to be a heterogeneous polyphase intrusion with an earlier weakly foliated biotite rich phase, and a later muscovite and tourmaline rich phase. Samples

from both phases were dated using U-Th-Pb IDTIMS. A sample representative of the older phase was collected from a 0.5 m thick sheet immediately beneath the STF and had deformational fabrics associated with STF movement. Two zircon fractions contained pre-Himalayan inherited components and had $^{207}Pb/^{206}Pb$ dates of 205 and 748 Ma. Two reversely discordant single grain monazite analyses and one concordant multigrain xenotime analysis had $^{207}Pb/^{235}U$ dates that ranged from 20.11 ± 0.1 to 20.22 ± 0.09 Ma. Three additional multigrain xenotime analyses were essentially concordant, and had $^{207}Pb/^{235}U$ dates that ranged from 19.39 ± 0.05 to 19.94 ± 0.06 Ma. Xenotimes from the three younger fractions were assumed to have suffered diffusive Pb loss, and the crystallization age of the granite was interpreted to be 20.2 ± 0.2 Ma based on the monazite and single oldest xenotime analyses. In addition, Searle et al. (1997) state that they could not rule out the possibility that the monazites and oldest xenotime fraction underwent Pb loss, so they considered 20.2 ± 0.2 Ma to be a minimum estimate of the granite's crystallization age.

A sample of the younger leucogranite phase was collected from a dike that cut across the regional foliation and S-C fabrics in the footwall of the STF, but was not seen to cut the STF itself, and was taken to be representative of the main lithology of the Shisha Pangma pluton (Searle et al., 1997). One multigrain fraction of zircon was discordant and had an imprecise $^{207}Pb/^{235}U$ date of 17.8 ± 0.3 Ma. Since some of the zircons contained visible cores, Searle et al. (1997) assumed that the apparent age reflected the presence of inherited zircon. Two normally discordant multigrain fractions of uraninite and two reversely discordant multigrain fractions of monazite had $^{207}Pb/^{235}U$ dates that ranged from 17.26 ± 0.03 to 17.37 ± 0.02 Ma, and the mean of these analyses, 17.3 ± 0.2 Ma, was taken to be the crystallization age of the main phase of the Shisha Pangma leucogranite (Searle et al., 1997).

A leucogranite from Nyalam was dated by Schärer et al. (1986) using U-Pb IDTIMS. Multigrain fractions of zircon all contained pre-Himalayan inheritance, with $^{207}Pb/^{206}Pb$ dates ranging from 1332 to 2218 Ma. Multigrain fractions of monazite showed no evidence for inheritance with $^{207}Pb/^{235}U$ dates that ranged from 16.2 to 17.4 Ma. From the monazite data, Schärer et al. (1986) concluded the Nyalam granite crystallized at 16.8 ± 0.6 Ma.

*Makalu*

The only geochronologic study of the Makalu pluton was done by Schärer (1984), in his classic study that described initial $^{230}Th$ disequilibrium in young monazites. Schärer used U-Pb IDTIMS to date zircon, monazite and xenotime from two Makalu samples, a medium grained 2-mica + tourmaline granite, and a muscovite-rich pegmatitic leucogranite with tourmaline and garnet. Three multigrain zircon fractions from the medium-grained sample had disequilibrium corrected $^{206}Pb/^{238}U$ dates that ranged from 19.0 to 24.2 Ma. Four multigrain monazite fractions, however, gave more consistent results, with disequilibrium corrected $^{206}Pb/^{238}U$ dates that ranged from 21.6 to 22 Ma with a mean of 21.9 ± 0.2 Ma, which Schärer interpreted to be the crystallization age of the granite. Multigrain monazite fractions from the pegmatitic sample also had fairly consistent, disequilibrium-corrected, $^{206}Pb/^{238}U$ dates which ranged from 23.5 to 24.5 Ma, with a mean of 24.0 ± 0.4 Ma, which Schärer interpreted to be the crystallization age of the pegmatite. Results from multigrain xenotime and zircon fractions, on the other hand, varied from 15.5 to 23.5 Ma and 18.3 to 22.9 Ma, respectively. Schärer (1984) assumed that the significant spread of concordant zircon and xenotime dates observed in both samples was due to variable amounts of Pb loss from the minerals, citing a rough correlation between apparent age and grain size, which one would expect if Pb was lost by volume diffusion.

*Everest Leucogranite*

Massive leucogranite bodies are spectacularly exposed on the south, west, and north faces of Nuptse, as well as on the southwest face of neighboring Everest. A granite sample from Mt. Everest was dated by Schärer et al. (1986) using the U-Pb IDTIMS method. Four fractions of zircon all contained a pre-Himalayan inherited component. Five multigrain monazite fractions, however, showed no evidence for inheritance and had $^{207}Pb/^{235}U$ dates that ranged from 13.9 to 14.8 Ma. The mean of these dates, 14.3 ± 0.6 Ma was taken to be the crystallization age of the granite. Unfortunately, it is not clear where this sample was collected, or if it was part of the main Everest-Nuptse pluton.

The most recent estimate of the age of the Everest granite comes from the work of Simpson et al. (2000) who used U-Pb IDTIMS to date monazite, xenotime, and uraninite from a sample of 2-mica + tourmaline granite collected from the main Everest pluton north of the Khumbu ice fall. One multigrain fraction of monazite contained an inherited component, but another multigrain monazite fraction and one multigrain xenotime fraction (both reversely discordant) had similar $^{207}Pb/^{235}U$ dates of 20.3 ± 0.5 and 21.0 ± 0.4 Ma, respectively. A single uraninite analysis was slightly normally discordant and had a $^{207}Pb/^{235}U$ date of 18.5 ± 0.4 Ma. Simpson et al. (2000) disregard the uraninite date, stating that the grain may in fact not be uraninite, and that the 18.5 Ma date represented a cooling age. The authors therefore concluded that the Everest granite crystallized between 20.5 and 21.3 Ma, based on the monazite and xenotime analyses.

*Bhutan*

A two-mica ± tourmaline leucogranite from the Khula Kangri pluton was dated using IMSIMS (Edwards & Harrison, 1997). Thirty-five analyses on twelve monazites yielded $^{208}Pb/^{232}Th$ dates that ranged from 10.0 ± 0.7 to 35.2 ± 0.6 Ma. Only six analyses yielded dates older than 14 Ma, and these were assumed to contain an inherited component from an earlier metamorphic event (Edwards & Harrison, 1997). The remaining analyses suggested a crystallization age for the granite of 12.5 ± 0.4 Ma.

Wu et al. (1998) dated granites from Wagye La and Gaowu, approximately 100 km west of Khula Kangri using IDTIMS. Four multigrain monazite fractions from the Wagye La granite were reversely discordant and had $^{207}Pb/^{235}U$ dates that ranged from 11.6-12.1 Ma. The average of those dates, 11.9 Ma, was interpreted to be the crystallization age of the granite. Two multigrain monazite fractions from the Gaowu granite obviously contained a pre-Himalayan inherited component, having $^{207}Pb/^{206}Pb$ dates of 102 and 272 Ma. Three additional multigrain fractions had $^{207}Pb/^{235}U$ dates that ranged from 24.1 to 25.2 Ma. One single grain monazite had a $^{207}Pb/^{235}U$ date of 22.9 ± 0.17 Ma which was interpreted to be the crystallization age of the granite, while the slightly older monazite fractions were interpreted to contain inherited components.

*Other Himalayan Leucogranites*

While most geochronologic studies have focused on determining the crystallization ages of the large Himalayan leucogranite plutons, the innumerable smaller dikes, sills, and migmatitic leucosomes present throughout the Greater Himalayan Sequence can provide important constraints on the timing of crustal melting and leucogranite formation. While multiple intrusive

phases may be difficult to identify within a pluton (e.g. Harrison et al. 1999), multiple intrusive phases can be identified easily by crosscutting relationships among dikes and sills. This next section reviews, region by region, geochronologic studies of these many unnamed leucogranite bodies.

*Western Himalaya, Zanskar*

Noble and Searle (1995) studied leucogranite melt pods from migmatites at two structural levels in the Zanskar, India region of the western Himalaya, along with an undeformed garnet + muscovite + biotite leucogranite interpreted to be the final separated melt derived from the migmatites. Multigrain fractions of monazite from a melt pod at deeper structural levels showed some pre-Himalayan inheritance, but three fractions without inherited components had $^{207}Pb/^{235}U$ dates that ranged from 20.5 to 19.6 Ma. One single zircon and three multigrain zircon fractions all had pre-Himalayan inheritance. The youngest monazite fractions were interpreted to have suffered some diffusive Pb-loss since younger fractions had higher U concentrations (~80000 ppm) than older fractions (~70000 ppm), and the crystallization age of the migmatitic melt pod was taken to be at least 20.6 Ma. A second migmatitic melt pod from a higher structural level yielded insufficient monazite for analysis, and $^{207}Pb/^{206}Pb$ dates for five zircon fractions were all ca. 460 Ma. An undeformed leucogranite thought to be derived from the migmatites contained inherited zircon, but no inherited monazite. Six slightly reversely discordant multigrain monazite fractions had $^{207}Pb/^{235}U$ dates that ranged from 20.39 to 21.06 Ma with a weighted mean of 20.8 ± 0.3 Ma, which was interpreted to be the crystallization age of the leucogranite (Noble and Searle, 1995). This age agreed with constraints placed on the timing of anatexis by the migmatitic melt pod.

*Central Himalaya*

Hodges et al. (1996) dated migmatitic leucosomes interpreted to be in situ melts, and leucogranitic dikes from the Modi Khola valley south of the Annapurna range in Central Nepal using U-Pb IDTIMS. Four multigrain fractions of monazite separated from a kyanite-bearing leucosome in the lower Greater Himalayan Sequence defined a linear array with $^{207}Pb/^{235}U$ dates that ranged from 22.5 Ma to 37.6 Ma. The youngest grain was reversely discordant, while the other three were highly normally discordant. The upper intercept of the discordia drawn through them (MSWD=1.6) suggested the incorporation of a ca. 450 Ma inherited component, and the youngest grain gave the best estimate of the crystallization age of the leucosome at 22.5 Ma. Five monazite fractions from a second kyanite bearing leucosome were reversely discordant and had $^{207}Pb/^{235}U$ dates that ranged from 28.0 to 31.6 Ma. This spread in apparent ages was interpreted to be the result of Pb loss since the monazites had high U concentrations (~1wt.%), although other possible interpretations such as inheritance from the metamorphic country rock or protracted monazite growth were also considered (Hodges et al., 1996).

Hodges et al. (1996) also dated two leucogranitic dikes. Two multigrain zircon fractions from a boudinaged dike had $^{207}Pb/^{235}U$ dates of 21.9 and 22.1 Ma. Both analyses were slightly normally discordant, and the high U concentrations (14000 ppm) led the authors to suspect that the grains suffered some Pb loss. Hodges et al. (1996) concluded that 22.1 Ma was "close to, but probably slightly less than," the crystallization age of the dike. Four multigrain fractions of zircon from an undeformed dike that cut across compositional layering were normally discordant and defined a linear array with a lower intercept of 22.1 +0.6/-3.6 Ma (MSWD=1.0) which was regarded as the crystallization age of the dike (Hodges et al., 1996).

Another study in the Annapurna region focused on samples from the Kali Gandaki valley. Godin et al. (2001) dated monazite and zircon from a kyanite-garnet-muscovite bearing migmatitic leucosome in the upper Greater Himalayan Sequence by IDTIMS. Five multigrain fractions of monazite and zircon and one single grain monazite were all normally discordant and defined a linear array with a lower intercept of 35 ± 3 Ma and an upper intercept of 460 ± 11 Ma. Godin et al. (2001) interpreted the lower intercept to be the magmatic crystallization age of the leucosome during kyanite-grade metamorphism. A weakly foliated leucogranitic dike that cut across extensional fabrics associated with the Annapurna detachment also was dated. Two multigrain fractions of zircon were highly discordant, suggesting the presence of an inherited component. Two fractions of monazite, one composed of a single grain fragment and the other composed of 5 round grains plotted slightly above concordia with $^{207}Pb/^{235}U$ dates of 22.9 ± 0.8 and 22.4 ± 0.7 Ma, respectively. Six euhedral grains composed a third monazite fraction that was concordant at 28.0 ± 0.4 Ma. The older apparent age of this analysis was interpreted to be the result of mixing between young (~22.5 Ma) monazite and an inherited component, and the crystallization age of the granite was interpreted to be ca. 22.5 Ma (Godin et al., 2001).

Coleman (1998) dated an undeformed leucogranite dike from the upper Dudh Khola valley in central Nepal by U-Pb IDTIMS. The two-mica + tourmaline dike cut across all foliations and intruded the contact between the Greater Himalayan Sequence and the overlying Tibetan Sedimentary Sequence. Three multigrain fractions of monazite had $^{207}Pb/^{235}U$ dates that ranged from 18.7 to 19.0 Ma, indicating crystallization at 18.8 ± 0.1 Ma (Coleman, 1998). Two multigrain fractions of zircon were highly normally discordant with $^{207}Pb/^{235}U$ dates of 22.0 and 30.1 Ma. These analyses were interpreted to be the result of mixing between a pre-Himalayan inherited component and a young 18-19 Ma component. The 18-19 Ma zircon component was

identified by one single grain and two multigrain fractions of zircon that had $^{207}Pb/^{235}U$ dates that ranged from 18.3 to 18.9 Ma and were all nearly concordant. The combined monazite and zircon data were interpreted to be consistent with dike crystallization between 18 and 19 Ma.

In the Central Himalaya of eastern Nepal, a series of dikes and sills from the Dudh Kosi valley in the Everest region were dated using U-Pb IDTIMS analyses of single grains of monazite, xenotime, and zircon (Chapter 2). Three undeformed crosscutting dikes from three different outcrops in the upper Greater Himalayan Sequence had similar crystallization ages of 18.28 ± 0.07 Ma, 17.6-18.0 Ma, and 17.74-18.33 Ma. Only the 18.28 Ma dike contained pre-Himalayan inherited monazite. Three concordant sills from two different outcrops also were dated. Two sills from different outcrops had similar crystallization ages of 21.33 ± 0.03 Ma and 21.80 ± 0.05 Ma, while the third had a minimum crystallization age of 18.36 Ma. Both of the ca. 21-22 Ma sills contained abundant concordant xenotime ranging in apparent age from ca. 26 Ma to ca. 23 Ma. On the basis of results from backscattered electron imaging of grains and analyzing fragments of single grains, these results were interpreted to indicate episodic to semi-continuous melting between ca. 23 and ca. 26 Ma. The migmatitic country rock from one of the same outcrops was shown by Viskupic and Hodges (2001) to have undergone anatectic melting between 24.8 and 25.4 Ma based on a combination of U-Pb IDTIMS geochronology and thermometry based on the partitioning of Y and Nd between monazite and xenotime.

## Discussion

### *Results from IDTIMS and IMSIMS Techniques*

Early U-Pb IDTIMS studies of Himalayan leucogranites used multigrain fractions of minerals, and the, often discordant, results were interpreted in terms of now outdated ideas about

Pb volume diffusion in monazite and xenotime. Interpreting geochronologic data from multigrain fractions can be complicated by the presence of inherited components, or by processes such as protracted mineral growth that lead to geologically significant variations in crystallization ages.

The high spatial resolution offered by the IMSIMS technique in combination with modern imaging techniques offers a powerful tool for physically recognizing, characterizing, and avoiding the inherited components that have made geochronologic studies of Himalayan leucogranites difficult. Unfortunately, many published IMSIMS studies of Himalayan leucogranites have not fully realized this advantage, leaving the possibility open that individual spot analyses overlap xenocrystic cores and magmatic rims. This makes the assignment of certain dates as being the result of inheritance more subjective. While IMSIMS dating is a useful technique because of its high spatial resolution, its inability to resolve small increments of time limits its value for providing anything but an average age. While an average age may suffice when a sample has only a single age population of accessory phases, most samples examined have more complicated accessory phase growth histories that cannot be understood with an average age (e.g. Δ33; Chapter 2).

Significant lowering of IDTIMS laboratory Pb blanks now allows analysis of fragments of single grains, so that different mineral growth phases (both inherited and non-inherited) can be physically separated and dated. The ability to analyze smaller grain fragments has necessitated the characterization of single grains before dissolution. This is being accomplished through backscattered electron and cathodoluminescence imaging of accessory phases in thin section (e.g. Simpson et al., 2000), or in grain mounts (e.g. Viskupic & Hodges, 2001; Chapter 2).

The high precision offered by the IDTIMS technique is ideal for evaluating the relative importance of protracted accessory phase growth. To take full advantage of the high precision, it is necessary to identify and physically isolate different mineral growth phases through a combination of imaging and microsampling. Future studies of Himalayan leucogranites hopefully will be more successful at determining anatectic histories by combining accessory phase characterization with high precision IDTIMS techniques.

*Reinterpretation of U-Th-Pb Data*

Knowing now that diffusive Pb loss in monazite and xenotime is unlikely at the magmatic temperatures of the Himalayan leucogranites, and that accessory phases can preserve histories of protracted melt crystallization, many of the geochronologic interpretations outlined above can be reinterpreted. For example, Schärer (1984) interpreted the crystallization ages of two samples of the Makalu granite to be 24.0 Ma and 21.9 Ma based on weighted mean U-Pb dates of monazite. In both samples, however, essentially concordant zircon and xenotime dates ranged from 15.5 to 23.5 Ma and 19.0 to 24.2 Ma, respectively, which Schärer interpreted to be due to variable Pb loss. An alternative hypothesis is that the spread in zircon and xenotime dates represents mixing between older and younger magmatic components that Schärer was not able to identify with analyses of multigrain fractions. If this were the case, there could be a magmatic phase of the Makalu pluton as young as 15.5 Ma.

Similarly, Searle et al. (1997) interpreted the age of the Shisha Pangma granite to be 20.2 Ma, the mean $^{207}Pb/^{235}U$ date of two single grain monazite analyses and one multigrain xenotime analysis. Three additional multigrain xenotime analyses, however, were nearly concordant with $^{207}Pb/^{235}U$ dates that ranged from 19.39 to 19.94 Ma, which Searle et al. (1997) assumed to be

the result of diffusive Pb loss. An alternative interpretation for the range of dates observed in the Shisha Pangma granite is that they reflect real variations in the timing of accessory phase crystallization so that the age of final granite crystallization is 19.4 Ma rather than 20.2 Ma.

Overall, the range in Himalayan granite crystallization ages reviewed above suggests there was a near-continuum of granite crystallization between 24 and 16 Ma, with additional granite crystallization at 14.3 Ma in the Everest region, and at 12.5 to 11.9 Ma in the eastern Himalaya of Bhutan. The earliest evidence for melting comes from the Everest region where protracted xenotime and zircon crystallization between 23 Ma and 26 Ma in two granite sills was interpreted to be the result of semi-continuous melt production (Chapter 2). Shortly after, at 23 Ma, the Shivling granite crystallized (Searle et al., 1999), followed by the Gaowu granite in Bhutan (Wu et al., 1998) and the Larkya La phase of the Manaslu pluton at 22.9 Ma (Harrison et al., 1999). The Gangotri granite crystallized at 22.4 Ma (Harrison et al., 1997). Leucosome formation at 22.5 Ma and granite dike crystallization at 22.1 Ma occurred in the Annapurna region (Hodges et al., 1996), and in Zanskar (Walker et al., 1999). Dike crystallization at 21.8 and 21.3 Ma occurred in the Everest region (Chapter 2), as well as in Zanskar at 21.3-21.4 Ma (Walker et al., 1999). At the same time, the Everest granite was crystallizing between 21.3 and 20.5 Ma (Simpson et al., 2000). Shortly after, migmatization and granite crystallization took place in Zanskar at 20.8 Ma and 20.6 Ma, respectively (Noble & Searle, 1995). A granite dike in the Everest region crystallized at 20.1 Ma (Simpson, 2002), followed by the crystallization of dikes in the Marsyandi at 18.8 Ma (Coleman, 1998), and in the Everest region at 18.0 and 17.5-18.3 Ma (Chapter 2). The Shisha Pangma granite was crystallizing at 17.3 Ma (Searle et al., 1997), followed by a granite in Nyalam at 16.8 Ma (Schärer et al., 1996), and granites in the Rongbuk Valley between 16.2 and 16.8 Ma (Hodges et al., 1998; Murphy & Harrison, 1999).

There is then an apparent hiatus in granite crystallization until a granite near Mt Everest crystallized at 14.3 Ma (Schärer et al., 1986), crystallization of the Khula Kangri granite at 12.5 Ma (Edwards & Harrison, 1997) and crystallization of the Wagye La granite at 11.9 Ma (Wu et al., 1998) in Bhutan.

*Spatial Distribution of Granite Crystallization Ages*

It is clear from the above discussion and from examination of Figure 1 that there are no along-strike trends in crystallization ages of the Himalayan leucogranites. In fact, almost the entire range of granite crystallization ages in the Himalaya has been recorded in one north-south transect through the Everest region (Schärer et al., 1986; Hodges et al., 1998; Murphy & Harrison, 1999; Simpson et al., 2000; Viskupic & Hodges, 2001; Simpson, 2002; Chapter 2). Furthermore, almost the entire history of anatectic melting in the Himalaya has been recorded in single outcrops (Chapter 2), demonstrating that geochronologic observations made at the outcrop scale in dikes and sills can mimic those made at the orogen scale. This is not a surprising result since many of the Himalayan leucogranites are described as being relatively unmixed amalgamations of melt fed by extensive dike networks. It is nonetheless an important result, as it implies that the conclusions drawn from investigations of relatively small-scale dikes and sills are relevant and applicable to understanding the evolution of larger scale plutons and Himalayan anatexis.

*Zircon, the Forgotten Mineral*

An important observation in the analysis of U-Pb data sets from Himalayan granites is that zircon does crystallize with no pre-Himalayan inheritance, potentially recording granite

crystallization ages (Schärer, 1984; Copeland et al., 1988; Searle et al., 1997; Hodges et al., 1998; Coleman, 1998; Bowring & Hodges, unpublished data; Chapter 2). Many Himalayan leucogranites were saturated with respect to zircon as well as monazite and xenotime. Due to the common presence of inherited zircon, and the use of the IMSIMS technique, which has focused on dating monazite, many geochronologists have not bothered to date zircon in Himalayan leucogranite samples. This avoidance of zircon in Himalayan geochronologic studies is clearly not necessary, and is in fact disadvantageous. Hopefully future studies will examine accessory mineral populations for magmatic zircon since such material can provide high precision crystallization ages.

**Implications for Models of Anatexis**

The age range of Himalayan anatexis and granite crystallization during the ca. 26-16 Ma time period with additional crystallization at ca. 14 Ma and ca. 12 Ma has implications for models of melt generation. These observations suggest that temperatures in the Himalayan metamorphic core were high enough to sustain anatexis (ca. 700°C) either continuously or episodically for over 10 million years. The earliest constrained slip on the South Tibetan fault system occurred at about 23 Ma in the western Himalaya of Zanskar (Searle, 1986) and 22.5 Ma in the Annapurna region (Hodges et al., 1996). Since the earliest movement on the STF postdates the earliest generation and crystallization of Himalayan leucogranites, it cannot be argued that decompression melting due to tectonic denudation was alone responsible for the generation of the Himalayan leucogranites. Likewise, the earliest constrained slip on the Main Central thrust system occurred between 23 and 20 Ma (Hubbard & Harrison, 1989; Hodges et al., 1996), and also postdates the earliest Himalayan anatexis. Heat sources for the earliest crustal

melting, therefore, could be related to the concentration of materials enriched in heat producing elements and the subsequent thermal maturation of the orogenic system (Molnar et al., 1983; Royden, 1993; Huerta et al., 1996, 1998, 1999). Slip on both the MCT and STF has been episodic throughout much of Miocene-Recent time (Hodges, 2000; Hodges et al., 2001). During the early part of this interval, these episodic displacements may have been responsible for episodic melt generation in the Himalaya.

## References


Arita, K. (1983) Origin of the inverted metamorphism of the lower Himalayas, central Nepal. Tectonophysics. V. 95, p. 43-60.

Asami, M., Suzuki, K., Grew, E.S. (2002) Chemical Th-U-total Pb dating by electron microprobe analysis of monazite, xenotime and zircon from the Archean Napier Complex, East Antarctica: evidence for ultra-high-temperature metamorphism at 2400 Ma. Precambrian Research, v. 114, p. 249-275.

Burchfiel, B.C., Chen, Z., Hodges, K.V., Liu, Y., Royden, L.H., Deng, C., Xu, J. (1992) The South Tibetan Detachment system, Himalayan orogen: Extension contemporaneous with and parallel to shortening in a collisional mouuntain belt. Geological Society of America Special Paper 269, Boulder CO, 41 p.

Catlos, E.J., Gilley, L.D., Harrison, T.M. (2002) Interpretation of monazite ages obtained via in situ analysis. Chemical Geology, v. 188, p. 193-215.

Catlos, E.J., Harrison, T.M., Kohn, M.J., Grove, M., Ryerson, F.J., Manning, C.E., Upreti, B.N. (2001) Geochronologic and thermobarometric constraints on the evolution of the Main Central Thrust, central Nepal Himalaya. Journal of Geophysical Reseasrch, v. 106, p. 16177-16204.

Cherniak, D.J., Watson, E.B. (2000) Pb diffusion in zircon. Chemical Geology, v. 172, p. 5-24.

Cherniak, D.J., Watson, E.B., Harrison, T.M., Grove, M. (2000) Pb diffusion in monazite: a progress report on a combined RBS/SIMS study [abs.]. EOS (Transactions, American Geohphysical Union). v. 81, p. S25.

Clemens, J.D., Vielzeuf, D. (1987) Constraints on melting and magma production in the crust. Earth and Planetary Science Letters, v. 86, p. 287-306.

Coleman, M.E. (1998) U-Pb constraints on Oligocene-Miocene deformation and anatexis within the central Himalaya, Marsyandi Valley, Nepal. American Journal of Science, v. 298, p. 553-571.

Copeland, P., Parrish, R.R., Harrison, T.M., (1988) Identification of inherited radiogenic Pb in monazite and its implications for U-Pb systematics. Nature, v. 333. p. 760-763.

Deniel, C., Vidal, P., Fernandez, A., Le Fort, P., Peucat, J.-J. (1987) Isotopic study of the Manaslu granite (Himalaya, Nepal): inferences on the age and source of Himalayan leucogranites. Contributions to Mineralogy and Petrology, v. 96, p. 78-92.

Edwards, M.A., Harrison, T.M. (1997) When did the roof collapse? Late Miocene north-south extension in the high Himalaya revealed by Th-Pb monazite dating of the Khula Kangri granite. Geology, v. 25, p. 543-546.

England, P., Le Fort, P., Molnar, P., Pêcher, A. (1992) Heat sources for Tertiary metamorphism and anatexis in the Annapurna-Manaslu region, central Nepal. Journal of Geophysical Research, v. 97, p. 2107-2128.

England, P., Molnar, P (1993) Cause and effect among thrust and normal faulting, anatectic melting and exhumation in the Himalaya, in Treloar, P.J., and Searle, M.P., (eds), Himalayan Tectonics: Geological Society of London Special Publication no. 74, p. 401-411.

Ferrara, G., Lombardo, B., Tonarini, S. (1983) Rb/Sr Geochronology of granites and gneisses from the Mount Everest region, Nepal Himalaya. Geologische Rundschau, v. 72, p. 119-136.

France-Lanord, C., Sheppard, S.M.F., Le Fort, P. (1988) Hydrogen and oxygen isotopic variations in the High Himalaya peraluminous Manaslu leucogranite: Evidence for heterogeneous sedimentary source. Geochim. Cosmochim. Acta, v. 52, p. 513-526.

Godin, L, Parrish, R.R., Brown, R.L., Hodges, K.V. (2001) Crustal thickening leading to exhumation of the Himalayan metamorphic core of central Nepal: Insight from U-Pb geochronology and $^{40}Ar/^{39}Ar$ thermochronology. Tectonics, v. 20, p. 729-747.

Guillot, S., Hodges, K., Le Fort, P., Pêcher, A. (1994) New constraints on the age of the Manaslu leucogranite: Evidence for episodic tectonic denudation in the central Himalayas. Geology, v. 22, p. 559-562.

Guillot, S., Hodges, K., Le Fort, P., Pêcher, A. (1994) New constraints on the age of the Manaslu leucogranite: Evidence for episodic tectonic denudation in the central Himalayas: Reply. Geology, v. 23, p. 479-480.

Guillot, S., Le Fort, P. (1995) Geochemical constraints on the bimodal origin of High Himalayan leucogranites. Lithos, v. 35, p. 221-234.

Guillot, S., Pêcher, A., Rochette, P., Le Fort, P. (1993) The emplacement of the Manaslu granite of central Nepal: Field and magnetic susceptibility constraints. In Treloar, P.J., and Searle, M.P (eds) Himalayan tectonics: Geological Society of London Special Publication no. 74, p.413-428.

Hamet, J., Allegre, C.-J. (1976) Rb-Sr systematics in granite from central Nepal (Manaslu): Significance of the Oligocene age and high $^{87}Sr/^{86}Sr$ ratio in Himalayan orogeny. Geology, v. 4, p. 470-472.

Hamet, J., Allegre, C.-J. (1978) Rb-Sr systematics in granite from central Nepal (Manaslu): Significance of the Oligocene age and high $^{87}Sr/^{86}Sr$ ratio in Himalayan orogeny: Reply. Geology, v. 6, p. 197.

Harris, N., Massey, J. (1994) Decompression and anatexis of Himalayan metapelites. Tectonics, v. 13, p. 1537-1546.

Harrison, T.M., Catlos, E.J., Montel, J.-M. (2002) U-Th-Pb dating of phosphate minerals. In: Kohn, M.J., Rakowan, J., Hughes, J.M. (eds.) Phosphates-Geochemical, Geobiological, and Materials Importance, Reviews in Mineralogy, v. 48, p. 523-558.

Harrison, T.M., Grove, M., Lovera, O.M., Catlos, E.J. (1998) A model for the origin of Himalayan anatexis and inverted metamorphism. Earth and Planetary Science Letters, v. 146, p.

Harrison, T.M., Grove, M., McKeegan, K.D., Coath, C.D., Lovera, O.M., Le Fort, P. (1999) Origin and episodic emplacement of the Manaslu intrusive complex, central Himalaya. Journal of Petrology, v. 40, p. 3-19.

Harrison, T.M., Lovera, O.M., Grove, M. (1997) New insights into the origin of two contrasting Himalayan granite belts. Geology, v. 25, p. 899-902.

Harrison, T.M., Mahon, K.I. (1995) New constraints on the age of the Manaslu leucogranite: Evidence for episodic tectonic denudation in the central Himalaya: Comment. Geology, v. 23, p. 478-479.

Harrison, T.M., McKeegan, K.D., LeFort, P. (1995) Detection of inherited monazite in the Manaslu leucogranite by $^{208}Pb/^{232}Th$ ion microprobe dating: Crystallization age and tectonic implications. Earth and Planetary Science Letters, v. 133, p. 271-282.

Hawkins, D.P., Bowring, S.A. (1997) U-Pb systematics of monazite and xenotime: case studies from the Paleoproterozoic of the Grand Canyon, Arizona. Contributions to Mineralogy and Petrology, v. 127, p. 87-103.

Hawkins, D.P., Bowring, S.A. (1999) U-Pb monazite, xenotime and titanite geochronological constraints on the prograde to post-peak metamorphic thermal history of Paleoproterozoic migmatites from the Grand Canyon, Arizona. Contributions to Mineralogy and Petrology, v. 134, p. 150-169.

Hodges, K.V. (2000) Tectonics of the Himalaya and southern Tibet from two perspectives. Geological Society of America Bulletin, v. 112, p. 324-350.

Hodges, K., Bowring, S., Davidek, K., Hawkins, D., Krol, M. (1998) Evidence for rapid displacement on Himalayan normal faults and the importance of tectonic denudation in the evolution of mountain ranges. Geology, v. 26, p. 483-486.

Hodges, K.V., Burchfiel, B.C., Royden, L.H., Chen, Z., Lui, Y. (1993) The metamorphic signature of contemporaneous extension and shortening in the central Himalayan orogen: Data from the Nyalam transect, southern Tibet. Journal of Metamorphic Geology, v. 11, p. 721-737.

Hodges, K.V., Hames, W.E., Olszewski, W.J., Burchfiel, B.C., Royden, L.H., Chen, Z. (1994) Thermobarometric and $^{40}Ar/^{39}Ar$ geochronologic constraints on Eohimalayan metamorphism in the Dinggye area, southern Tibet. Contributions to Mineralogy and Petrology, v. 117, p. 151-163.

Hodges, K.V., Hurtado, J.M., Whipplle, K.X. (2001) Southward extrusion of Tibetan crust and its effect on Himalayan tectonics. Tectonics, v. 20, p. 799-809.

Hodges, K.V., Parrish, R.R., Housh, T.B., Lux,, D.R., Burchfiel, B.C., Royden, L.H., Chen, Z. (1992) Simultaneous Miocene extension and shortening in the Himalayan orogen. Science, v. 258, p. 1466-1470.

Hodges, K.V., Parrish, R.R., Searle, M.P. (1996) Tectonic evolution of the central Annapurna Range, Nepalese Himalayas. Tectonics, v. 15, p. 1264-1291.

Hubbard, M.S., Harrison, T.M. (1989) $^{40}Ar/^{39}Ar$ age constraints on deformation and metamorphism in the Main Central thrust zone and Tibetan slab, eastern Nepal Himalaya. Tectonics, v. 8, p. 865-880.

Huerta, A.D., Royden, L.H., Hodges, K.V. (1996) The interdependence of deformational and thermal processes in mountain belts. Science, v. 273, p. 637-639.

Huerta, A.D., Royden, L.H., Hodges, K.V. (1998) The thermal structure of collisional orogens as a response to accretion, erosion and radiogenic heating. Journal of Geophysical Research, v. 103, p. 15287-15302.

Huerta, A.D., Royden, L.H., Hodges, K.V. (1999) The effects of accretion, erosion and radiogenic heat on the metamorphic evolution of collisional orogens. Journal of Metamorphic Geology, v. 17, p. 349-366.

Inger, S., Harris, N.B.W (1993) Geochemical constraints on leucogranite magmatism in the Langtang Valley, Nepal Himalaya. Journal of Petrology, v. 34, p. 345-368.

Kamber, B.S., Frei, R., Gibb, A.J. (1998) Pitfalls and new approaches in granulite chronometry. An example from the Limpopo Belt, Zimbabwe. Precambrian Research, v. 91, p. 269-574.

Kretz, R. (1983) Symbols for rock-forming minerals. American Mineralogist, v. 68, p. 277-279.

Le Fort, P. (1975) Himalayas: the collided range. Present knowledge of the continental arc. American Journal of Science, v. 275, p. 1-44.

Le Fort, P. (1981) Manaslu leucogranite: A collision signature of the Himalaya a model for its genesis and emplacement. Journal of Geoophysical Research, v. 86, p. 10545-10568.

Le Fort, P., Cuney, M., Deniel, C., France-Lanord, C., Sheppard, S.M.F., Upreti, B.N., Vidal, P. (1987) Crustal generation of the Himalayan leucogranites. Tectonophysics, v. 134, p. 39-57.

Maluski, H., Matte, P., Brunel, M. (1988) Argon39-Argon40 dating of metamorphic and plutonic events in the North and High Himalaya belts (southern Tibet-China). Tectonics, v. 7, p. 299-326.

Mattinson, J.M. (1973) Anomalous isotopic composition of lead in young zircons. Carnegie Institution of Washington Yearbook, v. 72, p. 613-616.

Molnar, P., Chen, W.P., Padovani, E. (1983) Calculated temperatures in overthrust terrains and possible combinations of heat sources responsible for the Tertiary granites in the Greater Himalaya. Journal of Geophysical Research, v. 88, p. 6415-6429.

Molnar, P., England, P. (1990) Temperatures, heat flux, and frictional stress near major thrust faults. Journal of Geophysical Research, v. 95, p. 4833-4856.

Murphy, M.A., Harrison, T.M. (1999) Relationship between leucogranites and the Qomolangma detachment in the Rongbuk Valley, south Tibet. Geology, v. 27, p. 831-834.

Noble, S.R., Searle, M.P. (1995) Age of crustal melting and leucogranite formation from U-Pb zircon and monazite dating in the western Himalaya, Zanskar, India. Geology, v. 23, p. 1135-1138.

Overstreet, W.C. (1967) The geologic occurrence of monazite. U.S. Geological Survey Professional Paper 530, 327 p.

Parrish, R.R. (1990) U-Pb dating of monazite and its application to geological problems Canadian Journal of Earth Sciences, v. 27, p. 1432-1450.

Parrish, R.R. (1990) U-Pb dating of monazite and its application to geological problems. Canadian Journal of Earth Sciences, v. 27, p. 1431-1450.

Patino Douce, A.E., Harris, N. (1998) Experimental constraints on Himalayan anatexis. Journal of Petrology, v. 39, p. 689-710.

Pinet, C., Jaupart, C. (1987) A thermal model for the distribution in space and time of the Himalayan granites. Earth and Planetary Science Letters, v. 84, p. 87-99.

Royden L.H. (1993) The steady state thermal structure of eroding orogenic belts and accretionary prisms. Journal of Geophysical Research, v. 98, p. 4487-4507.

Scaillet, B., France-Lanord, C., Le Fort, P. (1990) Badrinath-Gangotri plutons (Garhwal, India): petrological and geochemical evidence for fractionation processes in a High Himalayan leucogranite. Journal of Volcanology and Geothermal Research, v. 44, p. 163-188.

Scaillet, B., Pichavant, M., Roux, J. (1995) Experimental crystallization of leucogranite magmas. Journal of Petrolory, v. 36, p. 663-705.

Table 1 Summary of Himalayan granite geochronology.

| Reference | Notes | Mineral [a] | Method | no.non-inherited analyses | no. grains [b] | range in dates dates (Ma) | pre-Himalayan Inheritance Dates (Ma) | Interpreted Crystallization Age (Ma) | Error Ma |
|---|---|---|---|---|---|---|---|---|---|
| Zanskar Region, India | | | | | | | | | |
| Noble & Searle, 1995 | 2 mica + garnet | m | U-Pb TIMS | 6 | multigrain | 20.4-21.1 | none | 20.8 | 0.3 |
| Noble & Searle, 1995 | melt pod in migmatite | m | U-Pb TIMS | 3 | multigrain | 19.6-20.5 | 360-402 | 20.6 | min age |
| Walker et al., 1999 | undeformed granite | m | U-Pb TIMS | 3 | single | 21.5-24.1 | 332-453 | 21.4 | 0.1 |
| Walker et al., 1999 | undeformed granite | u | U-Pb TIMS | 4 | single | 21.2-21.4 | none | 21.4 | 0.1 |
| Walker et al., 1999 | undeformed granite 2 | m | U-Pb TIMS | 3 | single | 21 2-22.2 | 250 | 21.3 | 0.1 |
| Walker et al., 1999 | undeformed granite 2 | x | U-Pb TIMS | 1 | single | 21.4 | none | 21.3 | 0.1 |
| Walker et al., 1999 | undeformed granite 2 | u | U-Pb TIMS | 2 | single | 21.2-21 3 | none | 21.3 | 0.1 |
| Walker et al., 1999 | undeformed granite 3 | m | U-Pb TIMS | 3 | single | 21 9-22.2 | 130 | 22.1 | 0.4 |
| Walker et al., 1999 | undeformed granite 3 | u | U-Pb TIMS | 2 | single | 22.0-22.3 | none | 22.1 | 0.4 |
| Gangotri Pluton | | | | | | | | | |
| Harrison et al., 1997 | | m | Th-Pb SIMS | NR | NR | NR | NR | 22.4 | 0.5 |
| Shivling Pluton | | | | | | | | | |
| Harrison et al., 1997 | | m | Th-Pb SIMS | NR | NR | NR | NR | 21.9 | 0.5 |
| Searle et al., 1999 | tur+ms±bt granite | m | U-Pb TIMS | 4 | single | 22.9-24.06 | ca. 460 | 23.0 | 0.2 |
| Annapurna Region | | | | | | | | | |
| Hodges, et al, 1996 | leucosome | m | U-Pb TIMS | 1 | multigrain | 22.5 | 450 | 22.5 | 0.1 |
| Hodges, et al, 1996 | leucosome | m | U-Pb TIMS | 5 | 2single, 1multi | 20.8-31.6 | ? | 20.8 | min age |
| Hodges, et al, 1996 | post kinematic pegmatite | z | U-Pb TIMS | 4 | multigrain | 22.9-23.3 | yes | 22.1 | +0.6/-3.6 |
| Hodges, et al, 1996 | deformed pegmatite | z | U-Pb TIMS | 2 | multigrain | 21.9-22.1 | none | | |
| Godin, et al, 2001 | late kinematic dike | m | U-Pb TIMS | 3 | 1single, 2multi | 22.4-28 | none | ~22 | |
| Marsyandi Valley | | | | | | | | | |
| Coleman, 1998 | undeformed dike | m | U-Pb TIMS | 3 | multigrain | 18.7-19.0 | none | 18 8 | 0.1 |
| Coleman, 1998 | undeformed dike | z | U-Pb TIMS | 3 | 1single, 2multi | 18.3-18.9 | 150-300 | 18 8 | 0 1 |
| Manaslu Pluton | | | | | | | | | |
| Deniel et al., 1987 | | m | U-Pb TIMS | 1 | multigrain | 25.5 | - | 25.5 | 0.5 |
| Harrison et al., 1995 | 2 mica + tur | m | Th-Pb SIMS | 24 | 17 | 18.6-25.6 | none | 22.4 | 0.5 |
| Harrison et al., 1995 | Larkya La | m | Th-Pb SIMS | 81 | NR | NR, ca. 21-38 Ma | ca. 400-600 Ma | 22.9 | 0.6 |
| Harrison et al., 1995 | Bimtang | m | Th-Pb SIMS | 53 | NR | NR, ca.19-33 Ma | none | 19.3 | 0.3 |
| Shisha Pangma Pluton | | | | | | | | | |
| Searle et al., 1997 | weakly foliated bt granite | m | U-Pb TIMS | 2 | single | 20.1-20.2 | none | 20 2 | 0.2 |
| Searle et al., 1997 | weakly foliated bt granite | x | U-Pb TIMS | 4 | multigrain | 19.4-20.2 | none | 20.2 | 0 2 |
| Searle et al., 1997 | tur+ms+grt dike | z | U-Pb TIMS | 1 | multigrain | 17.8 | none | 17.3 | 0.2 |
| Searle et al., 1997 | tur+ms+grt dike | u | U-Pb TIMS | 2 | multigrain | 17.3-17.4 | none | 17.3 | 0.2 |
| Searle et al., 1997 | tur+ms+grt dike | m | U-Pb TIMS | 2 | multigrain | 17.27-17.3 | none | 17 3 | 0.2 |
| Nyalam | | | | | | | | | |
| Schärer et al., 1986 | migmatitic granite | m | U-Pb TIMS | 4 | multigrain | 16.8-17.9 | none | 16.8 | 0.6 |
| Rongbuk Valley | | | | | | | | | |
| Copeland et al., 1988 | Δ 33 | m | U-Pb TIMS | 5 | multigrain | 21-26 | 471 upper int | 20 | 1 |
| Copeland et al., 1988 | Δ 33 | z | U-Pb TIMS | 1 | 1 | 19 5 ± 0.8 | >500 | 20 | 1 |
| Hodges et al., 1992 | Δ 33 | x | U-Pb TIMS | 4 | single | 20.6-21.4 | none | 20.6-21.6 | |
| Harrison et al., 1995 | Δ 33 | m | Th-Pb SIMS | 30 | NR | 18-27 | none | 22 | +1/-0.5 |
| Bowring & Hodges, unpub. | Δ 33 | m | U-Pb TIMS | 10 | single | 20.5-25.2 | none | 20.51 | 0.12 |
| Bowring & Hodges, unpub. | Δ 33 | x | U-Pb TIMS | 7 | single | 20.58-21.37 | ? | 20.58 | 0.08 |
| Bowring & Hodges, unpub. | Δ 33 | z | U-Pb TIMS | 1 | multigrain | 20.61 | 297-499 | 20.61 | 0.8 |
| Bowring & Hodges, unpub | Δ 33 | u | U-Pb TIMS | 13 | single, fragments | 22.1-20.30 | none | ? | |
| Hodges et al., 1998 | mylonitized sill | m | U-Pb TIMS | 6 | 2single, 4 multi | 16.58-26.48 | none | 16.67 | 0 04 |
| Hodges et al., 1998 | mylonitized sill | z | U-Pb TIMS | 1 | single | 16.72 | 410 | 16.67 | 0.04 |
| Hodges et al., 1998 | mylonitized sill | x | U-Pb TIMS | 5 | single | 16.57-16.68 | none | 16.67 | 0.04 |
| Murphy & Harrison, 1999 | mylonitic sill below STF | m | Th-Pb SIMS | 10 | 8 | 14 8-17.8 | none | 16.2 | 0 8 |
| Murphy & Harrison, 1999 | crosscutting granite | m | Th-Pb SIMS | 10 | 9 | 15.2-19.6 | none | 16.8 | 0.8 |
| Murphy & Harrison, 1999 | dike deflected by STF shear | m | Th-Pb SIMS | 13 | 11 | 15.1-23.9 | none | 16.4 | 0.6 |
| Everest Region | | | | | | | | | |
| Schärer et al., 1986 | from Mt Everest | m | U-Pb TIMS | 5 | multigrain | 13.9-14.7 | none | 14 3 | 0.6 |
| Simpson et al., 2000 | Everest granite | m | U-Pb TIMS | 1 | multigrain | 20.3 | 296 | 20.5-21.3 | |
| Simpson et al., 2000 | Everest granite | x | U-Pb TIMS | 1 | multigrain | 21 | none | 20.5-21.3 | |
| Viskupic & Hodges, 2001 | migmatite 98E5 | m | U-Pb TIMS | 5 | single | 22.2-25.7 | 460 | 24.8-25.4 | |
| Viskupic & Hodges, 2001 | migmatite 98E5 | x | U-Pb TIMS | 9 | single | 17.6-28.4 | 470 | 24.8-25 4 | |
| Viskupic, Chapter 2 | crosscutting dike 98E6 | m | U-Pb TIMS | 4 | single | 17.8-18.1 | none | 18.00 | 0.18 |
| Viskupic, Chapter 2 | crosscutting dike 98E6 | x | U-Pb TIMS | 1 | single | 17.6 | none | 18.00 | 0.18 |
| Viskupic, Chapter 2 | sill 00SK08 | m | U-Pb TIMS | 5 | single | 18.36-19.58 | none | 18.36 | min age |
| Viskupic, Chapter 2 | sill 00SK09 | m | U-Pb TIMS | 2 | single | 18.4; 24 0 | none | 21.80 | 0.05 |
| Viskupic, Chapter 2 | sill 00SK09 | x | U-Pb TIMS | 12 | single | 23.6-25.4 | none | 21.80 | 0.05 |
| Viskupic, Chapter 2 | sill 00SK09 | z | U-Pb TIMS | 4 | multigrain | 21.8; 24 2-25.6 | none | 21.80 | 0.05 |
| Viskupic, Chapter 2 | crosscutting dike 00SK10 | m | U-Pb TIMS | 1 | single | 18.28 | 440 | 18.28 | 0.07 |
| Viskupic, Chapter 2 | sill 01SK54 | m | U-Pb TIMS | 4 | single | 21.3; 23.3 | none | 21.33 | 0.03 |
| Viskupic, Chapter 2 | sill 01SK54 | x | U-Pb TIMS | 7 | single | 21.3; 23.9-26.3 | none | 21 33 | 0.03 |
| Viskupic, Chapter 2 | crosscutting dike 01SK55 | m | U-Pb TIMS | 7 | single | 17.5-18.3 | none | 17.5-18.3 | |
| Viskupic, Chapter 2 | crosscutting dike 01SK55 | x | U-Pb TIMS | 1 | single | 17.85 | none | 17.5-18.3 | |
| Simpson, 2002 | 2 mica + tur dike, Lintgren | x | U-Pb TIMS | 1 | single | 16.4 | none | 17.5 | min age |
| Simpson, 2002 | grt+tur+ms dike | m | U-Pb TIMS | 1 | multigrain | 20 1 | >371 | 20.1 | 1.0 |
| Ama Dablam | | | | | | | | | |
| Simpson, 2002 | 2 mica + tur sill | m | U-Pb TIMS | 3 | multigrain | 16.9-20.8 | none | 17 | min age |
| Makalu Pluton | | | | | | | | | |
| Schärer, 1984 | med-grained 2 mica+tur | m | U-Pb TIMS | 4 | multigrain | 21.6-22.1 | none | 21.9 | 0.2 |
| Schärer, 1984 | med-grained 2 mica+tur | z | U-Pb TIMS | 3 | multigrain | 19.0-24.2 | none | 21.9 | 0.2 |
| Schärer, 1984 | pegmatitic tur+ms+grt | m | U-Pb TIMS | 5 | multigrain | 23.5-24.5 | none | 24 | 0.4 |
| Schärer, 1984 | pegmatitic tur+ms+grt | z | U-Pb TIMS | 5 | multigrain | 18.3-22.9 | none | 24 | 0.4 |
| Schärer, 1984 | pegmatitic tur+ms+grt | x | U-Pb TIMS | 4 | multigrain | 15.5-23.5 | none | 24 | 0.4 |
| Bhutan | | | | | | | | | |
| Edwards & Harrison, 1997 | Khula Kangri, 2 mica + tur | m | Th-Pb SIMS | 35 | 12 | 10-14; 21-35 | none | 12.5 | 0.4 |
| Wu et al., 1998 | Wayge La | m | U-Pb TIMS | 4 | multigrain | 11.6-12.1 | none | 11.9 | |
| Wu et al., 1998 | Gaowu | m | U-Pb TIMS | 4 | 1single, 3 multi | 22.9-25.2 | 102-272 | 22.9 | 0.17 |

(a) Minerals dated. m=monazite, x=xenotime, z=zircon, u=uraninite
(b) Number of grains analyzed per fraction, either single grains (single) or multigrains (multi). All SIMS analyses are reported as single grains

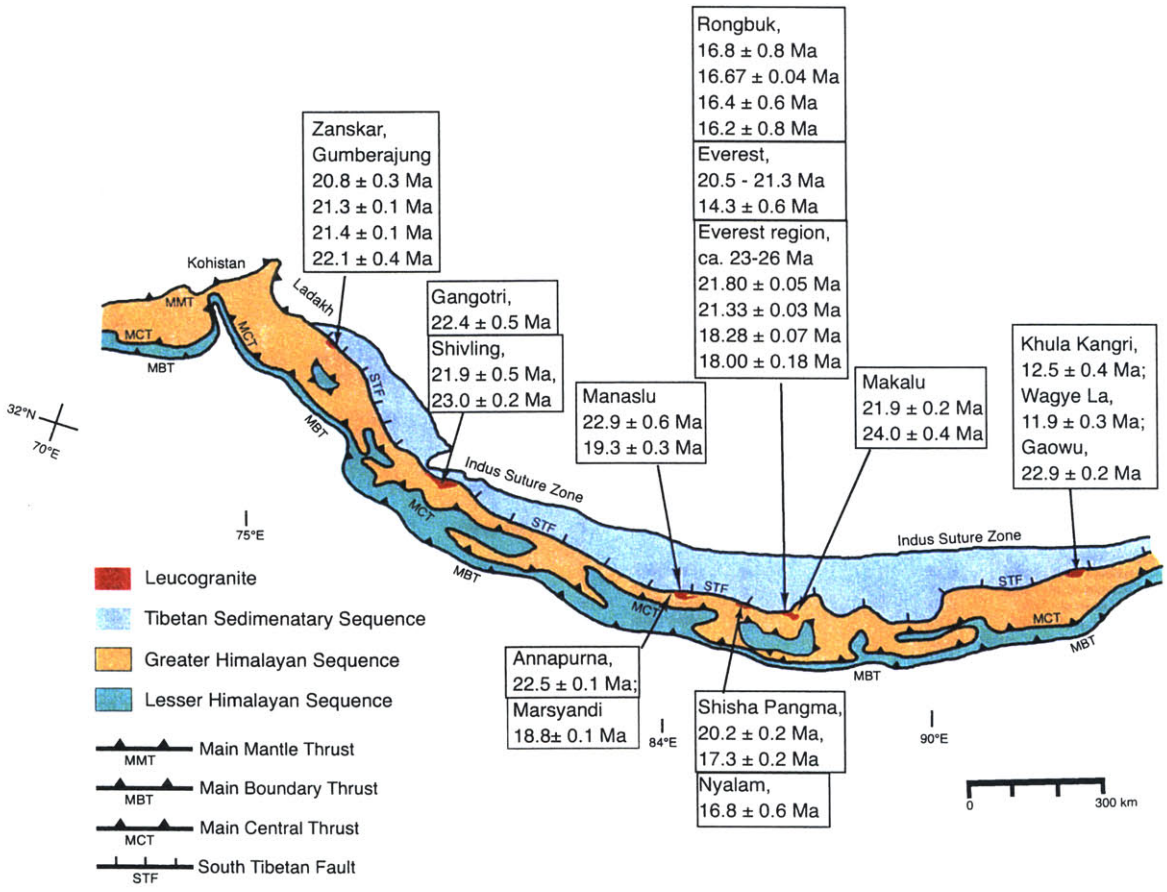


**Figure 1**. Geologic sketch map of the Himalayan orogen highlighting the locations and crystallization ages of leucogranites discussed in the text. References can be found in Table 1.

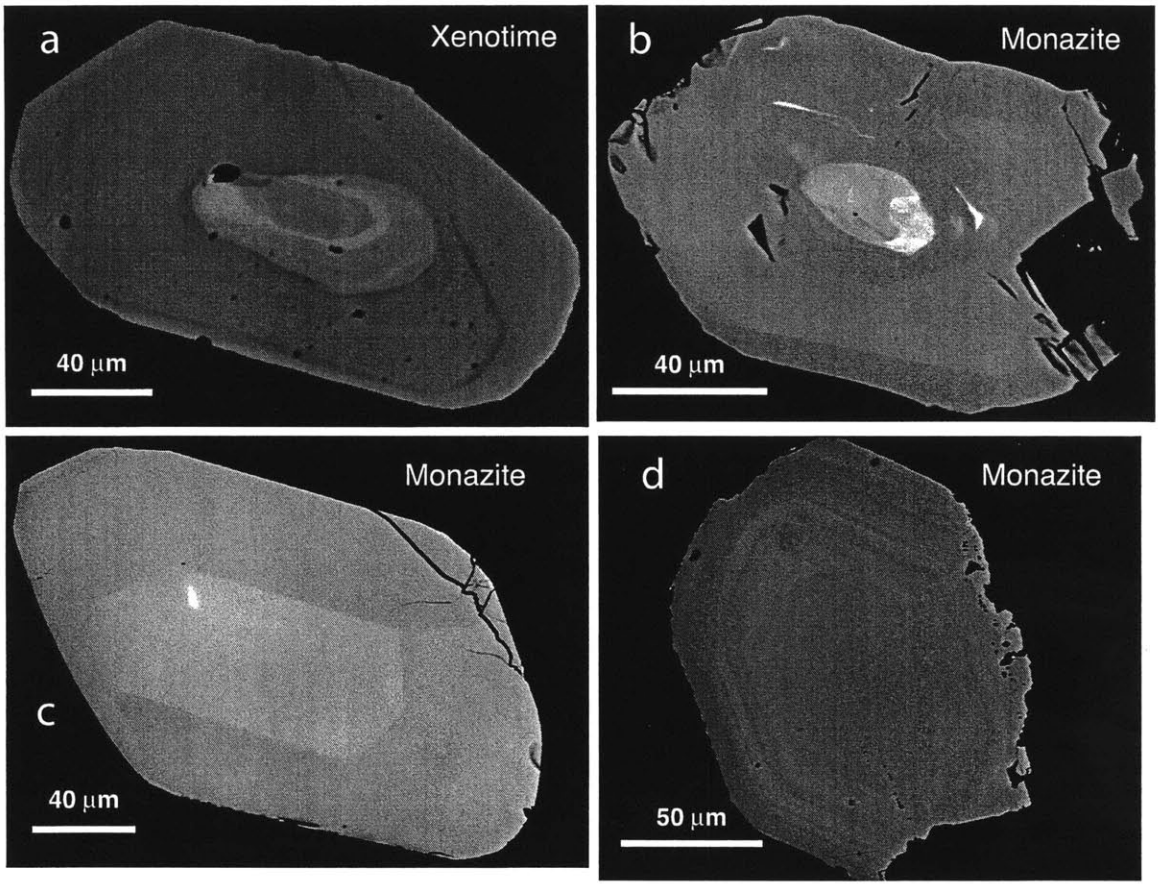


**Figure 2.** Examples of BSE images of monazite and xenotime. The xenotime in (a) has an oscillatory zoned core which is truncated and grown over by more homogeneous rim material. The monazite in (b) also contains an irregular shaped core, suggesting the presence of a xenocrystic component. The monazites in (c) and (d) show sector zoning and symmetric oscillatory zoning, respectively, indicative of magmatic growth.

# Chapter 5

## Summary of Thesis Findings

### Introduction

Anatectic melts in collisional orogens such as the Himalaya provide an important record of heat and mass transfer in the continental crust, and provide some of the most important constraints for the timing of deformational events. Therefore, understanding the tectonic evolution of the Himalayan orogen requires an understanding of the process of crustal anatexis as a function of time. This study was motivated by the need to expand our understanding of the process of crustal melting in the Himalayan orogen, and involved field, geochemical, and geochronological studies of leucogranites and the gneisses they intrude in the Everest region of eastern Nepal. The Everest region was chosen for detailed study due to the excellent exposure, relative abundance of leucogranites, and evidence for the intrusion of multiple generations of leucogranites. Results of these studies were reported in the previous four chapters, one published (Viskupic & Hodges, 2001), and the others as manuscripts about to be submitted. In this final chapter, I summarize the principal findings, reflect on how they change our perceptions regarding granitic magmatism during Himalayan orogenesis, and suggest themes for future research that would expand our understanding further.

### Thermal and Intrusive History of the Greater Himalayan Sequence in the Everest Region

The geochronologic and thermochronologic studies of three outcrops reported in Chapters 1 and 2 describe a consistent thermal and intrusive history for the upper Greater Himalayan Sequence. This history is summarized in Figure 1, where the anatectic, metamorphic, granite crystallization and cooling histories determined for the Namche Bazaar, Gokyo Ri, and

5th Lake outcrops are shown on a timeline. At all three outcrops, there is evidence that melting in the Greater Himalayan Sequence began as early as 25-26 Ma. At the structurally lowest Namche Bazaar outcrop, the combination of U-Pb geochronology and monazite-xenotime thermometry suggested that the Namche migmatitc orthogniess underwent partial melting between 24.8 and 25.4 Ma (Viskupic & Hodges, 2001). At the Gokyo Ri and 5th Lake outcrops, magmatic zircon, xenotime and monazite that crystallized between 23.6 and 25.6 Ma were preserved in granite sills that crystallized at 21.8 Ma and 21.3 Ma, respectively. Metamorphic monazite was growing in country rock gneisses between 23.3 Ma and 22.0 Ma (Namche Bazaar), at 22.6 Ma (Gokyo Ri), and between 21.0 Ma and 24.4 Ma (5th Lake). At the Namche Bazaar outcrop, the orthogneiss country rock cooled to ~530°C by 22 Ma. The 21.8 Ma and 23.3 Ma granite sills at the Gokyo Ri and 5th Lake outcrops, had cooled below 380°C by 19 Ma. Although the Greater Himalayan Sequence at these structural levels had cooled below temperatures appropriate for anatexis by 19 Ma, evidence for continued melting, at deeper structural levels, is provided by post-deformational leucogranite dikes at all three outcrops that crysttallized between 17.6 and 18.3 Ma. The concordance of $^{40}Ar/^{39}Ar$ biotite dates and U-Pb monazite dates from these dikes demonstrates that they cooled rapidly.

The thermal and intrusive history reported in Chapters 1 and 2 enhances our understanding of the pressure-temperature history of the upper Greater Himalayan Sequence (Figure 2) as determined by metamorphic studies in the Everest region by Pognante and Benna (1993), Simpson et al. (2000) and Simpson (2002). Several research groups working in the central and eastern Himalaya have found evidence for two major metamorphic "events" related to Himalayan orogenesis (see Hodges, 2000, for a review). In general, the M1 "Eohimalayan" event was characterized by higher pressures and somewhat lower temperatures than the M2

"Neohimalayan" event. In the Everest region, Pognante and Benna (1993) estimated peak Eohimalayan conditions to have been between 600-700°C at 7-8 kb, and peak Neohimalayan conditions to have been between 600-700°C at about 4 kb. Simpson, et al. (2000) constrained the timing of M1 and M2 to be ca. 32 Ma and 23 Ma, respectively, by dating metamorphic monazite from gneisses in the upper Greater Himalayan Sequence in the Everest region. Accessory phase growth associated with M1 metamorphism was not observed in the gneisses sampled as part of my thesis research. However, the timing of metamorphic monazite growth in gneisses at the Namche Bazaar, Gokyo Ri, and 5$^{th}$ Late outcrops corresponds to the timing of M2 metamorphism determined by Simpson et al. (2000). The earliest crustal melting in the Everest region took place between 26.3 and 23.6 Ma (Chapter 2) which is temporally associated with the implied decompression between M1 and M2 (Figure 2) metamorphism, suggesting a link between decompression and anatexis.

**Orogen-wide Intrusive History of the Greater Himalayan Sequence**

Granite crystallization ages from the entire orogen (Chapter 4) are summarized along with the anatectic, metamorphic, and cooling histories for the three Everest region outcrops in Figure 3. Clearly, crustal melting in the Greater Himalayan Sequence did not occur during one or two distinctive "events" of short duration, but rather was episodic to continuous over a broad time interval extending at least from ca. 26 to ca. 16 Ma. Previous suggestions that melting occurred in two phases at ca. 22 Ma and ca. 19 Ma (Harrison et al., 1998, 1999a) were based on limited geochronologic data from several of the largest Himalayan plutons. Some leucogranites in the orogen are still younger, with crystallization ages of ca. 14 and ca. 12 Ma, but whether these indicate and extension of the long-term melting process or distinct phases of melting

remains unclear. Evidence for melting over nearly ten million years is seen at the scale of the orogen (Chapter 4), at the regional scale (Chapters 1 and 2 + Rongbuk Valley; Hodges et al., 1998; Murphy & Harrison, 1999), and at the scale of single outcrops (Chapter 2). This protracted melting history implies that temperatures in regions of the Himalayan metamorphic core were high enough to sustain anatexis (>650°C) for over ten million years.

**Relationship Between Faulting and Anatexis**

The timing of earliest crustal melting in the Greater Himalayan sequence predates known movements on the MCT and STF by at least 3 million years (Hodges, 2000). However, as described above, this early crustal melting is temporally associated with decompression, which implies that either large-scale normal faulting began as early as 26 Ma, or that rapid erosional denudation was responsible for early decompression. If decompression was due solely to erosion, melting at 26 Ma could have initiated the development of the MCT or STF systems by crustal weakening due to the accumulation of melt (e.g. Hollister & Crawford, 1986; Nelson, et al., 1996). Alternately, if the rapid cooling experienced between ca. 21 and 19 Ma in the upper Greater Himalayan Sequence (Chapter 2) was the result of tectonic exhumation, later melting might have been caused by decompression. An inability to date displacement events on structures of the STF system independently of dating granites themselves prevents objective evaluation of these possibilities. Clearly, there is a temporal association between decompression and melt generation, but the results presented in this study do not constrain whether that decompression was related to tectonic or erosional unroofing.

**Melt Production and Mobilization**

Although melting in the Greater Himalayan Sequence began at least as early as 26 Ma, there is little evidence that this melt migrated from its source region. Xenotime, monazite and zircon that crystallized during this early period of melting between ca. 26 Ma and ca. 23 Ma were later entrained in melts that crystallized as sills at 21.8 and 21.3 Ma. Intrusion of these syn-kinematic sills is the first evidence for melt mobilization in the Everest region. The timing of this earliest melt mobilization roughly coincides with the emplacement of many of the largest plutons in the Himalaya (Chapter 4), and with the earliest know movements on the MCT and STF systems (Hodges, 2000), suggesting a link between tectonic reorganization and melt migration.

The data presented in Chapter 2 are consistent with a model for melt production in which episodic to semi-continuous pulses of melting in the same source region produce small volumes of melt that crystallize at slightly different times. Eventually, when the melt fraction becomes large enough to mobilize, or when melt migration is enhanced by deformation, the migrating melt incorporates products of the slightly older melts, likely redissolving some older accessory minerals, but incorporating others as xenocrysts. The result is a mobilized, low-temperature melt with an array of accessory minerals of different ages that record the time scales of anatexis in a single source region. The fact that small dikes (10-20 cm wide) can be emplaced in country rocks whose temperatures are far below those appropriate for melting (<400°C) suggests that granitic melts may travel long distances as thin dikes. This may also suggest the importance of deformation-enhanced melt migration, whereby the buildup of melt pressure leads to fracturing and channelized melt flow.

**Accessory Mineral Isotopic Studies**

The combination of U-Pb dating of monazite and xenotime with Nd isotopic characterization of the same grains (Chapter 3) is an important contribution of my thesis research. Because accessory minerals such as monazite, xenotime and apatite control the Nd budget of most granites and pelitic gneisses, the most reliable way to isotopically fingerprint a crustal melt is to determine the isotopic compositions of magmatic accessory minerals. Combining backscattered electron imaging and U-Pb geochronology allowed the identification of magmatic accessory minerals as well as the presence of minerals with inherited xenocrystic components. The observation that magmatic monazite almost always records the whole-rock Nd isotopic signature reflects the dominant role monazite plays in controlling the whole-rock's Nd isotopic budget. However, the observation that some magmatic monazites and all magmatic xenotimes have Nd isotopic compositions that are more (xenotime) or less (monazite) radiogenic than the whole-rock Nd isotopic composition supports a model for melt generation where accessory phases grow from melts that are isotopically heterogeneous at the scale of a hand sample.

Limited data from this study and from combined U-Pb and Nd studies of the Shisha Pangma (Searle et al., 1997) and Manaslu plutons (Harrison et al., 1999b) suggest that there may be a relationship between Nd isotopic composition and granite crystallization age, with younger melts in the same region having less radiogenic compositions. This trend may reflect a regional change in the leucogranite source composition with time, perhaps due to the exhaustion of high Sm/Nd minerals such as apatite and xenotime which would then have less leverage on the composition of crustal melts.

## Accessory Mineral Thermometry

The combination of U-Pb geochronology and accessory phase thermometry provides a powerful tool with which to directly link determinations of temperature and time. While the combination of U-Pb geochronology and quantitative monazite-xenotime thermometry (Chapter 1) provided important constraints on the anatectic and metamorphic history of the Namche migmatitic orthogneiss, the isotopic study in Chapter 3 suggests caution in applying this technique to accessoory phases that have been separated from their host rock. Monazite and xenotime from a single hand sample that crystallized at the same time may not be in isotopic equilibrium (Chapter 3). Future studies that utilize monazite-xenotime thermometry should follow the same guidelines that are used in the application of traditional thermobarometers, examining accessory minerals on the scale of a thin section, looking for monazite-xenotime pairs that are adjacent to each other where chemical equilibrium is more likely to have been achieved.

## Geochronologic Methods

The geochronologic review presented in Chapter 4 shows that, until recently, most U-Pb IDTIMS studies of Himalayan leucogranites did not include attempts to understand the mineralogical "history" of the accessory phases being dated. Young overgrowths on old grains are common, and even single-crystal dates of accessory minerals may not be enough to decipher the crystallization history of a polygenetic accessory mineral suite. In an effort to better understand the nature of such suites, some researchers (e.g., Harrison et al., 1995) have employed the high spatial resolution of the ion microprobe in the dating of Himalayan leucogranites. Unfortunately, none of the "IMSIMS" studies to date have been accompanied by high-resolution backscattered electron or cathodoluminescence imaging necessary to interpret

fully the geochronologic results in the context of intracrystalline zoning. Without such context, IMSIMS data are no more useful than IDTIMS data for carefully sampled grain fragments when exploring age variability in zoned crystals. Moreover, the IMSIMS technique suffers from much higher analytical imprecision. This is particularly striking when comparing IDTIMS and IMSIMS data for granites containing relatively simple accessory mineral suites. Figure 4 is a direct comparison of data from two published geochronologic studies of a single, large leucogranitic sill in the Rongbuk Valley of southern Tibet; the IDTIMS monazite, xenotime and zircon data of Hodges et al. (1998) show considerably greater consistency among independent analyses than the IMSIMS monazite data of Murphy and Harrison (1999). The large analytical uncertainties associated with individual IMSIMS analyses make the geologic significance of the range in dates difficult to evaluate, and result in an estimation for the crystallization age of the sill that is roughly twenty times less precise than the corresponding IDTIMS estimation.

The techniques I used for imaging and cutting individual grains of monazite and xenotime largely followed the work of Hawkins and Bowring (1997, 1999). The studies reported here represent the first effort to systematically apply these techniques to the dating of Himalayan leucogranites. The advantages of dating imaged grains and grain fragments with the high-precision IDTIMS technique are clearly shown in Chapters 1 and 2.

The best approach to dating such young, low-temperature granites should start with grain characterization using backscattered electron or cathodoluminescence imaging. Once grains are characterized in terms of inclusion suites, zoning patterns, and the potential presence of inherited components, grains can be selected for analysis, or cut to isolate different growth phases before analysis. In the case where only a single-aged population of accessory minerals is present, the IMSIMS technique can provide an easily interpreted granite crystallization age. When a higher

precision technique is needed, such as when a sample contains accessory minerals with a range of crystallization ages, IDTIMS analyses of carefully selected single grains and grain fragments provide the best approach to understanding granite genesis and crystallization. Dating a variety of accessory minerals (zircon, monazite, xenotime, uraninite) is also an important approach to take since different accessory phases may provide information about different periods during the melt generation and crystallization process. In particular, the common avoidance of zircon in geochronologic studies of Himalayan leucogranites is unnecessary. Although inherited zircon is common in Himalayan leucogranites, magmatic zircon with no pre-Himalayan inheritance also occurs, and may provide some of the most precise estimates of granite crystallization ages.

**Future Work**

The demonstration that geochronologic and geochemical observations at the outcrop scale mimic those at the pluton scale suggests that systematic studies of accessible, small-scale melts are appropriate, and in some cases favorable, ways to investigate the anatectic history of the Himalayan orogen. This observation alone suggests a new starting point for future studies of Himalayan leucogranites.

There are several avenues of future research that follow from the results in Chapter 3 on the Nd and Sr isotopic signatures in accessory phases. The most obvious is that the Nd isotopic compositions of additional xenotimes need to be measured in order to be more confident in, or to disprove, my hypothesis that xenotimes have more radiogenic Nd isotopic compositions than monazites in the same rock. In addition to more xenotime analyses, it may also prove important to determine the Nd isotopic signatures of apatite and garnet in suspected source rocks and in granites in order to understand better their role in processes of metamorphism and anatexis, and

their value in the determination of whole-rock isotopic signatures. Based on limited data, I suggest that Nd isotopic compositions might preserve a record of changing source-rock composition with time, with younger leucogranites accessing a less radiogenic source composition. This hypothesis can be tested with combined U-Pb and Nd isotopic studies.

One of the intriguing results described in Chapter 2 is the preservation of older magmatic accessory phases in younger granite sills. The fact that these early non-mobilized melt products were entrained and transported in syn-kinematic dikes provides a case for deformation-enhanced melt migration. It is, perhaps, not surprising that deformation-enhanced melt migration could have played a role in the emplacement of Himalayan leucogranites. It is surprising, however, that my evidence for its having taken place resides in the geochemistry of accessory minerals, and is not entirely based on field observations such as the presence of melt in shear zones (e.g. Brown & Solar, 1998). Given the observation that so many Himalayan leucogranites contain accessory phases of a variety of ages (Table 1; Chapter 4), the Himalaya may provide a place to study the processes of melt migration based on geochemical as well as on field observations. The presence of older magmatic accessory minerals in other syn-kinematic granites could provide further evidence for the importance of deformation in the migration of crustal melts.

Finally, the observations that anatectic melts were generated in the Greater Himalayan Sequence over approximately 10 million years, that the entire history of melting is preserved in small regions, and that some granites were generated and intruded during or after rapid cooling of the upper Greater Himalayan Sequence, show that the Greater Himalayan Sequence experienced a complex thermal history. The constraints provided by these observations should be used to inspire and evaluate future thermal and tectonic models for the evolution of the Himalayan orogen.

## References


Brown, M., Solar, G.S. (1998) Shear-zone systems and melts: feedback relations and self-organization in orogenic belts. Journal of Structural Geology, v. 20, p. 211-227.

Harrison, T.M., Grove, M., Lovera, O.M., Catlos, E.J. (1998) A model for the origin of Himalayan anatexis and inverted metamorphism. Journal of Geophysical Research, v. 103, p. 27017-27032.

Harrison, T.M., Grove, M., Lovera, O.M., Catlos, E.J., D;Andrea, J. (1999a) The origin of Himalayan anatexis and inverted metamorphism: models and constraints. Journal of Asian Earth Sciences, v. 17, p. 755-772.

Harrison, T.M., Grove, M., McKeegan, K.D., Coath, C.D., Lovera, O.M., Le Fort, P. (1999b) Origin and episodic emplacement of the Manaslu intrusive complex, central Himalaya. Journal of Petrology, v. 40, p. 3-19.

Harrison, T.M., McKeegan, K.D., Le Fort, P. (1995) Detection of inherited monazite in the Manaslu leucogranite by $^{208}Pb/^{232}Th$ ion microprobe dating: Crystallization age and tectonic implications. Earth and Planetary Science Letters, v. 133, p. 271-282.

Hawkins, D.P., Bowring, S.A. (1997) U-Pb systematics of monazite and xenotime: case studies from the Paleoproterozoic of the Grand Canyon, Arizona. Contributions to Mineralogy and Petrology, v. 127, p. 87-103.

Hawkins, D.P., Bowring, S.A. (1999) U-Pb monazite, xenotime and titanite geochronological constraints on the prograde to post-peak metamorphic thermal history of Paleoproterozoic migmatites from the Grand Canyon, Arizona. Contributions to Mineralogy and Petrology, v. 134, p. 150-169.

Hodges, K.V. (2000) Tectonics of the Himalaya and southern Tibet from two perspectives. Geological Society of America Bulletin, v. 112, p. 324-350.

Hodges, K., Bowring, S., Davidek, K., Hawkins, D., Krol, M. (1998) Evidence for rapid displacement on Himalayan normal faults and the importance of tectonic denudation in the evolution of mountain ranges. Geology, v. 26, p. 483-486.

Hollister, L.S., Crawford, M.L. (1986) Melt-enhanced deformation: A major tectonic process. Geology, v. 14, p. 558-561.

Le Breton, N., Thompson, A.B. (1988) Fluid-absent (dehydration) melting of biotite in metapelites in the early stages of crustal anatexis. Contributions to Mineralogy and Petrology, v. 99, p. 226-237.

Mukhopadhyay, B., Holdaway, M.J. (1994) Cordierite-garnet-sillimanite-quartz equilibrium I: new experimental calibration in the system $FeO-Al_2O_3-SiO_2-H_2O$ and certain $P-T-X(H_2O)$ relations. Contributions to Mineralogy and Petrology, v. 116, p. 462-472.

Murphy, M.A., Harrison, T.M. (1999) Relationship between leucogranites and the Qomolangma detachment in the Rongbuk Valley, south Tibet. Geology, v. 27, p. 831-834.

Nelson, K.D., et al. (1996) Partially molten middle crust beneath Southern Tibet: Synthesis of project INDEPTH results. Science, v. 274, p. 1684-1688.

Pognante, U., Benna, P. (1993) Metamorphic zonation, migmatization and leucogranites along the Everest transect of eastern Nepal and Tibet: record of an exhumation history. In Treloar, P.J., Searle, M.P. (eds). Himalayan Tectonics. Geological Society of London Special Publication no. 74, p. 323-340.

Searle, M.P., Parrish, R.R., Hodges, K.V., Hurford, A., Ayres, M.W., Whitehouse, M.J. (1997) Shisha Pangma leucogranite, south Tibetan Himalaya: field relations, geochemistry, age, origin, and emplacement. Journal of Geology, v. 105, p. 295-317.

Simpson, R.L. (2002) Metamorphism, melting and extension at the top of the High Himalayan slab, Mount Everest region, Nepal and Tibet. Ph.D thesis, University of Oxford.

Simpson, R.L, Parrish, R.R., Searle, M.P., Waters, J.D. (2000) Two episodes of monazite crystallization during metamorphism and crustal melting in the Everest region of the Nepalese Himalaya. Geology, v. 28, p. 403-406.

Spear, F.S. (1993) Metamorphic Phase Equilibria and Pressure-Temperature-Time Paths. Mineralogical Society of America Monograph, Washington, D.C., 799 p.

Viskupic, K., Hodges, K.V. (2001) Monazite-xenotime thermochronometry: methodology and an example from the Nepalese Himalaya. Contributions to Mineralogy and Petrology, v. 141, p. 233-247.

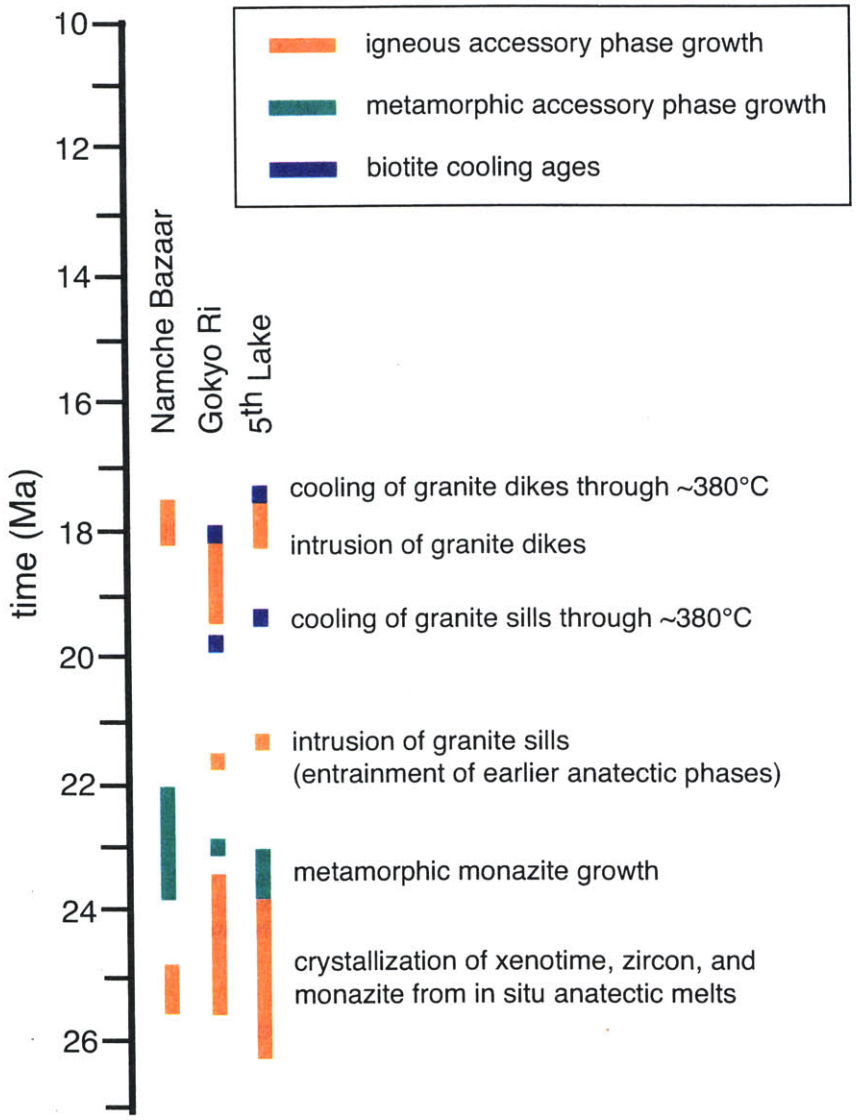


**Figure 1**. Timeline illustrating the thermal and anatectic evolution of the upper Greater Himalayan Sequence in the Everest region as determined in Chapters 1 and 2.

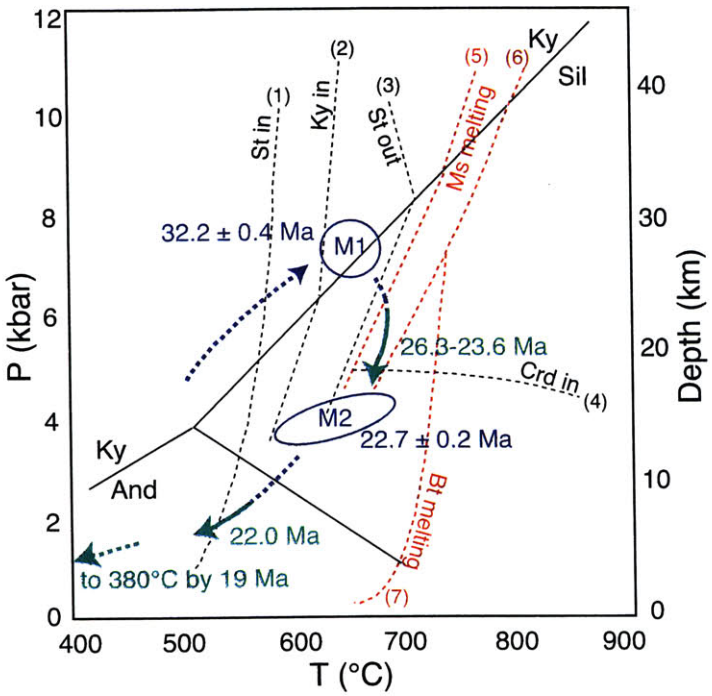


(1) Grt + Chl = St + Bt + V (Spear, 1993)
(2) St + Chl = Bt + Ky + V (Spear, 1993)
(3) St = Grt + Bt + As + V (Spear, 1993)
(4) Alm + Sil + Qtz + V = Crd (Mukhopadhyay & Holdaway, 1994)
(5) Ms + Ab + Qtz = Kfs + As + Melt (Le Breton & Thompson, 1988)
(6) Ms + An + Qtz = Kfs + Ab + Melt (Le Breton & Thompson, 1988)
(7) Bt + Als + Pl + Qtz = Grt + Kfs + Melt (Le Breton & Thompson, 1988)

**Figure 2**. Pressure-temperature evolution of the upper Greater Himalayan Sequence in the Everest region. PT path and dates in blue from Simpson et al. (2000) and Simpson (2002). PT path and dates in green from this study. Figure modified from Simpson (2002).

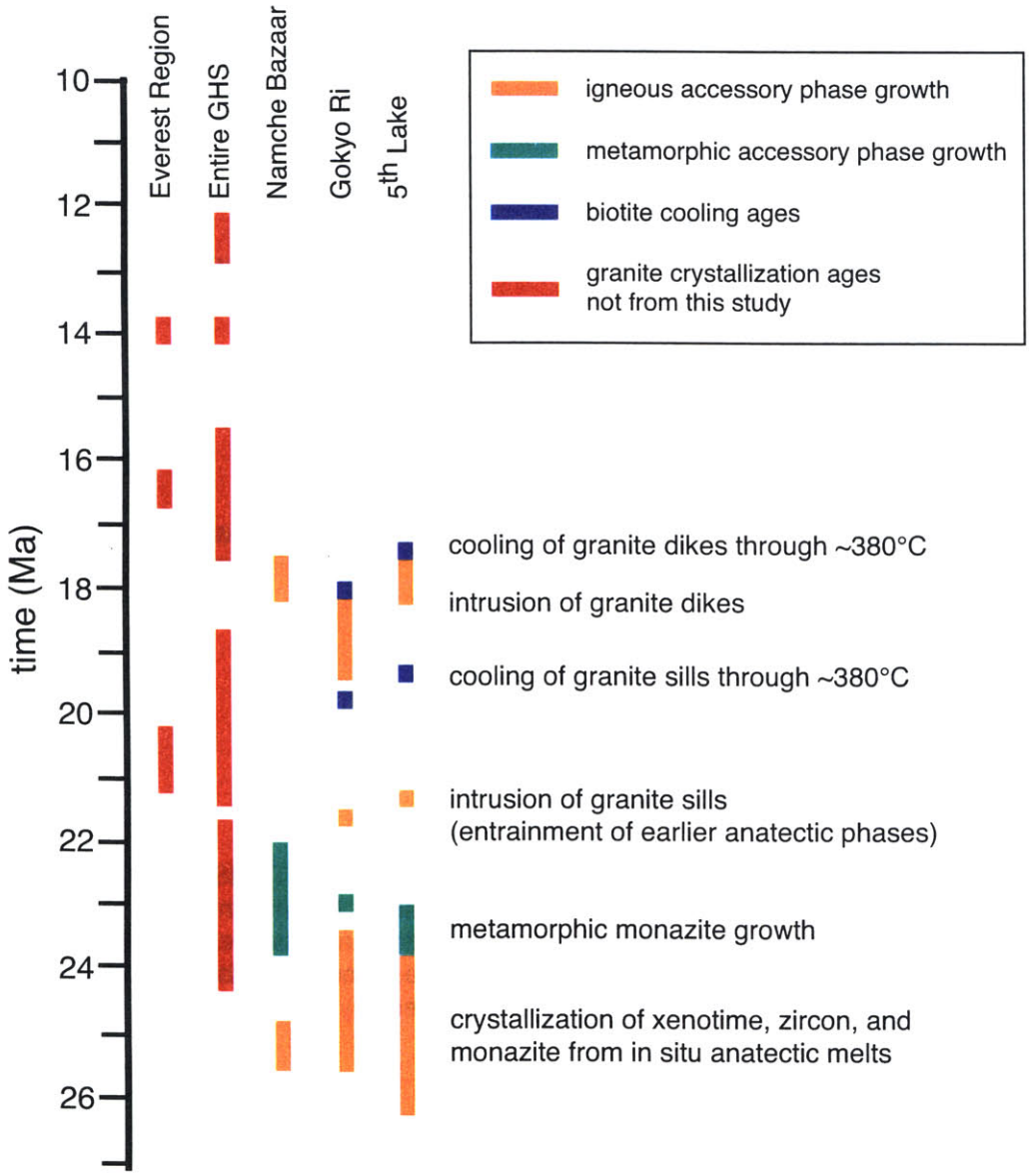


**Figure 3.** Timeline illustrating the thermal and anatectic history of the Greater Himalayan Sequence in the Himalayan orogen. References for dates in red can be found in Chapter 4.

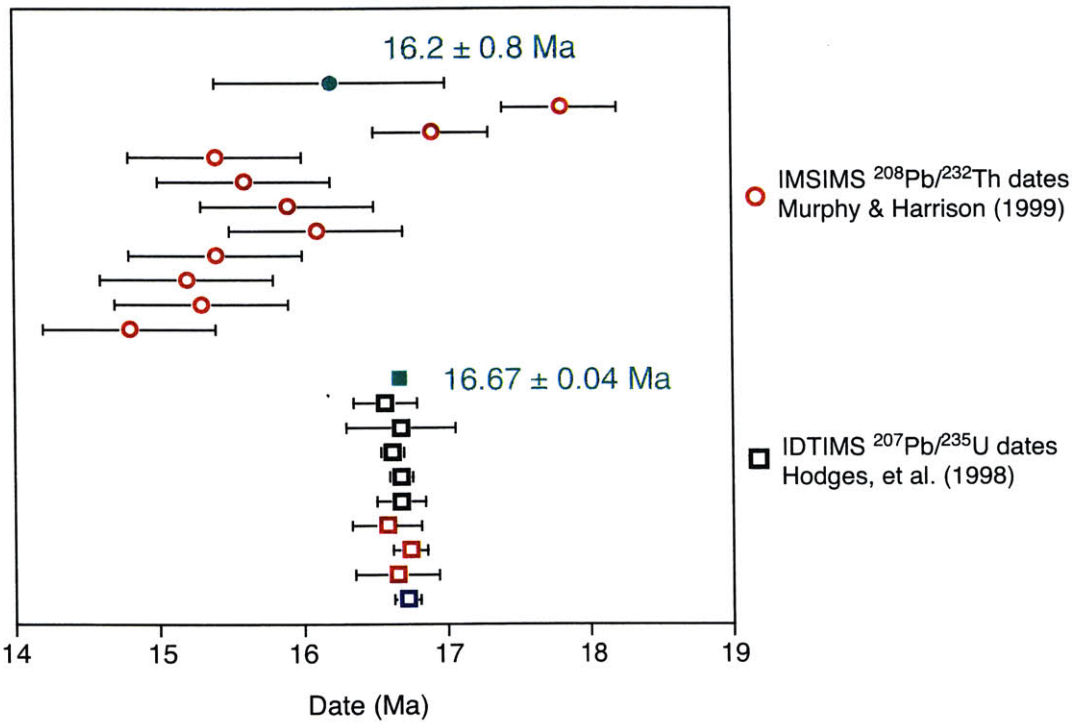


**Figure 4**. Comparison between IMSIMS (round symbols) and IDTIMS analyses (square symbols) from a granite sill in the Rongbuk Valley. Open symbols indicate individual analyses where red=monazite, black=xenotime, and blue=zircon. Weighted mean dates, interpreted by the respective authors to be granite crystallization ages, with two standard errors, are indicated by the filled green symbols.